2015-01-14

Near Optimal Indoor Localization With Coherent Array Reconciliation Tomography

Antti Koski

Worcester Polytechnic Institute

NEAR OPTIMAL INDOOR LOCALIZATION WITH
COHERENT ARRAY RECONCILIATION TOMOGRAPHY

by

Antti E. Koski

A Dissertation
Submitted to the Faculty
of the
WORCESTER POLYTECHNIC INSTITUTE
in partial fulfillment of the requirements for the
Degree of Doctor of Philosophy
in
Electrical and Computer Engineering
by

_____

February 2015

APPROVED:

_____
Dean David Cyganski, Major Advisor

_____
Professor R. James Duckworth

_____
Professor Homer Walker

Abstract

Our increased reliance on localization devices such as GPS navigation has led to an increased demand for localization solutions in all environments, including indoors. Indoor localization has received considerable attention in the last several years for a number of application areas including first responder localization to targeted advertising and social networking. The difficult multipath encountered indoors degrades the performance of RF based localization solutions and so far no optimal solution has been published.

This dissertation presents an algorithm called Coherent Array Reconciliation Tomography (CART), which is a Direct Positioning Algorithm (DPA) that incorporates signal fusion to perform a simultaneous leading edge and position estimate for a superior localization solution in a high multipath environment. The CART algorithm produces position estimates that are near optimal in the sense that they achieve nearly the best theoretical accuracy possible using an Impulse Radio (IR) Ultra-Wideband (UWB) waveform. Several existing algorithms are compared to CART including a traditional two step Leading Edge Detection (LED) algorithm, Singular value Array Reconciliation Tomography (SART), and Transactional Array Reconciliation Tomography (TART) by simulation and experimentation. As shown under heavy simulated multipath conditions, where traditional LED produces a limited solution and the SART and TART algorithms fail, the CART algorithm produces a near statistically optimal solution. Finally, the CART algorithm was also successfully demonstrated experimentally in a laboratory environment by application to the fire fighter homing device that has been a part of the ongoing research at Worcester Polytechnic Institute (WPI).

Contents

List of Figures

List of Tables

Chapter 1

Introduction

Indoor localization has received considerable attention in the last decade due to potential commercial interests, personal safety benefits, and other application areas that directly benefit our lives. The inoperability of Global Positioning Systems (GPS) inside most structures has lead researchers searching for new solutions to address the demand for more precise and robust localization solutions. The commercial sector is interested in improving the customer experiences in novel ways through localization and the first responder community is interested in saving lives, e.g. in search and rescue operations.

Recently, new waveforms such as Ultra-Wideband (UWB) Impulse Radio (IR) using Time of Arrival (TOA) have come under scrutiny as a potential contender for a viable solution to indoor localization. The primary benefits of an UWB IR waveform for indoor localization is its ability to separate channel reflectors more precisely than their narrowband counterparts due to their fine time resolution and their resistance to multipath fading [1]. In fact, UWB is heavily used in ground penetrating radars [2] due to these benefits. Similarly, UWB allows more precise and robust localization in difficult indoor multipath environments, where physical structures prevent a direct Line of Sight (LOS) from transmitter to receiver.

This dissertation considers the case of one coherent UWB transmitter and multiple coherent UWB receivers in an unknown indoor multipath environment. By coherence we mean that the receivers know the transmit time, which enables TOA localization as opposed to Time Difference of Arrival (TDOA) localization. The method of achieving coherence is discussed later in this section. In addition, we always assume the direct path signal from the transmitter to the receiver exists with a defined Signal to Noise Ratio (SNR).

In most cases authors [3] [4] [5] describe TOA localization using the traditional two step approach

in which ranging and positioning are performed as two independent steps. This involves estimating the leading edge of the transmitted waveform at individual receiver locations to determine the range from the transmitter to each receiver, followed by some algorithm to find the transmitter position using the ranges. The Leading Edge Detection (LED) algorithms typically include some combination of a Matched Filter (MF), an energy detector, and a threshold, followed by a search to determine the first arriving peak as seen in [6] and many other publications. The positioning algorithm can be based on a mechanism as simple as a minimization or Weighted Least Squares (WLS) solution for the location satisfying the constraints imposed by the range estimates as seen in [7].

Consider, for example, the sensor setup shown in Figure 1.1a in an ideal environment free of multipath, noise, and fading effects. For this example, there exists a single transmitter at (x_m, y_m) and four receivers in a square. If the transmitter transmits a very narrow pulse seen as a band limited impulse, the received waveforms would look similar to Figure 1.1b. The received waveforms are dependent on the time it takes for the signal to propagate through the environment to the receiver. The range from the transmitter to the receivers can be measured as the time of the peak of the band limited impulse or when the signal leading edge arrived prior to the peak, depending on how the system is calibrated. In the traditional two step approach, the estimate of ranges from the transmitter to each receiver is done independently and is the first step in localization. The independently estimated ranges suggest the transmitter can lie on a circle in two dimensions centered at the respective receiver as seen by example in Figure 1.1c. The estimate in Cartesian coordinates is produced by computing the intersection of these circles and is the second step of the two step approach.

The problem with the two step approaches is that they treat each receiver signal independently and they treat the localization as two independent steps. The independent range estimates under multipath conditions will likely not have a single point of intersection as shown in the ideal example in Figure 1.1c. The ranges will therefore present an inconsistent set of constraints to the positioning algorithm. In addition, there is also some known dependence between the data at each receiver if their locations are known and there exists a single transmitter, as is the case for the treatment in this dissertation. Literature describes the method of using the raw received data to produce a direct estimate of position in a single step as Direct Positioning Algorithms (DPA). Closas, et. al [8] conclude that improved accuracy and robustness can be achieved by considering the fact that the signal originated from the same source. The same conclusion is drawn by Navarro, et. al in [9] where UWB TOA data is used to compare the two step procedure to a DPA by simulation. Other DPAs introduced in literature are the Singular value Array Reconciliation Tomography (SART) [10] [11] and the Transactional Array Reconciliation

(a) Sensor Setup

(b) Received Data

(c) Intersection of Circles
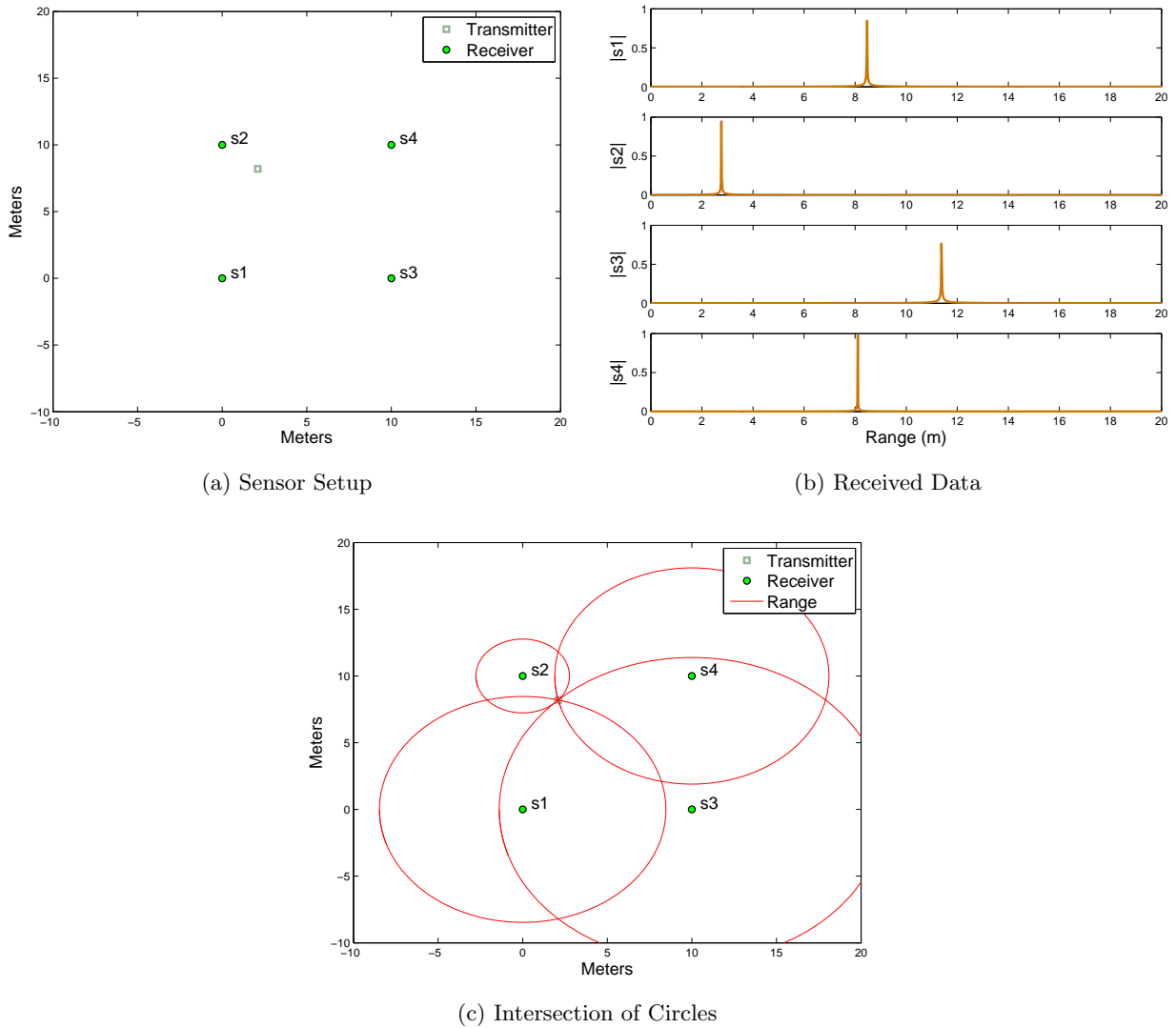
Figure 1.1: (a) Example sensor setup, (b) example data at each receiver, (c) circles using estimated ranges.

Tomography (TART) [12], which require the signal at each receiver along with knowledge of receiver positions. In the case of the SART algorithm which computes a TDOA solution, synchronization of the transmitter to the receiver is not required, whereas the TART algorithm which performs TOA estimation requires synchronization.

Few papers exist on the direct positioning methods while many papers exist using the two step approaches. This is likely due to the nature of problems and how their solutions have evolved over time. For example, WiFi localization methods such as [13] [14] always rely on existing infrastructure that measures Receive Signal Strength (RSS) to produce estimates of independent ranges or to characterize

WiFi environments. The added complexity of DPAs also may prevent practical implementations since they are often computed in a greedy manner.

Bialer, et. al. [15] express a Maximum Likelihood (ML) Direct Position Estimate (DPE) based the collection of received data. The method expands upon their previous ML TOA estimation method using a single transmitter and a single receiver [16]. As shown, the method partitions the received signal into two segments: one that is expected to contain noise only and one that is expected to contain the leading edge of the transmitted signal along with noise samples. The ML DPE algorithm, however, requires the computation of a power delay profile, which is based upon a channel model or a measured channel impulse response. In reality, specular reflectors exist that will distort the ML DPE metric in an unknown environment when using a modeled channel and a measured channel impulse response is only optimal for a specific location and sensor geometry. In addition, the ML DPE is based on a power metric, when in reality there exists coherence among the received leading edges that can be included in the localization metric.

We recognize that the SART and TART algorithms were designed to use a wideband multicarrier non-impulsive signal [17] and was not designed to take advantage of UWB Impulse Radio (IR) waveform features. A new algorithm is needed to take advantage of the UWB IR features with the same computational principles. In this dissertation, we present a new DPA called Coherent Array Reconciliation Tomography (CART) based on the segmentation of the received signals into two segments as was done in [15]: one that should contain the leading edge of the signal embedded in noise and one that should contain noise only. The CART algorithm produces a simultaneous leading edge and position estimate based upon a search of consistent ranges to produce the simultaneous best estimate. The computation is performed in a greedy manner typically using a single independent data capture from each receiver, regardless of channel delay profile or unknown channel characteristics.

So far, nothing has been mentioned about the practical implementation requirements of the example system seen in Figure 1.1a. We simply show a transmitter and four receivers in an ideal environment. In reality, the received signal will be corrupted by multipath, additional reflections that bounce off walls, furniture, and other objects in the indoor environment. In addition, the signal experiences excess delay and attenuation dependent on the building materials. We can model these effects as seen in Section 2.1. Even more fundamentally, how do we collect UWB data that preserves the TOA information? We could have a tethered solution where the transmitter and receivers are all connected by wire to a central data collection system. Others have also asked this question, which has led to advancements in the area of wireless synchronization.

The untethered requirement has led to the development of Two Way Ranging (TWR) systems for localization [18]. The primary operating principle of TWR, as discussed in Section 5.1, is that one requesting unit sends a pulse that is detected by a responding unit. The responding unit then sends a pulse that is received by the requesting unit. The requesting unit then performs a computation to determine the distance of the responding unit based on the duration of the TWR event. The primary advantage of this TWR method is that clock synchronization is not required between the requester and responder [19], enabling wireless range measurement. The drawback is that each TWR event is considered an independent measurement with no obvious correlation over time as sensors move in a dynamic fashion. It is also not immediately possible to combine the signals from multiple receivers using signal fusion. This is particularly important in the highly specular UWB environments where small movements can cause dramatic changes in the wireless channel response.

Research in this area, such as [20] [21], has focused on improving the localization accuracy or estimation accuracy of the TWR event, but has not addressed the dynamic sensor movement problem. The author of [17] uses the sampled channel data to synchronize two periodic transmitted waveforms using a stationary reference transmitter, but make no mention of dynamic sensors. In this dissertation, we also present a method that enables wireless data collection using the requester and responder raw channel samples to estimate the transmit time, which in turn is used to preserve TOA information. In this dissertation, this new method of data alignment is used to collect experimental data using Time Domain's PulseOn 410 (P410) UWB device. The experiments compare the localization performance of the traditional two step approach using LED, to two existing DPAs, SART and TART, followed by a comparison to the new CART algorithm using Mean Squared Error (MSE) analysis and by Cumulative Density Function (CDF) of errors.

The primary contribution of this dissertation is the development of the CART algorithm that combines LED, direct positioning, and coherent integration of the direct signal path information obtained from the requester and responder devices. The CART algorithm is suitable for UWB TOA data and requires no prior characterization or anchor nodes for successful operation. Another contribution includes the comparison of the performance of several existing algorithms, SART, TART and the conventional two step LED method to CART using the standard IEEE 802.15.4a multipath model for the indoor office environment. Also, a new algorithm that preserves TOA information from a Two Way Ranging (TWR) conversation is developed along with the application of the CART algorithm to the real problem of first responder localization using a wand homing device. The wand homing device application also includes a theoretical wand length analysis based on the statistical Cramer Rao Lower Bound.

Even though the requester and responder units used in the TWR event are transceivers, we refer to the requester unit and associated hardware as the receiver and we refer to the responder and associated hardware as the transmitter. For more information on the hardware details, see Chapter 5.

This paper is organized as follows: Chapter 2 provides the necessary background to the two step Leading Edge Detector (LED), SART, and TART algorithms for localization. For further information on any of these methods, we refer the reader to the cited sources in the respective subsections. Chapter 3 introduces the CART algorithm. Chapter 4 shows the simulation results using the IEEE 802.15.4a CM4 model of an indoor office environment. Chapter 5 introduces the hardware used to perform synchronized data collection. In Chapter 6, we demonstrate the CART algorithm using recent data collected at Worcester Polytechnic Institute in two test environments. Chapter 7 presents the results of the fire fighter homing device implementation, in which we fuse RF data and a gyroscopic based motion solution using the CART algorithm.

Chapter 2

Background

This chapter provides the necessary background on the traditional two-step localization algorithm using an independent Leading Edge Detector (LED) for each receiver as is commonly used in literature. Also provided is an explanation of two Direct Positioning algorithms, Singular value Array Reconciliation Tomography (SART) and Transactional Array Reconciliation Tomography (TART). In addition, we briefly introduce the Inverse Synthetic Array Reconciliation Tomography (ISART) algorithm in the final section. Although we show the full multipath signal model, we assume the most basic case of a single transmitter and multiple receivers using an ideal channel with no multipath when presenting examples in this chapter.

2.1 Signal Model

A signal that has propagated through a multipath environment can be modeled as a summation of L_i reflectors with different delay paths to $i = 1..N$ receiving antennas. Mathematically, we can write the signal at the ith receiver as

$$s_i(t) \quad = \quad \sum_{l=1}^{L_i} c_{l,i}\, p(t - \tau_{l,i}) + n_i(t) \tag{2.1}$$

where, $c_{l,i}$ represents the magnitude of the lth reflector in the environment to the ith antenna, $\tau_{l,i} = r_{l,i}/c$ is the lth delay from the transmitter to the ith receiver, c is the speed of light, $r_{l,i}$ is the range from the transmitter to the ith receiver following the lth propagation path, $p(t)$ is the transmitted waveform, and $n_i(t)$ is the additive white Gaussian noise with variance σ_i^2. The indices $_{l,i}$ indicate the lth path to the ith receiver, assigning $_{1,i}$ as the direct path to the ith receiver.

The frequency domain representation used by the Direct Positioning Algorithms (DPAs) can be computed using the Fourier Transform (FT) of the model and can be written as

$$
\begin{aligned}
S_i(w) &= \sum_{l=1}^{L_i} c_{l,i} P(w) e^{-jw\tau_{l,i}} + N_i(w) \\
&= P(w) \sum_{l=1}^{L_i} c_{l,i} e^{-jw\tau_{l,i}} + N_i(w) \\
&= P(w) H_i(w) + N_i(w)
\end{aligned}
\tag{2.2}
$$

where $P(w)$ represents the FT of the transmitted signal, $H_i(w)$ represents the FT of the channel model to the ith receiver, and $N_i(w)$ the FT of the noise with power spectral density of $N_{0,i}/2$.

Under Line of Sight (LOS) conditions to receiver i, the direct path $c_{1,i}$ has the largest magnitude of all L_i reflectors. Under Non-Line of Sight (NLOS) conditions, the direct path may or may not exist in a practical data collection system and certainly does not posses the largest magnitude of the several path components. For the purposes of this dissertation, we assume the direct path exists with a Signal to Noise (SNR) that is defined in Section 4.2 as $E_{p,i}/N_{0,i}$, where $E_{p,i}$ is the average energy of the signal. For more details refer to Section 4.2. Also, when the ideal conditions of no multipath are mentioned, that refers to the case of $L_i = 1 \, \forall \, i \in 1..N$.

Digital analysis requires the discretized form of the model, which can be written as

$$
S_i[k] = P[k] \sum_{l=1}^{L_i} c_{l,i} e^{-j2\pi f_k \tau_{l,i}} + N_i[k]
\tag{2.3}
$$

where

$$
f_k = f_{dec} \frac{k-1}{M}, k = 1..M
\tag{2.4}
$$

with M frequency samples captured with known sample rate f_{dec}. For the purposes of this paper, the sample rate is always fixed to the sample rate of the P410 hardware and is $f_{dec} = \frac{1}{(32)(1.907e-12)}$. For more details regarding this sample rate, see Section 5.1.

2.2 Leading Edge Detector (LED)

Figure 2.1 shows the standard two step method for localization based on LED. As seen, an independent range estimate is produced at each receiver followed by a Cartesian estimate using the collection of range estimates. For the simulations in Chapter 4, the range estimates are produced using a Leading Edge Detector (LED) similar to the standard LED detector in [6]. For experimental evaluation in
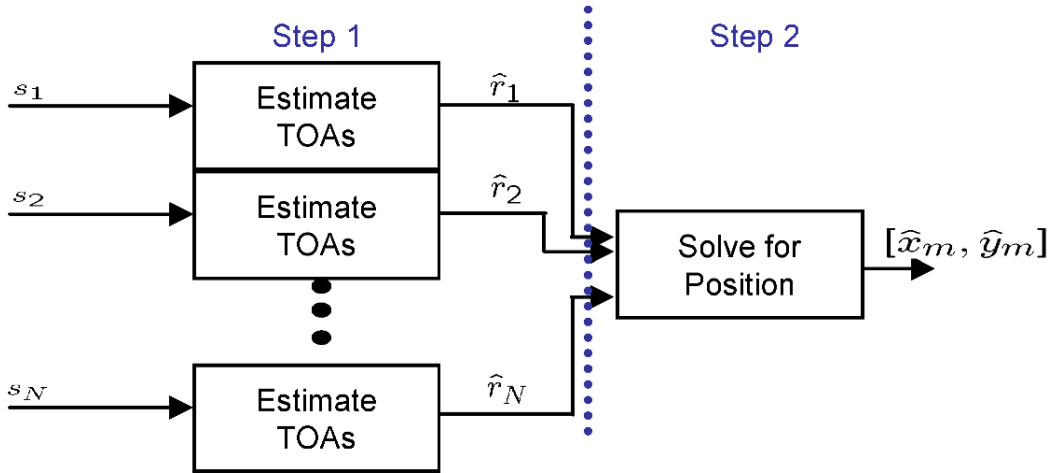
Figure 2.1: Overview of the two step method for localization based on Leading Edge Detection (LED)

Chapter 6, the LED is done by Time Domain's algorithm in the P410 hardware. The simulated LED contains a Matched Filter (MF), followed by a simple threshold and first peak estimation. If no peaks exceed the calculated threshold, the largest peak of the waveform is chosen as the direct path.

Mathematically, the MF is applied to the input signal using

$$\bar{s}_i[k] \quad = \quad \mathbf{F}^{-1}\left(S_i[k]S_{tx}^*[k]\right) \tag{2.5}$$

where $S_{tx}[k]$ is the known transmitted waveform in the frequency domain, $\mathbf{F}^{-1}$ is the Inverse Discrete Fourier Transform and * is the conjugate operator. For the purposes of this dissertation, the known transmit waveform is always the transmit waveform used by the P410 hardware. The magnitude of the transmit waveform is generated using MATLAB code from Time Domain's web site [22] and the magnitude of which is shown in the top of Figure 2.2 labeled $|p(t)|$.

The first step in the LED algorithm is to define a threshold, above which we declare a detection. In our simulations, the threshold is calculated as

$$\bar{t} \quad = \quad 2 \max |\bar{s}_i[k]| \ , \ k \in 1..60 \tag{2.6}$$

which represents a threshold that is approximately 3 dB above the peak absolute noise value in the first 60 samples of the TOA preserved MF solution. These first 60 samples correspond to range zero to range $60\frac{c}{f_{dec}}$ in the signal of the ith receiver. The next step in the simulated LED algorithm is to determine the first peak that is larger than $\bar{t}$. Algorithmically we define this as

$$\check{\tau}_{1,i} \, f_{dec} = \begin{cases} \text{min value of k} & \text{if } \exists \text{ k}, \ \check{s}_i[k] > \bar{t}, \\ \text{value of k that corresponds to } \max |\bar{s}_i[k]| & \text{otherwise} \end{cases} \tag{2.7}$$
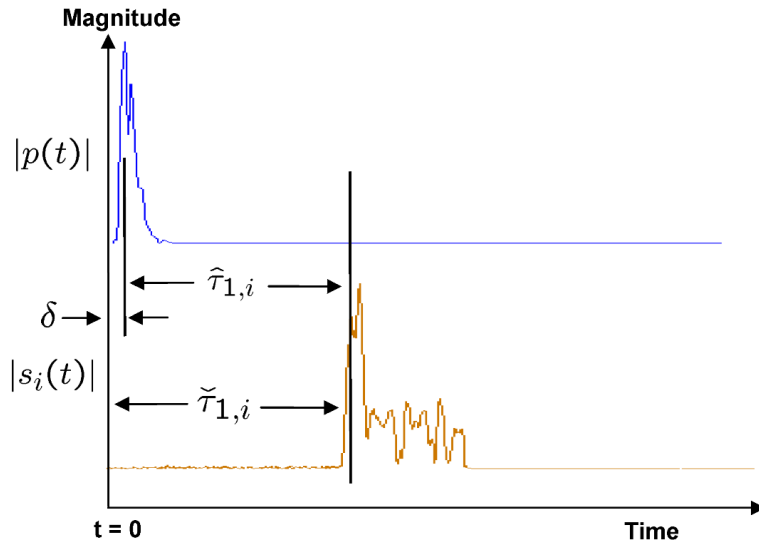
Figure 2.2: Example of Leading Edge Detection used for simulation

where $\check{s}_i[k]$ contains only the peaks of the match filtered waveform $\bar{s}_i[k]$, $\check{\tau}_{1,i}$ represents the TOA of the first peak, and f_{dec} is the sample rate of the data. This portion of the algorithm states that the first peak determines the TOA if a peak exists greater than the threshold, else the maximum value of the waveform determines the TOA. The factor f_{dec} is used to convert the peak TOA time into samples.

Furthermore, the estimate of the TOA to the first path is defined as

$$\hat{\tau}_i \;=\; \hat{\tau}_{1,i} \;=\; \check{\tau}_{1,i} - \delta \tag{2.8}$$

where δ is a calibration factor determined by maximizing the cost function (under the no noise, no multipath condition) seen in equation (2.10). Also, $\hat{\tau}_i = \hat{\tau}_{1,i}$ is a notational change implying that if $l = 1$ is not specified, the implied reference is to the direct path. This calibration factor is needed to ensure we properly align the circles to the transmitter position using the known P410 waveform.

Figure 2.2 shows an example of the LED used for the simulation at work. The transmitter generates the known waveform $p(t)$ at time $t = 0$. Notice that the peak of the waveform is not aligned to $t = 0$, but rather the leading edge of the transmit waveform, which necessitates the calibration factor δ. The delayed transmitted signal, along with multipath components as modeled by equation (2.1), arrive at the ith receiver some time later. We calculate the threshold from the first 60 samples taken at the sample rate defined by f_{dec}. The first peak is determined as shown in the figure since there exists a threshold crossing. We then calculate the range from the transmitter to the ith receiver as

$$\hat{r}_i \;=\; \hat{\tau}_i \, c \tag{2.9}$$

(a) Sensor Setup

(b) $\zeta_{(x,y)_L}$
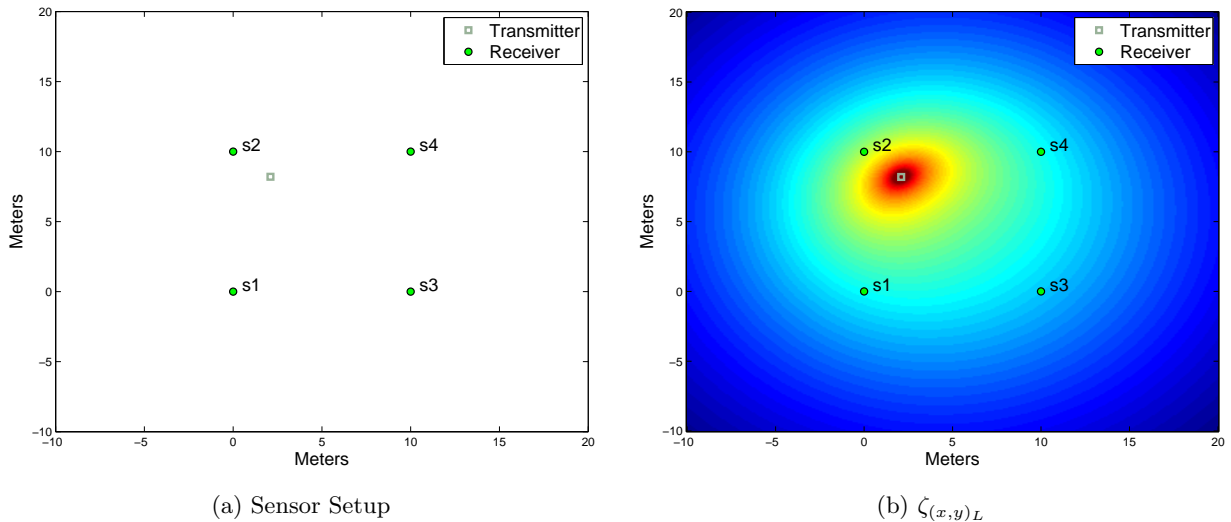
Figure 2.3: (a) Example sensor setup and (b) brute force plot of the minimization cost function, defined as $\zeta_{(x,y)_L}$.

where c is the speed of light.

Referring again to Figure 2.1, the second step of the two step localization based on LED requires using the ensemble of range estimates to produce a Cartesian position estimate. The Cartesian position estimate could be computed using the minimization

$$\begin{bmatrix} \hat{x}_m \\ \hat{y}_m \end{bmatrix} = \min_{x,y} \|(x - s_x)^2 + (y - s_y)^2 - \hat{r}^2\| \tag{2.10}$$

where $\| \cdot \|$ represents the two norm, $s_x = [s_{x,1} \ s_{x,2} \ \cdots \ s_{x,N}]^T$ and $s_y = [s_{y,1} \ s_{y,2} \ \cdots \ s_{y,N}]^T$ contains the two dimensional position of all the receivers, $\hat{r} = [\hat{r}_1 \ \hat{r}_2 \ \cdots \ \hat{r}_N]^T$ is a vector with all the estimated ranges, and $[\hat{x}_m \ \hat{y}_m]^T$ is the estimated Cartesian position.

Instead of solving the minimization, in this dissertation we plot the cost function defined by equation (2.10). We define this metric as

$$\zeta_{(x,y)_L} = \frac{1}{\|(x - s_x)^2 + (y - s_y)^2 - (\hat{r})^2\|} \tag{2.11}$$

where x and y are discrete scan grid points plugged into the cost function defined by the inverse of (2.10). This metric's value over the entire scan grid can be conveniently viewed as an image and will be referred to as the metric image. The subscript L refers to the the two step LED based method and ζ refers to the final metric. The result can be seen in Figure 2.3b using our previous example of a single transmitter surrounded by four receivers. In this case, we can see clearly that the transmitter position

is identified as the strongest peak in the metric image. The estimate of the transmitter position is then defined as

$$\begin{bmatrix} \hat{x}_m \\ \hat{y}_m \end{bmatrix} = \max_{x,y} \zeta_{(x,y)_L} \tag{2.12}$$

which defines the maximum cost function computed at points on a discrete scan grid defined by $x = x_{min} .. x_{max}$ and $y = y_{min} .. y_{max}$, with a step size of Δ_x and Δ_y respectively. The fixed scan grid is used so that we have a similar computation and analysis as that employed by the soon to be discussed DPAs: SART, TART, and CART.

2.3 Singular value Array Reconciliation Tomography (SART)

The Singular Value Array Reconciliation Tomography (SART) algorithm [11] is a DPA where synchronization is not required between the transmitter and receivers, hence it is a TDOA algorithm. It was originally designed for use with a Multi-Carrier Wideband (MCW) waveform as described in [23]. To produce a SART position estimate, a search of the desired spatial region is required and is typically computed in a greedy manner. The search is accomplished by defining a discretized scan grid $x = x_{min} \cdots x_{max}$ and $y = y_{min} \cdots y_{max}$ with some defined resolution. At each scan grid location, a metric is computed in order to produce a metric map based image. This is similar to the brute force method described in the previous section, Section 2.2, describing the plot of the cost function. In the case of the SART algorithm, however, we define a different metric instead of a computation of the least squares fit based cost function. The metric at each scan grid location is based upon the signal data directly and does not require a LED on signals from individual receivers.

The SART algorithm begins by defining a full $M \times N$ data matrix of raw frequency domain data as

$$A = \begin{bmatrix} S_1[1] & S_2[1] & \cdots & S_N[1] \\ S_1[2] & S_2[2] & & S_N[2] \\ \vdots & \vdots & & \vdots \\ S_1[M] & S_2[M] & \cdots & S_N[M] \end{bmatrix} \tag{2.13}$$

where $S_i[k]$ is the kth frequency sample of the ith receiver as defined by (2.3), M represents the total number of frequency samples per receiver and N is the number of receivers. For example, as seen in Figure 2.4a with our ongoing single transmitter and four receiver setup, if the P410 waveform is

(a) Sensor Setup

(b) Received Data

(c) $\mathbf{F}^{-1}(A)$
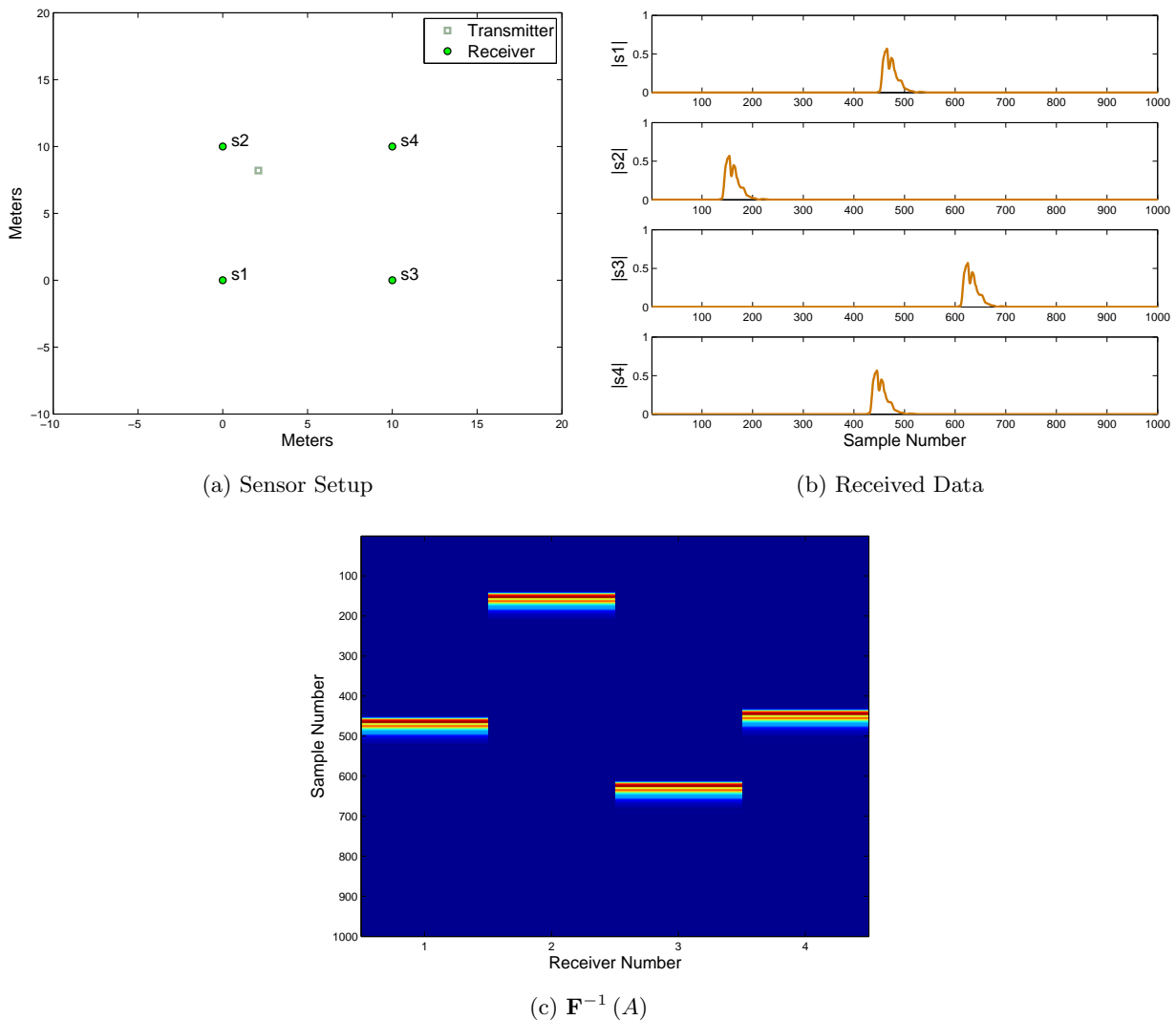
Figure 2.4: (a) Example sensor setup, (b) example signal at each receiver using the P410 waveform, and (c) the Inverse Discrete Fourier Transform (IDFT) of the columns of the data matrix A.

transmitted in an ideal environment without fading, noise, or multipath, we would receive the data in Figure 2.4b. Figure 2.4b shows the magnitude of the simulated received signal at each receiver, delayed by the appropriate amount depending on distance. We see that since receiver 2 is closest in this example, the transmitted waveform arrives at that location first, followed by receiver 4, 1, and then 3. If we take take all four of these waveforms and stack the data into columns, we would get the Inverse Discrete Fourier Transform (IDFT) of the columns of the defined matrix A as seen in Figure 2.4c.

Next, We allow the current scan grid to span $x = x_{min} \cdots x_{max}$ and $y = y_{min} \cdots y_{max}$ with some
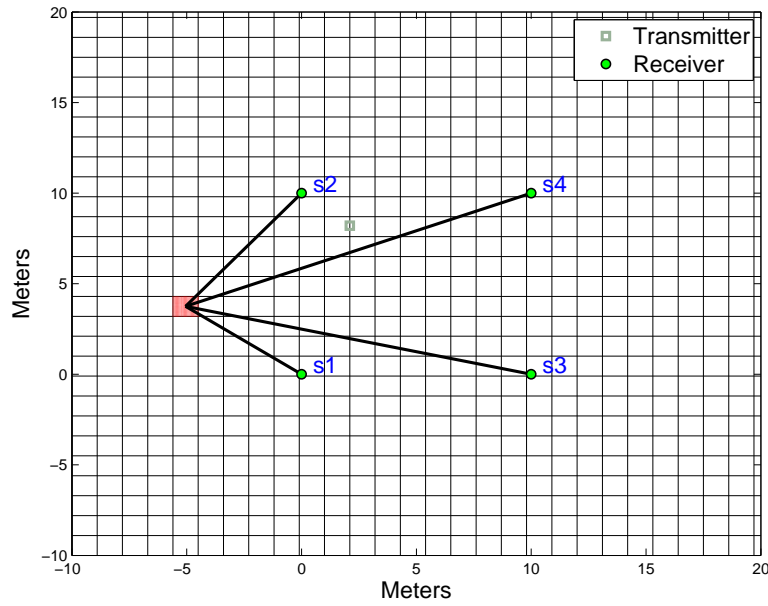
Figure 2.5: Example of discretized Cartesian space

defined granularity Δ_x and Δ_y as shown in Figure 2.5. With known receiver locations at $(s_{x,i}, s_{y,i})$, we can define a $M \times N$ re-phasing matrix

$$
B(x,y) = \begin{bmatrix}
e^{j2\pi f_1 \bar{\tau}_1} & e^{j2\pi f_1 \bar{\tau}_2} & & e^{j2\pi f_1 \bar{\tau}_N} \\
e^{j2\pi f_2 \bar{\tau}_1} & e^{j2\pi f_2 \bar{\tau}_2} & \cdots & e^{j2\pi f_2 \bar{\tau}_N} \\
\vdots & \vdots & & \vdots \\
e^{j2\pi f_M \bar{\tau}_1} & e^{j2\pi f_M \bar{\tau}_2} & & e^{j2\pi f_M \bar{\tau}_N}
\end{bmatrix}
\tag{2.14}
$$

where

$$
\bar{\tau}_i = \frac{1}{c}\sqrt{(s_{x,x} - x)^2 + (s_{y,i} - y)^2}
$$

for $i = 1..N$ represents the time delay from the current scan grid position to the i_{th} receiver and f_k for $k = 1..M$ are as defined in equation (2.4).

The purpose of the rephasing matrix is to remove time delays from the data matrix A that were caused by the delay through the propagation channel. To do this we define a rephased data matrix at the (x, y) scan grid location as

$$
D_{(x,y)} = A .* B(x,y)
\tag{2.15}
$$

where the $.*$ operator is defined as the MATLAB element wise multiplication (Hadamard product [24]) of the data matrix A with the rephasing matrix $B(x,y)$.
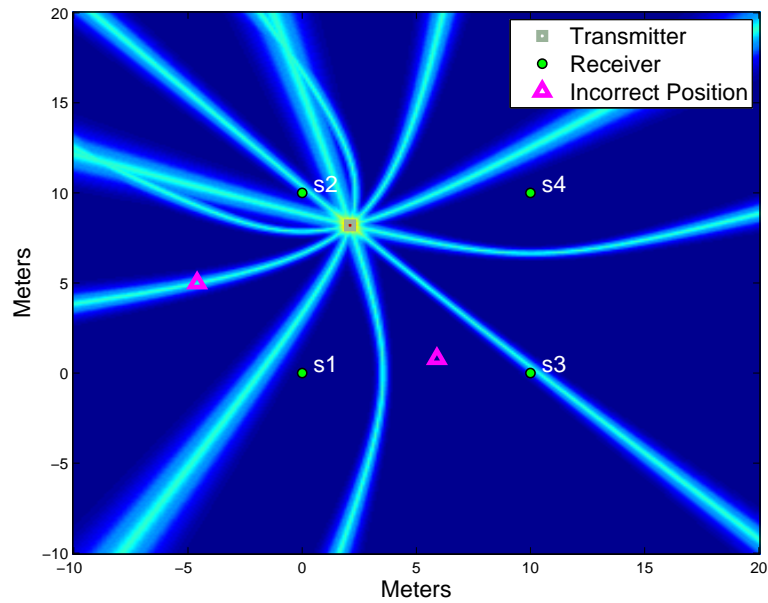
Figure 2.6: Example SART metric image, defined as $\zeta_{(x,y)_S}$

The elements of the rephased data matrix can be defined as

$$D_{(x,y)_{ki}} \quad = \quad S_i[k]e^{j2\pi f_k \bar{\tau}_i}$$

where k defines the row, i defines the column. If we make the assumption that the current scan grid position is the transmitter position ($\tau_{1,i} = \bar{\tau}_i$), then

$$D_{(x,y)_{ki}} \quad = \quad \sum_{l=1}^{L_i} c_{l,i}\, P[k]\, e^{-j2\pi f_k(\tau_{l,i}-\bar{\tau}_i)}$$

$$= \quad c_{1,i}\, P[k] + P[k] \sum_{l=2}^{L_i} c_{l,i}\, e^{-j2\pi f_k(\tau_{l,i}-\bar{\tau}_i)}$$

where the phase factor of the $l = 1$ term was eliminated. This shows that the rephased signal takes the form of a complex magnitude multiplied transmit waveform plus the sum of remaining rephased multipath components under the condition when the current scan grid is equal to the transmitter position. If we assume the ideal condition without multipath or noise, then the elements of the rephased data matrix are

$$D_{(x,y)_{ki}} \quad = \quad c_{1,i}\, P[k].$$

Under this no-multipath example, all the columns would therefore present the transmit waveform $P[k]$ multiplied by a complex scalar $c_{1,i}$. We recognize this as strong linear dependence across the

columns of the rephased data matrix. We can use the Singular Value Decomposition (SVD) to define

$$D_{(x,y)} \quad = \quad U_D S_D V_D$$

where U_D and V_D define a orthonormal basis for the row and column space respectively and S_D is a diagonal matrix with entries $[\sigma_{S1}^2 \ \sigma_{S1}^2 \ \cdots \ \sigma_{SN}^2]$ under the assumption that $N < M$. The largest singular value is used as the SART metric

$$\zeta_{(x,y)_S} \quad = \quad \sigma_{S1}^2 \tag{2.16}$$

which produces a measure of the linear dependence across the columns of data. The estimate of the transmitter position is then obtained in a fashion similar to (2.12) in that we take the Cartesian position that produced the maximum metric as signifying the optimum estimate.

We again refer to our sensor setup in Figure 2.4a under ideal channel conditions with the P410 transmit waveform. The received data matrix was shown in Figure 2.4c. When this data is processed according to the SART algorithm described above, the result is the metric image seen in Figure 2.6. The metric image reveals that the intersection of hyperbolas define the maximum in the image. With four receivers, we see that there are six unique hyperbolas, which are defined by the time differences of arrival between all receiver pair combinations.

It is also instructive to examine portions of this metric by illustration. Figure 2.6 also shows several incorrect scan grid positions, specifically at (5.9,0.8) and (-4.6,5). The rephased data matrix at these two points and the rephased data matrix at the correct scan grid location can be seen in Figure 2.7. When computing the SART metric at (5.9,0.8) we compute the rephased data matrix as seen in Figure 2.7a. At this scan grid location, there is no linear dependence across the column space of the data, so the largest singular value of the data matrix's decomposition is relatively small. When computing the SART metric at (-4.6,5), there is linear dependence between receiver 2 and receiver 3, increasing the metric from the nominal level of no linear dependence. At the correct scan grid location, meaning that the transmitter position is the scan grid location at (x_m, y_m), there is strong linear dependence across the columns. This is clearly evident from examination of the IDFT of the rephased matrix in Figure 2.7c.

(a) $\mathbf{F}^{-1}\left(D_{(5.9,0.8)}\right)$

(b) $\mathbf{F}^{-1}\left(D_{(-4.6,5)}\right)$

(c) $\mathbf{F}^{-1}\left(D_{(x_m,y_m)}\right)$
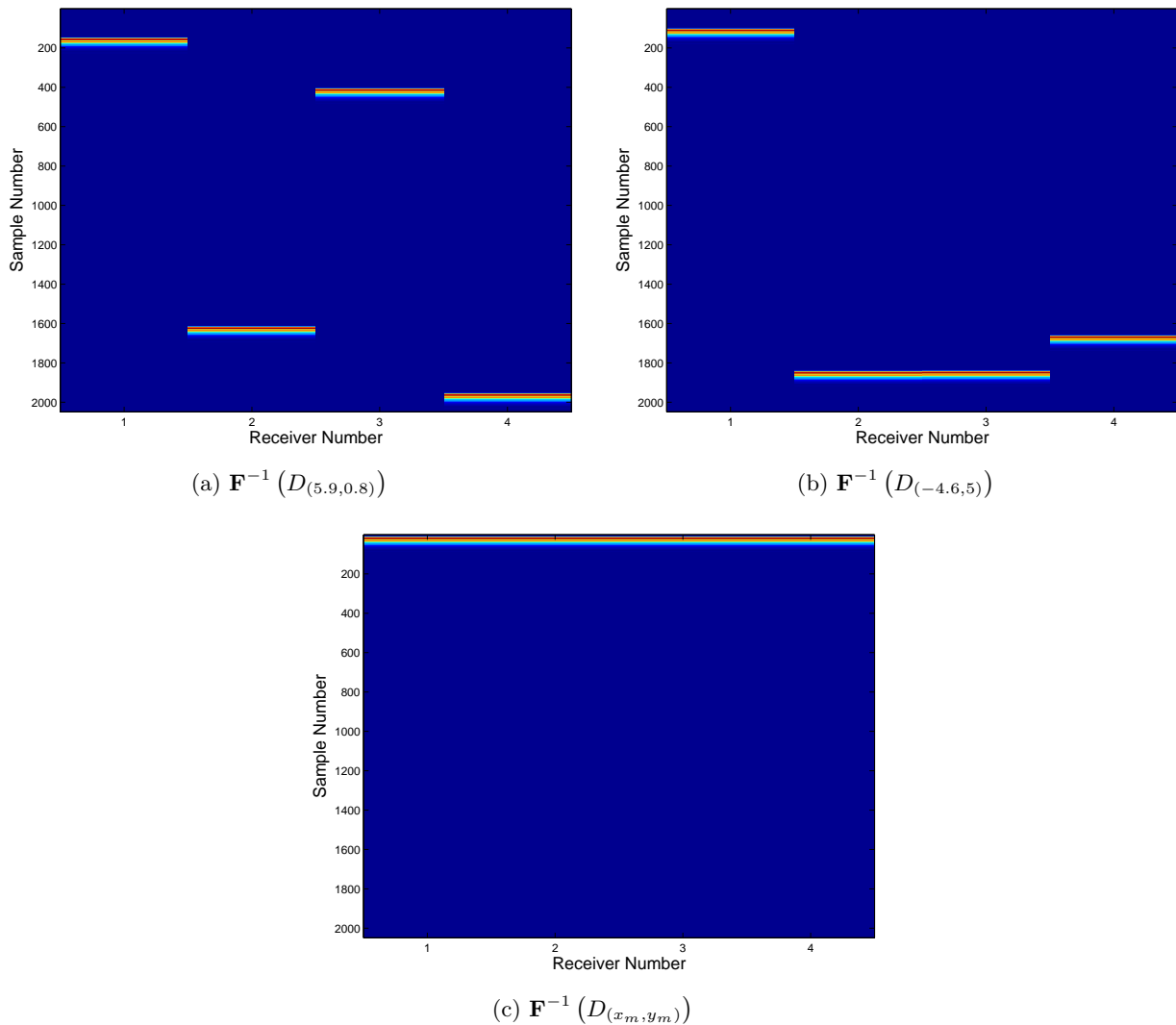
Figure 2.7: (a) The IDFT of the rephased data matrix at (5.9,0.8) illustrating no linear dependence, (b) at (-4.6,5) with some linear dependence, and (c) at the true transmitter position with most linear dependence.

2.4 Transactional Array Reconciliation Tomography (TART)

The Transactional Array Reconciliation Tomography (TART) algorithm [25] was developed as part of the WPI's Precision Personal Locator (PPL) program to enable TOA testing for multipath mitigation in indoor environments. In order to achieve synchronization of the transmitter to receivers, a transaction of data between the transmitter and receivers is performed, hence the word transactional in the title. Unlike the SART algorithm, which obtains a TDOA result by SVD based processing of the data such a way as to ignore a common time shift across all received signals, TART is configured

to obtain a TOA solution. Similar to the SART algorithm, it was also designed to be used with a Multi-Carrier Wideband (MCW) waveform.

The TART algorithm is similar to the SART algorithm in that a desired spatial region is searched, but now a different metric is used to produce the metric image. We again have the two matrices A and B from equations (2.13) and (2.14), which are element wise multiplied together at each scan grid location to produce matrix $D_{(x,y)}$ as in (2.15). We now define the rephased data matrix in the time domain as

$$Z_{(x,y)} = \mathbf{F}^{-1}\left(D_{(x,y)}\right) \tag{2.17}$$

where we take the Inverse Discrete Fourier Transform of the columns of the rephased data matrix $D_{(x,y)}$. There exists an SVD based processing method with an augmented matrix using $D_{(x,y)}$ that yields a metric which obtains its peak at a TOA solution. This SVD method is well approximated by the reduced computation form

$$\zeta_{(x,y)_T} = \sum_{k=1}^{\beta}\sum_{i=1}^{N}|Z_{(x,y)_{k,i}}| \tag{2.18}$$

where β is the number of time domain samples to include in the summation and $_{k,i}$ is the k, i^{th} element of the matrix Z. This summation includes terms indexed over two dimensions: first k, with values from 1 to β, that spans the sample space and second, i with values from 1 to N that spans the number of receivers. It is important to note that the original author [25] simply used the case of $\beta = 1$ for reduced computational complexity, but for the purposes of this paper, when we reference the TART algorithm, we use a $\beta = 5$ due to the nature of our transmit waveform. The estimate of the transmitter position is obtained in a fashion similar to (2.12) for the two step LED where we take the maximum of the metric image.

The elements of the rephased data matrix in the time domain can be defined as

$$Z_{(x,y)_{ki}} = \sum_{l=1}^{L_i} c_{l,i}\, p[k - (\tau_{l,i} - \bar{\tau}_i)\, f_{dec}] + n_i[k] \tag{2.19}$$

where k defines the row, i defines the column of the matrix Z. If we make the assumption that the current scan grid position is the transmitter position ($\tau_{1,i} = \bar{\tau}_i$), then

$$Z_{(x,y)_{ki}} = c_{1,i}\, p[k] + \sum_{l=2}^{L_i} c_{l,i}\, p[k - (\tau_{l,i} - \bar{\tau}_i)\, f_{dec}] + n_i[k] \tag{2.20}$$

where the time delay to the direct path was eliminated. If we assume the ideal condition without multipath or noise, then the elements of the rephased data matrix are

$$Z_{(x,y)_{ki}} = c_{1,i}\, p[k]. \tag{2.21}$$
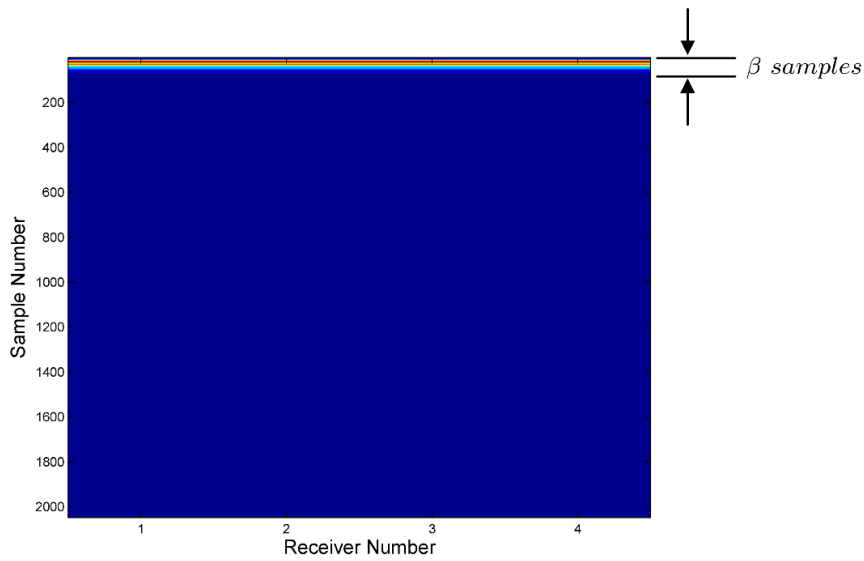
(a) $Z_{(x_m, y_m)}$
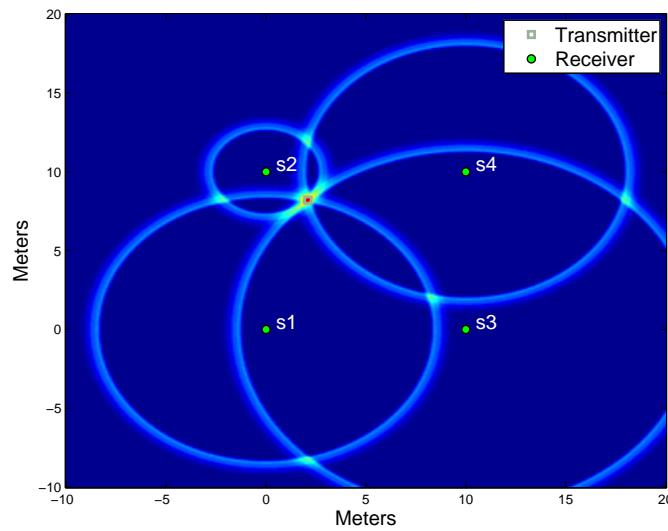
(b) $\zeta_{(x,y)_T}$

Figure 2.8: (a) $Z_{(x_m, y_m)}$ showing β samples and (b) an example TART metric image

Under this assumption, it is clear that when the current scan grid location is equal to the transmitter position, then all the receivers have the same waveform time aligned at the top of the matrix Z. Figure 2.8a shows the rephased data matrix under these conditions. The final TART metric in (2.18) shows that the magnitude value is taken of the samples, which is to ensure that the phases of $c_{1,i}$ terms in (2.21) do not constructively destroy the metric.

You may also notice that this metric is dependent on the shape of the transmitted waveform. In

order to ensure maximum energy at $p[0]$ for the metric, it is often wise to compute the MF solution as is done in the LED prior to computing the TART metric image, or to include additional samples of $\bar{s}_i[m]$ to capture the energy of the signal efficiently in the metric. In this work, we also compute the MF prior to applying this algorithm.

Figure 2.8a shows $Z_{(x_m, y_m)}$ along with the region that is defined by β samples when the current scan grid position is equal to the transmitter position. When signal content is shifted into this top region of matrix Z as we search the scan grid, the absolute sum of all data points increases, increasing the TART metric. If we consider our ongoing example sensor setup seen in Figure 2.4a under ideal channel conditions with the P410 transmit waveform, we get the received data matrix as was shown in Figure 2.4c. When this data is processed according to the TART algorithm described above, the result is the metric image seen in Figure 2.8b. The transmitter position is seen as the intersection of the four circles in the metric image, indicating a TOA algorithm.

2.5   Inverse Synthetic Array Reconciliation Tomography (ISART)

Cavanaugh [26] introduced the ISART algorithm as a method to fuse a motion solution with the SART algorithm. The motion solution was computed using a low cost Inertial Navigation System (INS) into a Kalman Filter. As is conclusively shown, one can benefit from the fusion of superior short term information from the INS with the stability of the RF for a better localization performance in a heavy multipath environment [26]. Since the CART algorithm does not require a motion solution, we do not compare the performance of the CART algorithm to the ISART algorithm in simulation. Rather, we compare the CART algorithm to the ISART algorithm in Section 6.1 in the same test environment where the ISART has a motion solution and the CART algorithm does not. In addition, we explore using a gyroscope to determine some motion information that allows fusion of RF data by the CART algorithm in Chapter 7 when we explore the fire fighter homing device application.

Chapter 3

Coherent Array Reconciliation Tomography (CART)

The Coherent Array Reconciliation Tomography (CART) algorithm is introduced in this chapter. The CART algorithm takes advantage of the Signal to Noise Ratio (SNR) improvement that is achieved by integrating multiple signals together. In this case, the leading edge of the transmitted waveform is coherently integrated to improve the SNR of the direct path signal and therefore it improves our localization performance. In this chapter, we provide an introduction to coherent integration, followed by a motivation for the development of the CART metric. Then, we discuss the details of the CART algorithm.

3.1 Coherent Integration

Coherent integration is the process of adding multiple waveforms in order to improve the SNR and is central to the understanding of the CART algorithm. Suppose that we had n frames of the signal from (2.3), which can be written as

$$
\begin{aligned}
S_{i,1}[k] &= P[k]H_i[k] + N_{i,1}[k] \\
S_{i,2}[k] &= P[k]H_i[k] + N_{i,2}[k] \\
&\vdots \\
S_{i,n}[k] &= P[k]H_i[k] + N_{i,n}[k]
\end{aligned}
\tag{3.1}
$$

where

$$H_i[k] = \sum_{l=1}^{L_i} c_{l,i}\, e^{-j2\pi f_k \tau_{l,i}}$$

represents the discretized channel model to the ith receiver. The only difference between $S_{i,l}[k]\, \forall\, l \in 1..n$ is the instance of the white Gaussian noise process. The SNR of the lth frame at the ith sensor would be

$$SNR_{i,l} = \frac{\frac{1}{M}\sum_{k=0}^{M-1} |P[k]H_i[k]|^2}{N_{0,i}} \tag{3.2}$$

$$= \frac{P_{S_i}}{N_{0,i}} \tag{3.3}$$

where $N_{0,i}$ is the noise power of each frame and P_{S_i} is the signal power. If we then sum n frames to get

$$
\begin{aligned}
S_i[k] &= \sum_{l=1}^{n} S_{i,l}[k] \\
&= \sum_{l=1}^{n} P[k]H_i[k] + \sum_{l=1}^{n} N_{i,l}[k] \\
&= nP[k]H_i[k] + \sum_{l=1}^{n} N_{i,l}[k]
\end{aligned}
\tag{3.4}
$$

where the signal terms $P[k]H_i[k]$ would add coherently and the noise terms $N_{i,l}[k]$ would add non-coherently. Presumably, this would result in an improvement in the SNR of $S_i[k]$ in (3.4). Mathematically, the SNR after the summation would be

$$
\begin{aligned}
SNR_i &= \frac{\frac{1}{M}\sum_{k=0}^{M-1} |nP[k]H_i[k]|^2}{\sum_{l=1}^{n} N_{0,i}} \\
&= \frac{n^2 P_{S_i}}{n N_{0,i}} \\
&= n\frac{P_{S_i}}{N_{0,i}}
\end{aligned}
\tag{3.5}
$$

which indicates an improvement of n is achieved by coherent integration.

In practice, it is not always the case that the signal term $P[k]H_i[k]$ in (3.1) can be coherently summed. Sometimes there exists a set of signals that must be modeled as

$$
\begin{aligned}
S_{i,1}[k] &= c_1\, P[k]H_i[k] + N_{i,1}[k] \\
S_{i,2}[k] &= c_2\, P[k]H_i[k] + N_{i,2}[k] \\
&\vdots \\
S_{i,n}[k] &= c_n\, P[k]H_i[k] + N_{i,n}[k]
\end{aligned}
\tag{3.6}
$$

where $c_l \, \forall \, l \in 1..n$ is a complex scalar with an amplitude and phase component. If we were to sum these equations as in (3.4), the result could potentially be disastrous in that some terms could completely cancel each other. The solution is to estimate the c_l terms prior to the summation. One way to do that is to use SVD averaging.

Suppose we generate a matrix of samples from the new model seen in (3.6), which we write as

$$
\begin{aligned}
A_i \;=\; & \begin{bmatrix}
S_{i,1}[1] & S_{i,2}[1] & \cdots & S_{i,n}[1] \\
S_{i,1}[2] & S_{i,2}[2] & & S_{i,n}[2] \\
\vdots & \vdots & & \vdots \\
S_{i,1}[M] & S_{i,2}[M] & & S_{i,n}[M]
\end{bmatrix} \\
=\; & \begin{bmatrix}
c_1 \, P[1] H_i[1] & \cdots & c_n \, P[1] H_i[1] \\
\vdots & & \vdots \\
c_1 \, P[M] H_i[M] & \cdots & c_n \, P[M] H_i[M]
\end{bmatrix} + N_i \\
=\; & A_{i,1} + N_i
\end{aligned}
\tag{3.7}
$$

where N_i is a matrix with the noise and $A_{i,1}$ contains the signal component. If we decompose the matrix A_i using the SVD as

$$
A_i \;=\; U_i \Sigma_i V_i^H
\tag{3.8}
$$

where $U_i = [u_{i,1} \; u_{i,2} \; \cdots \; u_{i,M}]$, $V_i = [v_{i,1} \; v_{i,2} \; \cdots \; v_{i,n}]$ are orthonormal bases for the row and column spaces, and Σ_i is a diagonal matrix with elements $[\sigma_{i,1}^2 \; \sigma_{i,2}^2 \; \cdots \; \sigma_{i,n}^2]$. The decomposition can also be written as

$$
A_i \;=\; \sum_{l=1}^{r} u_{i,l} \, \sigma_{i,l}^2 \, v_{i,l}^H
\tag{3.9}
$$

where matrix A_i has a rank of r. The summation can be broken into the signal subspace and noise subspace and re-written as

$$
A_i \;=\; \sum_{l=1}^{r_s} u_{i,l} \, \sigma_{i,l}^2 \, v_{i,l}^H \;+\; \sum_{l=r_s+1}^{r} u_{i,l} \, \sigma_{i,l}^2 \, v_{i,l}^H
\tag{3.10}
$$

where r_s represents the rank of the signal subspace and $r - r_s$ is the rank of the noise subspace. From our modeled equations seen in (3.6), we would have $r_s = 1$ and $r = n$. We also assume that the noise power $N_{0,i}$ in each frame is sufficiently small compared to P_{S_i} so that the SVD can properly resolve $u_{i,1}$ as the vector that spans the signal subspace in the sample dimension defined by the true signal

$P[k]H_i[k]$. If that is the case, the vector $v_{i,1}$ would span the signal subspace of the frame dimension and would contain an estimate of the phase relationships of the terms c_l.

Since $r_s = 1$, we can write the $_MXn$ matrix that represents the signal subspace as

$$A_{i,1} = u_{i,1}\,\sigma_{i,1}^2\,v_{i,1}^H \tag{3.11}$$

which can be used to determine the average signal component in the signal subspace. To do this, we first we recognize that the matrix notation for the sum of the signals in (3.6) can be written as

$$S_i[k] = \begin{bmatrix} P[1]H_i[1] & \cdots & P[1]H_i[1] \\ \vdots & & \vdots \\ P[M]H_i[M] & \cdots & P[M]H_i[M] \end{bmatrix} \begin{bmatrix} c_1 \\ \vdots \\ c_n \end{bmatrix} = A_{i,s}\,c_i \tag{3.12}$$

where $A_{i,s}$ represents the signal only matrix without the unknown phase term and c_i represents the vector of complex scalars. Referring to (3.11), we can undo the unknown phase terms of the computed signal subspace using the conjugate of the estimated unknown phases to get

$$S_i[k] = A_{i,s}\,c_i = A_{i,1}\,v_{i,1}\,\sqrt{n} \tag{3.13}$$

where $\sqrt{n}$ reverses the normalization performed by the SVD on $v_{i,1}$ when making V_i^H an orthonormal basis. We can now solve (3.11) for $A_{i,1}\,v_{i,1}\,\sqrt{n}$ to get

$$S_i[k] = u_{i,1}\,\sigma_{i,1}^2/\sqrt{n} \tag{3.14}$$

where we have allowed the SVD to solve for the unknown complex amplitude components c_l. This equation computes the SVD average of the columns of A_i in (3.7). This SVD averaging method is used to increase the SNR of the leading edge of the ensemble of RF input data to the CART algorithm in order to produce a more accurate position estimate.

3.2 Motivation

The Singular value Array Reconciliation Tomography (SART) and Transactional Array Reconciliation Tomography (TART) algorithms discussed in Section 2.3 and Section 2.4 were designed for a multi-carrier wideband non-impulsive signal and were not designed to take advantage of Ultra-wideband (UWB) Impulse Radio (IR) waveform features. Literature presents the traditional two step Leading Edge Detection (LED) method discussed in Section 2.2 as a common solution for indoor localization using UWB IR where the transmitter is synchronized to the receivers (TOA localization). The problem

(a) Consistent system of position constraints   (b) Inconsistent system of position constraints
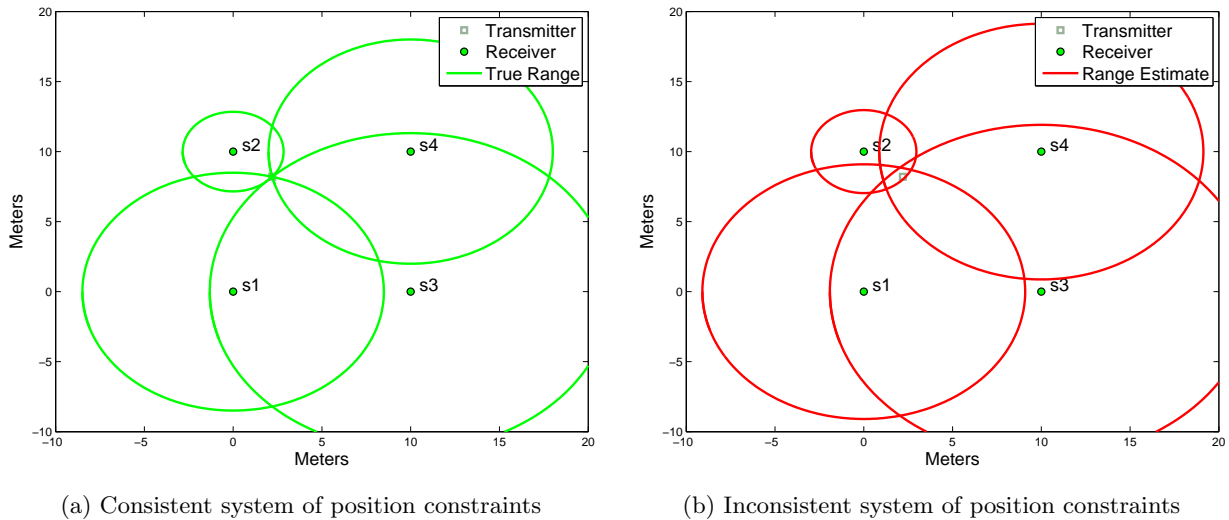
Figure 3.1: (a) Shows a consistent system of position constraints due to exact ranges and (b) shows an inconsistent system of position constraints due to errors in the range estimates from the transmitter to each receiver

with the traditional two step LED method is that it presents an inconsistent set of position constraints to the position solver due to range estimation errors. Figure 3.1a shows a consistent system of position constraints if the correct ranges were known. We see that there is a single unique solution at the true transmitter position that satisfies the range constraints imposed by (2.10). Figure 3.1b shows the inconsistent system of position constraints that result from errors in the range estimates from the transmitter to each receiver. We see that there is no single position that can satisfy the localization constraints, but rather there are several intersections of pairs of circles. This inconsistency leads to reduced performance for the traditional two step LED method.

Since the SART and TART algorithms were not designed for UWB IR waveforms and the traditional two step LED method is subject to reduced performance due to the inconsistent constraints and the lack of coherent integration of the direct path signal, we recognize a need for a new approach. The new approach should have features similar to the SART and TART algorithms in principle, where we search position solutions that are consistent and are of interest, hence a Direct Positioning Algorithm (DPA).

The new approach introduced in this chapter is called Coherent Array Reconciliation Tomography (CART). The CART algorithm is developed for the UWB IR waveform in which only consistent solutions are searched and was designed based on the segmentation of the received signals into two

segments: one that should contain the leading edge of the received signals embedded in noise and one that should contain noise only. The CART algorithm produces a simultaneous leading edge and position estimate based upon a search of consistent ranges to produce the simultaneous best estimate using signal fusion.

3.3   CART Regions

Coherent Array Reconciliation Tomography (CART) has features similar to the first two DPAs, SART and TART, in that we wish to define a discretized spatial region we wish to search. At each scan grid position, we also produce a metric that represents a measure of the likelihood of the transmitter origin. This metric's value over the entire scan grid can be conveniently viewed as an image and will be referred to here as the metric image. As mentioned before, the CART algorithm coherently integrates the leading edge of all the receiver data available as part of the computation of this metric.

Assuming that we have the full data matrix of frequency data from (2.13) and the re-phasing matrix from (2.14) at each scan grid location, we again produce the element wise multiplication of A and $B(x,y)$ as seen in (2.15). The scan grid position in the Cartesian domain is (x,y) and the corresponding rephased data matrix in the frequency domain is defined as $D_{(x,y)}$. As was done in the TART algorithm in equation (2.17), we also take the IDFT of the data matrix rephased to the current scan grid location, which we again denote by $Z_{(x,y)} = \mathbf{F}^{-1}[D_{(x,y)}]$.

The CART metric at each scan grid position is computed by first breaking $Z_{(x,y)}$ into two regions of interest. The first region, which we denote by the matrix $F_{(x,y)}$, contains the first α elements of each column of $Z_{(x,y)}$ and the second region, which we denote by $G_{(x,y)}$, contains the last γ elements of $Z_{(x,y)}$. In MATALB notation we can write these regions as $F_{(x,y)} = Z_{(x,y)}(1 : \alpha, :)$ and $G_{(x,y)} = Z_{(x,y)}(end - \gamma + 1 : end, :)$. These regions are chosen to take advantage of the periodicity of the time shift in the frequency domain, where indices not in the set (1..M) are evaluated with modulus of M so that time shifts resulting in indices less than 1 become relative to M. If (x_m, y_m) is the true transmitter position, $F_{(x_m, y_m)}$ will contain the leading edge of the transmitted signal and $G_{(x_m, y_m)}$ will contain noise only. When the current scan grid designated position under test is not the true transmitter position, $F_{(x \neq x_m, y \neq y_m)}$ will likely not contain the leading edge and $G_{(x \neq x_m, y \neq y_m)}$ will likely contain direct path or multipath signal in noise. The CART metric utilizes this knowledge in the formation of a likelihood that the transmitter originated from the current scan grid designated position under test.

Figure 3.2a shows an example scan along with a point (2.5,7) highlighted in red. When this scan

(a) Example Discretized Scan Grid

(b) $Z_{(2.5,7)}$
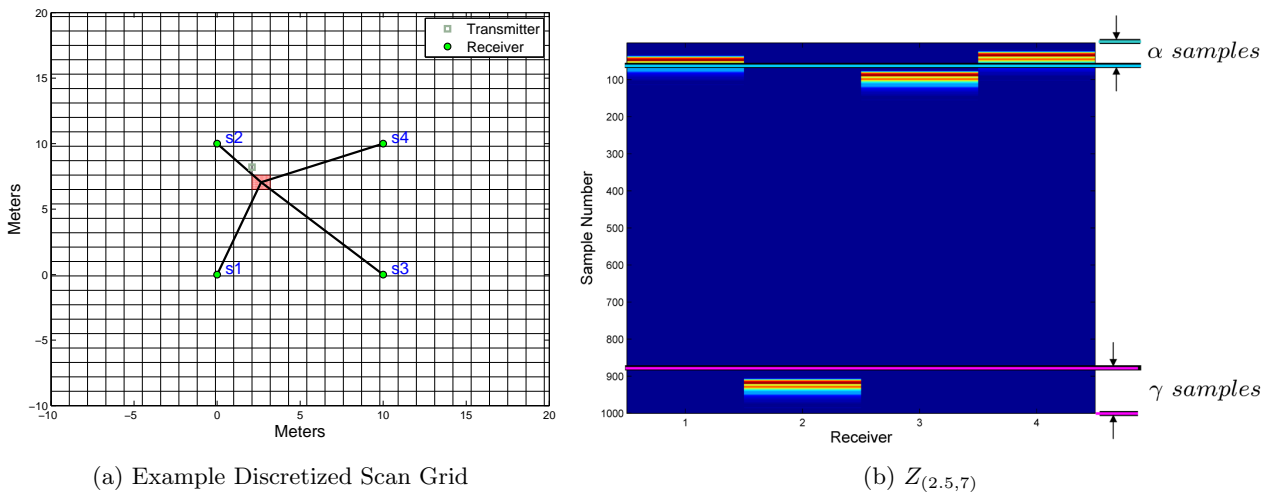
Figure 3.2: (a) Shows a discretized scan grid and point (2.5,7) and (b) shows the resulting rephased data matrix $Z_{(2.5,7)}$ along with the α samples that make up region $F_{(x,y)}$ and the γ samples that make up region $G_{(x,y)}$

grid location is chosen, the resulting shifted data matrix $Z_{(2.5,7)}$ is shown in Figure 3.2b. Further examination of receiver 2 data shows that the current scan grid location of (2.5,7) is farther in range than the true transmitter position. The result is that the signal of receiver 2 is wrapped around and shifted into the $G_{(x,y)}$ region. The presence of anything other than noise content in the $G_{(x,y)}$ region should therefore result in a reduced metric value.

3.4   CART Submetrics

The final CART metric is a combination of three submetrics: the similarity submetric, SVD submetric, and the power submetric. It is important to note that the three submetrics were developed to improve the robustness of experimental position results based upon our observations of outcomes on introducing experimental data. The power submetric worked reasonably well in simulation using heavy multipath, but performed poorly in the presence of interference in experiments using an off the shelf ultra-wideband (UWB) data collection system. It was found by experimentation and simulation that the combination of these three submetrics resulted in the most robust localization solution. For more information on the hardware experimentation, see Chapter 6.

At each scangrid position, we start with the following computations:

$$F_{(x,y)} \quad = \quad U_F \, \Sigma_F \, V_F^H \tag{3.15}$$

$$G_{(x,y)} \quad = \quad U_G \, \Sigma_G \, V_G^H \tag{3.16}$$

$$\bar{F}_{(x,y)} \quad = \quad \frac{1}{N\alpha} \sum_{j=0}^{\alpha-1} \sum_{i=1}^{N} |f_{i,j_{(x,y)}}|^2 \tag{3.17}$$

$$\bar{G}_{(x,y)} \quad = \quad \frac{1}{N\gamma} \sum_{j=0}^{\gamma-1} \sum_{i=1}^{N} |g_{i,j_{(x,y)}}|^2 \tag{3.18}$$

where ^{H} represents the conjugate transpose, $f_{i,j_{(x,y)}}$ is the i,j^{th} element of the matrix $F_{(x,y)}$, $g_{i,j_{(x,y)}}$ is the i,j^{th} element of the matrix $G_{(x,y)}$, $U_F \, \Sigma_F \, V_F$ represents the SVD of the matrix $F_{(x,y)}$, and $U_G \, \Sigma_G \, V_G^H$ represents the SVD of the matrix $G_{(x,y)}$. $\bar{F}_{(x,y)}$ and $\bar{G}_{(x,y)}$ represent the power in the respective regions of the Z matrix and the SVD's reveal information that describes the degree of linear dependence of the respective regions of the Z matrix along with generating a useful orthonormal basis.

3.4.1 Similarity Submetric

At the correct scan grid location under the no multipath condition, the region defined by $F_{(x,y)}$ contains the same signal for each receiver; the leading edge of the transmitted waveform. The first submetric is therefore derived from the coherent integration of the leading edge of the transmitted waveform using the singular vector extracted from U_F matrix that corresponds to the the first singular value and spans the sample signal space of the matrix $F_{(x,y)}$. We first define the components of the SVD as

$$U_F \quad = \quad [u_{F,1} \; u_{F,2} \; \cdots \; u_{F,M}] \tag{3.19}$$

$$\Sigma_F \quad = \quad diag\left([\sigma_{F,1}^2 \; \sigma_{F,2}^2 \; \cdots \; \sigma_{F,N}^2]\right) \tag{3.20}$$

$$V_F \quad = \quad [v_{F,1} \; v_{F,2} \; \cdots \; v_{F,N}], \tag{3.21}$$

from which $u_{F,1}$ is used to define

$$\hat{w} \quad = \quad u_{F,1}^T s_{\alpha,tx}^H (s_{\alpha,tx}^H s_{\alpha,tx})^{-1} \tag{3.22}$$

where $s_{\alpha,tx}$ is the known leading edge portion of the transmit waveform. The final similarity submetric is then defined as

$$\frac{1}{\eta_{(x,y)}} \quad = \quad \frac{1}{\sum_{l=0}^{\alpha-1} |u_{F,1} - \hat{w} \, s_{\alpha,tx}|} \tag{3.23}$$

(a) $|\hat{w}|$

(b) $\frac{1}{\eta_{(x,y)}}$

(c) $\frac{1}{\eta_{(x,y)}}$ Zoomed
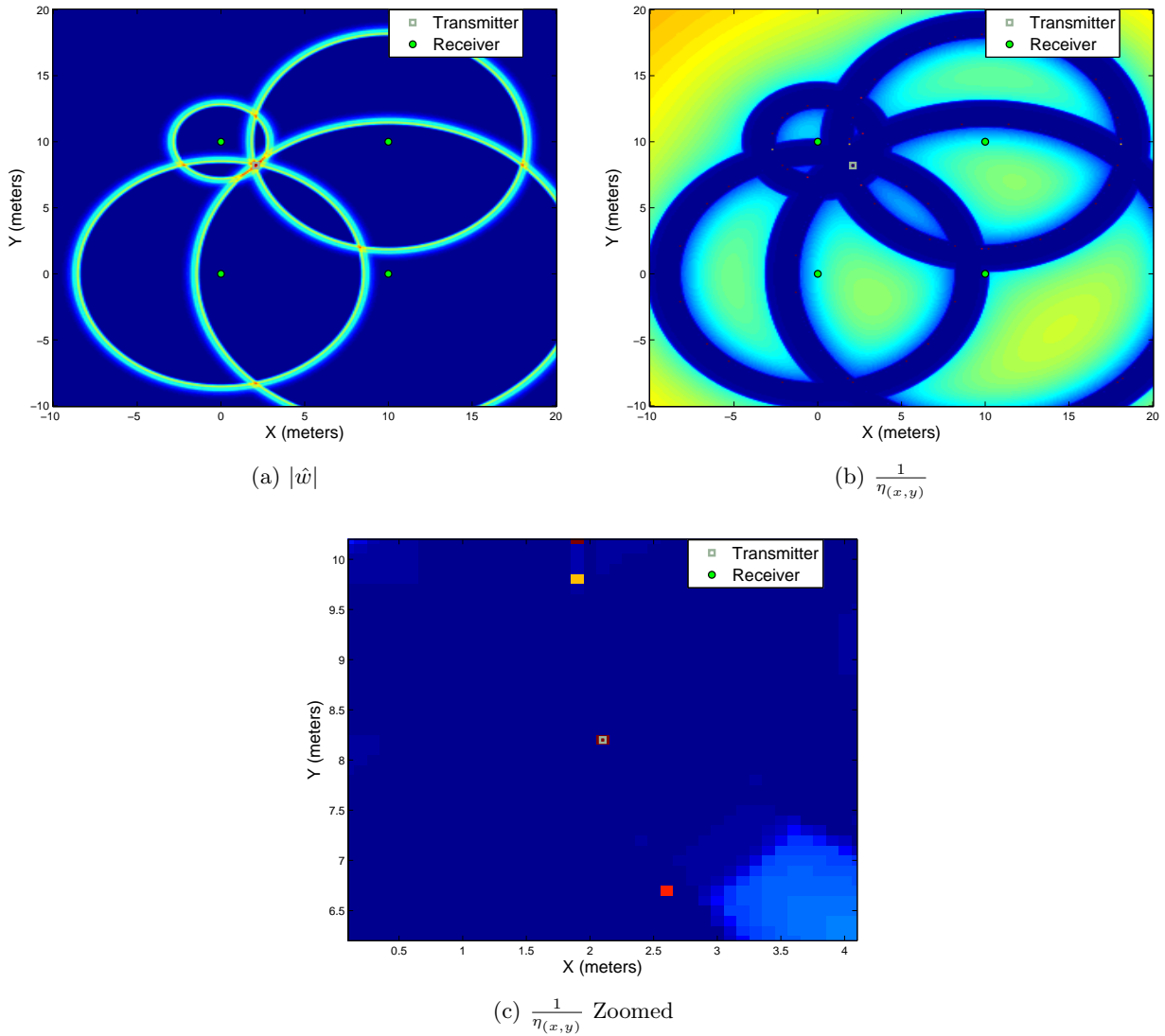
Figure 3.3: Similarity Submetric

where at each scan grid designated position, we have a measure of how much signal content is remaining after removing the known leading edge from the signal computed by the SVD of the matrix $F_{(x,y)}$.

Figure 3.3 shows the similarity submetric components for the ongoing four receiver configuration seen in Figure 2.4. Figure 3.3a shows the magnitude of the computed weight $\hat{w}$. As expected, when the region defined by the matrix $F_{(x,y)}$ contains the known leading edge waveform, $\hat{w}$ has a larger magnitude. At the known transmitter position, $|\hat{w}|$ is the largest. Figure 3.3b shows the metric $\frac{1}{\eta_{(x,y)}}$ as defined by (3.23). This portion of the metric indicates how much signal content was removed by the subtraction. Figure 3.3c shows the same $\frac{1}{\eta_{(x,y)}}$ metric, but zoomed centered on the transmitter position. The transmitter position has the highest metric, which means that the most amount of signal

content was removed at that scan grid location.

3.4.2 SVD Submetric

The SVD submetric uses components from the SVD of both the $F_{(x,y)}$ and $G_{(x,y)}$ matrices. Specifically, we use the largest singular value of $F_{(x,y)}$, which was defined in (3.20) as $\sigma_{F,1}^2$ and the largest singular value from $G_{(x,y)}$ along with it's corresponding singular vector that spans the receiver signal space. If we define the decomposition components of $G_{(x,y)}$ defined in (3.16) as

$$U_G = [u_{G,1}\ u_{G,2}\ \cdots\ u_{G,M}] \tag{3.24}$$

$$\Sigma_G = diag\left([\sigma_{G,1}^2\ \sigma_{G,2}^2\ \cdots\ \sigma_{G,N}^2]\right) \tag{3.25}$$

$$V_G = [v_{G,1}\ v_{G,2}\ \cdots\ v_{G,N}] \tag{3.26}$$

then mathematically we identify $\sigma_{G,1}^2$ and $v_{G,1}$ as the largest singular value and the corresponding right singular vector as the elements of interest for the SVD submetric.

Recall, we earlier stated that when the current scan grid location under test coincides with the true transmitter position, the matrix $F_{(x,y)}$ will have signal content and the matrix $G_{(x,y)}$ will only have noise. To determine a measure of linear dependence in the signal in $F_{(x,y)}$, we identify the largest singular value, $\sigma_{F,1}^2$ to be of interest to the SVD submetric. To measure linear dependence in the matrix $G_{(x,y)}$, we compute

$$\xi_{(x,y)} = |\sigma_{G,1}^2 v_{G,1}|, \tag{3.27}$$

which is a $_{NX1}$ vector that represents the contribution of each receiver to the largest singular value of the matrix $G_{(x,y)}$ at each scan grid location. Under scan grid test conditions where signal content has been shifted into $G_{(x,y)}$, there will be a larger measure of linear dependence than under the condition of noise only. Once all scan grid points have been computed we will have a 3 dimensional matrix. The first two dimensions are the x and y scan grid, and the third dimension contains N elements, one for each receiver. The notation

$$\xi_{i,(x,y)} \quad i = 1..N \tag{3.28}$$

will be used to describe the individual elements of $\xi_{(x,y)}$ and ξ_i will be used describe the values of the 2 dimensional matrix of all scan grid locations to the ith receiver. If we define the distance from receiver i to the current scan grid location as

$$R_{i,(x,y)} = \sqrt{(x - s_{x,i})^2 + (y - s_{y,i})^2} \tag{3.29}$$

(a) ξ_1

(b) ξ_2

(c) ξ_3

(d) ξ_4
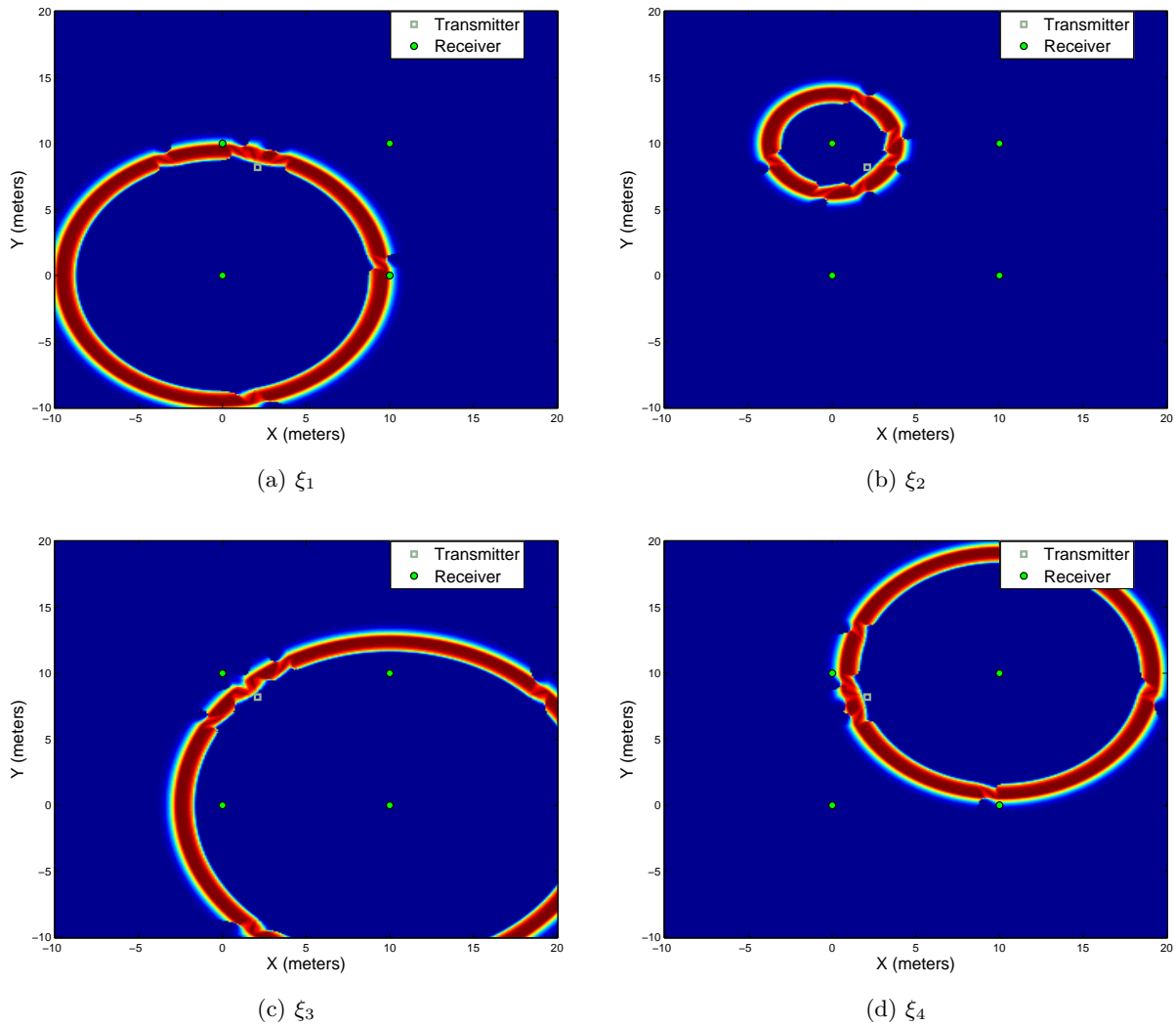
Figure 3.4: The SVD based contribution of the ith receiver submetric in (a) receiver 1, (b) receiver 2, (c) receiver 3, and (d) receiver 4 to the G region singular value ($\xi_{i,(x,y)}$)

then we can define the set of all scan grid locations relative to the ith receiver less than $R_{i,(x,y)}$ as $\bigcup_i$. We then compute the maximum value

$$\bar{\xi}_{i,(x,y)} \quad = \quad \max |\xi_{i,\forall\,(x,y)\,\in\,\bigcup_i}| \tag{3.30}$$

that has been produced by the ith receiver data to the largest singular value of $G_{(x,y)}$. The term $\bar{\xi}_{i,(x,y)}$ represents the maximum contribution receiver i has made to the largest singular value of the matrix $G_{(x,y)}$ as a function of range.

For example, Figure 3.4 shows the 4 metric images defined by ξ_i for $i = 1..4$ using the example scenario shown in Figure 2.4. Each metric image represents the contribution of the receiver to the

(a) $\bar{\xi}_1$

(b) $\bar{\xi}_2$

(c) $\bar{\xi}_3$

(d) $\bar{\xi}_4$
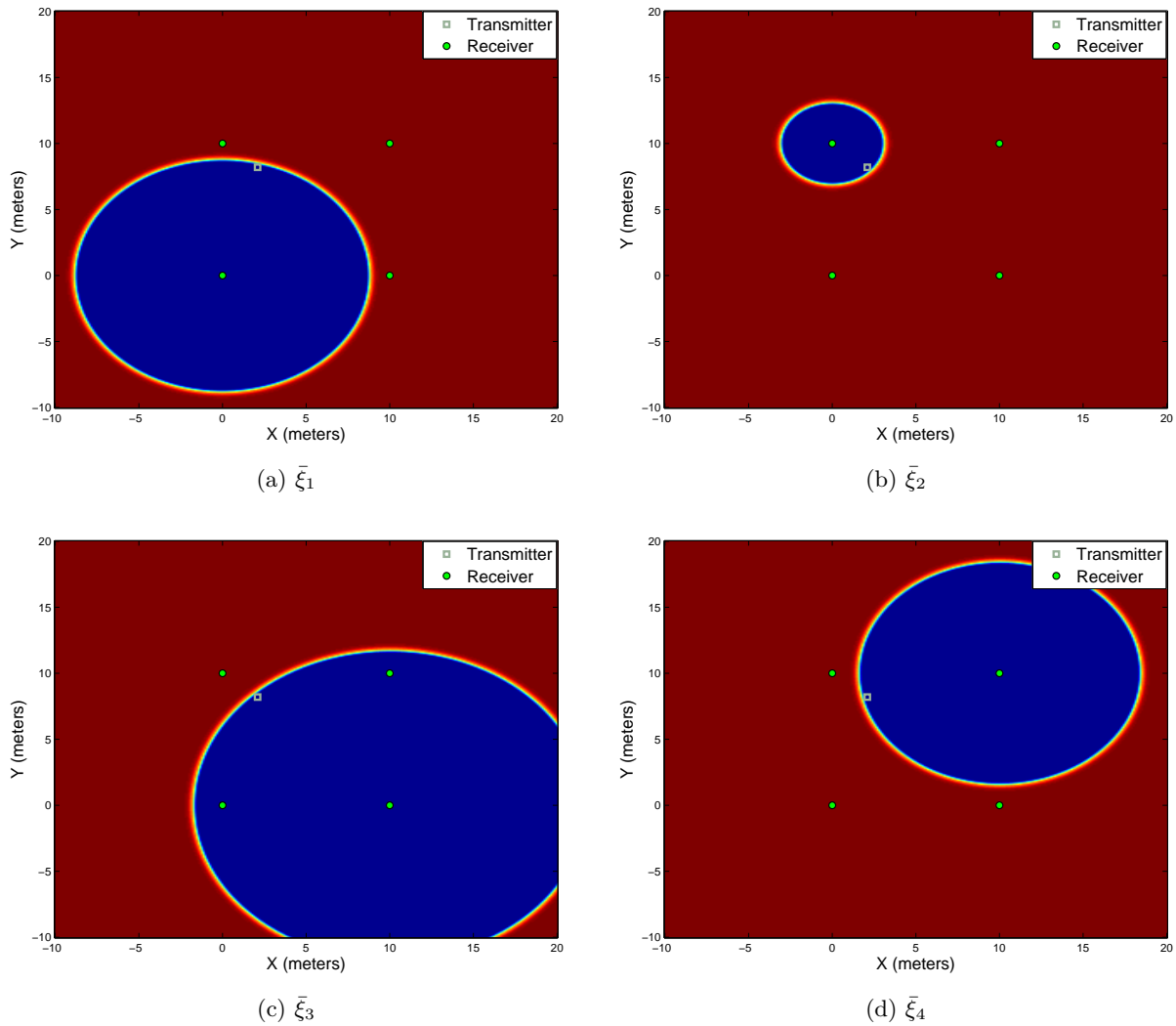
Figure 3.5: The SVD based contribution of the ith receiver submetric as a function of range in (a) receiver 1, (b) receiver 2, (c) receiver 3, and (d) receiver 4 to the G region singular value $(\bar{\xi}_{i,(x,y)})$

singular value in the region defined by the $G_{(x,y)}$ matrix. As the waveform is shifted farther in range than the true distance as seen in receiver 2 by the location (2.5,7) in Figure 3.2b, the $G_{(x,y)}$ matrix has a large singular value due to signal content. As the range to a receiver increases even further, the signal is shifted into and then out of the region defined by the matrix $G_{(x,y)}$. To capture this condition, we compute the maximum contribution the individual receiver has made to the singular value as a function of range. Figure 3.5 shows the maximum contribution as a function of range, $\bar{\xi}_i$. If we closely examine and compare Figure 3.4b and Figure 3.5b, we see that just beyond the true transmitter position, the submetric value increases. The maximum as a function of range holds the max value and a circle with

(a) $\sigma_{F,1}^2$

(b) $\frac{1}{\bar{\xi}_{(x,y)}}$

(c) $\frac{\sigma_{F,1}^2}{\bar{\xi}_{(x,y)}}$

(d) $\frac{\sigma_{F,1}^2}{\bar{\xi}_{(x,y)}}$ Zoomed
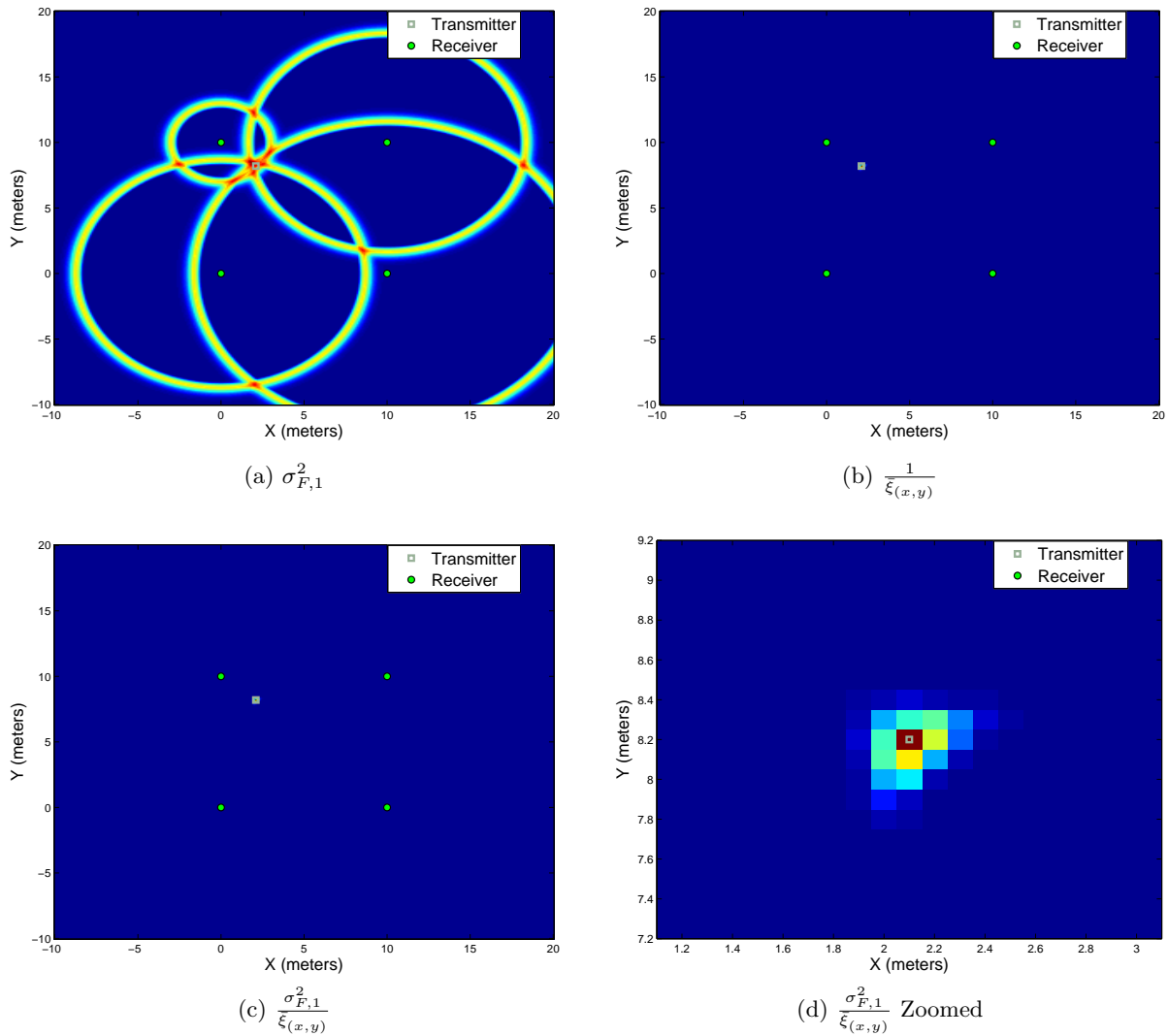
Figure 3.6: The SVD submetric components (a) largest singular value in $F_{(x,y)}$, (b) contribution of ith receiver, (c) final SVD submetric, and (d) final SVD submetric zoomed near true transmitter position showing a single peak

sharp contrast is created just beyond the true transmitter position. This is due to the signal entering (being shifted into) and exiting the $G_{(x,y)}$ region first contributing and then not contributing to the largest singular value of the scan grid position under consideration.

We then combine all N of these metric maps together to form

$$\bar{\xi}_{(x,y)} \quad = \quad \sum_{i=1}^{N} \bar{\xi}_{i,(x,y)} \tag{3.31}$$

which is the sum of the max metric maps along the receiver dimension. The term $\bar{\xi}_{(x,y)}$ represents the

contribution of the ith receiver, producing a small value when signal content has not yet been seen in all receivers as a function of range. Finally, we define the SVD submetric as

$$\frac{\sigma_{F,1}^2}{\bar{\xi}_{(x,y)}} \tag{3.32}$$

where $\sigma_{F,1}^2$ acts as a normalization factor.

Figure 3.6 shows an example of the components that make up the SVD submetric using the ongoing scenario shown in Figure 2.4. Figure 3.6a shows the largest singular value, $\sigma_{F,1}^2$, of the signal region defined by the matrix $F_{(x,y)}$ at each scan grid location. This looks similar to the TART metric, but it is now a coherent summation of the data that has been shifted into the signal region at each scan grid location. Figure 3.6b is the denominator of the SVD submetric, which provides an indication of the contribution of the each receiver to the largest singular value of the noise region defined by $G_{(x,y)}$. If no receiver contributes to the singular value, resulting in a small singular value, this metric is large. The final SVD metric is shown in Figure 3.6c and shown zoomed in Figure 3.6d near the true transmitter position.

3.4.3   Power Submetric

The third and final submetric is simply a ratio of the power in each region. Using (3.17) and (3.18), we define the power submetric as

$$\frac{\bar{F}_{(x,y)}}{\bar{G}_{(x,y)}}. \tag{3.33}$$

At the correct scan grid location, we expect the signal content in $F_{(x,y)}$ and noise in $G_{(x,y)}$. As signal content increases in $F_{(x,y)}$, the power submetric increases. If signal content protracts itself from $G_{(x,y)}$, the power submetric decreases. The maximum of the power metric under ideal conditions (no interference) will always be at the transmitter location where the power of the signal is large in the $F_{(x,y)}$ region and the power of $G_{(x,y)}$ is small with only noise, both conditions which increase the power submetric.

Figure 3.7 shows the components of the power submetric using our ongoing example of a known waveform transmitted in a ideal channel with no multipath. Figure 3.7a shows the power in the signal region defined by the matrix $F_{(x,y)}$ and Figure 3.7b shows the inverse of the power in the noise region defined by the matrix $G_{(x,y)}$ at each scan grid location. If the noise region defined by the matrix $G_{(x,y)}$ has noise only as is the case at the true transmitter position, $\bar{G}_{(x,y)}$ is small, resulting in a larger power submetric. Figure 3.7c shows the power submetric combining the powers in both signal and

(a) $\bar{F}_{(x,y)}$

(b) $\frac{1}{\bar{G}_{(x,y)}}$

(c) $\frac{\bar{F}_{(x,y)}}{\bar{G}_{(x,y)}}$

(d) $\frac{\bar{F}_{(x,y)}}{\bar{G}_{(x,y)}}$ Zoomed
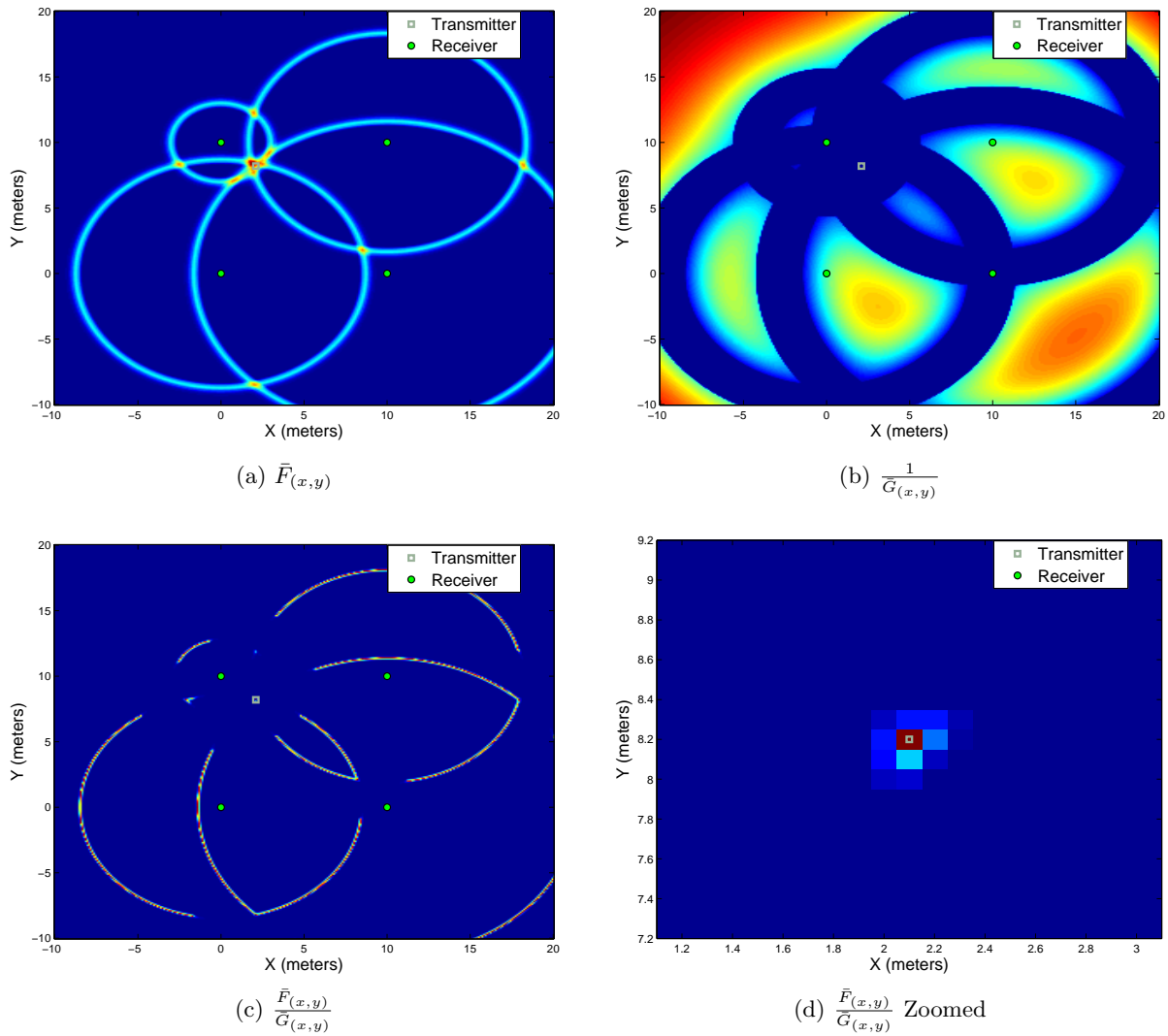
Figure 3.7: The power submetric components (a) power in $F_{(x,y)}$, (b) inverse of power in $G_{(x,y)}$, (c) final power submetric, and (d) final power submetric zoomed near true transmitter position showing a single peak

noise regions and Figure 3.7d shows the power submetric zoomed on the transmitter position showing a single peak that well defines the true transmitter position in this example.

3.5 Minimum Submetrics

We could define the final submetric from (3.23), (3.32), and (3.33) as

$$\frac{1}{\eta_{(x,y)}} \frac{\sigma_{F,1}^2}{\bar{\xi}_{(x,y)}} \frac{\bar{F}_{(x,y)}}{\bar{G}_{(x,y)}} \tag{3.34}$$

where each subcomponent is simply multiplied together to influence the final metric. The problem with this formulation is that if any component of the denominator is small, the final metric could become very large. In order to avoid this exaggeration, we develop a minimum submetric based on the first few samples. This is similar in intent to what is done in the construction of the two step LED algorithm described in Section 2.2, where we defined the threshold based on the first 60 samples in (2.8). The CART metric similarly needs a computation based on the first α samples under the same assumption to the LED algorithm that no signal exists in that region.

Similar to the definition of region $F_{(x,y)}$ in Section 3.3, we begin by taking the first α samples of A (in MATLAB notation $\bar{A} = A(1:\alpha,:)$). The only difference between $F_{(x,y)}$ and $\bar{A}$ is that $\bar{A}$ is not subject to the rephasing performed by $B_{(x,y)}$. Next, as was done with the submetrics, we compute the SVD

$$\bar{A} = U_{\bar{A}} \Sigma_{\bar{A}} V_{\bar{A}}^H \tag{3.35}$$

and define the decomposition components as

$$U_{\bar{A}} = [u_{\bar{A},1} \; u_{\bar{A},2} \; \cdots \; u_{\bar{A},M}] \tag{3.36}$$

$$\Sigma_{\bar{A}} = diag\left([\sigma_{\bar{A},1}^2 \; \sigma_{\bar{A},2}^2 \; \cdots \; \sigma_{\bar{A},N}^2]\right) \tag{3.37}$$

$$V_{\bar{A}} = [v_{\bar{A},1} \; v_{\bar{A},2} \; \cdots \; v_{\bar{A},N}]. \tag{3.38}$$

Finally, we compute the three minimum submetrics as

$$\eta\Upsilon = \sum_{l=0}^{\alpha-1} |u_{\bar{A},1} - (u_{\bar{A},1}^T s_{\alpha,tx}^* (s_{\alpha,tx}^H s_{\alpha,tx})^{-1}) s_{\alpha,tx}| \tag{3.39}$$

$$\sigma_\Upsilon^2 = \sigma_{\bar{A},1}^2 \tag{3.40}$$

$$P_\Upsilon = \frac{1}{N\alpha} \sum_{j=0}^{\alpha-1} \sum_{i=1}^{N} |\bar{A}_{i,j}|^2 \tag{3.41}$$

where $u_{\bar{A},1}$ is the first singular vector that spans the row space (sample dimension) of $\bar{A}$, $s_{\alpha,tx}$ is the leading edge of the known transmit waveform as defined in (3.22), $\sigma_{\bar{A},1}^2$ is the first singular value of $\bar{A}$, and $\bar{A}_{i,j}$ is the i,j^{th} element of the matrix $\bar{A}$. These three minimum metrics serve as a measure of the noise in the signal system and is used to limit unwanted peaks in the CART metric.

3.6   Final CART Metric

The final metric is computed using the data matrix A from (2.13). The first optional step is to compute a maximum power on the input signal that limits the signal power to the maximum threshold level set by the LED algorithm computed in Section 2.2. We briefly mention this limiting operation in the next chapter, but leave it to the reader for further experimentation. In general, it appears that performing a power limiter operation prior to the CART algorithm improves the performance in a heavy multipath environment, but perhaps reduces the performance under LOS high SNR conditions. The next step is to normalize each column to their respective 1-norms in the time domain. This ensures that large amounts of energy seen at a single receiver do not overshadow the final metric. Next, assuming that we have the full data matrix of frequency data from (2.13) and the rephasing matrix from (2.14) at each scan grid location, we again produce the element wise multiplication of A and $B(x,y)$ as seen in (2.15). The scan grid position in the Cartesian domain is (x,y) and the corresponding rephased data matrix in the frequency domain is defined as $D_{(x,y)}$. As was done in the TART algorithm in equation (2.17), we also take the IDFT of the data matrix rephased to the current scan grid location, which we again denote by $Z_{(x,y)} = \mathbf{F}^{-1}[D_{(x,y)}]$.

Next, the matrices $F_{(x,y)}$ and $G_{(x,y)}$ are defined as in Section 3.3, which define the signal portion and noise portion respectively. Using these two matrices, we compute the similarity, SVD, and power submetrics as discussed in Section 3.4. Using the original data matrix A, we also compute the minimum metrics as in Section 3.5.

Combining all of these submetrics, we define the final CART metric as

$$\zeta_{(x,y)_C} = \frac{1}{(\eta_{(x,y)} + \eta_\Upsilon)} \frac{\sigma_{F,1}^2}{(\bar{\xi}_{(x,y)} + \sigma_\Upsilon^2)} \frac{\bar{F}_{(x,y)}}{(\bar{G}_{(x,y)} + P_\Upsilon)} \tag{3.42}$$

which contains a power ratio, a coherent addition of the signal energy in the $F_{(x,y)}$ signal region, and utilizes the known transmit waveform. The noise calibration values $(\eta_\Upsilon, \sigma_\Upsilon^2, P_\Upsilon)$ are added to the metric to reasonably limit the computed submetrics values $(\eta_{(x,y)}, \bar{\xi}_{(x,y)}, \bar{G}_{(x,y)})$ at each scangrid location from causing an unrealistically large value in the output metric. It is apparent that if there is a decrease in the power in the noise $G_{(x,y)}$ region or if the known transmit signal is removed from the coherent SVD solution more precisely, the CART metric is increased. If there is more power and a larger singular value in the $F_{(x,y)}$ signal region, the CART metric is increased.

Figure 3.8 summarizes the three submetrics shown in Section 3.4. Combining these submetrics with the minimum submetrics as in (3.42) results in the metric image seen in Figure 3.9, with Figure 3.9a being the full metric image and Figure 3.9b shows the region around the true transmitter position.

(a) Similarity Submetric, $\frac{1}{(\eta_{(x,y)}+\eta_\Upsilon)}$

(b) SVD Submetric, $\frac{\sigma_{F,1}^2}{(\bar{\xi}_{(x,y)}+\sigma_\Upsilon^2)}$

(c) Power Submetric, $\frac{\bar{F}_{(x,y)}}{(\bar{G}_{(x,y)}+P\Upsilon)}$
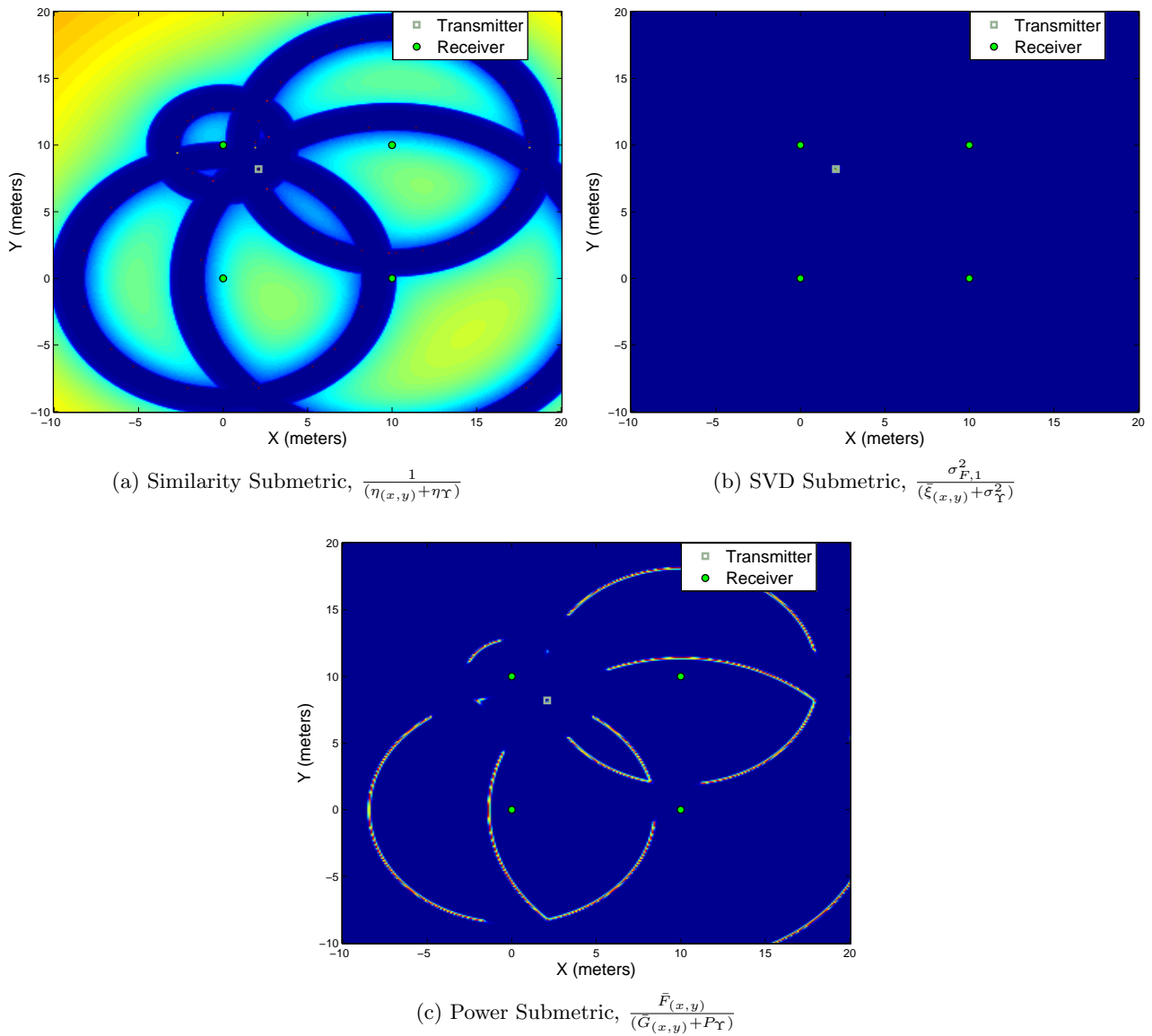
Figure 3.8: Summary of three CART submetrics

A single scan grid location is illuminated in the metric image using the P410 waveform with an ideal channel model with no multipath and no noise.
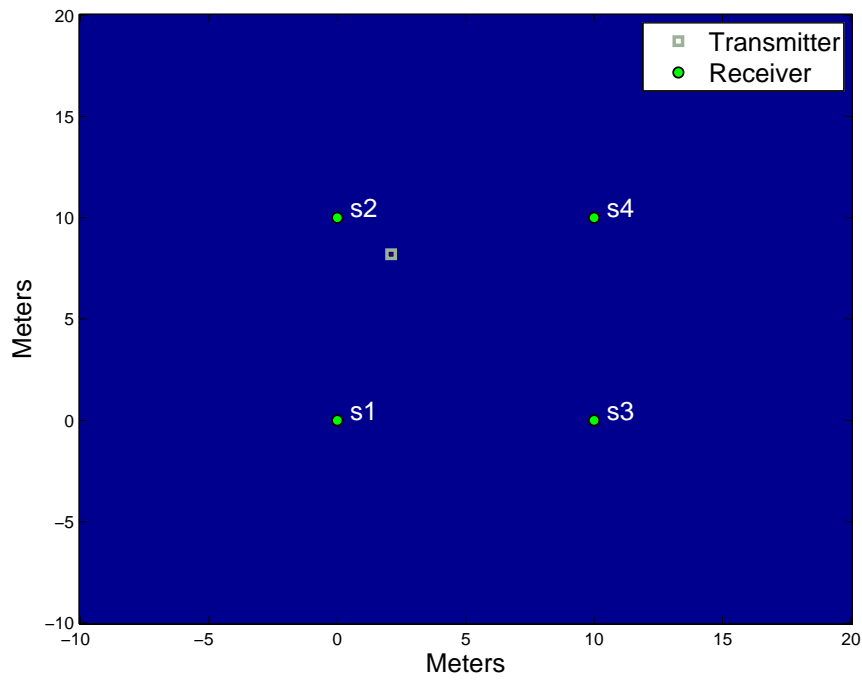
(a) $\zeta_{(x,y)_C}$
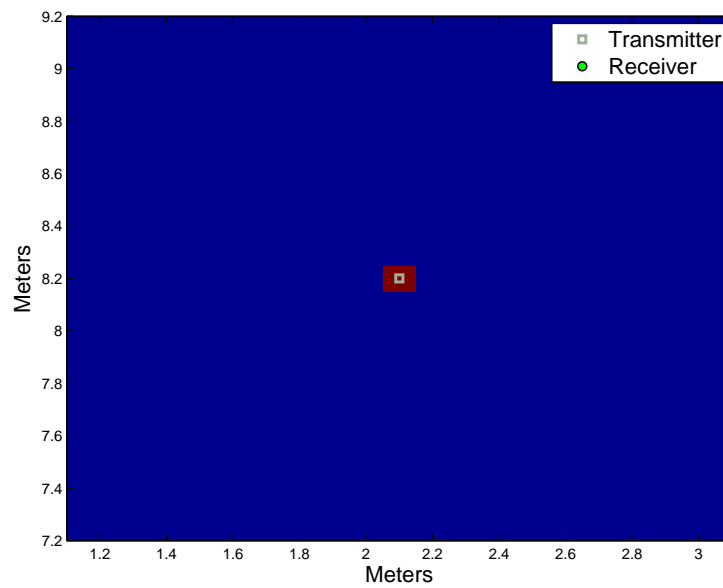
(b) $\zeta_{(x,y)_C}$ Zoomed

Figure 3.9: Final CART metric image using known transmit waveform in a simulated environment with no multipath

Chapter 4

Theoretical Analysis using Simulated Multipath

Starting in Chapter 2, as seen in Figure 2.4, we introduced the ideal channel model with no fading, multipath, or noise to illustrate how the two step LED, SART, TART, and CART algorithms behave using the P410 transmit waveform. The ideal model was carried forward by example in this dissertation until now. We now wish to examine the performance of each algorithm in the presence of multipath by simulation.
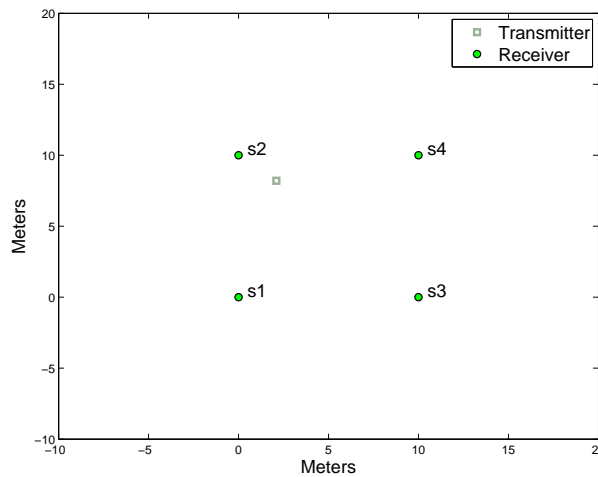
Figure 4.1: Simulation Setup

Simulation is a useful tool in understanding the performance of algorithms without the need for expensive and time consuming data collections. With the understanding that the conclusions from

(a) Simulated Data

(b) $\mathbf{F}^{-1}(A)$
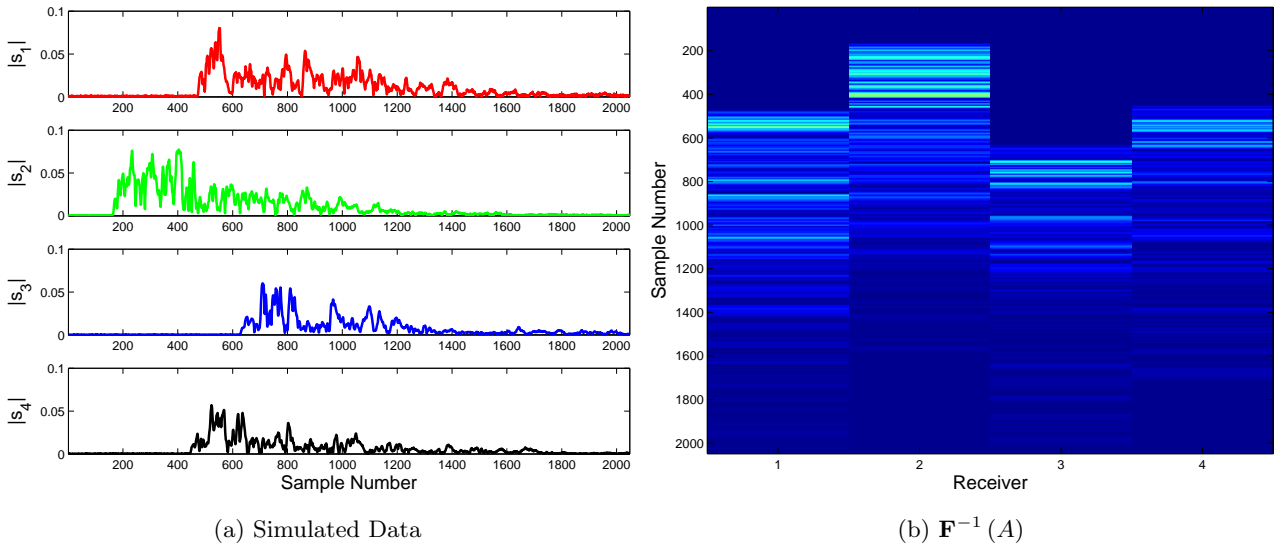
Figure 4.2: (a) Contains an example of simulated data using the IEEE 802.15.4a CM4 indoor multipath model, and (b) shows the resulting data matrix in the time domain

simulation are only as good as the models that drive them, we wish to use the most accurate indoor multipath model possible. The industry standard in the area of indoor localization is the IEEE 802.15.4a [27], which provides MATLAB code for uniformity in simulation.

For this section, we use the standard IEEE 802.15.4a CM4 indoor multipath model for the office environment to generate simulated waveforms from one transmitter to four receivers as shown in Figure 4.1. The transmitter was placed with an (x_m, y_m) position of (2.11,8.21) and the receive antennas were placed at (0,0), (0,10), (10,0), and (10,10), all in meters. Since the CART algorithm utilizes the knowledge of the transmitted waveform, we also compute the Matched Filter (MF) solution prior to computing the the LED, SART, and TART solutions.

The errors of the two step LED, and DPAs SART, TART, and CART algorithms are analyzed in several ways, first as a comparison of the Mean Squared Error (MSE) to an estimated theoretical limit set by the Cramer Rao Lower Bound, second as a plot of Cumulative Density Function (CDF) of the errors, and last as a plot of Root Mean Squared (RMS) error. Before we present the performance results of the simulation, we show by example the superior performance of the CART algorithm in comparison to the other three methods considered.

4.1 Simulation Example

The sensor configuration for the simulation chapter is seen in Figure 4.1. The IEEE 802.15.4a CM4 [27] indoor multipath model was used to generate an appropriate impulse response between the transmitter and all receivers without the propagation delay. The generated impulse response is then used to produce a simulated received waveform at each receiver. This is done by convolving the impulse response with the known P410 transmit waveform followed by a proper time shift representing the delay due to the associated range for each receiver position relative to the transmitter position. An example of the simulated data can be seen in Figure 4.2, which shows the magnitude of the signal at each receiver as well as the IDFT of the resulting data matrix A as defined by equation (2.13) under high signal to noise conditions. A detailed look at Figure 4.2a shows significant multipath structure along with fading effects. The direct path signal at all four receivers is nowhere near the peak power of the waveform and it is obvious when comparing to the ideal simulation in Figure 2.4b that there are many closely spaced time delays in the indoor office environment multipath model that cause overlap of the transmitted waveform. Both of these characteristics of the received waveform make it difficult to localize the transmitter.

The three existing algorithms discussed in Chapter 2 are first applied to the same data. Figure 4.3a to Figure 4.3c show the example data processed using the two step LED method, SART, and TART. Under this simulated heavy multipath, the SART and TART algorithms fail to produce a good position estimate, highlighting the problem with existing DPAs that were not designed for UWB IR waveforms in heavy multipath. The two step LED method produces a reasonable estimate somewhat near the true transmitter position. The problem is still that the overlap of received pulses produces constructive addition and destructive cancelation of the received waveform, resulting in a larger variance in the single independent range estimates.

Figure 4.3d shows the result when the same data is processed using the new CART algorithm introduced in Chapter 3. A coherent combination of the direct path signals is used to perform a leading edge detection on the ensemble of received data. The result is a single scan grid position that has significantly more energy than its neighbors. Figure 4.4b shows the CART result zoomed near the true transmitter position, from which the pixel closest to the true transmitter position is easily chosen for this example data. As a comparison, we also show the two step LED zoomed with the same axes in Figure 4.4a.

It is also instructive to examine the submetrics of CART and how they combine to generate this

(a) LED
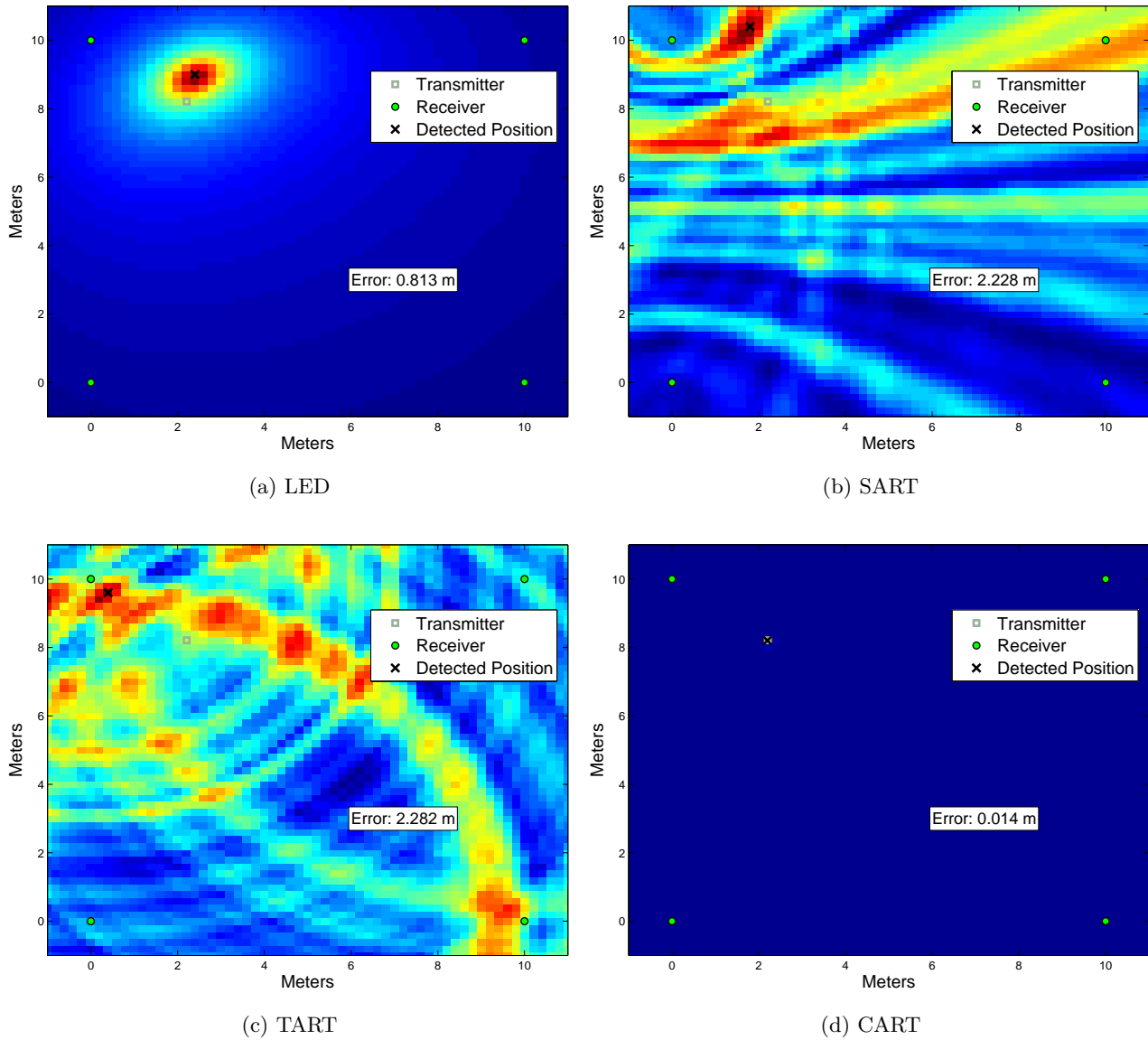
(b) SART

(c) TART

(d) CART

Figure 4.3: The example data was processed using (a) two step LED method, (b) SART, (c) TART, (d) CART.

solution. Figure 4.5 shows the contribution of each receiver to the G region as defined in Section 3.3 and seen in Figure 3.2b. The structure of the multipath as it enters the G region is evident in these four metric images. The maximum contribution as a function of range to each receiver is seen in Figure 4.6. The complex structure of the multipath has been reduced to produce these more simple metric images. Summing these metric images, and producing the final SVD submetric, results in the metric image seen in Figure 4.7b. The other submetrics, similarity and power, are also seen in Figure 4.7. Each of

(a) LED
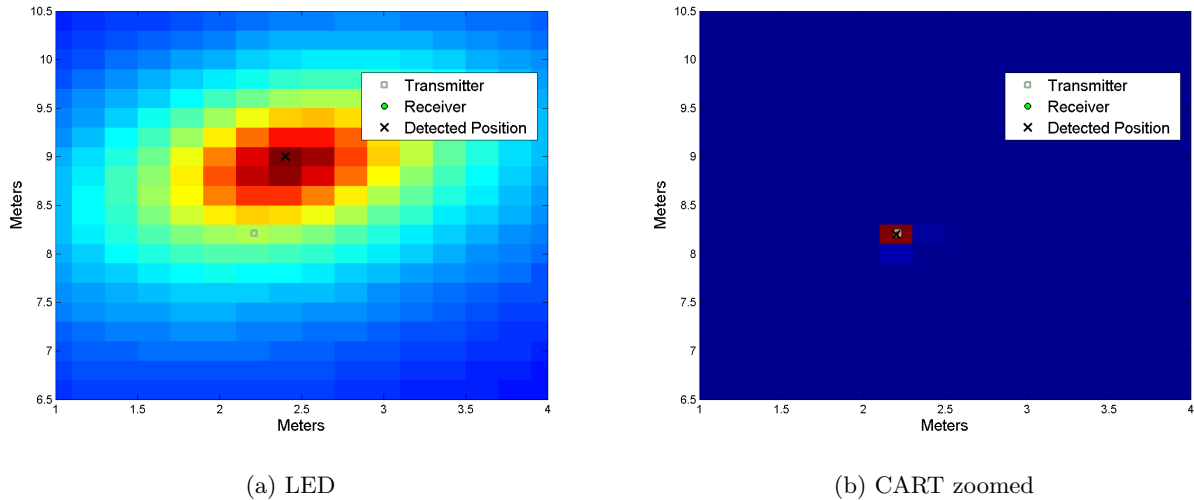
(b) CART zoomed

Figure 4.4: The example data was processed using (a) the two step LED zoomed near the true transmitter position and (b) CART zoomed near the true transmitter position.

these produce a high value near the true transmitter position, that when combined, produce the single scan grid localization solution from the extremely difficult multipath data used in this example.

This simulation demonstrates that the CART algorithm can have some immunity to the large multipath of indoor environments. Further statistical analysis of performance is required to properly examine the benefits of the CART algorithm and how it compares to the other existing algorithms under the heavy multipath conditions of indoor environments. In the example in this section, we introduced multipath to the signal, but no noise. To fairly analyze the performance of each algorithm, we wish to add multipath and noise and measure the performance of each algorithm as a function of the SNR.

(a) ξ_1

(b) ξ_2

(c) ξ_3

(d) ξ_4
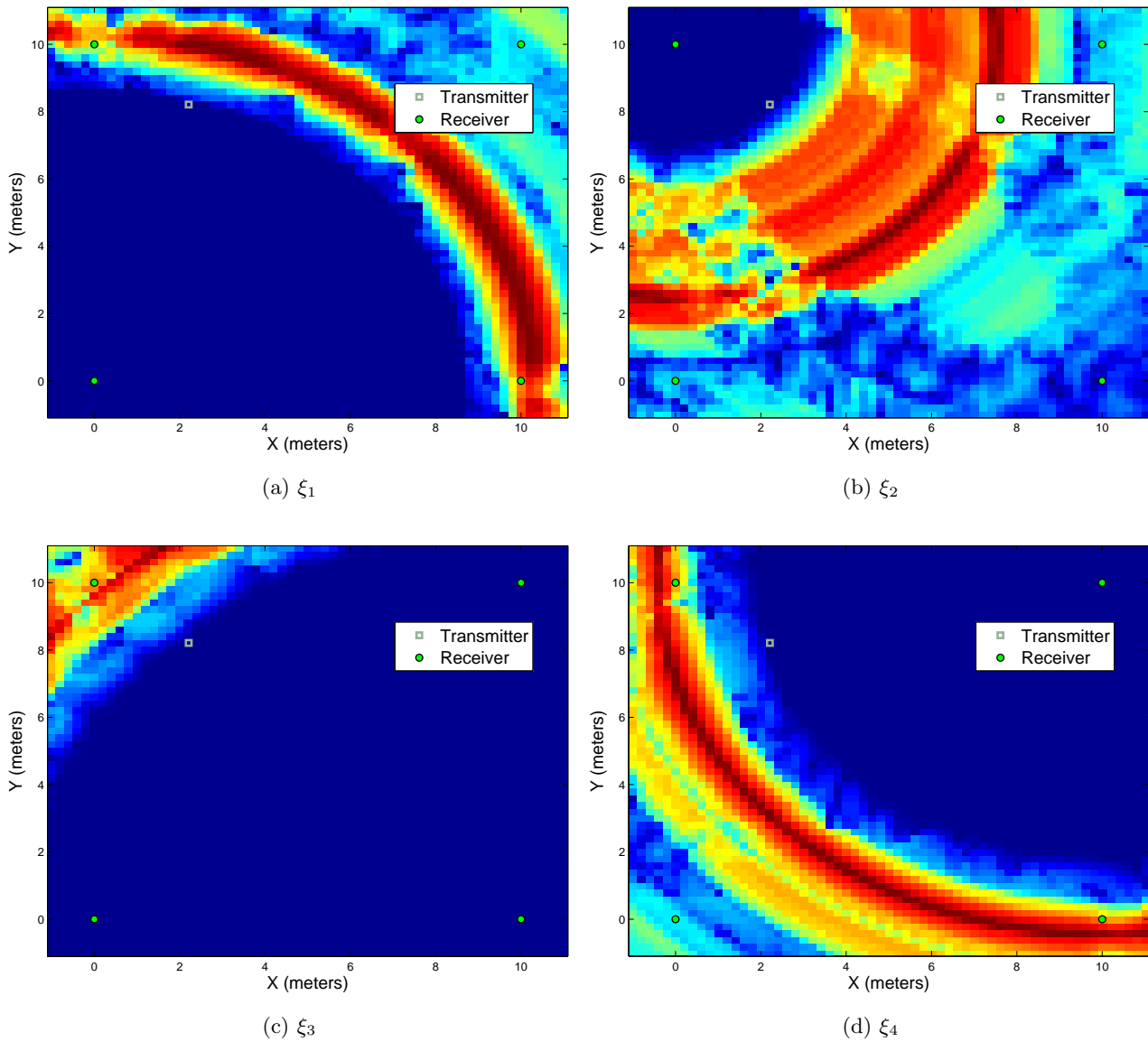
Figure 4.5: The contribution of (a) receiver 1, (b) receiver 2, (c) receiver 3, and (d) receiver 4 to the G region largest singular value (ξ_i). For each receiver, we see no signal structure is evident in the G region until the scan grid under test passes the true transmitter position in range. Scan grid positions farther in range than the true transmitter position begin to produce some interesting patterns due to multipath based upon the amount of signal that is contributed to the largest singular value of the G region by the respective receiver.

(a) $\bar{\xi}_1$

(b) $\bar{\xi}_2$

(c) $\bar{\xi}_3$

(d) $\bar{\xi}_4$
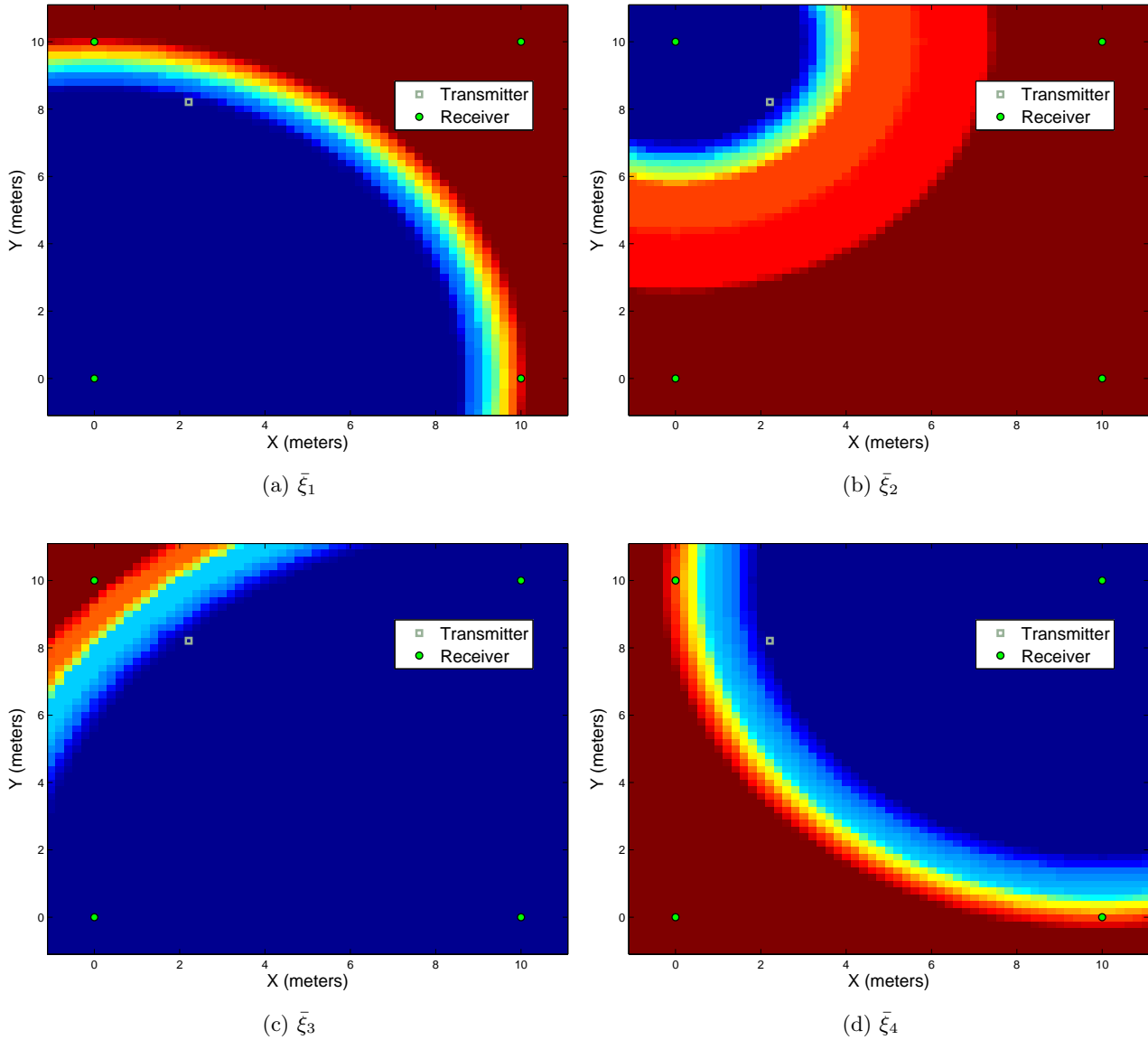
Figure 4.6: The largest contribution as a function of range made by (a) receiver 1, (b) receiver 2, (c) receiver 3, and (d) receiver 4 to the G region largest singular value ($\bar{\xi}_i$) at each scan grid location. The submetric ξ_i seen in Figure 4.5 is now modified to have the largest value seen as a function of range from the respective receiver. This captures the case of a large multipath signal entering and then exiting the G region as we compute the metric image based on the desired scan grid.
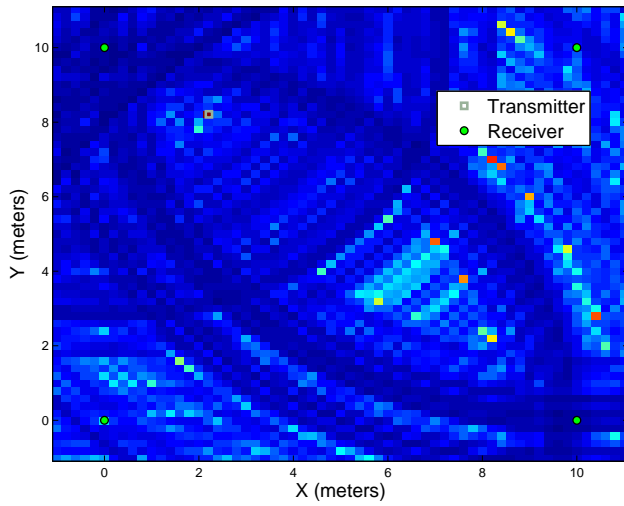
(a) Similarity submetric, $\frac{1}{(\eta_{(x,y)}+\eta_\Upsilon)}$
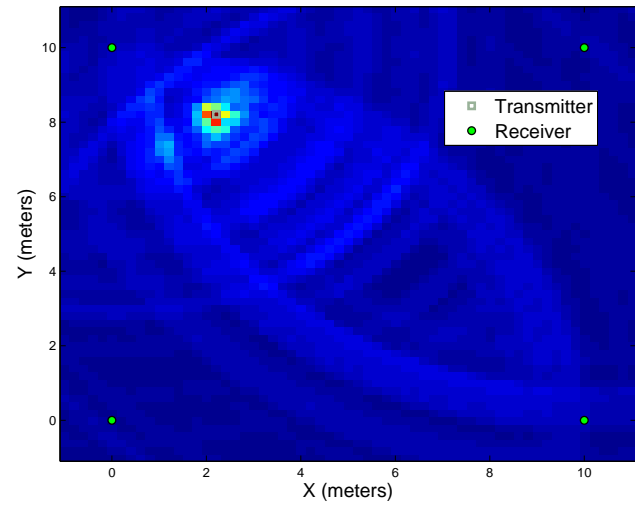
(b) SVD submetric, $\frac{\sigma^2_{F,1}}{(\bar{\xi}_{(x,y)}+\sigma^2_\Upsilon)}$
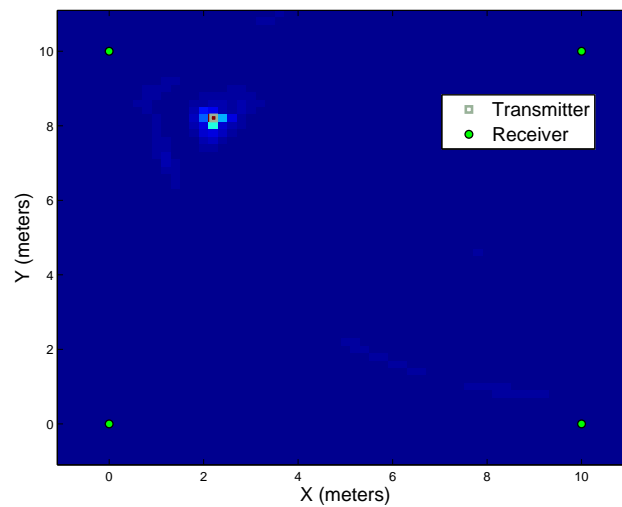
(c) Power submetric, $\frac{\bar{F}_{(x,y)}}{(\bar{G}_{(x,y)}+P_\Upsilon)}$

Figure 4.7: The three submetrics of the CART algorithm: (a) shows the similarity, (b) SVD, and (c) power submetrics

4.2 Cramer Rao Lower Bound (CRLB)

One way to compare the performance of each of the two step LED, SART, TART, and CART algorithms is to compare the Mean Squared Error (MSE) of the Cartesian estimates to the theoretical best performance any unbiased estimator of the Cartesian position can achieve when the signals at each receiver are corrupted by multipath and noise. This theoretical bound is called the Cramer Rao Lower Bound (CRLB). Realistically, it it impractical to determine an exact bound due to the nature of the simulated multipath, so we approximate the CRLB based upon the work of Dardari [6], Kaune [28], and Kay [29].

The approximated CRLB is computed based upon the two step procedure for position estimation seen in Figure 2.1. The range estimates of the first step are bound based upon multipath conditions, and the position estimates of the second step are bound based upon the known geometry of the transmitter and receivers combined with the range estimate variances.

To begin the analysis, we need to re-define the model in equation (2.1) by explicitly representing the average energy of the received signal as a factor in the expression for $s_i(t)$,

$$s_i(t) \;=\; \sqrt{E_{p,i}} \sum_{l=1}^{L_i} \alpha_{l,i} \, p(t - \tau_{l,i}) + n_i(t) \tag{4.1}$$

where $E_{p,i}$ is the average energy of the waveform at the ith receiver, $n_i(t)$ is the additive white Gaussian noise with power spectral density of $\frac{N_{0,i}}{2}$, and the multipath components are normalized such that

$$\sum_{l=1}^{L_i} E[\alpha_{l,i}^2] \;=\; 1. \tag{4.2}$$

With this new formulation of the channel model, Dardari, et. al [6] point out that the variance of the independent range estimates in the multipath environment are bounded by

$$V[\hat{r}_i] \;\geq\; \frac{c^2}{8\pi^2 \alpha_{1,i}^2 \beta^2 SNR_i} \tag{4.3}$$

where $V[\cdot]$ is the variance operator, $\hat{r}_i$ is as defined by equation (2.9), the Signal to Noise Ratio (SNR) at the ith receiver is defined as

$$SNR_i \;=\; \frac{E_{p,i}}{N_{0,i}} \tag{4.4}$$

and the transmitted waveform bandwidth is defined by

$$\beta^2 \;=\; \frac{\int_{-\infty}^{\infty} f^2 |P(f)|^2 df}{\int_{-\infty}^{\infty} |P(f)|^2 df}. \tag{4.5}$$

This formulation gives us a bound on the independent range estimates, $\hat{r}_i$, which is the first step of the two step position estimate as discussed in Section 2.2. Next, we generalize the analysis shown in [28] to accommodate arbitrary receiver geometries and carry the range variances forward.

To begin the second step in the analysis, we start by stating that we have noise corrupted measurements of a set of ranges from the unknown transmitter position to a set of known receivers. This is modeled as

$$y_i \;=\; r_i + v_i, \;\; i = 1..N \tag{4.6}$$

where r_i is the range from the ith receiver to the transmitter, N is the number of receivers, and v_i is additive noise. Putting this measurement in terms of the Cartesian parameters we care about gives

$$y_i \;=\; \sqrt{(x_m - s_{x,i})^2 + (y_m - s_{y,i})^2} + v_i \tag{4.7}$$

where x_m and y_m describe the 2 dimensional Cartesian position of the unknown transmitter and $s_{x,i}$, $s_{y,i}$ contains the known receiver positions. The set of unknown parameters to estimate is then defined as $\Theta = [x_m \; y_m]^T$.

If the measurement noise v_i is assumed to be Gaussian noise and is defined by

$$v_i \;\sim\; N(h(\Theta), R(\Theta)) \tag{4.8}$$

then we can write the likelihood function as

$$p(\mathbf{y}|\Theta) \;=\; \frac{1}{\sqrt{|2\pi R(\Theta)|}} e^{-\frac{1}{2}(y-h(\Theta))^T R^{-1}(\Theta)(y-h(\Theta))} \tag{4.9}$$

where $\mathbf{h}(\Theta) = [h_1(\Theta), \ldots, h_N(\Theta)]^T$ is a complete set of observation functions and $\mathbf{y} = (y_1, \ldots, y_N)^T$ is a complete measurement set. This formulation states that given the unknown parameters Θ, the probability density function is the standard Gaussian multivariate random distribution with mean $h(\Theta)$ and covariance $R(\Theta)$.

The variance of the unknown parameters are then bounded by

$$V[\hat{\Theta}] \;\geq\; J^{-1}(\Theta) \tag{4.10}$$

where $J(\Theta)$ is the Fisher Information Matrix with $_{lk}$ elements defined as [29]

$$[J(\Theta)]_{lk} \;=\; -E\Big[\frac{\partial^2 \ln p(\mathbf{y}|\Theta)}{\partial \Theta_l \partial \Theta_k}\Big], \tag{4.11}$$

where $l = 1..2$ and $k = 1..2$ are the row and column indices of the matrix J (spanning the 2 unknown parameters in our case), $E[\cdot]$ is the expectation operation and ln is the natural log operation. The expression $ln\, p(\mathbf{y}|\Theta)$ is referred to as the log-likelihood function.

Knowing the likelihood function allows us to proceed and compute the elements of the Fisher Information Matrix defined in (4.11). The complete derivation is published by Kay [29], p. 73 and states that the Fisher Information Matrix can be expressed as [29], p. 47

$$[J(\Theta)]_{lk} = \left(\frac{\partial \mathbf{h}(\Theta)}{\partial \Theta_l}\right)^T R^{-1}(\Theta)\left(\frac{\partial \mathbf{h}(\Theta)}{\partial \Theta_k}\right) + \frac{1}{2}tr\left(R^{-1}(\Theta)\frac{\partial R(\Theta)}{\partial \Theta_l}R^{-1}(\Theta)\frac{\partial R(\Theta)}{\partial \Theta_k}\right) \qquad (4.12)$$

where $l = 1..2$ and $k = 1..2$ are the row and column indices of the matrix J (spanning the 2 unknown parameters), tr is the trace operator, and

$$\frac{\partial \mathbf{h}(\Theta)}{\partial \Theta_l} = \begin{bmatrix} \frac{\partial \left[\mathbf{h}(\Theta)\right]_1}{\partial \Theta_l} \\ \frac{\partial \left[\mathbf{h}(\Theta)\right]_2}{\partial \Theta_l} \\ \vdots \\ \frac{\partial \left[\mathbf{h}(\Theta)\right]_N}{\partial \Theta_l} \end{bmatrix}. \qquad (4.13)$$

This is a general solution for the Fisher Information Matrix that, in this case, is useful in the computation of the CRLB.

If we examine equation (4.7) and point out that $\mathbf{h}(\Theta)$ in equation (4.9) can be written as

$$\mathbf{h}(\Theta) = \begin{bmatrix} \sqrt{(x_m - s_{x,1})^2 + (y_m - s_{y,1})^2} \\ \sqrt{(x_m - s_{x,2})^2 + (y_m - s_{y,2})^2} \\ \vdots \\ \sqrt{(x_m - s_{x,N})^2 + (y_m - s_{y,N})^2} \end{bmatrix} \qquad (4.14)$$

which is a $N \times 1$ vector of observation functions. This vector of functions describe how the measurement set $\mathbf{y}$ is related to the unknown parameters. As required by equation (4.12), the partial derivative would then be

$$\frac{\partial \mathbf{h}(\Theta)}{\partial \Theta_l} = \begin{bmatrix} \frac{\partial}{\partial \Theta_l}\sqrt{(x_m - s_{x,1})^2 + (y_m - s_{y,1})^2} \\ \frac{\partial}{\partial \Theta_l}\sqrt{(x_m - s_{x,2})^2 + (y_m - s_{y,2})^2} \\ \vdots \\ \frac{\partial}{\partial \Theta_l}\sqrt{(x_m - s_{x,N})^2 + (y_m - s_{y,N})^2} \end{bmatrix}. \qquad (4.15)$$

To move this analysis forward, we make the assumption that the noise variance of the range estimate is not effected by the unknown transmitter position. This allows us to simplify this analysis by stating

that the average energy in each receiver is the same at all receivers. Mathematically, we state this as

$$E_{p,i} \;=\; E_p \; \forall \; i \tag{4.16}$$

where E_p now defines the average energy at all the receivers. If we further make the assumption that all the noise power is the same in all the receivers, then it is also true that

$$SNR_i \;=\; SNR \; \forall \; i. \tag{4.17}$$

As long as we assign the SNR in this manner when performing the Monte Carlo simulation, the comparison of MSE from the two step LED, SART, TART, and CART algorithms to this estimated CRLB is valid.

Since the noise variance of the range estimate is not affected by the transmitter position, we can also define the covariance matrix as $R(\Theta) = R = \sigma^2 I_{NxN}$, where I_{NxN} is a $N \times N$ identity matrix. Under this assumption, (4.12) simplifies to

$$[J(\Theta)]_{lk} \;=\; \Big(\frac{\partial \mathbf{h}(\Theta)}{\partial \Theta_l}\Big)^T R^{-1} \Big(\frac{\partial \mathbf{h}(\Theta)}{\partial \Theta_k}\Big) \tag{4.18}$$

where the tr operator is no longer a factor since $\frac{\partial R(\Theta)}{\partial \Theta_l} = 0 \; \forall \; l$. Furthermore, this is equivalent to

$$J(\Theta) \;=\; \frac{\partial \mathbf{h}^T}{\partial \Theta} R^{-1} \frac{\partial \mathbf{h}}{\partial \Theta} \tag{4.19}$$

where $\frac{\partial \mathbf{h}}{\partial \Theta}$ is the Jacobian of the measurement set $\mathbf{h}$ with respect to the unknown parameter set Θ. Computing the Jacobian using (4.14) and the parameters $\Theta = [x_m \, y_m]^T$ gives us

$$\frac{\partial \mathbf{h}}{\partial \Theta} = \begin{bmatrix} \frac{x_m - s_{x,1}}{\sqrt{(x_m - s_{x,1})^2 + (y_m - s_{y,1})^2}} & \frac{y_m - s_{y,1}}{\sqrt{(x_m - s_{x,1})^2 + (y_m - s_{y,1})^2}} \\ \frac{x_m - s_{x,2}}{\sqrt{(x_m - s_{x,2})^2 + (y_m - s_{y,2})^2}} & \frac{y_m - s_{y,2}}{\sqrt{(x_m - s_{x,2})^2 + (y_m - s_{y,2})^2}} \\ \vdots & \vdots \\ \frac{x_m - s_{x,N}}{\sqrt{(x_m - s_{x,N})^2 + (y_m - s_{y,N})^2}} & \frac{y_m - s_{y,N}}{\sqrt{(x_m - s_{x,N})^2 + (y_m - s_{y,N})^2}} \end{bmatrix} = \begin{bmatrix} \frac{x_m - s_{x,1}}{r_1} & \frac{y_m - s_{y,1}}{r_1} \\ \frac{x_m - s_{x,2}}{r_2} & \frac{y_m - s_{y,2}}{r_2} \\ \vdots & \vdots \\ \frac{x_m - s_{x,N}}{r_N} & \frac{y_m - s_{y,N}}{r_N} \end{bmatrix} \tag{4.20}$$

and

$$J(\Theta) = \begin{bmatrix} \frac{x_m - s_{x,1}}{r_1} & \frac{x_m - s_{x,2}}{r_2} & \cdots & \frac{x_m - s_{x,N}}{r_N} \\ \frac{y_m - s_{y,1}}{r_1} & \frac{y_m - s_{y,2}}{r_2} & \cdots & \frac{y_m - s_{y,N}}{r_N} \end{bmatrix} \begin{bmatrix} \frac{1}{\sigma^2} & 0 & \cdots & 0 \\ 0 & \frac{1}{\sigma^2} & \ddots & \vdots \\ \vdots & \ddots & \ddots & 0 \\ 0 & \cdots & 0 & \frac{1}{\sigma^2} \end{bmatrix} \begin{bmatrix} \frac{x_m - s_{x,1}}{r_1} & \frac{y_m - s_{y,1}}{r_1} \\ \frac{x_m - s_{x,2}}{r_2} & \frac{y_m - s_{y,2}}{r_2} \\ \vdots & \vdots \\ \frac{x_m - s_{x,N}}{r_N} & \frac{y_m - s_{y,N}}{r_N} \end{bmatrix} \tag{4.21}$$

which is the generalization of the case in [28] without the unknown time delay constant and using equal variance for all receivers. The Fisher Information Matrix then equals

$$J(\Theta) = \frac{1}{\sigma^2} \begin{bmatrix} \sum_{i=1}^{N} \frac{(s_{x,i}-x_m)^2}{r_i^2} & \sum_{i=1}^{N} \frac{(s_{x,i}-x_m)(s_{y,i}-y_m)}{r_i^2} \\ \sum_{i=1}^{N} \frac{(s_{x,i}-x_m)(s_{y,i}-y_m)}{r_i^2} & \sum_{i=1}^{N} \frac{(s_{y,i}-y_m)^2}{r_i^2} \end{bmatrix} \tag{4.22}$$

and applying the matrix inversion lemma gives us the inverse of $J(\Theta)$ as required by (4.10) as

$$J^{-1}(\Theta) = \sigma^2 \begin{bmatrix} \frac{1}{\Upsilon} \sum_{i=1}^{N} \frac{(s_{y,i}-y_m)^2}{r_i^2} & -\frac{1}{\Upsilon} \sum_{i=1}^{N} \frac{(s_{x,i}-x_m)(s_{y,i}-y_m)}{r_i^2} \\ -\frac{1}{\Upsilon} \sum_{i=1}^{N} \frac{(s_{x,i}-x_m)(s_{y,i}-y_m)}{r_i^2} & \frac{1}{\Upsilon} \sum_{i=1}^{N} \frac{(s_{x,i}-x_m)^2}{r_i^2} \end{bmatrix} \tag{4.23}$$

where

$$\Upsilon = \left(\sum_{i=1}^{N} \frac{(s_{x,i}-x_m)^2}{r_i^2} \right) \left(\sum_{i=1}^{N} \frac{(s_{y,i}-y_m)^2}{r_i^2} \right) - \left(\sum_{i=1}^{N} \frac{(s_{x,i}-x_m)(s_{y,i}-y_m)}{r_i^2} \right)^2 .$$

The variance of the unknown parameters are therefore bounded by

$$V[\hat{x}_m] \geq \frac{\sigma^2}{\Upsilon} \sum_{i=1}^{N} \frac{(s_{y,i}-y_m)^2}{r_i^2} \tag{4.24}$$

$$V[\hat{y}_m] \geq \frac{\sigma^2}{\Upsilon} \sum_{i=1}^{N} \frac{(s_{x,i}-x_m)^2}{r_i^2} \tag{4.25}$$

using N receive antennas at known locations.

If the independent range estimates were efficient estimates, meaning they achieved the CRLB for the first step, we can substitute

$$\sigma^2 = \frac{c^2}{8\pi^2 \alpha_{1,i}^2 \beta^2 SNR} \tag{4.26}$$

into (4.24) and (4.25) to get the CRLB of the unknown transmitter position as

$$V[\hat{x}_m] \geq \frac{c^2}{8\pi^2 \alpha_1^2 \beta^2 SNR} \frac{1}{\Upsilon} \sum_{i=1}^{N} \frac{(s_{y,i}-y_m)^2}{r_i^2} \tag{4.27}$$

$$V[\hat{y}_m] \geq \frac{c^2}{8\pi^2 \alpha_1^2 \beta^2 SNR} \frac{1}{\Upsilon} \sum_{i=1}^{N} \frac{(s_{x,i}-x_m)^2}{r_i^2} \tag{4.28}$$

for the multipath condition, where

$$\alpha_1 = \frac{1}{N\bar{M}_c} \sum_{i=1}^{N} \sum_{j=1}^{\bar{M}_c} |\alpha_{1,i_j}| \tag{4.29}$$

where $\bar{M}_c$ is a large number much greater than the number of total Monte Carlo simulations included in the MSE estimates and α_{1,i_j} is the simulated direct path normalized magnitude to the ith receiver for the jth modeled multipath scenario. This averages over many cases of direct path magnitude relative to the respective multipath components in order to produce a measure of α_1.

4.3   Mean Squared Error (MSE) and CRLB vs. Signal to Noise Ratio (SNR)

Having derived the appropriate CRLB for the multiple receiver location problem in multipath, we can now compare the simulated Mean Squared Error (MSE) for each of the two step LED, SART, TART, and CART algorithms to the theoretical lower bound on the estimates $\hat{x}_m$ and $\hat{y}_m$. For the simulation to be presented here, we ran 300 Monte Carlo trials at each SNR setting from -34 to 10 dB in 2 dB steps. When setting the SNR value, we chose the same SNR for all 4 receivers as is required for the assumptions that produced (4.18). The true transmitter position was chosen as $(x_m, x_y) = (2.11, 8.21)$, with a scan grid defined by $x_{min} = -1$, $x_{max} = 11$, $y_{min} = -1$, $y_{max} = 11$ with a $\Delta_x = 0.2$ and $\Delta_y = 0.2$, all in meters and a $\alpha = 20$ and $\gamma = 60$ for the CART algorithm. With these parameters, the smallest possible errors due to grid quantization are

$$\varepsilon_{s,x} \;\; = \;\; x_m - 2.2 \;\; = \;\; 0.09 \;\; = \;\; -20.9\,dB \tag{4.30}$$

$$\varepsilon_{s,y} \;\; = \;\; y_m - 2.2 \;\; = \;\; 0.01 \;\; = \;\; -40\,dB \tag{4.31}$$

which determine the minimum X and Y errors possible in the simulation. We call these limits the scan grid performance limit.

Figure 4.8 shows the CRLB compared to the MSE of each algorithm, the two step LED, SART, TART, and CART. In addition, we show the scan grid limit on each error plot. It is clear that the SART and TART algorithms completely fail under the presence of the level of heavy multipath used in this simulation as they were not designed to take advantage of the UWB IR waveform features. This failure was seen in the example in Section 4.1, where the SART and TART metric images demonstrated poor results. The two step LED algorithm does quite well in the low SNR regions, but then reaches a performance limit at around -8 dB of MSE in both the X and Y error plots. This equates to a respectable mean absolute location error of about 0.4 meters. The CART algorithm, however, performs remarkably well in slightly higher signal to noise ratios. At about -10 dB SNR, it reaches near the CRLB limit in both X and Y error plots. Once the X error reaches the scan grid limit, it levels off close to the -20.9 dB level defined by $\varepsilon_{s,x}$. The Y error continues to show a more and more accurate estimate as the SNR level increases, following the CRLB closely. The final X error is about -20 dB, which equates to about 0.1 meter mean absolute error, a factor of 4 times better than the two step LED, only limited by the scan grid imposed limit. The Y error reaches a remarkable -34 dB of MSE at 10 dB SNR, which equates to about a 0.02 meter mean absolute error, a 20 times improvement over the two step LED
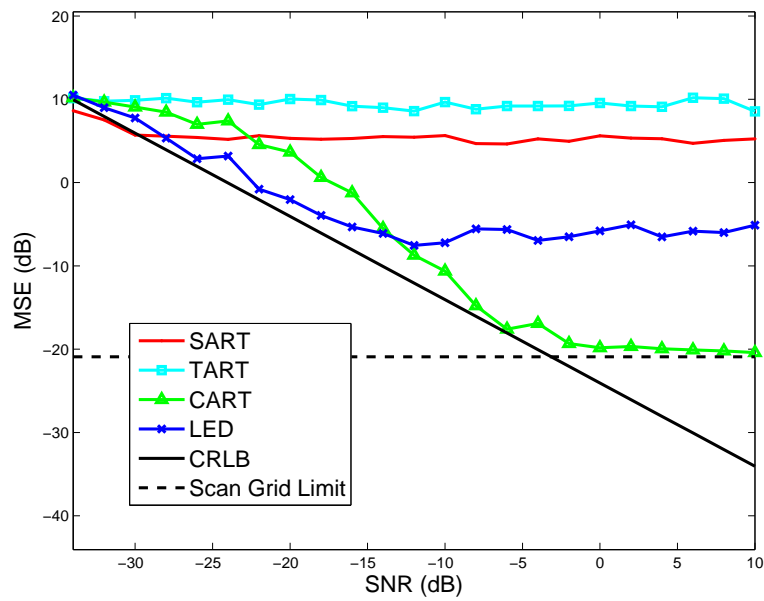
(a) X Errors
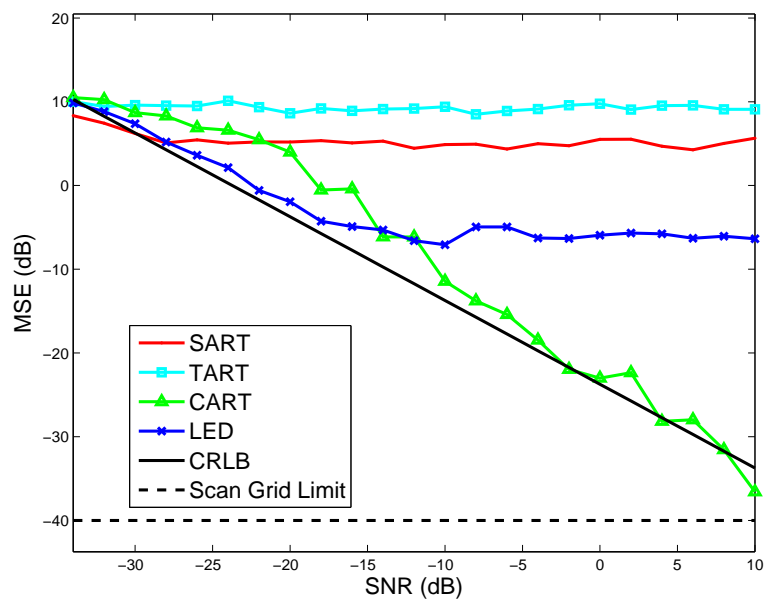
(b) Y Errors

Figure 4.8: SART, TART, CART, and LED performance compared to the Cramer Rao Lower Bound (CRLB) using 300 trials at each SNR setting

method. This demonstrates the near efficiency of the CART algorithm, that is, it produces an estimate that is near the best theoretically possible estimate of the parameters x_m and y_m as described by the CRLB.

4.4 Cumulative Density Function (CDF) of Position Errors

Another way to examine the errors is to plot the Cumulative Density Function (CDF) of the error. We again use the same simulation scenario as described in Section 4.3, where the true transmitter position is $(x_m, y_m) = (2.11, 8.21)$, with a scan grid defined by $x_{min} = -1$, $x_{max} = 11$, $y_{min} = -1$, $y_{max} = 11$ with a $\Delta_x = 0.2$, $\Delta_y = 0.2$, and a $\alpha = 20$ and $\gamma = 60$ for the CART algorithm. The errors were saved for 300 Monte Carlo trials and for SNRs from -34 to 10 in 2 dB steps.
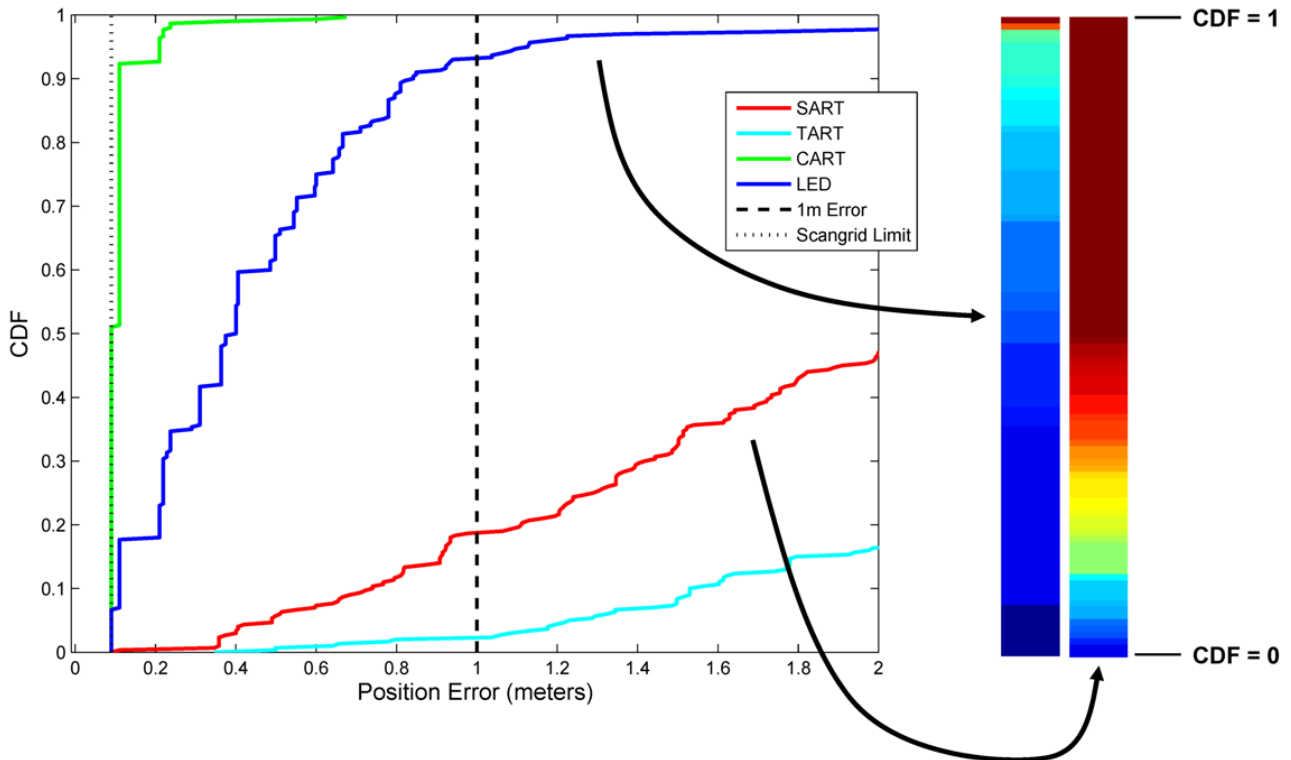
Figure 4.9: Cumulative Density Function (CDF) of the position error at 0 dB Signal to Noise Ratio (SNR)

To produce the CDF of position error plot, we calculate the magnitude of the error vector at each Monte Carlo trial using

$$\hat{\epsilon}_r = \sqrt{(x_m - \hat{x}_m)^2 + (y_m - \hat{y}_m)^2} \tag{4.32}$$

where we refer to $\hat{\epsilon}_r$ as the position error. The errors from each Monte Carlo trial is then sorted from the smallest to the largest. We then plot the the absolute errors as a function of the normalized number of Monte Carlo trials. Figure 4.9 shows the resulting CDF based on our measurements at a setting

of 0 dB SNR. The plots also show a span of 2 meters error, highlighting the 1 meter error and the minimum error imposed by the scan grid limit as defined in (4.30) and (4.31). For this simulation, the performance of the CART algorithm is clearly the best. The TART and SART algorithms hardly produce an error less than 1 meter. The two step LED algorithm performs reasonably well, producing an error of about 0.4 meters 50% of the time. The CART algorithm produces estimates that are less than 1 meter all the time with errors less than about 0.1 meters 92% of the time in this example using 0 dB SNR.

We can also represent each of these curves using a colorbar seen in the right of Figure 4.9. The position on the colorbar represents the current CDF from 0 to 1 and the color indicates the resulting position error that has been limited to a maximum of 2 meters. For example, the LED algorithm results can be represented by a colorbar that is mostly dark blue due to the smaller position errors until it turns to red near the top, where the position errors are maximized to 2 meters. The performance of the SART algorithm can be represented by the colorbar that is dark red from approximately the 50% CDF location to a CDF value of 1, indicating that approximately 50% of the time, the SART algorithm produces an error greater than 2 meters.

We also plot all the position error CDFs as a function of all simulated SNR in Figure 4.10. The errors have been limited to 2 meters on the color scale. The colorbars from Figure 4.9 have been rotated clockwise and inserted into the images in 4.10a and Figure 4.10b at the 0 dB SNR setting. These images reveal the robustness of the CART algorithm. If sufficient signal power is present, the CART algorithm always produces an estimate of position with error of less than a meter. The common two step LED method still produces errors larger than 2 meters, even though the SNR is relatively good between 0 and 10 dB. The SART and TART algorithms usually produce poor estimates.

(a) LED Position Errors

(b) SART Position Errors

(c) TART Position Errors

(d) CART Position Errors
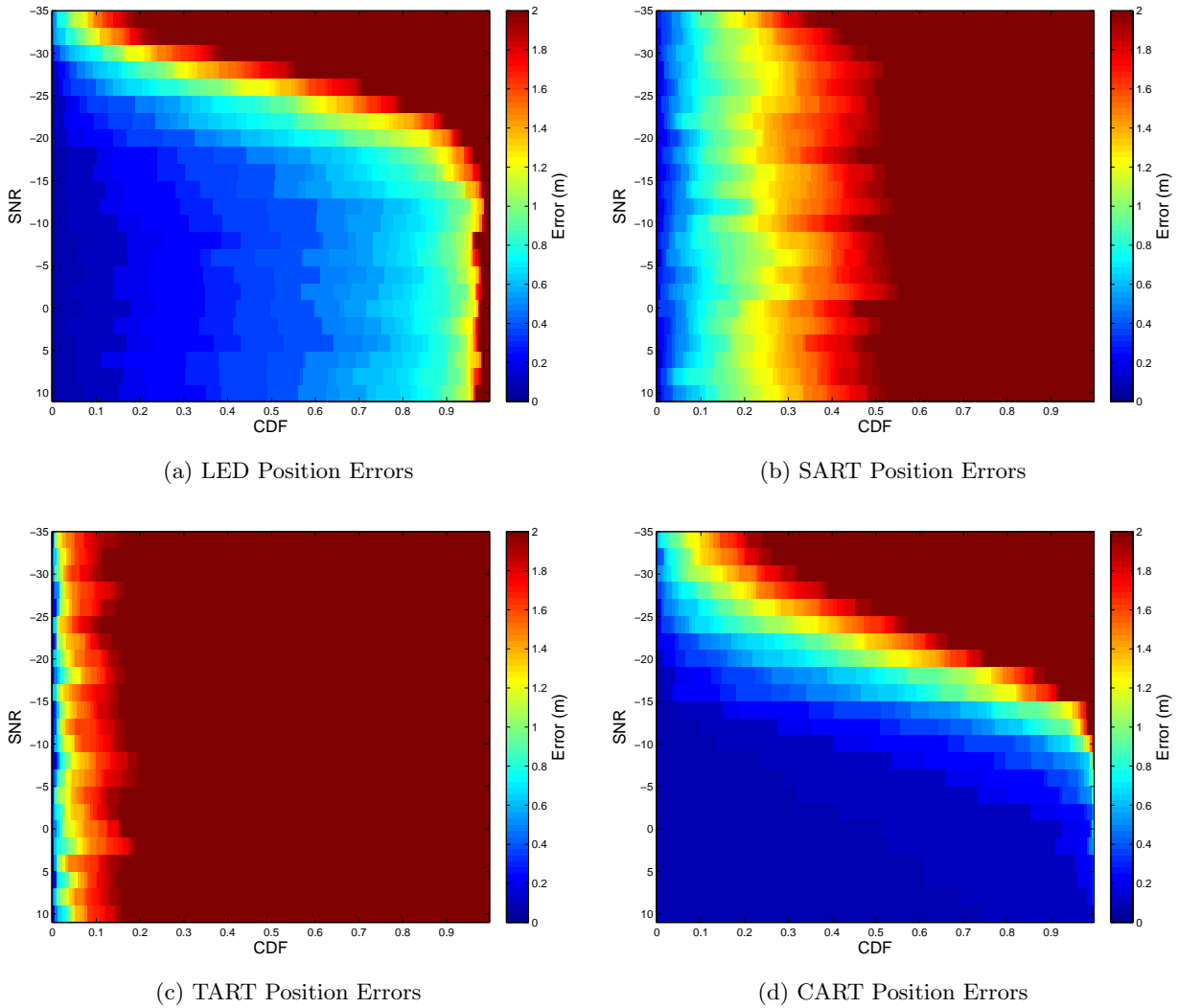
Figure 4.10: Cumulative Density Function (CDF) of the position error at each Signal to Noise Ratio (SNR) limited to 2 meters error for the (a) LED, (b) SART, (c) TART, and (d) CART algorithms

4.5 Root Mean Squared (RMS) Error vs. SNR

In Section 4.3 we compared the MSE to the CRLB as a function of SNR. It is also instructive to examine the Root Mean Squared (RMS) error, where we calculate the square root of the mean of all the $\hat{\epsilon}_r$ from (4.32) that resulted from the 300 Monte Carlo trials.

Figure 4.11 shows the RMS error for each SART, TART, CART, and LED algorithms as a function of SNR. The SART and TART algorithms perform poorly as all the previous analysis has shown. The LED algorithm performs the best in the very low SNR region between about -35 to -15 dB SNR. The CART algorithm performs the best in the SNR region between -15 dB and higher. As we saw in Figure
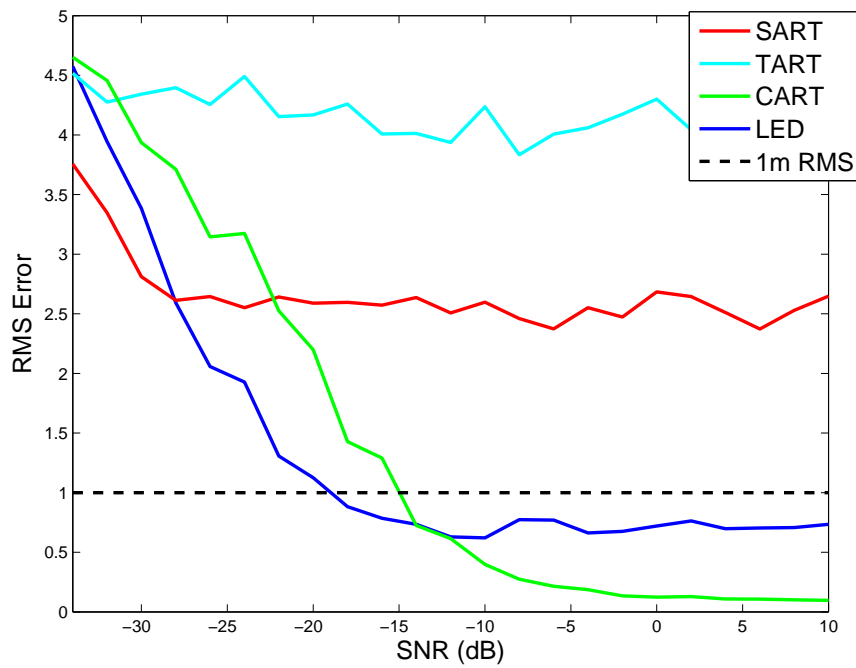
Figure 4.11: RMS Error position estimates for 300 Monte Carlo trials using the SART, TART, CART, and LED algorithms

4.8, the CART error in this SNR region is primarily limited by the chosen scan grid resolution in this simulation example. We are able to easily obtain sub meter accuracy in this simulation using both the LED and CART algorithms. The CART algorithm, however, is able to achieve a much smaller error in -15 dB and higher values of SNR.

Chapter 5

Data Collection Hardware

To further validate the CART algorithm, we need to collect and analyze data in a controlled experiment. Simulation is unable to capture the real world effects on receivers such as unknown interference and non Gaussian noise conditions. We, therefore, must devise a collection strategy that enables this evaluation. This means the collection must preserve the TOA information of the UWB waveform as it propagates through the channel.

This chapter presents a new Two Way Ranging (TWR) alignment algorithm that preserves the TOA information that enables experimentation. The new collection method uses measurements provided by the off the shelf Ultra-Wideband (UWB) Impulse Radio (IR) device to estimate the transmit time of a TWR conversation. This alignment allows us to use a single radio receiver and move it from survey point to survey point while preserving TOA information. This new method also allows for dynamic movement of both transmitter and receiver for the wand application in Chapter 7 when we explore data fusion using a simple motion model and RF data captures.

The data collection hardware uses Time Domain's PulseOn 410 (P410) UWB ranging radios. The P410 is capable of operating as a ranging device, a radar, or a communication device using a series of narrow pulses repeated at approximately 10.1 MHz. The pulse widths are on the order of 500 ps, giving a rough 2 GHz of bandwidth centered around 4.1 GHz. The commercial version transmits a total of -15 dBm of power, which is the maximum allowed by FCC Part 15 UWB devices. As stated in P410 documentation [30], the pulses are "coherently integrated" to produce a measurement of the channel or receive data. Also, channel independence and data communication is achieved using modifications to position, pulse rate, and/or phase changes in the pulse train.

Two P410 units are used to form the collection system, a requester and a responder. The requester,
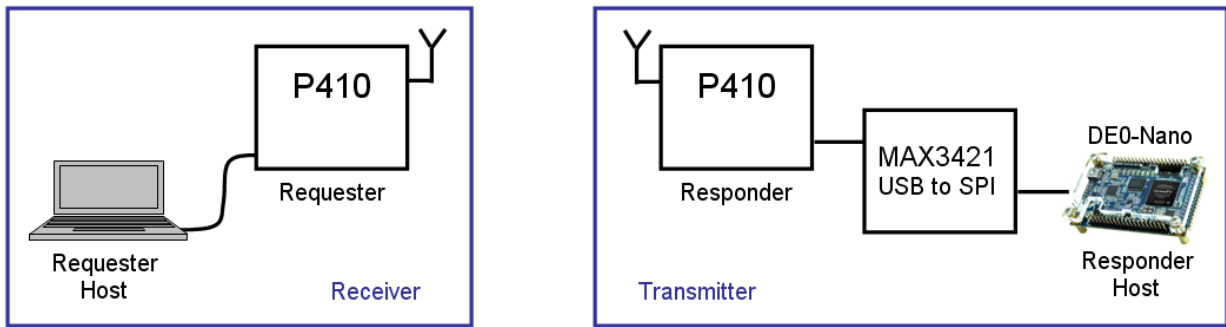
Figure 5.1: Overview of hardware used for data collection

which is part of the receiver, is connected to a laptop through a standard Universal Serial Bus (USB) adapter. The responder, which is part of the transmitter, is connected by USB to a custom Field Programmable Gate Array (FPGA) soft core embedded processor through a MAX3421 USB to 4-wire SPI Bus. Figure 5.1 shows an overview of the hardware configuration used for this experimental implementation along with the various hardware components that make up the transmitter and receiver. We refer to the laptop connected to the requester as the requester host and the embedded device connected to the responder as the responder host. The requester host laptop and the P410 requester unit make up the receiver hardware. The responder host embedded device, the MAX3421 USB to SPI chip, and the P410 responder make up the transmitter hardware.

In this chapter, we first introduce the two way time of flight measurement followed by an example data collection using the P410 to highlight the difficulty with ranging in a multipath environment. Next, we present the modifications necessary to estimate the transmit time, which enables the preservation of the TOA information of the received waveform. Then, we discusses the synchronization performance of the proposed method. For more information on the details of the embedded device that is part of the transmitter unit, we refer the reader to Appendix A

5.1 Two Way Time of Flight

The range measurement provided by the Time Domain P410 evaluation kit is based upon a two way transaction between a requester and a responder unit [31]. Figure 5.2 shows the relevant timing signals related to the transaction. First, at time $t = 0$, the requester sends a series of short pulses in the form of a packet at approximately a 10 MHz rate (single pulse shown in figure). After some unknown time of flight, t_f, and after a lock is acquired on the incoming pulse (t_{rlock}), the responder samples

and records the data near the critical point of arrival. The lock spot detection system can be thought of as an oscilloscope trigger system, capable of storing and retrieving data that both immediately precedes and succeeds the trigger position in the input waveform. After a fixed amount of turn around time, t_T, relative to the responder lock spot, the responder sends a pulse packet back to the requester. The requester then locks onto the responders transmission at time t_{tlock}, around which it samples and records the arriving pulse that has been corrupted by noise and channel multipath. The recorded raw data samples for the two way time of flight measurement is called scan data.
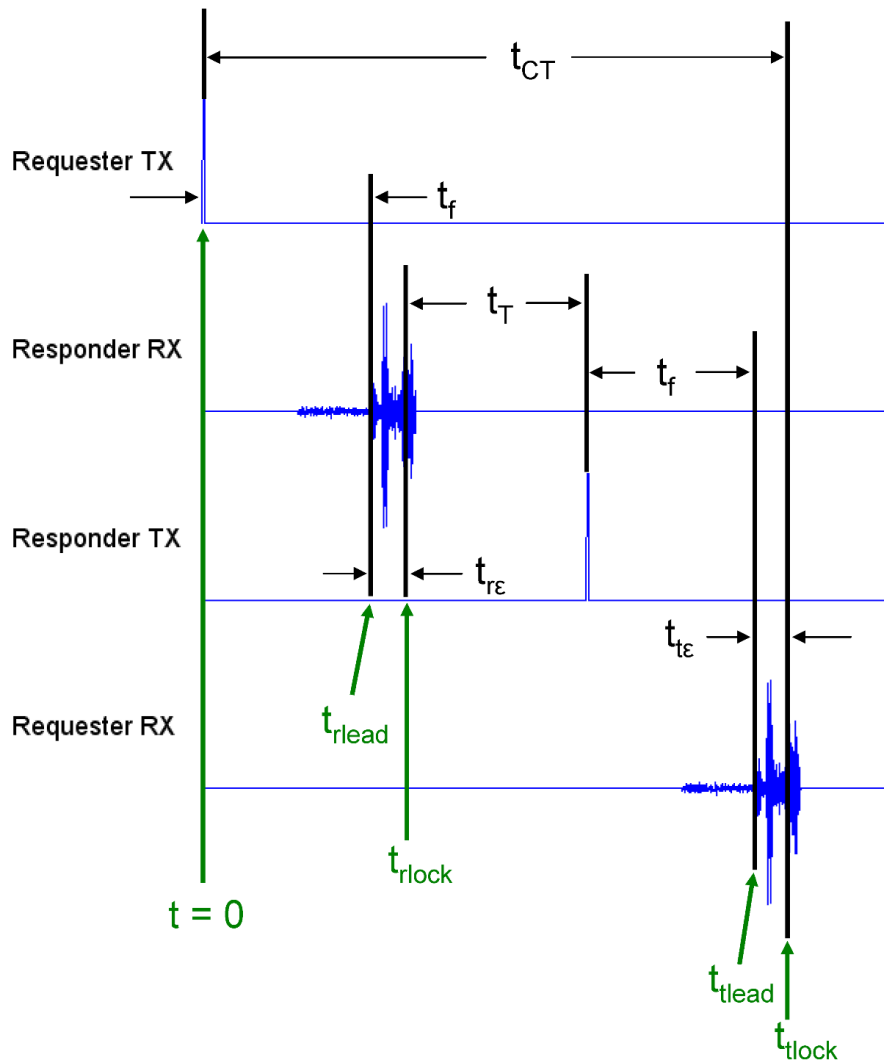
Figure 5.2: Two Way Ranging (TWR) transaction example

The time of the entire transaction can be written as

$$t_{CT} \quad = \quad 2t_f + t_{r\epsilon} + t_T + t_{t\epsilon} \tag{5.1}$$

where $t_{r\epsilon}$ and $t_{t\epsilon}$ are the difference between the true time of arrival of the pulse and the lock spot of the responder and requester unit. The desire is to extract the range between the requester and responder antenna from the time of flight using

$$r \;=\; t_f c \tag{5.2}$$

where c is the speed of light and r is the range between the requester and responder antennas.

The P410 units send several messages to their respective hosts when connected during this two way range transaction. One message it sends is the RCM_RANGE_INFO (0x0201) message [32], which contains a field named Precision Range Measurement (PRM). The PRM provides an estimate of the range between the requester and responder antennas by estimating $t_{r\epsilon}$ and $t_{t\epsilon}$ using a leading edge detection algorithm on the recorded scan data in the responder and requester. There also exists a coarse range measurement (Coarse TOF) in the RCM_RANGE_INFO (0x0201) message sent by the P410 to the host controller. This coarse range measurement contains the number of samples in the TWR transaction time, minus the number of samples in the turn around time (t_T). Mathematically, this value can be defined as

$$C_{TOF} \;=\; (t_{CT} - t_T)f_s$$

where $f_s = \frac{1}{t_{bin}}$ is the sample rate used by the P410, $t_{bin} = 1.907ps$ is the sample period, and C_{TOF} is the measurement from the RCM_RANGE_INFO message. We can use this coarse TOF as follows

$$t_{CT} \;=\; C_{TOF}/f_s = t_{CT} - t_T = 2t_f + t_{r\epsilon} + t_{t\epsilon}$$

to obtain an equation that describes the range measurement using C_{TOF}.

Additional messages can be sent by the P410 to its connected host upon request. One such message of interest is the RCM_FULL_SCAN_INFO (0xF201) message. This message is sent when requested to its connected host whenever a two way transaction takes place. The requester sends this packet to its host and the responder sends this packet to its host. This packet is of interest since it contains the raw recorded samples of the received waveform, or scan data, of each P410 unit. Solving for the range between the requester and responder, we get

$$\hat{r} \;=\; \frac{c}{2}(C_{TOF}/f_s - \hat{t}_{r\epsilon} - \hat{t}_{t\epsilon}) \tag{5.3}$$

where $\hat{t}_{r\epsilon}$, $\hat{t}_{t\epsilon}$, and $\hat{r}$ are all estimates. Also supplied in the RCM_FULL_SCAN_INFO message are the lock spot and leading edge detection sample positions provided by the P410 hardware, which can be

used to compute the estimates of these variables as follows

$$\hat{t}_{r\epsilon} = (n_{rlock} - \hat{n}_{rlead})/f_{dec} \tag{5.4}$$

$$\hat{t}_{t\epsilon} = (n_{tlock} - \hat{n}_{tlead})/f_{dec} \tag{5.5}$$

where n_{tlock} and $\hat{n}_{tlead}$ are the requester lock spot and leading edge reported in samples, n_{rlock} and $\hat{n}_{rlead}$ are the responder lock spot and leading edge reported in samples, and f_{dec} is the sample rate of the scan data. It is important to note that the scan data sent in the RCM_FULL_SCAN_INFO message is a decimated representation of the scan data. The field named Scan Step reports the decimation factor, which we name n_{step}. By default the decimation factor is 32, which makes the scan data sample rate $f_{dec} = \frac{fs}{n_{step}} = \frac{fs}{32}$. The RCM API [32] document states that Scan Step is simply "the amount of time between each sample in bins", which mentions no filtering prior to decimating. It is probable that the samples are accumulated, resulting in a low pass filtered signal representation.

To evaluate the performance of the P410 out of the box and to provide context for our new alignment algorithm, we next conduct an experiment in a Line of Sight (LOS) and a blocked direct path condition. These two conditions demonstrate the difficulty of ranging in a high multipath environment, especially with a blocked direct path.

5.2   P410 Experimentation

For our experiment, we set up two P410 units separated by a range of 2868mm measured by a laser range finder from antenna to antenna. Figure 5.3 shows the two scenarios considered, one with line of sight and one with a blocked direct path, both in a high multipath indoor lab environment. In Figure 5.3a, the requester and responder are both clearly seen and highlighted by a red circle. In Figure 5.3b, the requester is only seen and the direct path is blocked by a large metal sheet and a computer monitor. Both units were connected to the same host laptop so all relevant data can be captured.

We first examine the contents of the RCM_FULL_SCAN_INFO (0xF201) message, which contains the raw samples of the received waveform. Each P410 unit sends this message to the attached host when enabled by configuration. This allows us to plot the waveform as seen by the requester when transmitted by the responder and we can plot the waveform as seen by the responder when transmitted by the requester.

Figure 5.4 shows the scan data sent by the requester and responder units to the host under the LOS test conditions. The requester message is obtained from the case when the responder transmits the

(a) Line of Sight

(b) Blocked Direct Path
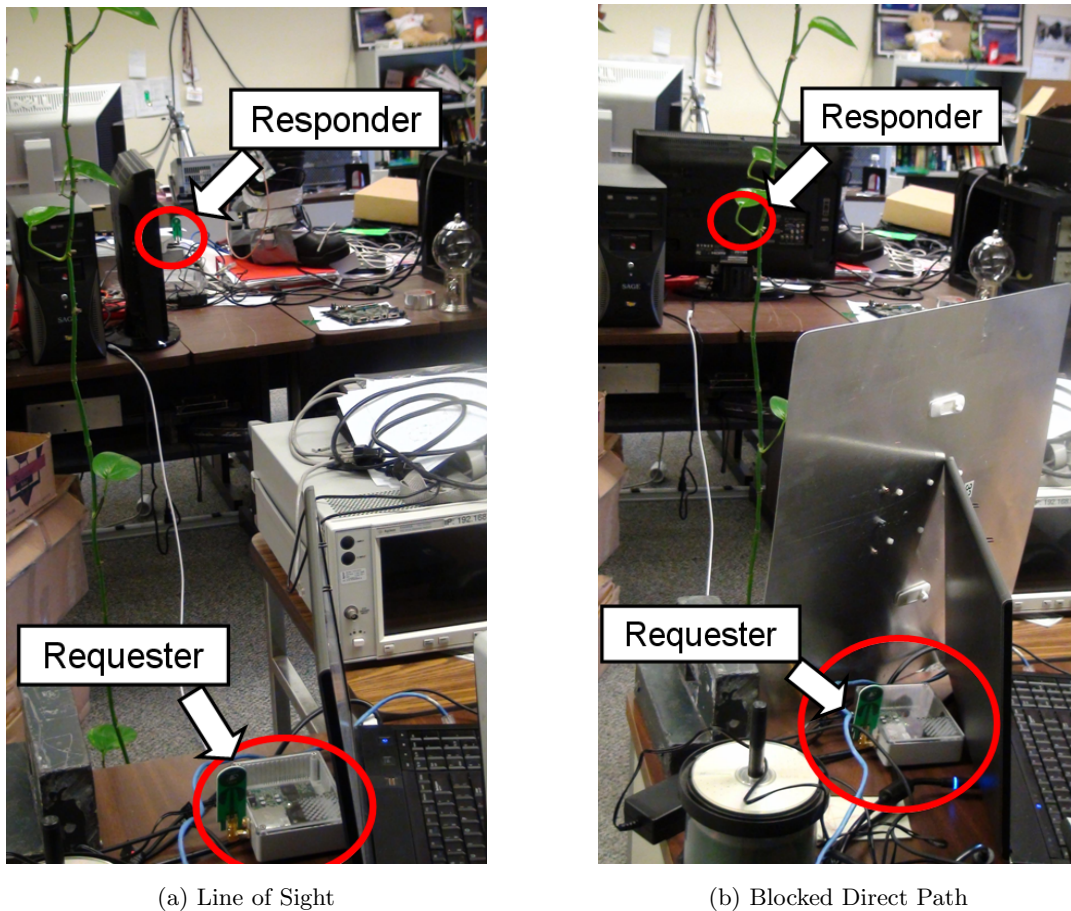
Figure 5.3: P410 devices setup with (a) line of sight and (b) blocked direct path

waveform and it is received by the requester. The responder message is obtained from the case when the requester transmits the waveform and it is received by the responder. As an example, Figure 5.4a and Figure 5.4b show the raw sampled data of the first TWR transaction at the respective units. The blue x is the lock spot and the green x is the leading edge position. Figure 5.4c and Figure 5.4d show the absolute value of all scan data recorded for this test, with each column representing a different TWR transaction at the respective units. The green dots show the leading edge positions as reported by the unit and the blue dots are the lock spots.

Recall that we stated that the lock spot can be thought of as an oscilloscope trigger point, where the scan data is stored representing the input waveform in a window that includes the lock spot. The plots in Figure 5.4 are all aligned to the lock spot which is always located at sample 1475 of the scan data and are therefore dependent on the received waveform, regardless of the range between the requester and responder. In the standard TWR transaction, the received waveform at the requester
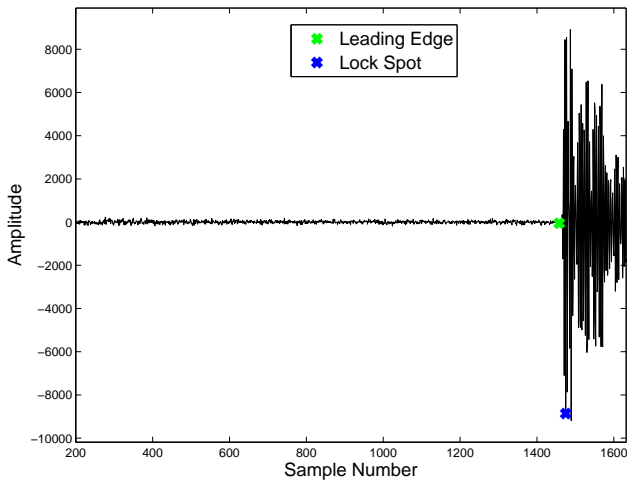
(a) Single scan from Requester
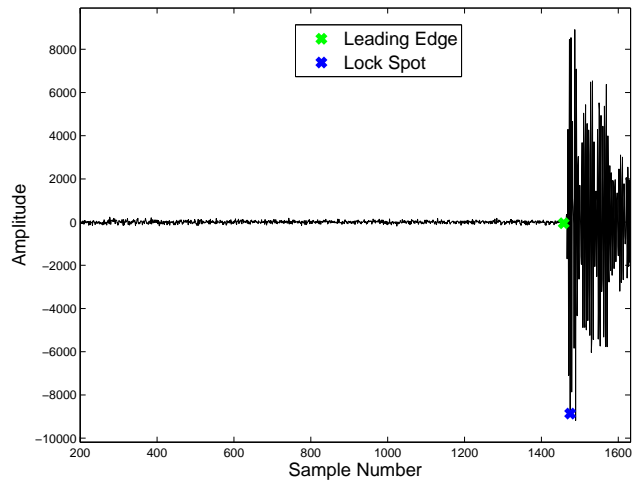
(b) Single scan from Responder
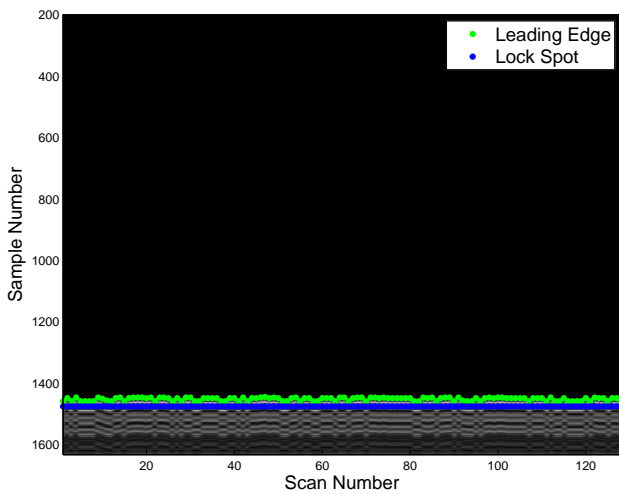
(c) All Requester Data
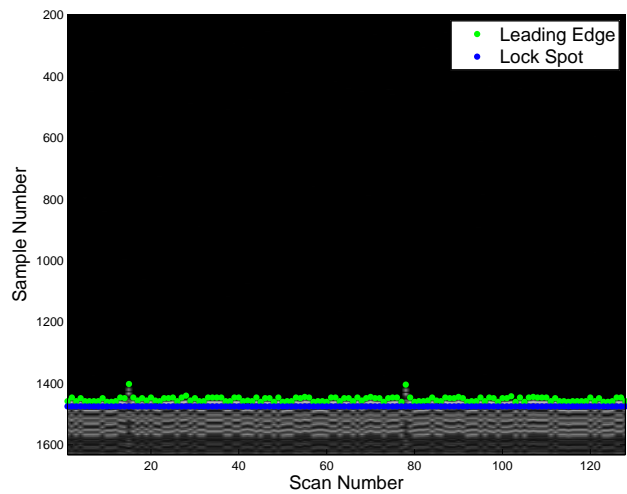
(d) All Responder Data

Figure 5.4: Line of Sight scan data from (a)(c) requester and (b)(d) responder aligned to lock spot

and responder units is used to determine the respective leading edges, from which a range is derived based on equation (5.3), (5.4), and (5.5).

Figure 5.5 shows the scan data sent by the requester and responder units to the host under the blocked direct path test conditions. The scan data are displayed in the same manner as for the LOS data. It is informative to notice that the leading edge position in the amplitude in Figure 5.5a appears quite inaccurate. The green x, which is the P410's estimated leading edge position, can be seen after signal data is observed in the plot. Clearly, this leads to an inaccurate range computation using equation (5.3).
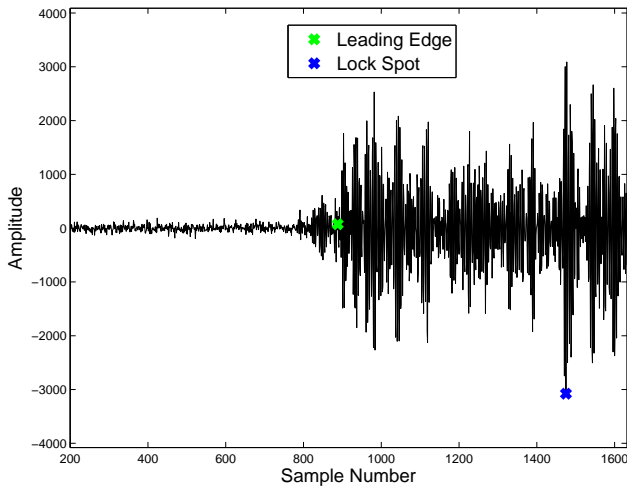
(a) Single scan from Requester
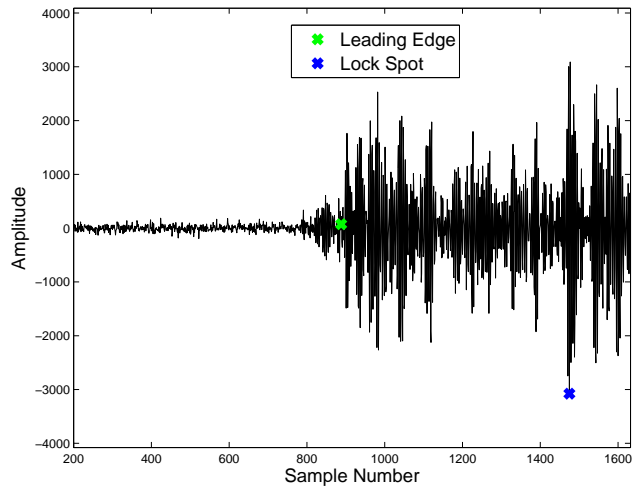
(b) Single scan from Responder
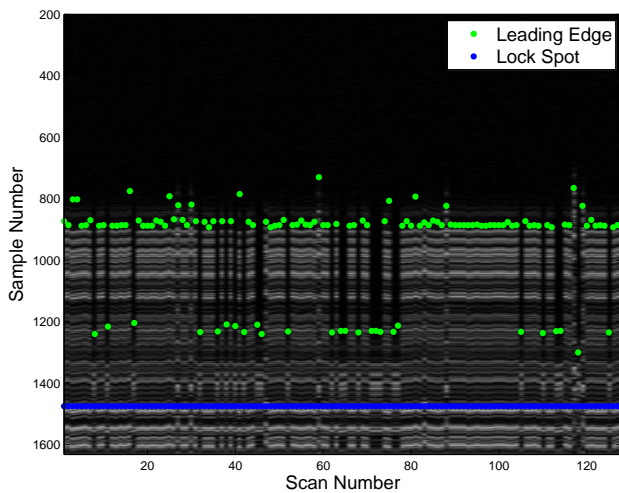
(c) All Requester Data
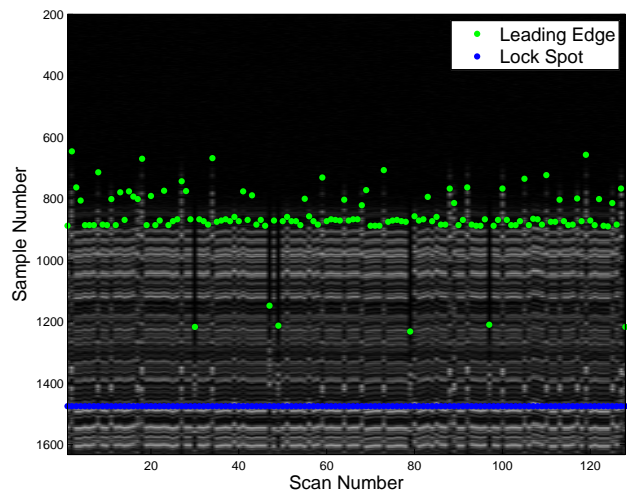
(d) All Responder Data

Figure 5.5: Blocked direct path scan data from (a)(c) requester and (b)(d) responder aligned to lock spot

We again point out that the scan data plotted in Figure 5.5c and Figure 5.5d are aligned to the lock spot at sample 1475. The result in this blocked direct path example is that the leading edge appears at different positions in the waveform relative to the lock spot due to the heavy multipath and small direct path signal. This leads to the raw sampled scan data having wild variations from one TWR transaction to the next as seen in Figure 5.5c and Figure 5.5d.

Last, as seen in Figure 5.6, we plot the Precision Range Measurement (PRM) reported in the RCM_RANGE_INFO message for both the LOS and blocked direct path tests with the same range
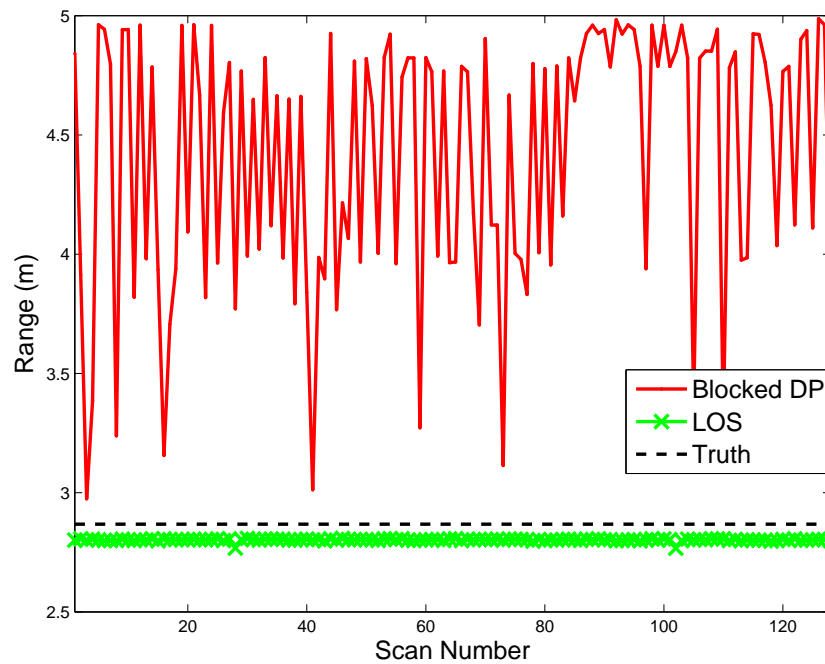
Figure 5.6: Precision Range Measurement (PRM) reported by the requesting P410 unit

between the requester and responder P410 units. The LOS PRM is shown in green, the blocked direct path PRM is shown in red and the true range is shown in black. The LOS PRM, while offset by the bias is otherwise very stable in value consistent with the fact that the range was not varied during this test. If desired, the LOS PRM bias can be calibrated away using Time Domain's calibration method. Also, as expected based on the scan data, the accuracy of the blocked direct path test is poor having grossly overestimated the range with wild variation due to the inaccurate leading edge computation performed in the P410 hardware.

This simple test demonstrates the difficulty of indoor positioning under heavy multipath conditions. In the case of the blocked direct path test, the direct path signal is so weak the leading edge detection performed by the P410 hardware is unable to correctly determine the range using a single TWR transaction. Taking multiple PRM measurements where the leading edge is determined independently from each TWR transaction will result in a poor range measurement. This is due to the fact that we are unable to perform a leading edge detection on the direct path signal since it will always be overshadowed by a large amount of noise. In fact, the average of all the PRM measurements is 4.42 meters under the blocked direct path conditions in this example, which still produces an error of 1.55 meters. The condition of low Signal to Noise (SNR) of the direct path must be overcome so we can

properly perform a leading edge detection on a higher SNR received direct path signal.

5.3 Data Alignment

In order to produce a more accurate range estimate under blocked direct path conditions, we need to produce a more accurate estimate of $t_{r\epsilon}$ and $t_{t\epsilon}$ from (5.3). One way to achieve more accurate estimates is to align and in some way fuse the information from the signals received from multiple two way time of flight transactions to increase the Signal to Noise Ratio (SNR) of the direct path signal. If we can achieve data alignment, we can experiment with the benefits of coherent processing by using the CART algorithm for positioning. First, we begin by substituting (5.4) and (5.5) into (5.3), so that

$$
\begin{aligned}
r &= \frac{c}{2}(C_{TOF}/f_s - (n_{rlock} - n_{rlead})/f_{dec} - (n_{tlock} - n_{tlead})/f_{dec}) \\
&= \frac{c}{2f_s}(C_{TOF} - n_{step}(n_{rlock} - n_{rlead}) - n_{step}(n_{tlock} - n_{tlead})) \quad (5.6)
\end{aligned}
$$

where n_{tlock} and n_{tlead} are the requester lock spot and leading edge reported in samples, n_{rlock} and n_{rlead} are the responder lock spot and leading edge reported in samples. Using this notation, n_{tlead} and n_{rlead} are the true leading edge positions and not estimates. The range in (5.6) can be converted to units of samples by multiplying both sides by the sample rate and dividing by the speed of light to get

$$
\begin{aligned}
r\frac{f_s}{c} &= \frac{1}{2}(C_{TOF} - n_{step}(n_{rlock} - n_{rlead}) - n_{step}(n_{tlock} - n_{tlead})) \\
r_n &= \frac{1}{2}(C_{TOF} - n_{step}n_{rlock} + n_{step}n_{rlead} - n_{step}n_{tlock} + n_{step}n_{tlead})
\end{aligned}
$$

where r_n is the range in sample units. We can then add and subtract $n_{step}n_{tlead}$ to the equation to get

$$
\begin{aligned}
r_n &= \frac{1}{2}(C_{TOF} - n_{step}n_{rlock} + n_{step}n_{rlead} - n_{step}n_{tlock} + n_{step}n_{tlead} + n_{step}n_{tlead} - n_{step}n_{tlead}) \\
&= \frac{1}{2}(C_{TOF} - n_{step}n_{rlock} - n_{step}n_{tlock} + 2n_{step}n_{tlead} + n_{step}n_\Delta) \quad (5.7)
\end{aligned}
$$

where $n_\Delta = n_{rlead} - n_{tlead}$ is the difference between the requester scan data and responder scan data in number of samples using the sample rate f_{dec} as sent in the RCM_FULL_SCAN_INFO scan data field.

We can estimate the time difference and therefore the range difference in samples between the two scan data by observing the maximum of the cross correlation, given by

$$
\hat{n}_\Delta = \max_m \left| E[s_r[n+m]s_t^*[n]] \right| \quad (5.8)
$$

where $E[\cdot]$ is the statistical expectation operator, $s_r[n]$ is the nth sample of the complex form of the responder scan data waveform, and $s_t[n]$ is the nth sample of the complex form of the requester scan

(a) Line of Sight Setup   (b) Blocked Direct Path Setup
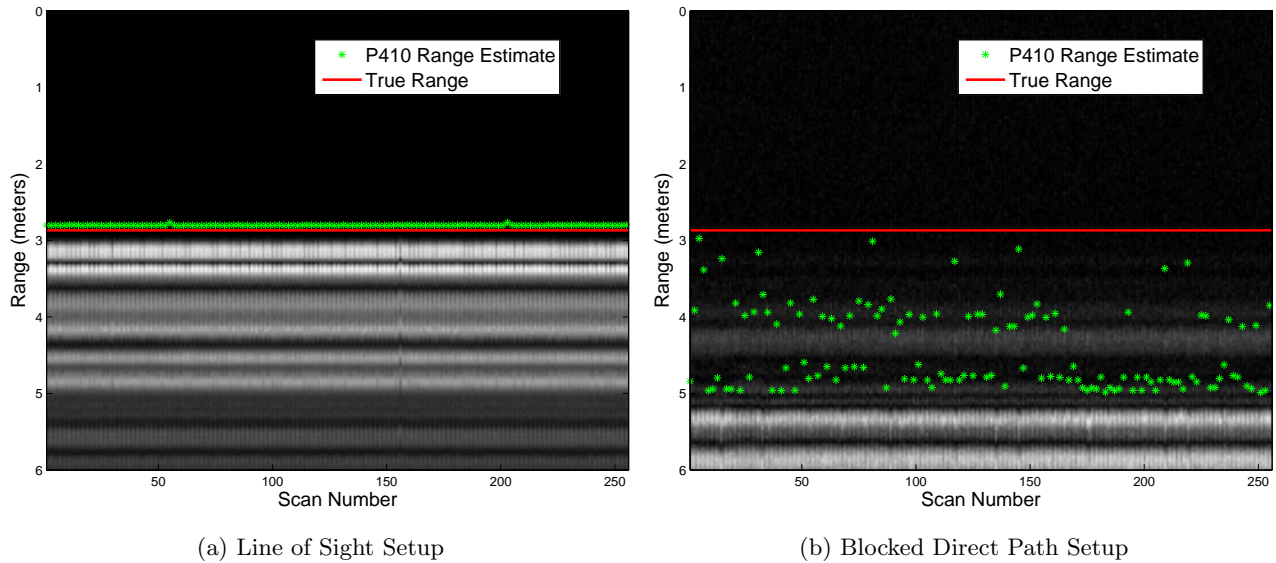
Figure 5.7: Time aligned scan data (a) Line of Sight and (b) Blocked Direct Path. These data are aligned to range 0.

data waveform. The complex form of the scan data can be computed using a technique described by Marple [33]. The estimate $\hat{n}_\Delta$ is the value of m where the cross correlation achieves a maximum. Using this estimate, we can solve (5.7) for the sample, $\hat{n}_{tlead}$, that corresponds to the leading edge in the requester scan data and is relative to the transmit time of the responder. We write

$$\hat{n}_{tlead} \quad = \quad -\frac{1}{2n_{step}}(C_{TOF} - n_{step}n_{rlock} - n_{step}n_{tlock} + n_{step}\hat{n}_\Delta - 2r_n) \tag{5.9}$$

which for $r_n = 0$ is

$$\hat{n}_{tlead} \quad = \quad -\frac{1}{2n_{step}}(C_{TOF} - n_{step}n_{rlock} - n_{step}n_{tlock} + n_{step}\hat{n}_\Delta). \tag{5.10}$$

This equation describes the sample that corresponds to the transmit time of the responder unit and equivalently, range 0 in the requester scan data. The estimate $\hat{n}_{tlead}$ is of course corrupted by the inaccuracy of the estimate $\hat{n}_\Delta$. Once we estimate the sample in the scan data that corresponds to range 0, we can align all two way time of flight measurements from one interrogation to the next. This method also assumes sufficient reciprocity of the channel in that the TWR measurement is nearly identical for the case of when the requester transmits and when the responder transmits.

If we perform the time alignment on the data shown in Figure 5.4 and Figure 5.5 as described above, we get what is seen in Figure 5.7. This figure shows the absolute value of all the scan data, where the requester and responder scan data are interlaced (i.e. requester scan data is odd value scan

(a) Scan data   (b) Scan data zoomed
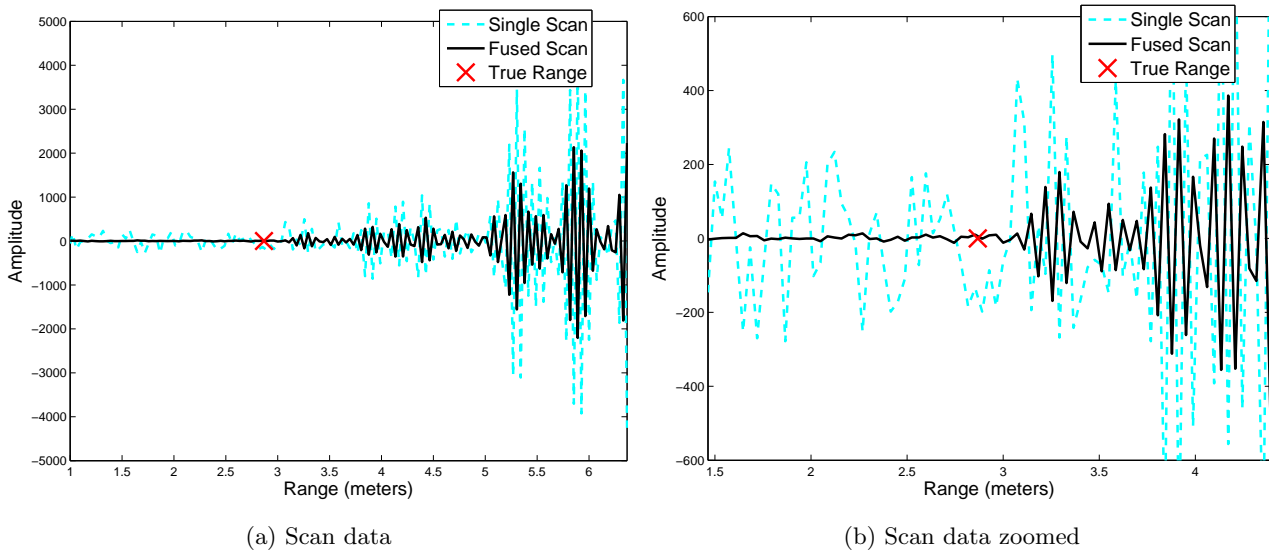
Figure 5.8: Demonstrating improved SNR by coherent integration, showing (a) a single scan and fusion of all TWR measurements, and (b) same data zoomed near the true range

numbers and the responder scan data is even value scan numbers). The data is no longer aligned to a lock spot, but is aligned to a range of zero meters in both the LOS and blocked direct path images. Small errors can still be seen in these images due to the errors in the estimate $\hat{n}_\Delta$, but a clear alignment is seen. Since we have stationary requester and responder positions, the true range can be plotted in red as a constant in both figures. The P410 PRM estimates are also plotted for each the LOS and blocked direct path tests. Under the LOS conditions, the PRM is consistently close to the true range. Under the blocked direct path conditions, we see the PRM varies wildly for each scan number due to the inability of the P410 to determine the true range under poor direct path signal SNR conditions.

Once time alignment is achieved, we can perform coherent integration to fuse all the scans from the blocked direct path test condition in order to improve the SNR of the direct path signal. Figure 5.8a demonstrates an improvement in the direct path signal SNR by applying the coherent integration technique described in Section 3.1 to the scan data in Figure 5.7b. The same data is also plotted in Figure 5.8b, where we zoom near the true range. Without quantifying the improvement in SNR of the direct path signal theoretically, the point here is to demonstrate that there is an advantage to performing synchronization of the scan data of the two way transaction. If we were to perform a leading edge detection on the fused solution, we would achieve better range estimates than in the single scan case.

5.4 Synchronization Performance

The theoretical performance of the time alignment can be computed using the method described in [34]. Given two signals, in this case the scan data $s_r[m]$ and $s_t[n]$, we can compute the time difference as described by the cross correlation in 5.8. The theoretical standard deviation of this time difference is

$$\sigma_{TD} = \frac{1}{\beta} \frac{1}{\sqrt{BT\gamma}}$$

where B is the noise bandwidth at the receiver, T is the integration time, γ is the Signal to Noise Ratio (SNR), and

$$\beta = \sqrt{\frac{\int_{-\infty}^{\infty} f^2 |P(f)|^2 df}{\int_{-\infty}^{\infty} |P(f)|^2 df}}. \tag{5.11}$$

is the effective bandwidth with known transmit spectrum $P(f)$. Therefore, we we can define the standard deviation of $\hat{n}_{tlead}$ as

$$\sigma(\hat{n}_{tlead}) = \frac{f_{dec}}{2} \frac{1}{3.72e9} \frac{1}{\sqrt{26\gamma}} \tag{5.12}$$

where $\beta = 3.72e9$ Hz and $BT = 26$ samples, calculated from the known transmit waveform published in [35] under the name "Sample MATLAB CLEAN Algorithm code".

In this experiment, we do not have the ability to capture the true transmit time of the responder unit from inside the P410 hardware. We, therefore, cannot use (5.12) to validate the performance. Instead, we use the collected stationary recordings discussed above and analyze the relative alignment errors between scan data frames using either the P410 estimates to align the data or equation (5.10) to align the data. Under line of sight conditions, the P410 is able to produce accurate estimates of position, which result in accurate alignment. Under blocked direct path conditions, the estimates of the leading edge are inaccurate, leading to poor alignment.

Test	Alignment Method	Max	Standard Deviation
Line	P410 $\hat{t}_{r\epsilon}$, $\hat{t}_{t\epsilon}$	0.1933 ns	0.0627 ns
of Sight	Equation (5.10)	0.1433 ns	0.0279 ns
Blocked	P410 $\hat{t}_{r\epsilon}$, $\hat{t}_{t\epsilon}$	18.23 ns	4.12 ns
Direct Path	Equation (5.10)	0.0834 ns	0.0196 ns

Table 5.1: Relative errors of stationary recordings

Table 5.1 summarizes the relative errors for both LOS and blocked direct path experiments. The standard deviation under line of sight conditions are similar, with the P410 leading edge based alignment

achieving around 0.06 ns and the method presented here using (5.10) achieves 0.03 ns. The standard deviation of the errors under blocked direct path is 4.12 ns when using the P410 estimates to align the data while a standard deviation of 0.0196 ns can be achieved using the method presented here using (5.10).

5.5   Dynamic Motion
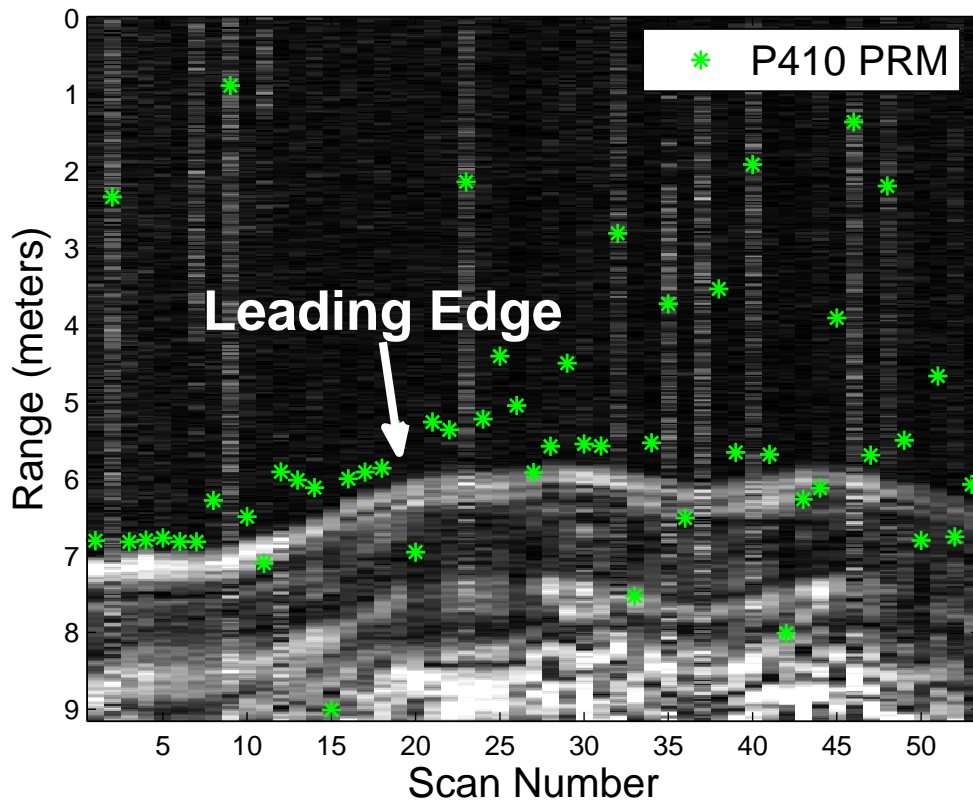
Figure 5.9: Example of data alignment according to equation (5.10) with arbitrary responder motion.

So far, in this ongoing blocked direct path test example, we have demonstrated an improvement in SNR of the direct path once synchronization is achieved in the two way transaction by using signal fusion and a motion solution. In the previous example, we have a known motion solution: two stationary P410 units. It is also possible to achieve synchronization of the TWR transaction under some requester and/or responder motion.

An example of data alignment during a test in which there is arbitrary motion of the responder

can also be seen in Figure 5.9, where the range between the requester and responder change over time. The scan data were collected at approximately a 4 Hz rate (with a TWR conversation time of approximately 3 milliseconds) in an indoor environment with an obstruction placed between the two P410 units, creating a different blocked direct path scenario than was presented previously in the stationary test case. The x-axis is the scan number, the y-axis is the range of the transmitter relative to the receiver, and the gray scale intensity shows magnitude of each TWR measurement. We notice that the leading edge position in the TWR measurement is seen starting at around a range of 7 meters on scan number 1 and then moves closer in range to the requester to about 6 meters by scan number 20 as the responder is moved. If one had a motion solution, we could fuse all of these frames together for an improved range estimate as was demonstrated and seen in Figure 5.8.

In this example of arbitrary motion, we do not know the true range for each measurement. Therefore, we cannot plot a red truth line as was done for the stationary example seen in Figure 5.7. In addition, we point out that there is interference in the TWR measurements that cause the P410 to estimate the range incorrectly. An example of interference can be seen in scan number 2, 9, 23, and several others. Signal fusion using a motion solution would also reduce the impact of the interference. The fusion process would consider the interference as additional additive noise.

If the responder scan data is not available, one could correlate two adjacently captured requester scan data in order to estimate the change in the waveform similar to the suggestion in [36]. In order to align the two waveforms properly, one would need to attempt to compensate for different lock spot positions. The result would not reveal true motion, but only relative motion with potential errors due to lock spot differences. It also would occur at a slower update rate, which would reduce the maximum allowed velocity of the requester/responder pair in order to preserve channel reciprocity. The method of synchronization presented in this dissertation for the TWR transaction has an advantage in that the estimated alignment is independent of true motion under the assumption of a small interval between requester/responder measurement exchanges relative to the distance traveled during the time. For example in the experiment conducted and depicted in Figure 5.9, the TWR transaction time interval was about 3 milliseconds while the greatest velocity of the radio was approximately 0.4 meters per second, hence the change of distance during the measurement interval was limited to 0.1 centimeters. Ideally, one would want to perform the transaction at the same time, perhaps over different channels, but this is not possible with P410 hardware and will not be explored further.

Chapter 6

Experimental Results

The experimental results presented in this chapter use the new data collection method described in Chapter 5 to evaluate the two step LED, SART, TART, and CART algorithms in two test environments. First, we collect and analyze data in the AK315 research laboratory on the third floor of Atwater Kent building on the Worcester Polytechnic Institute (WPI) campus. Second, we collect and analyze data in AK317A, the same computer laboratory used in [26] to evaluate the performance of the ISART algorithm. A brief comparison is made between the performance of the ISART algorithm and the CART algorithm at the end of this chapter.

6.1 AK315 Research Laboratory

Multiple measurements can be combined as shown in Chapter 2 and 3 to produce a more accurate estimate of the transmitter position. In this section, we compare the LED, SART, TART, and CART algorithms by fusing the data captures from a receiver placed at multiple survey locations in hopes of producing a more accurate estimate of a stationary transmitter position in AK315 Research Laboratory.

6.1.1 Data Collection

A data collection effort was carried out to explore the indoor localization capabilities of the LED, SART and TART algorithms, and to validate the CART algorithm using the TWR alignment procedure. The transmitter was placed behind a large metal cabinet in a large open lab environment cluttered with equipment and desks. Twenty three points were surveyed around the indoor environment, in the same large lab and behind large metal studded walls in the hallways. Figure 6.1 shows the floor plan view of the test setup in AK315 on the 3rd floor of the Atwater Kent building of Worcester Polytechnic

Institute. Figure 6.2 shows pictures of the transmitter mounted on a tripod behind the large metal cabinet.
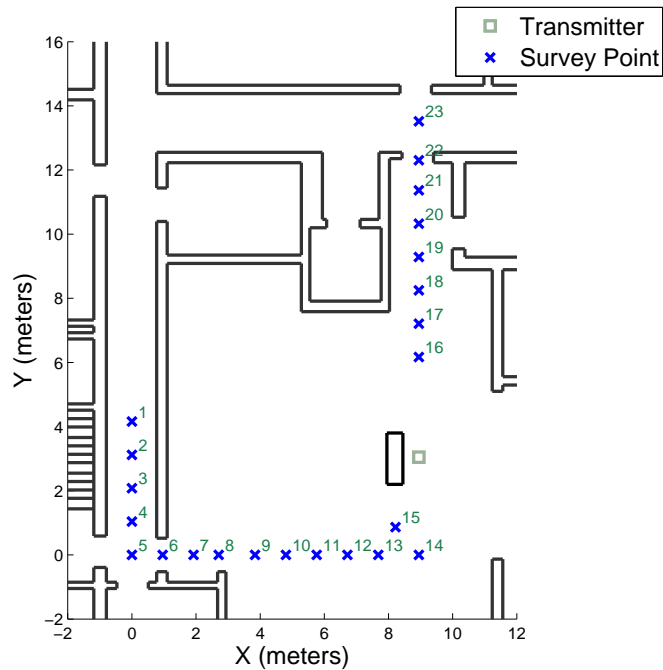
Figure 6.1: Atwater Kent 3rd floor room AK315 test setup

As the floor plan shows, survey points 1-5 and 23 are outside the large laboratory. The doors on survey points 6 and 22 were open when all measurements were taken by the receiver. The transmitter was placed 1.49 meters above the floor and the receiver was placed 1.54 meters above the floor on each survey point, one at a time. Approximately 500 measurements were made at each survey point, all of which were then time aligned and used in the following analysis.

Figure 6.3 shows the absolute value of a single measurement from a receiver placed at each survey point, aligned using the method described in Chapter 5. Also shown are the mean (and three standard deviation bar) of the P410 PRM at each survey point in white and surveyed truth ranges using green x's. The P410 operates remarkably well under LOS conditions with a tight variance as seen in the data collected when the receiver was placed on survey points 13-19. Under blocked direct path conditions of receiver locations 1-8, however, a large variance in the PRM is evident. We see that the white circle (indicating the native P410 range estimate) and three standard deviation bar at receiver location 1 does not overlap the green x. The P410 never produces a correct range estimate due to the large multipath component in the data capture at receiver location 1.

(a) View of transmitter

(b) View towards hallway

Figure 6.2: Transmitter pictures for the Atwater Kent 315 Laboratory test
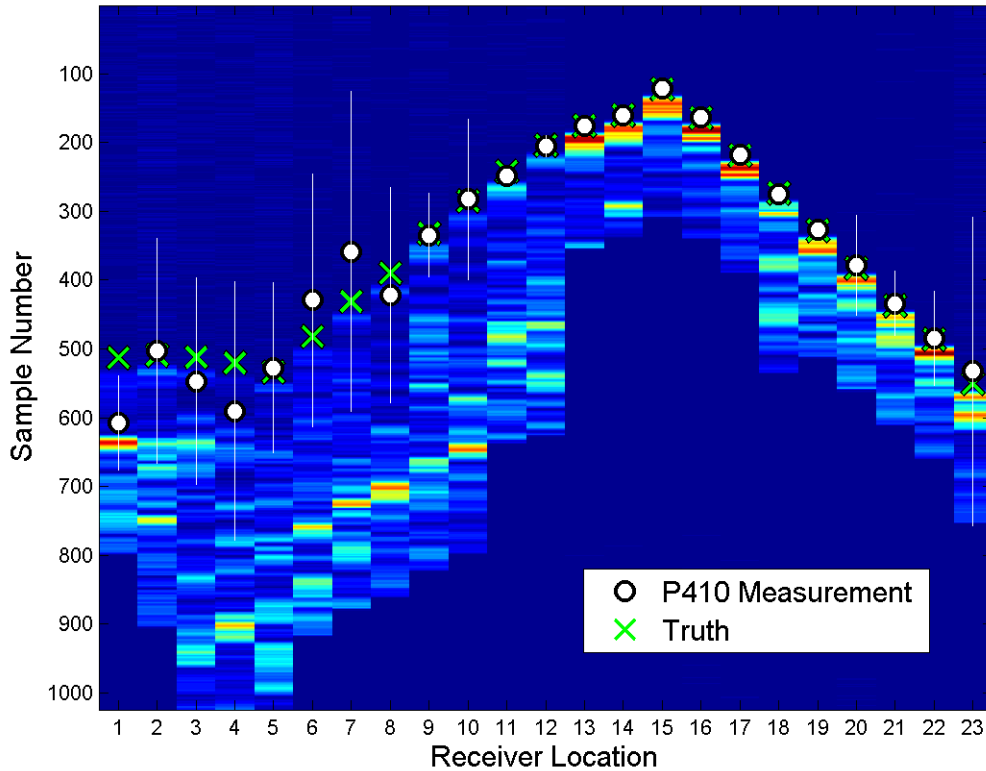
Figure 6.3: AK315 raw data showing the P410 measurements in white and the truth using green x's

6.1.2 Metric Image Examples

Figures 6.4 and 6.5 show several example location metric images using the LED, SART, TART, and CART algorithms using a single measurement at each survey point and various subsets of the full group of 23 measurements from all 23 receiver locations. The peaks of these metric images, shown by a black x, would be selected as the location estimates. Additional metric images from this test can be found in Appendix C. The LED metric images are produced by a brute force plot of the cost function described in section 2.2 using the P410 PRM result as the range estimate. For the direct positioning algorithms SART, TART, and CART, the respective metric maps are shown using a single measurement, which is represented by a single frame of time aligned scan data. For these example metric images for the AK315 test, the true transmitter position is $(x_m, y_m) = (9.32, 2.93)$, with a scan grid defined by $x_{min} = -1$, $x_{max} = 11$, $y_{min} = -1$, $y_{max} = 15$ with a $\Delta_x = 0.2$ and $\Delta_y = 0.2$, and $\alpha = 20$ and $\gamma = 60$ for the CART algorithm.
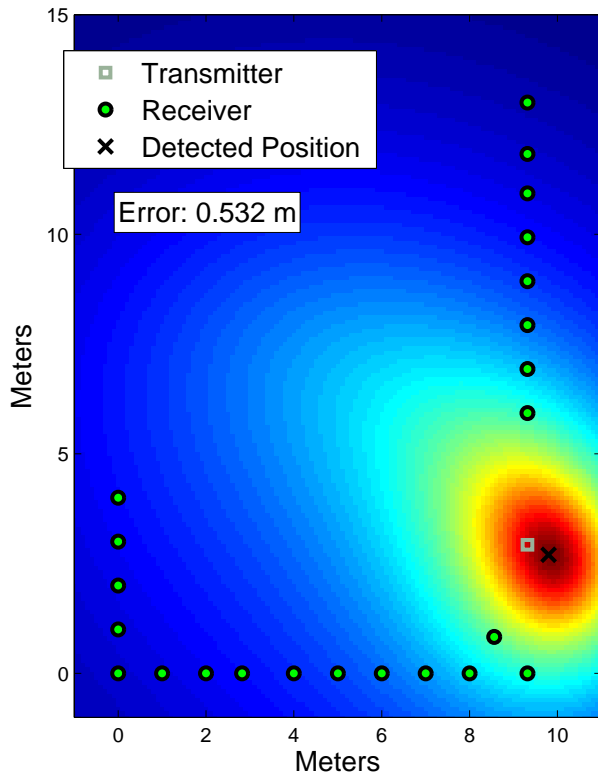
(a) LED
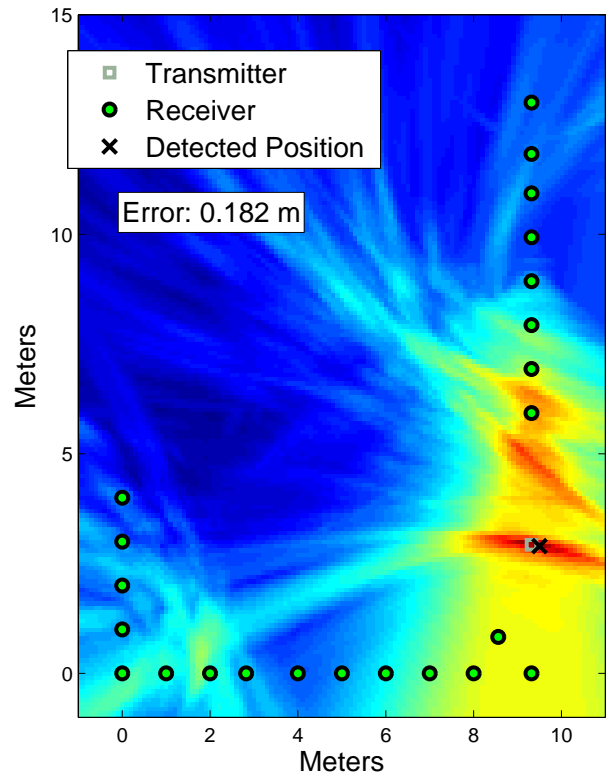
(b) SART
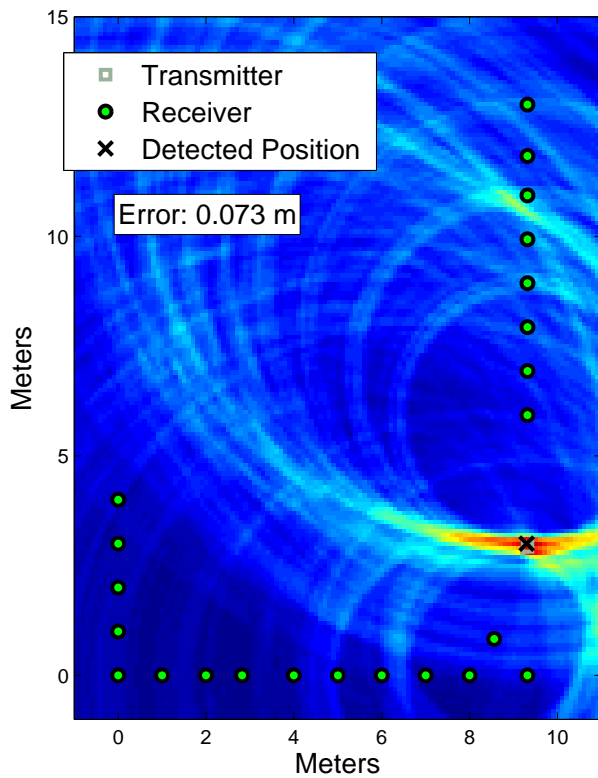
(c) TART
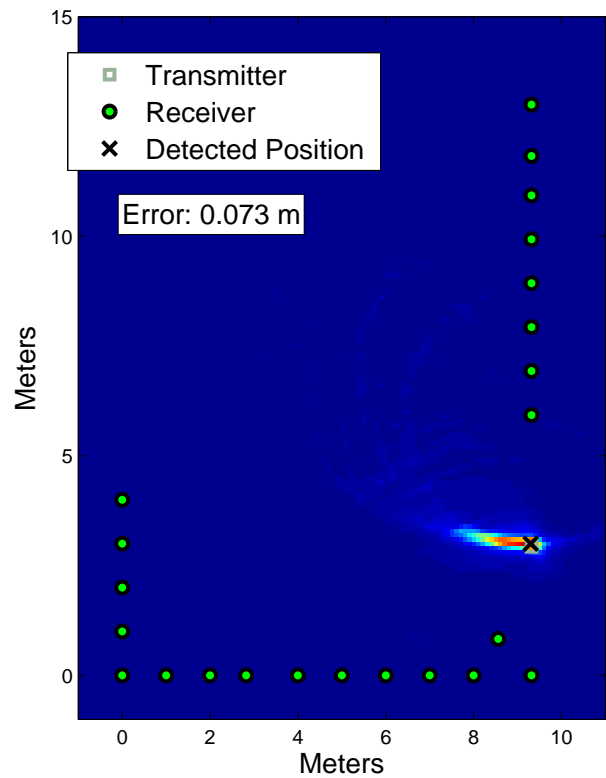
(d) CART

Figure 6.4: Atwater Kent 3rd floor data collection metric image examples using data from receiver locations 1-23
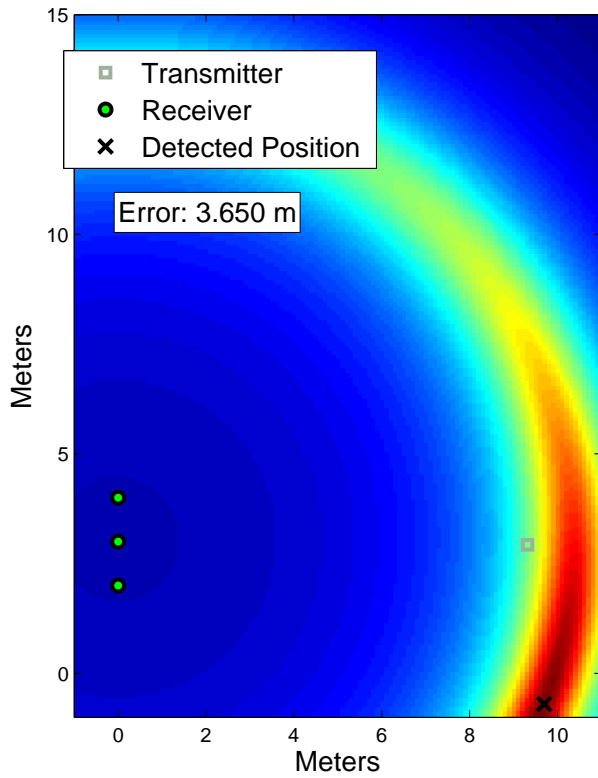
(a) LED
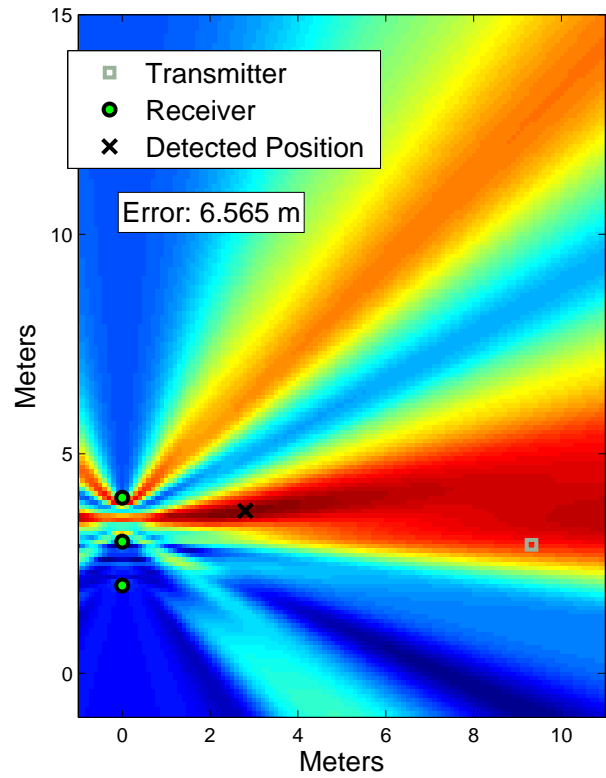
(b) SART
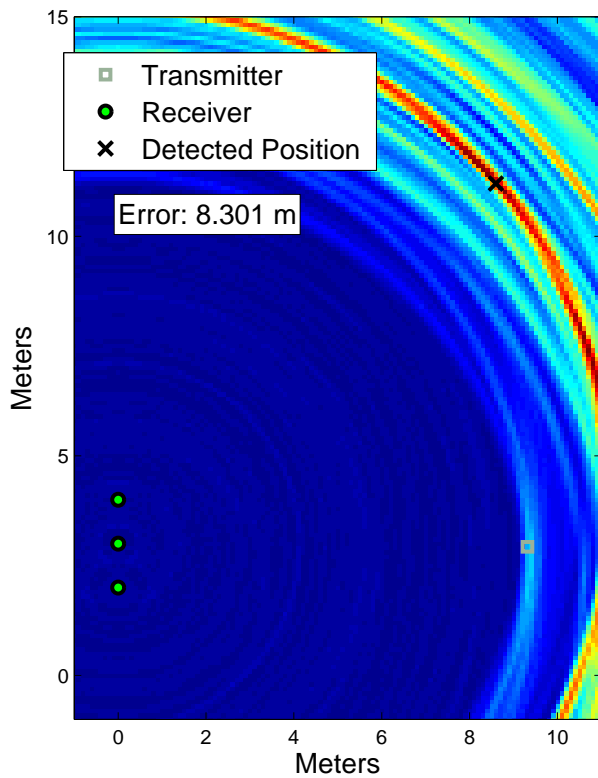
(c) TART
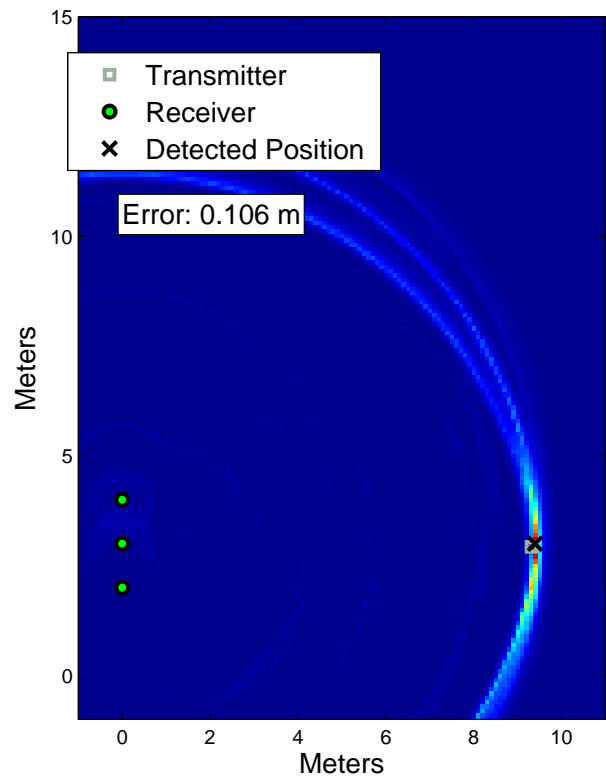
(d) CART

Figure 6.5: Atwater Kent 3rd floor data collection metric image examples using data from 3 receiver locations that produce the poorest geometry: 1, 2, 3
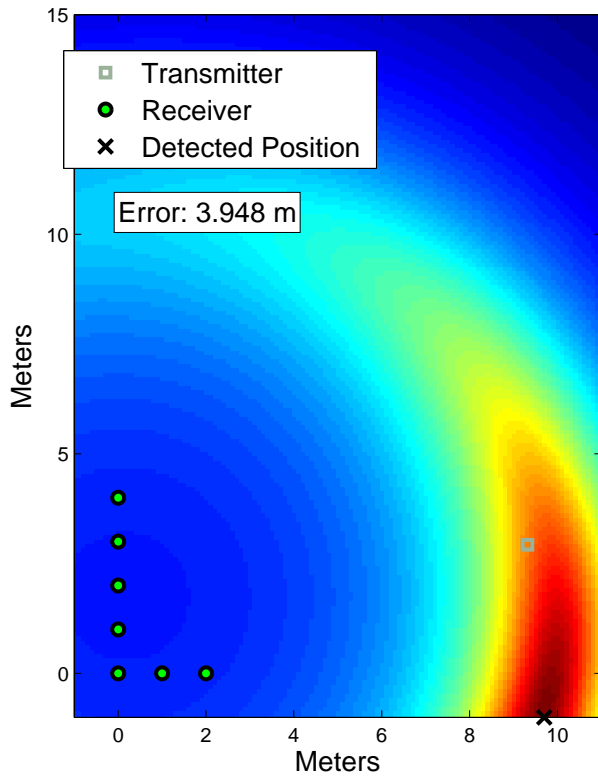
(a) LED
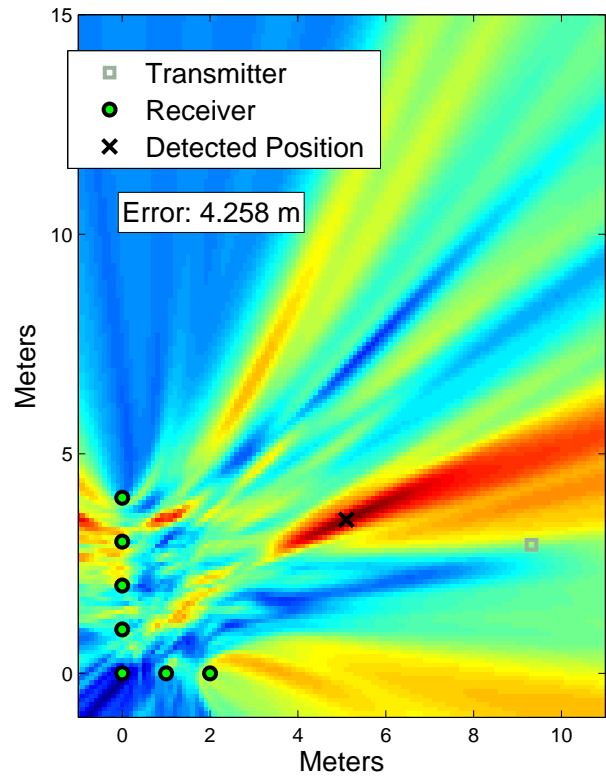
(b) SART
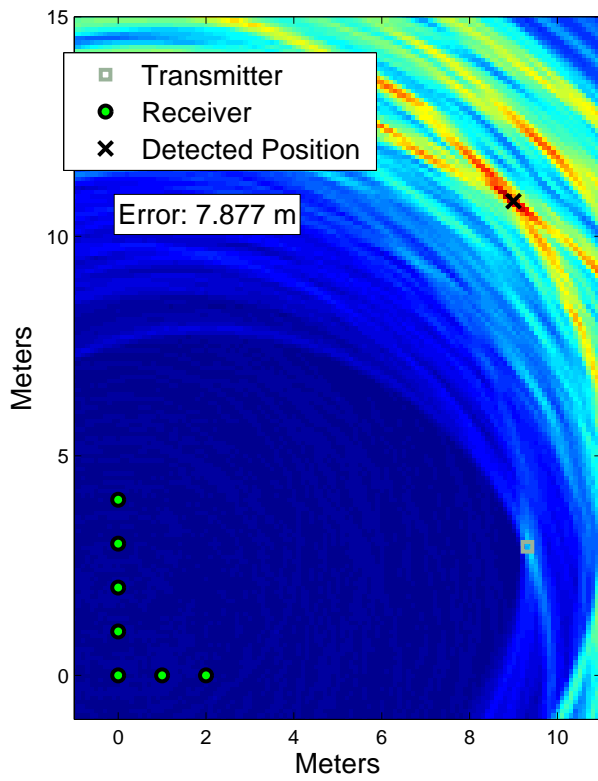
(c) TART
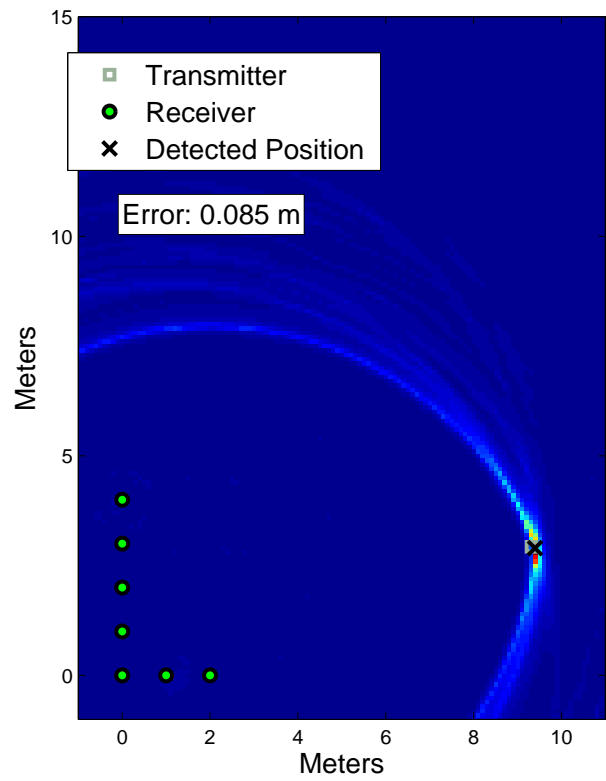
(d) CART

Figure 6.6: Atwater Kent 3rd floor data collection metric image examples using data from 7 blocked LOS receiver locations: 1-7

If a single measurement from a receiver placed at all the survey points is included in the computation of the metric image as shown in Figure 6.4, all the algorithms produce a submeter estimate. In this case, there is sufficient LOS data to overcome the detrimental effects of the multipath in the SART and TART algorithms. The CART algorithm produces a good estimate and the LED algorithm performs the worst. If we decrease the number of receivers to three, the minimum required for a unique 2 dimensional solution, the CART algorithm outperforms the two step LED algorithm as seen in Figure 6.5. In fact, despite this being such a restrictive geometry, the CART algorithm is able to determine the transmitter position quite accurately, with well below a meter of error.
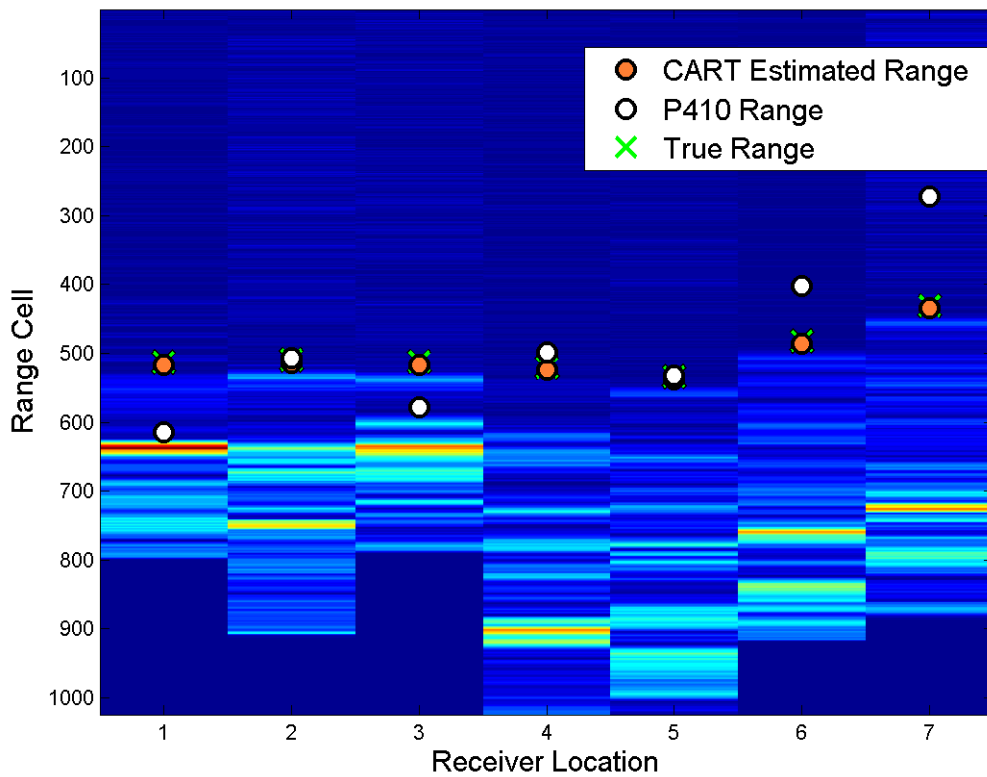
Figure 6.7: Measurements at receiver locations 1-7 for the AK315 test

To highlight the benefit of the CART algorithm, we focus our attention on the most difficult blocked direct path locations using only data from receiver locations 1 through 7. If we combine a single measurement from each location, we get the metric images seen in Figure 6.6. We can see that SART and TART fail to produce a good estimate as expected based on simulation results. The two step LED algorithm has an error around 4 meters while the CART algorithm again produces a sub
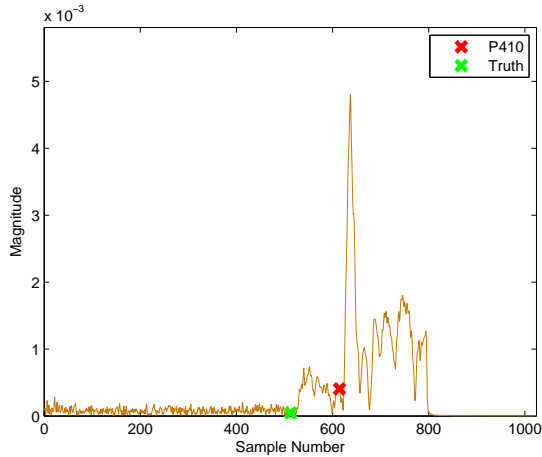
(a) Receiver location 1 measurement
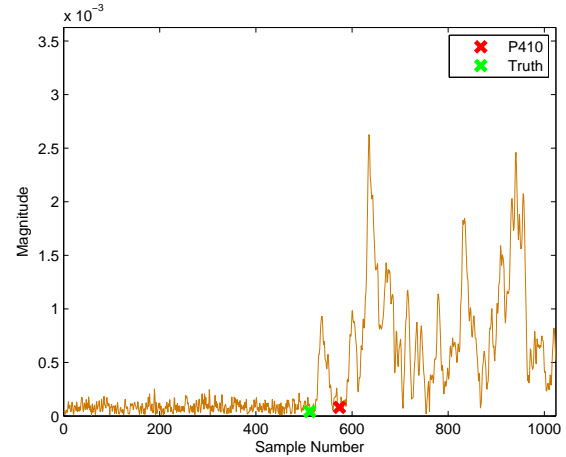
(b) Receiver location 3 measurement

Figure 6.8: Atwater Kent 3rd floor data collection measurement details using data from 7 receiver locations

meter accurate estimate.

It is instructive to examine the cause of the poor LED estimate when combining 7 blocked direct path PRMs. Figure 6.7 shows the magnitude of the seven measurements from receiver locations 1-7 that is used by the P410 to produced the 7 independent PRMs. Also shown as white circles are the P410 calculated ranges and the true range using a green x. In addition, the estimated ranges to each survey location using the CART algorithm is shown with an orange circle. It is obvious that there are several large range errors in the P410 PRMs. For example, measurements from receiver locations 1 and 3 produce errors in the PRM from the P410. The magnitude of the measurement data are shown in Figure 6.8a and 6.8b respectively from receiver locations 1 and 3. The P410 incorrectly estimates the leading edge positions resulting in a poor range estimate as shown by a red x instead of being near the true range shown by a green x. The cause of these poor estimates is the large spike in magnitude of the measurement due to a strong multipath component. These poor range estimates contribute to the large error when using the LED algorithm. This example shows the sensitivity of the two step minimization LED algorithm to inconsistent constraints and how it produces inaccurate range estimates whereas the CART algorithm suffers from no such problem.

Number	Receivers Used	Number	Receivers Used	Number	Receivers Used
		35	7, 6, 5, 4	70	7, 6, 5, 4, 3
1	7, 6, 4	36	7, 6, 5, 3	71	7, 6, 5, 4, 2
2	7, 6, 3	37	7, 6, 5, 2	72	7, 6, 5, 4, 1
3	7, 6, 2	38	7, 6, 5, 1	73	7, 6, 5, 3, 2
4	7, 6, 1	39	7, 6, 4, 3	74	7, 6, 5, 3, 1
5	7, 5, 4	40	7, 6, 4, 2	75	7, 6, 5, 2, 1
6	7, 5, 3	41	7, 6, 4, 1	76	7, 6, 4, 3, 2
7	7, 5, 2	42	7, 6, 3, 2	77	7, 6, 4, 3, 1
8	7, 5, 1	43	7, 6, 3, 1	78	7, 6, 4, 2, 1
9	7, 4, 3	44	7, 6, 2, 1	79	7, 6, 3, 2, 1
10	7, 4, 2	45	7, 5, 4, 3	80	7, 5, 4, 3, 2
11	7, 4, 1	46	7, 5, 4, 2	81	7, 5, 4, 3, 1
12	7, 3, 2	47	7, 5, 4, 1	82	7, 5, 4, 2, 1
13	7, 3, 1	48	7, 5, 3, 2	83	7, 5, 3, 2, 1
14	7, 2, 1	49	7, 5, 3, 1	84	7, 4, 3, 2, 1
15	6, 5, 4	50	7, 5, 2, 1	85	6, 5, 4, 3, 2
16	6, 5, 3	51	7, 4, 3, 2	86	6, 5, 4, 3, 1
17	6, 5, 2	52	7, 4, 3, 1	87	6, 5, 4, 2, 1
18	6, 5, 1	53	7, 4, 2, 1	88	6, 5, 3, 2, 1
19	6, 4, 3	54	7, 3, 2, 1	89	6, 4, 3, 2, 1
20	6, 4, 2	55	6, 5, 4, 3	90	5, 4, 3, 2, 1
21	6, 4, 1	56	6, 5, 4, 2		
22	6, 3, 2	57	6, 5, 4, 1		
23	6, 3, 1	58	6, 5, 3, 2		
24	6, 2, 1	59	6, 5, 3, 1		
25	5, 4, 3	60	6, 5, 2, 1		
26	5, 4, 2	61	6, 4, 3, 2		
27	5, 4, 1	62	6, 4, 3, 1		
28	5, 3, 2	63	6, 4, 2, 1		
29	5, 3, 1	64	6, 3, 2, 1		
30	5, 2, 1	65	5, 4, 3, 2		
31	4, 3, 2	66	5, 4, 3, 1		
32	4, 3, 1	67	5, 4, 2, 1		
33	4, 2, 1	68	5, 3, 2, 1		
34	3, 2, 1	69	4, 3, 2, 1		

Table 6.1: Sensor configuration number vs. receivers used

(a) Position Errors

(b) Position Errors Zoomed
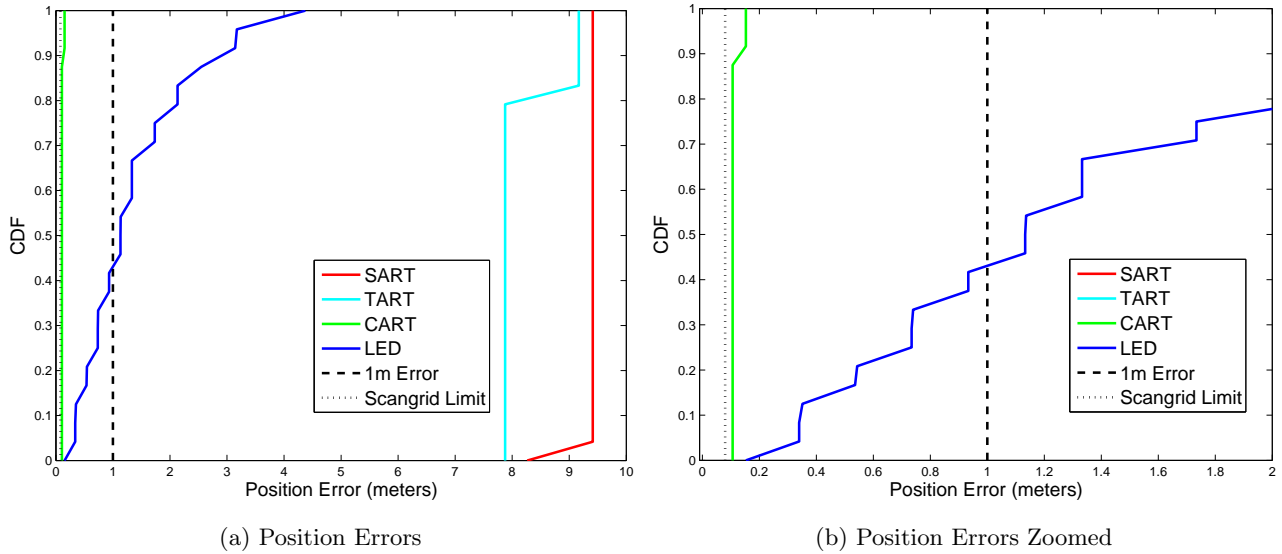
Figure 6.9: Cumulative Density Functions (CDF) of all LED, SART, TART, and CART using sensor configuration 8 (receivers 7,5,1) showing (a) position errors, and (b) position errors zoomed around 1 meter error

6.1.3 CDF of Position Errors

Similar to what we did in the simulation chapter, we can quantify the performance of these algorithms by computing the CDF and RMS position errors under various sensor configurations using (4.32). Table 6.1 describes 90 different sensor configurations and the survey points used for each configuration. Only the first 7 survey points are used in this analysis in order to pick the most difficult blocked direct path sensor positions, which represent the most difficult multipath encountered for this experiment. The 7 survey points used are divided into 3, 4, and 5 pair sensor combinations. The table shows the 3 pairs in the first two columns, 4 pairs in the next two, and 5 pairs in the last two columns. These sensor combinations produce different geometries that provide another dimension of analysis for the CDF and RMS error calculations. In addition, we use 25 measurements to produce 25 independent estimates of transmitter position for each sensor configuration using each the LED, SART, TART, and CART algorithms.

Figure 6.9 shows the CDF of the LED, SART, TART, and CART algorithms using sensor configuration number 8 from Table 6.1, which uses data from receivers at survey points 7, 5, and 1. This sensor configuration was selected arbitrarily for this example. Figure 6.9a shows the full position error CDF and Figure 6.9b shows the position errors zoomed on the 1 meter of position error mark. The

(a) LED Position Errors

(b) SART Position Errors

(c) TART Position Errors

(d) CART Position Errors
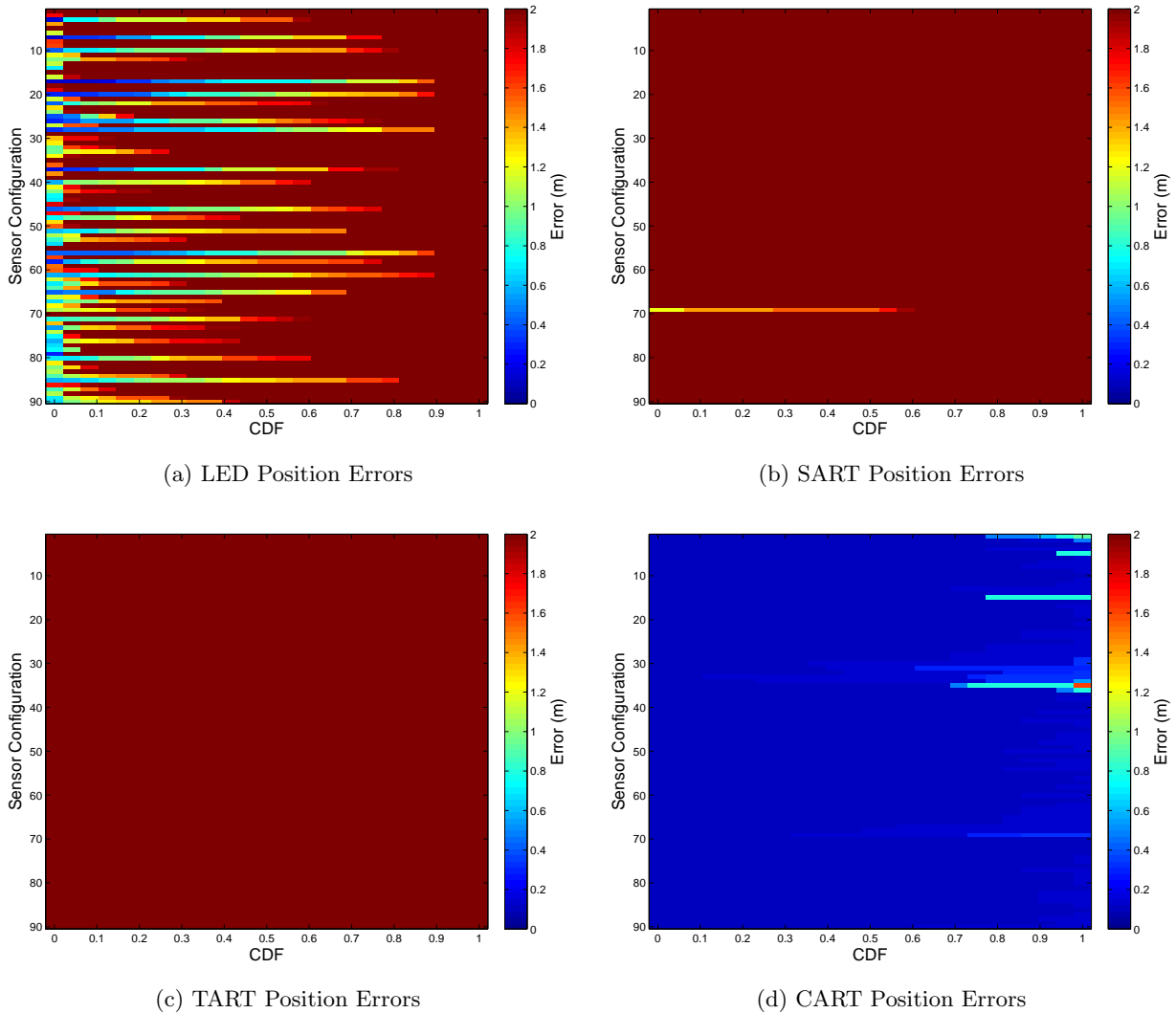
Figure 6.10: Cumulative Density Function (CDF) of position error at each 90 sensor configurations for the AK315 data set limited to 2 meters error for (a) LED, (b) SART, (c) TART, and (d) CART

CART algorithm consistently produces remarkably accurate position estimates, well below a meter of error. In this case, the error seems to be limited primarily by the scan grid imposed limit.

Figure 6.10 shows the position error CDFs for all 90 sensor configurations with the error magnitude limited to 2 meters error on the color bar. As expected, the SART and TART algorithms perform poorly, hardly ever or never producing a position estimate within 2 meters of the true transmitter position. The two step LED algorithm sometimes produces position estimates that are less than a meter as is evident in Figure 6.10a, but at a low probability of around 30% or less, depending on the sensor configuration. The CART algorithm far outperforms the LED, SART, and TART algorithms

(a) RMS Errors

(b) Zoomed on CART RMS Errors

Figure 6.11: RMS position error using 25 measurements for each sensor configuration 1 through 90. (a) Shows full position errors and (b) shows position errors zoomed on CART position errors

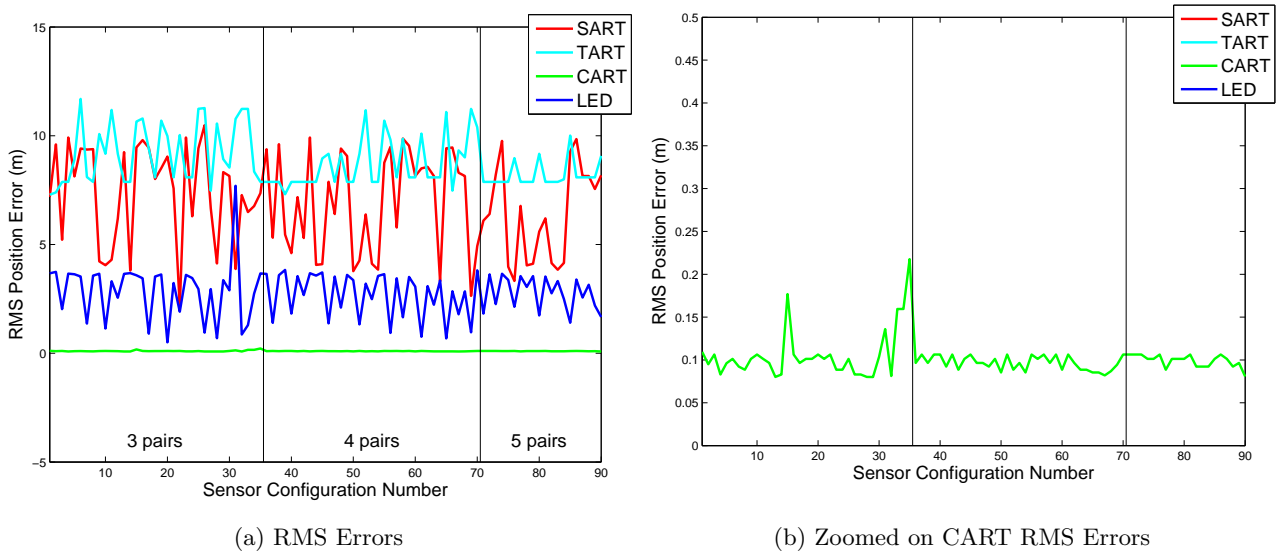in this experiment using the most difficult geometry and blocked direct path data. Examining Figure 6.10d, we see that regardless of the sensor configuration (geometry) chosen, the CART algorithm always produces an error less than a meter well over 90% of the time.

6.1.4 RMS Errors

We can compute the root of the mean of the squared error as another performance metric of the position error. Figure 6.11 shows the RMS position errors using 25 measurements at each of the 90 sensor configurations defined by Table 6.1. In Figure 6.11 we show the RMS position errors of the LED, SART, TART, and CART algorithms for each 90 sensor configurations. The LED algorithm produces a minimum RMS error of about 0.50 meters using sensor configuration 20 and a maximum RMS error of 7.7 using sensor configuration 31. Figure 6.11b shows just the CART RMS position error in more detail. The minimum RMS error is 0.08 meters using sensor configuration 29 and the maximum is around 0.22 meters using sensor configuration 35. This again demonstrates the robustness of the CART algorithm in which it is able to consistently produce accurate estimates less than a meter of RMS error even under poor sensor geometry.

Table 6.2 shows the RMS position error for all 3, 4, and 5 pair sensor combinations shown in Table 6.1 as well as the RMS error of all 90 sensor combinations. The LED algorithm performs with an RMS error on the order of about 3 meters and the CART algorithm performs with an RMS error of about

Algorithm	3 Pairs	4 Pairs	5 Pairs	All Data
LED	3.1734	2.8824	2.9087	3.0016
SART	7.7385	7.3719	6.6542	7.3545
TART	9.3948	8.7093	8.3469	8.8937
CART	0.1049	0.1021	0.0996	0.1026

Table 6.2: RMS position errors in meters for different sensor configurations as defined by Table 6.1

0.10 meters. This shows that the CART algorithm presents approximately a 30 times improvement over the LED algorithm in this experiment and both are much better than the SART and TART algorithms in this high multipath environment.

6.1.5 Raw Errors

The average of 25 position estimates for all 90 sensor configurations defined in Table 6.1 are plotted in Figure 6.12. Figure 6.12a shows the two step LED algorithm producing a strong cluster of position estimates in the lower right corner. This is likely due to the scan grid limit of -1 meters placed on the x axis in the brute force computation of the LED cost function. It is possible the errors for the LED could be larger, but were limited to this region due to this method of computation. The SART and TART algorithms produce the position estimates seen in Figure 6.12b and Figure 6.12c respectively. Both of these algorithms clearly produce large errors with a large uncertainty in this indoor experiment using the first 7 survey points. The CART algorithm position estimates are seen in Figure 6.12d, which show a tight cluster right around the true transmitter position. This visualization of the errors for each sensor configuration highlight the capability of the CART algorithm compared to current existing algorithms.

88

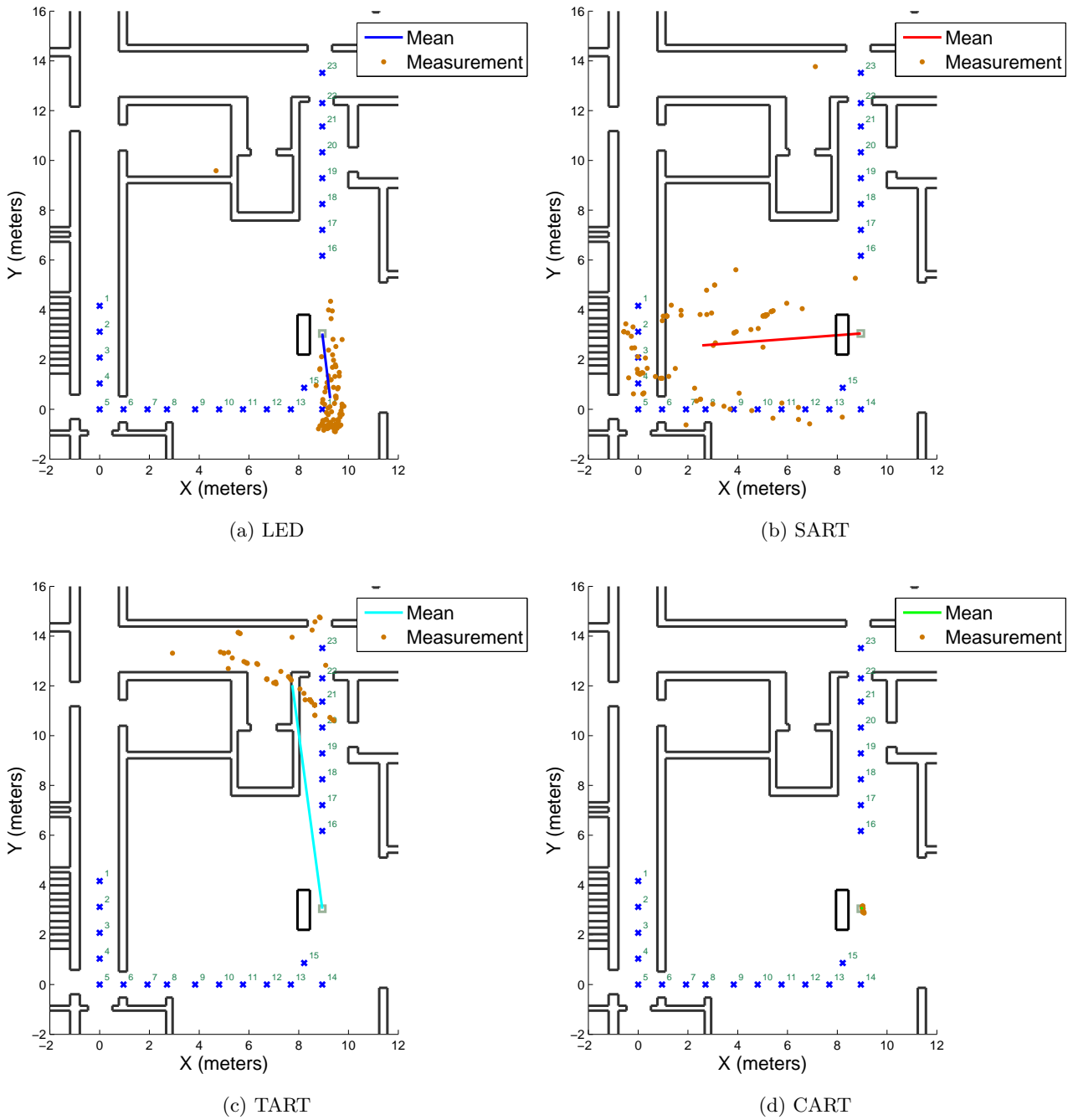Figure 6.12: Average position estimates for all 90 sensor configurations for algorithms (a) LED, (b) SART, (c) TART, and (d) CART, along with mean error vectors for all sensor configurations

6.2 AK317A Computer Laboratory

In the previous section, we examined the errors of a single transmitter position using a variety of different receiver geometries in an indoor multipath environment. In this section, we present data

collected in WPI's Atwater Kent Building room AK317A. This was the most difficult multipath location used by [26] to explore the fusion of inertial navigation data with RF data using the ISART algorithm. As [26] points out, the AK building is a brick and steel building with all the walls being steel studded. This computer lab also has metal backed white boards, electrical panels, large metal cabinets, hardware equipment, and metal framed furniture. Analysis in this section compares the LED, SART, TART, and CART algorithms using the transmitter and receiver hardware described in Chapter 5. The last subsection, Section 6.2.6, compares the results of the CART algorithm to the results obtained by [26] using the ISART algorithm.

6.2.1 Data Collection

Nineteen points were surveyed around the exterior hallway outside the laboratory behind the white board and/or large metal studded walls, marked by a blue x in Figure 6.13a. Fourteen transmitter positions were surveyed inside the computer laboratory, marked by cyan squares. During the measurement campaign, it quickly became apparent that the metal indoor environment is severely attenuating the UWB signal. At most of the receiver locations the receiver cannot even detect the UWB waveform at all the transmitter locations using the maximum power of -15 dBm allowed under FCC regulations. Therefore, we only use data from receiver locations 8 through 13, as seen in Figure 6.13b. These 6 receiver locations are the only locations at which the device is able to detect and measure the transmitted waveform for all 14 mobile transmitter locations.

Figure 6.14 shows pictures of the transmitter used in this experiment mounted 0.56 meters off the floor inside the AK317A computer laboratory at survey point 22. Figure 6.14a shows the view from the transmitter position. Figure 6.14b shows the view to the transmitter from standing height. These pictures show the metal furniture, equipment, and building materials that make this a very difficult multipath environment. In addition, the transmitter height is now below the desk level close to the height of the surrounding chairs, further exasperating the multipath.

The receiver was mounted on a tripod 1.615 meters above the floor outside in the hallway, as seen in Figure 6.15. The data collection consisted of placing the transmitter 0.56 meters off the floor on a single transmitter survey point, then moving the receiver to each receiver survey point 8 through 13 one at a time while performing measurements. The transmitter was then placed on the next transmitter survey point and each receiver survey point was used to attempt a measurement. The process was repeated until all 14 transmitter survey points were used for the data collection. At each transmitter/receiver survey position pair roughly 500 frames were attempted. Limited by the ability of the P410 to detect
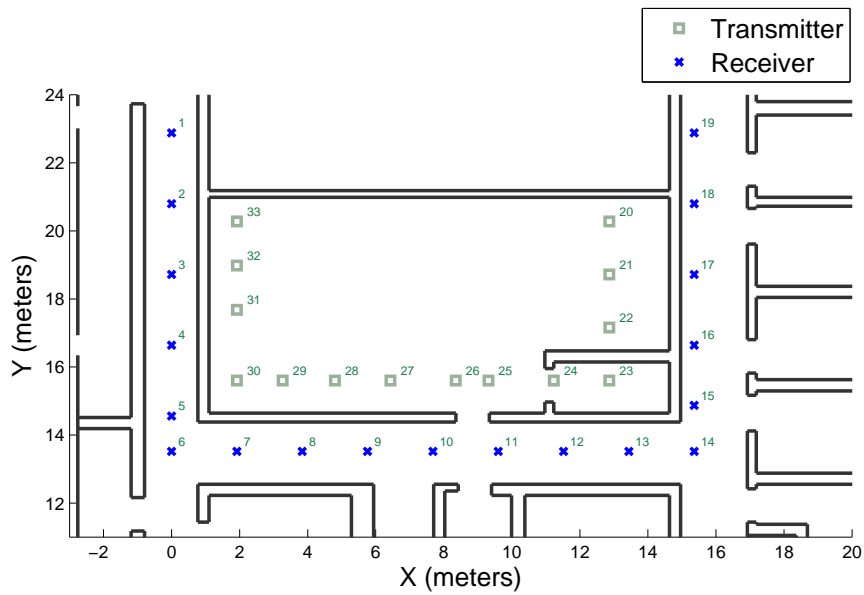
(a) All surveyed receiver locations
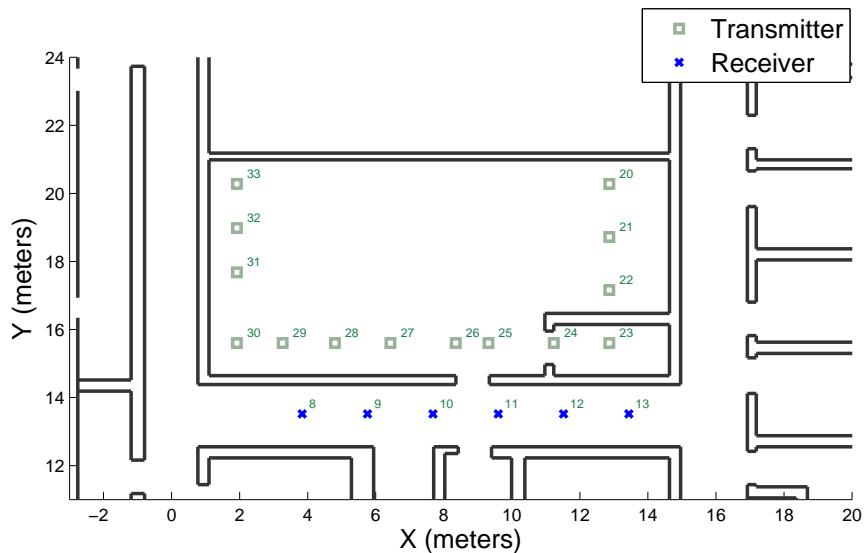
(b) Receiver locations used in analysis

Figure 6.13: Atwater Kent room AK317A test setup showing (a) all surveyed positions and (b) receiver locations that result in a measurement of the transmitted waveform from all transmitter locations

the RF waveform in this environment, we only were able to produce between 29 and 464 TOA preserved measurements for each attempted transmitter/receiver pair.

Figure 6.16 shows the absolute value of aligned scan data, using the method described in Chapter 5, from a receiver placed at all 6 survey points with the transmitter placed on survey point 33. Also shown are the mean (and three standard deviation bar) of the P410 PRM from the receiver placed
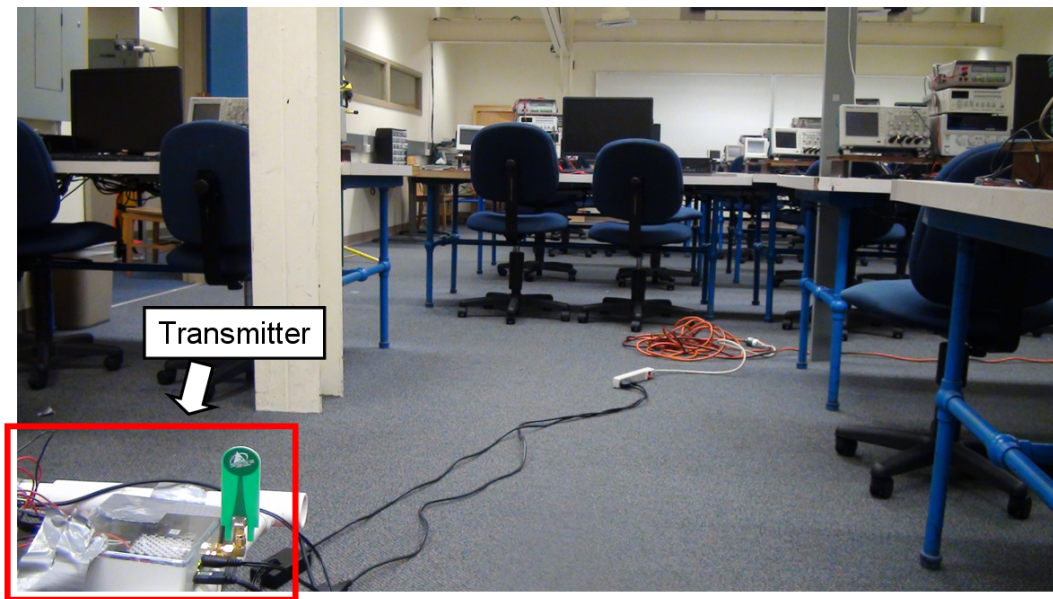
(a) View from transmitter
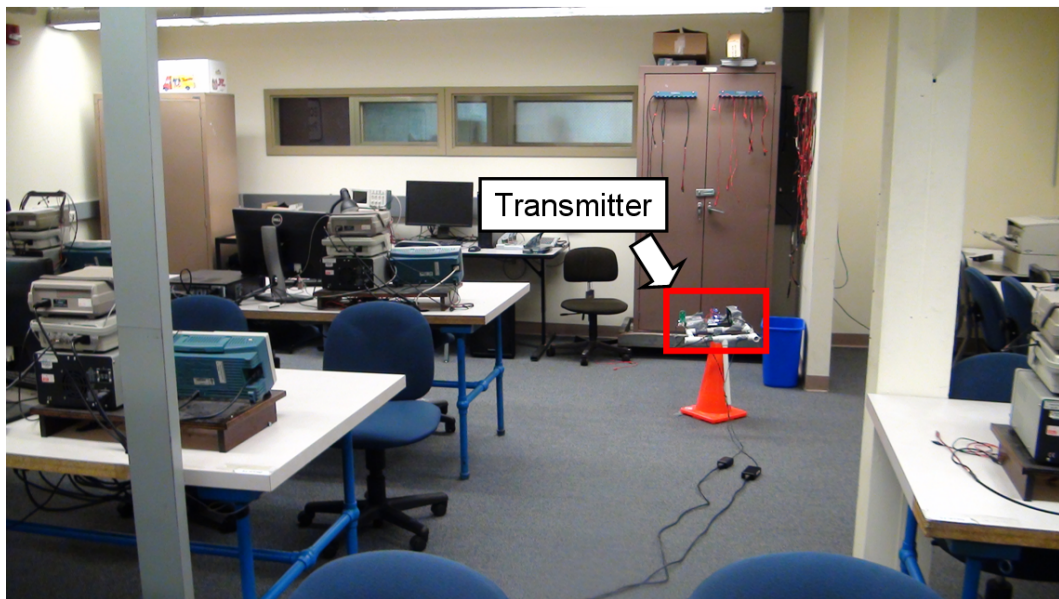
(b) View of transmitter

Figure 6.14: Shows the transmitter in the AK317A computer lab at survey point 22 (a) from behind the transmitter antenna and (b) from standing height

at each survey point in white and measured truth positions using green x's. The P410 operates with a larger variance under these blocked direct path conditions. The PRM produced by the P410 with the receiver placed on survey point 12 is rarely even close to the correct solution and the PRM from survey point 13 has a very large variance. These errors contribute to errors in the LED algorithm as
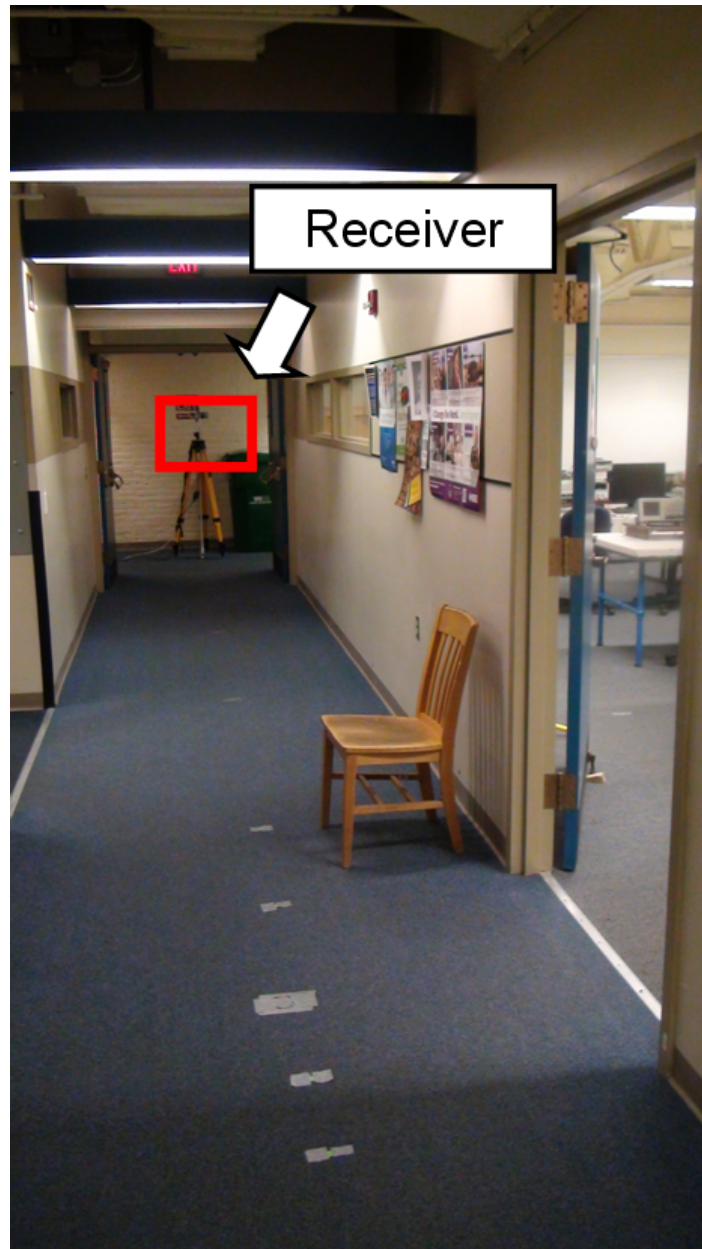
Figure 6.15: Shows the receiver on a tripod located at survey point 6

explained in the previous section when the analysis for the AK315 test was presented.
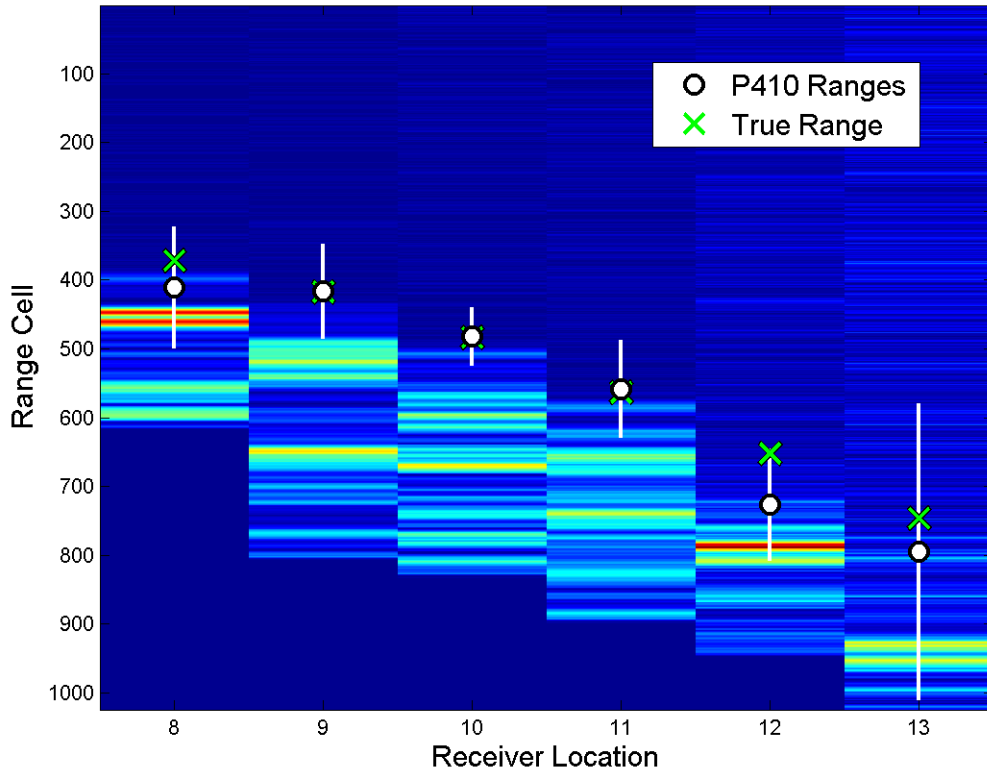
Figure 6.16: Shows the P410 measurements and 3 σ bound in white and the truth using green x's for all receiver locations 8 - 13 while the transmitter was placed on survey point 33 for the AK317 test

6.2.2 Metric Image Examples

Figures 6.17, 6.18, and 6.19 show several example metric images obtained using the LED, SART, TART, and CART algorithms and using a single measurement from each receiver location. Additional metric images from this test can be found in Appendix D. The LED metric images are produced by a brute force plot of the cost function described in section 2.2 using the P410 PRM as the range estimate. The direct positioning algorithms SART, TART, and CART are the metrics described in section 2.3, section 2.4, and Chapter 3 respectively. A black x marks the detected position in each metric image, which represents the maximum metric value in the metric image. For the data analysis presented for the AK317A test, the scan grid is defined by $x_{min} = -1$, $x_{max} = 19$, $y_{min} = 12$, $y_{max} = 24$ with a $\Delta_x = 0.1$, $\Delta_y = 0.1$, and a $\alpha = 20$ and $\gamma = 60$ for the CART algorithm.

Figure 6.17 shows the worst geometry from the AK317A test. If only one measurement is used

(a) LED

(b) SART

(c) TART

(d) CART

Figure 6.17: Example metric images for a transmitter at survey position 33 using algorithms (a) LED, (b) SART, (c) TART, and (d) CART

at each receiver location, the CART algorithm is the only algorithm to produce a submeter accurate estimate with an error of 0.1 meters. The LED algorithm produces an estimate with an error of 4.17 meters and the SART and TART algorithms again have poor performance. If we choose the best geometry using the measurements with the mobile transmitter on survey point 25 as seen in Figure 6.18, the CART and LED algorithms are able to produce a submeter accurate estimate of position. In this case the error in the LED algorithm produces an estimate of position with an error of 0.4 meters and the CART algorithm position error 0.224 meters. The SART and TART algorithms fail again. Another example metric image can be seen in Figure 6.19, where the mobile transmitter is placed on

(a) LED

(b) SART

(c) TART

(d) CART

Figure 6.18: Example metric images for a transmitter at survey point 25 using algorithms (a) LED, (b) SART, (c) TART, and (d) CART

survey point 20. Here the LED produces an estimate with an error of approximately 1.4 meters and the CART algorithm produces a position estimate with an error of 0.224 meters. All of these metric image examples show the SART and TART algorithms failing to produce a good estimate in this high multipath environment while the LED produces reasonable results in some cases, all while the CART algorithm produces the good results.
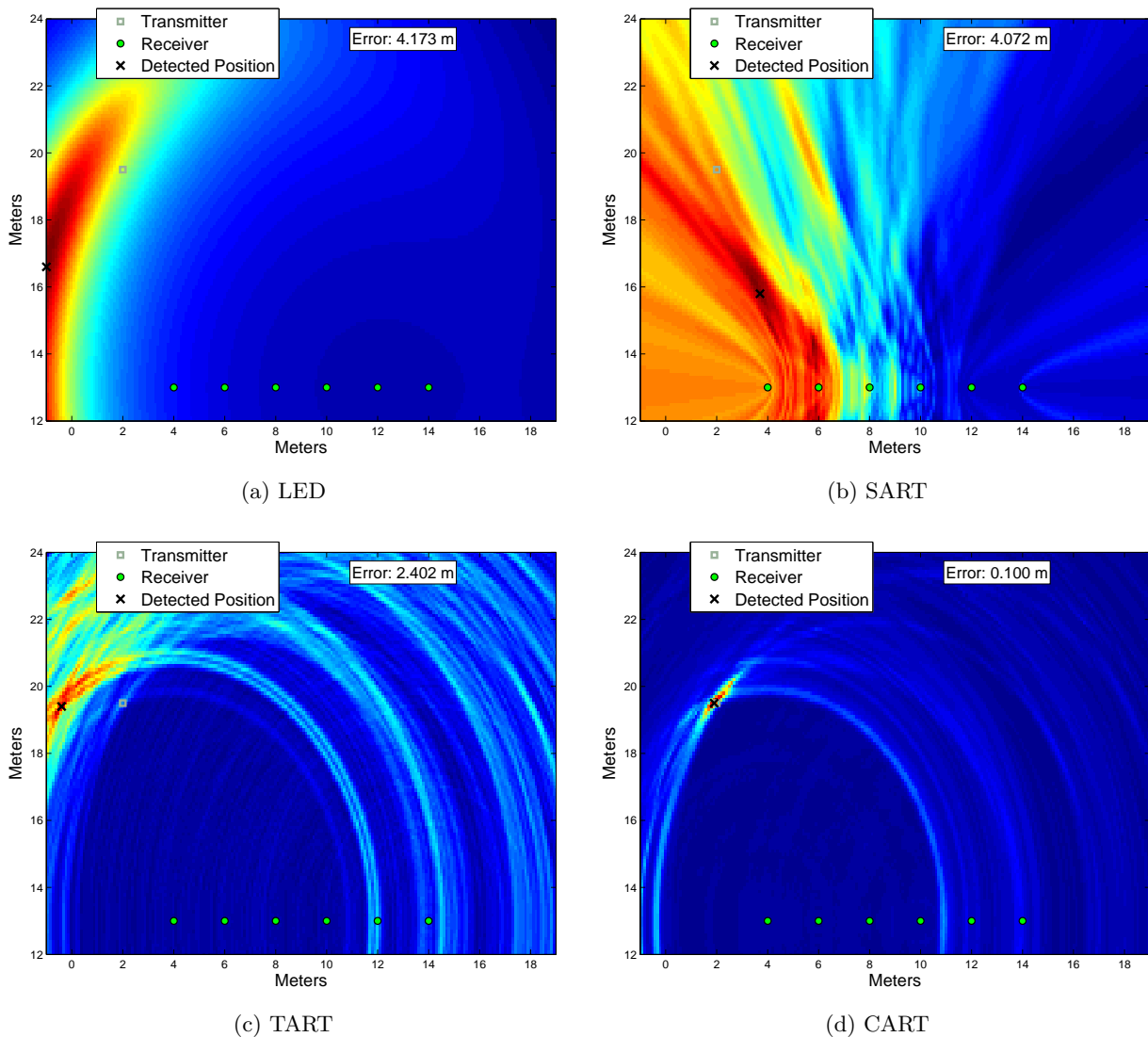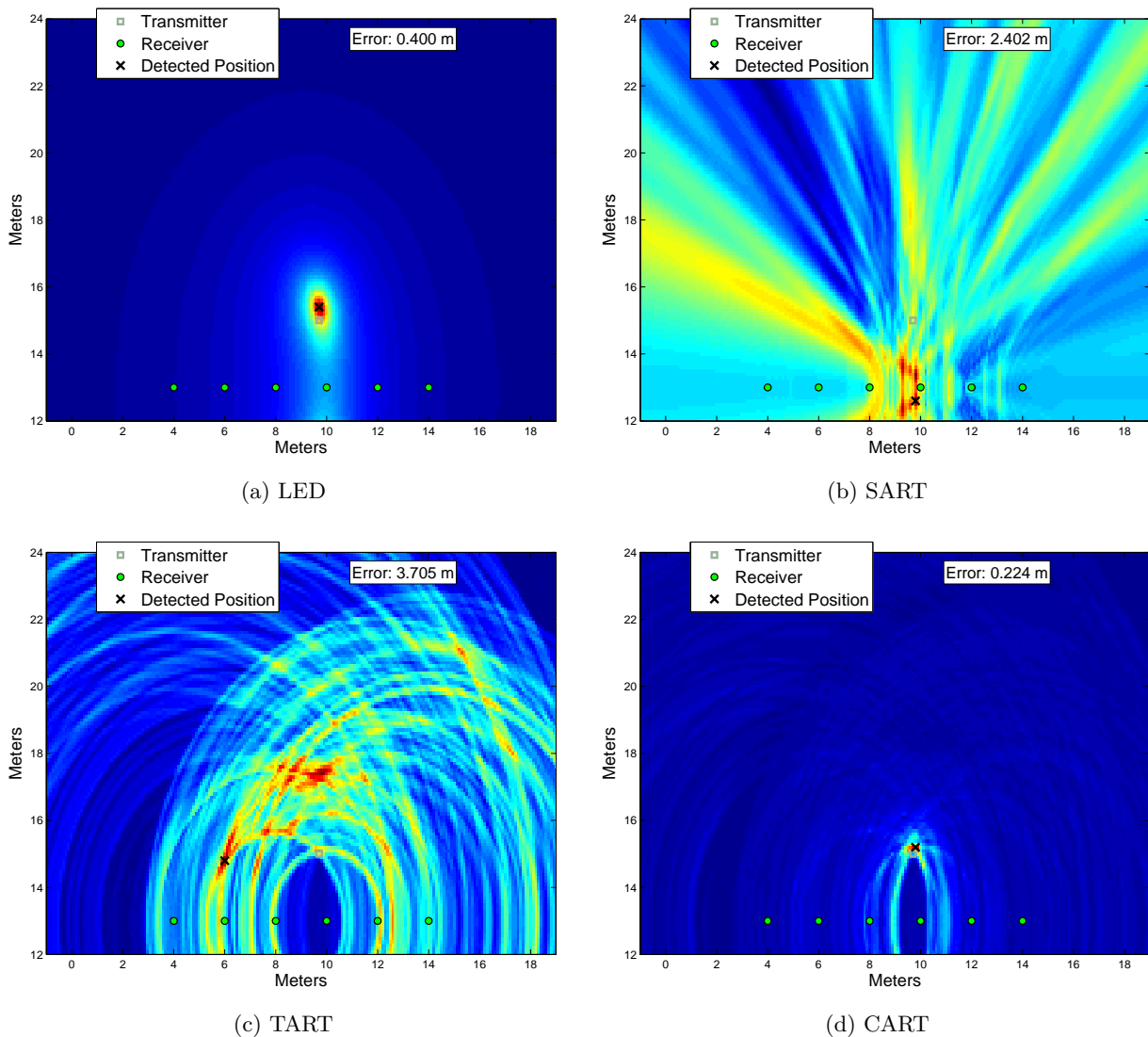
(a) LED
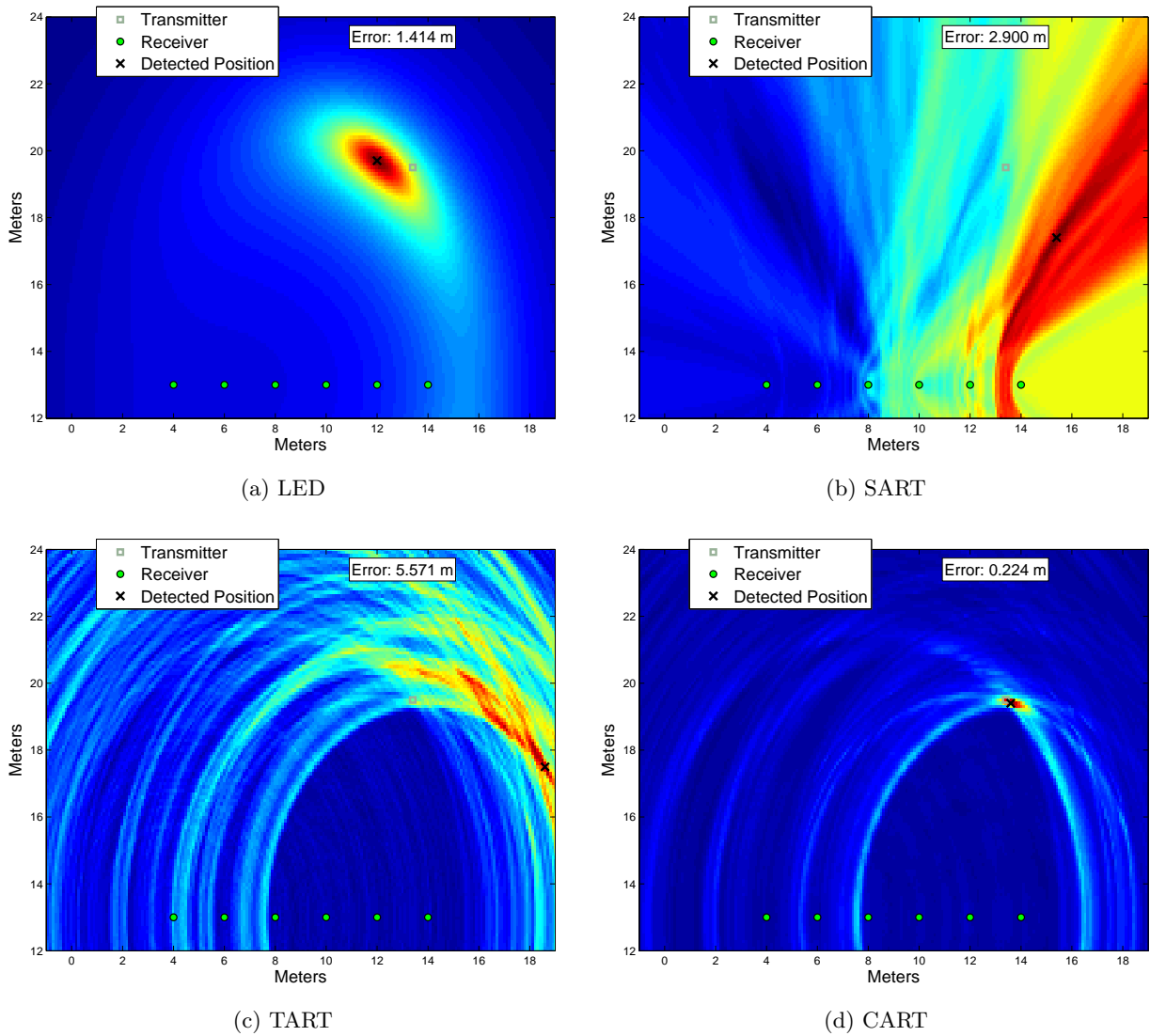
(b) SART

(c) TART

(d) CART

Figure 6.19: Example metric images for a transmitter at survey point 20 using algorithms (a) LED, (b) SART, (c) TART, and (d) CART

6.2.3 CDF of Position Errors

We can quantify the performance of these algorithms by computing the CDF and RMS errors using (4.32), which combines the X and Y errors into a single position error. For the CDF and RMS analysis, we use 15 independent measurements for each transmitter/receiver pair. This produces 15 independent estimates of transmitter position for each transmitter position using each algorithm, LED, SART, TART, and CART.

Figure 6.20a shows the CDF of estimated transmitter position errors for the case when the trans-

(a) Position Errors   (b) Position Errors Zoomed

Figure 6.20: CDF of position errors for transmitter at survey point 32 showing (a) all position errors, and (b) position errors zoomed around 1 meter error.

mitter is placed on survey point 32. Figure 6.20b shows the same figure zoomed around 1 meter of position error. We see the SART and TART algorithms produce errors that are consistently well above 1 meter all of the time. The LED algorithm produces a 1 meter accurate position estimate slightly less than 40% of the time. The CART algorithm always produces a submeter accurate position estimate and always produces an estimate with less than about 0.2 meters.

Figure 6.21 shows the position error CDFs for all 14 transmitter locations from 20 to 33 where the error magnitude has been limited to 2 meters error on the color bar. The SART and TART algorithms typically perform poorly, but on occasion are able to produce a good estimate if sufficient LOS data is present. This is the case for the TART algorithm at transmitter location 24, 27, or 29 as seen from Figure 6.21c where much blue is seen indicating a good estimate. The metric images for the LED, SART, TART, and CART algorithms under the condition of transmitter location 29 can be seen in Appendix B, Figure D.5. The SART algorithm is able to produce a good set of estimates when the transmitter is on position 23, but mostly fails to produce good position estimates. The metric images for the LED, SART, TART, and CART algorithms when the transmitter is on position 23 can be see in Appendix B, Figure D.3.

The LED algorithm outperforms the SART and TART algorithms in this heavy multipath environment. Examining Figure 6.21a, we see that there is indeed a lot of blue, indicating a good estimate much of the time. The CART algorithm, however, far outperforms the LED, SART, and TART algo-

(a) LED
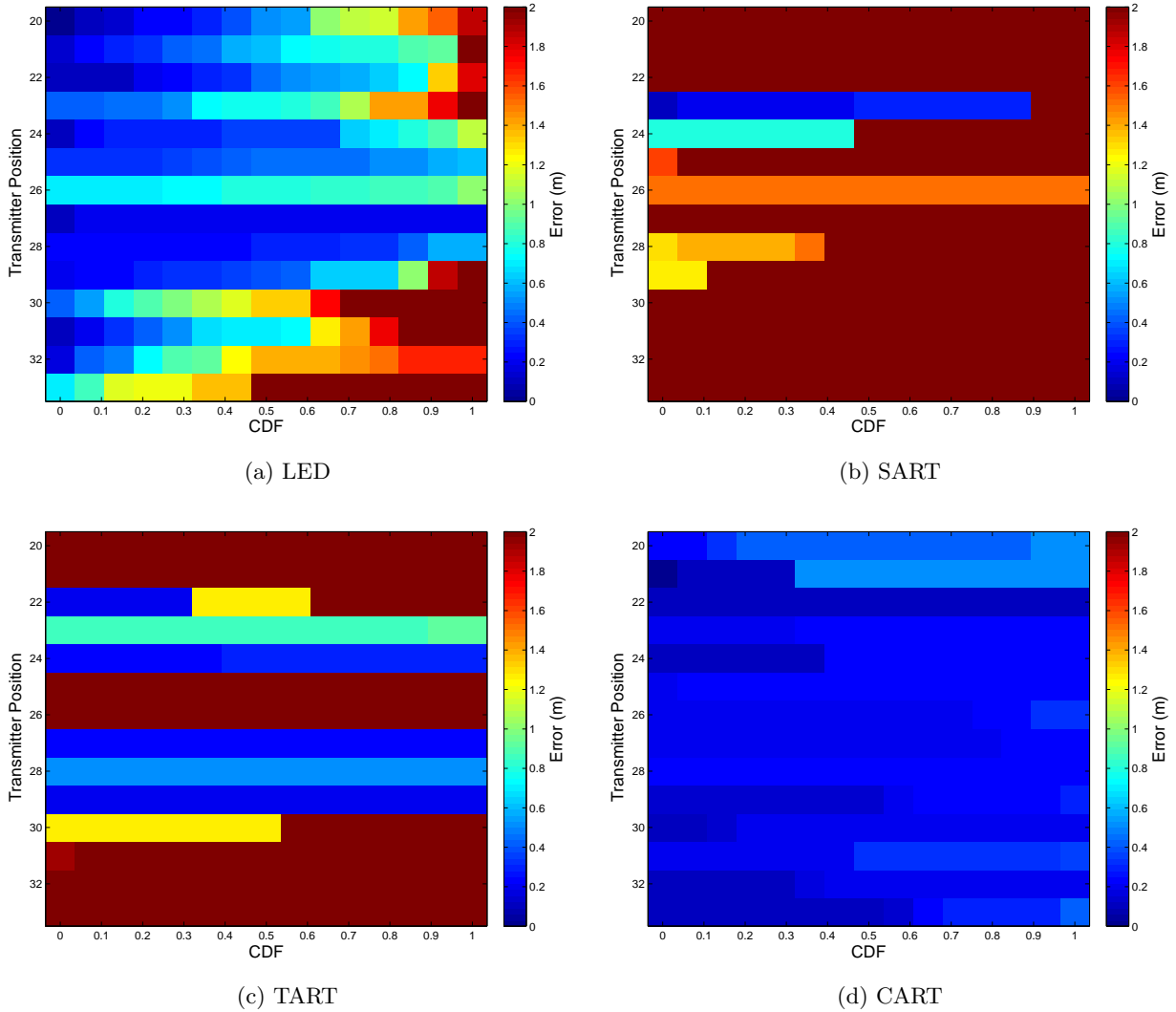
(b) SART

(c) TART

(d) CART

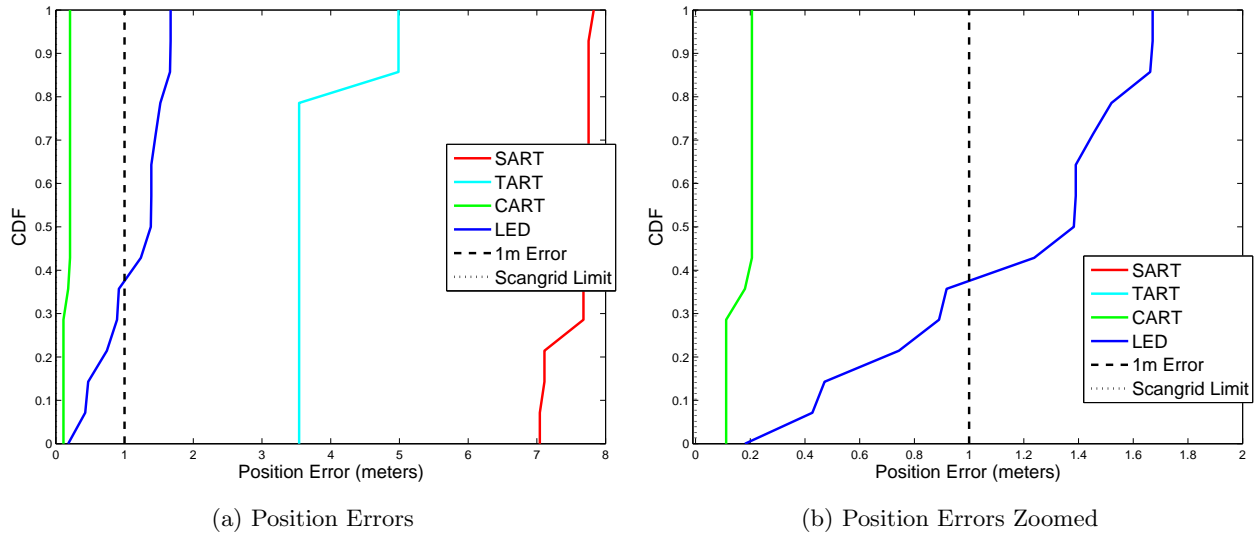Figure 6.21: CDF of position errors at each transmitter location from 20 to 33 using algorithms (a) LED, (b) SART, (c) TART, and (d) CART

rithms in this experiment. Figure 6.21d shows that regardless of the transmitter location, the CART algorithm always produces an error less than a meter 100% of the time. Again, we see the robustness of the CART algorithm in the presence of heavy multipath, even in this difficult indoor environment where the transmitted signal is difficult to detect in the two way transaction.

6.2.4 RMS Errors

We can compute the root of the mean of the squared error as another performance metric of the position error. Figure 6.22 shows the RMS position errors using 15 measurements to produce 15

(a) RMS Errors   (b) Zoomed on CART RMS Errors

Figure 6.22: RMS position error for all transmitter locations (a) showing full position errors and (b) zoomed on CART position errors

independent position estimates at each of the 14 transmitter positions using the LED, SART, TART, and CART algorithms. Figure 6.22b shows the same image zoomed on the CART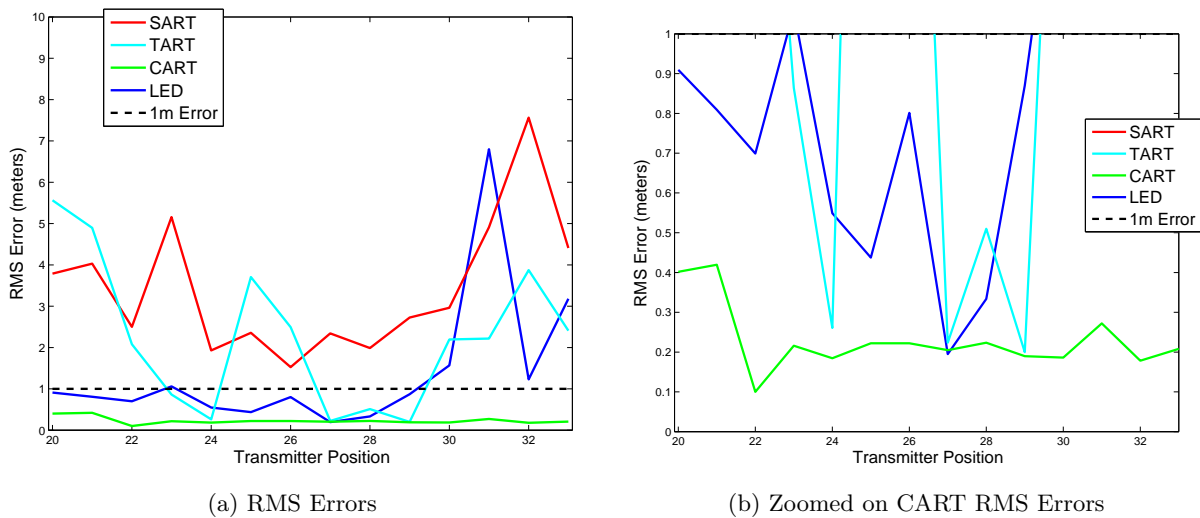 RMS position error. The LED algorithm produces a minimum RMS error of about 0.19 meters when the mobile transmitter is at survey point 27 and a maximum RMS error of 6.5 when the mobile transmitter is at survey point 31. The minimum RMS error using the CART algorithm is around 0.1 meters when the transmitter is at survey point 22 and the maximum is around 0.42 when the mobile transmitter is on survey point 21.

| Algorithm	RMS Error
LED	2.1621
SART	3.7931
TART	2.8141
CART	0.2447

Table 6.3: RMS position errors

Table 6.4 shows the total RMS position errors for each algorithm. The SART, TART, and LED algorithms fail to collectively produce a position estimate with less than a meter RMS error. The CART algorithm produces position estimates with an RMS error of 0.2447 meters, almost 9 times better than the existing LED method in this highly multipath environment.

6.2.5 Raw Errors

All 15 position estimates for all 14 transmitter locations using the SART and TART algorithms are plotted in Figure 6.23 along with an error vector that is defined by the mean of the position estimates. Figure 6.24 shows all 15 position estimates for all 14 transmitter locations using the LED and CART algorithms. Figure 6.23a shows the SART algorithm position estimates and Figure 6.23b shows the TART algorithm position estimates. Both algorithms produce estimates and error vectors that vary wildly from the true transmitter position. Figure 6.24a shows the two step LED algorithm estimates. Careful examination of the figure shows that the position estimates have a large variance even though the mean error vector indicates a good estimate. Look at survey point 22 or 30, for example, where the individual estimates are widely distributed over the image while the mean error vector is very close to the true transmitter location. The CART algorithm estimates, shown in Figure 6.24b, show tightly clustered position estimates around each survey point and corresponding small position error vectors. This visualization of the errors for each sensor configuration highlight the capability of the CART algorithm compared to current existing algorithms.
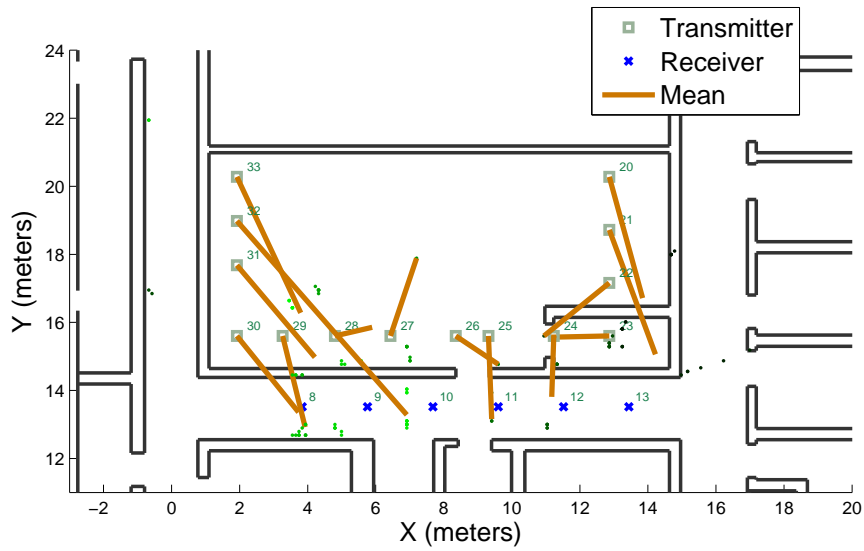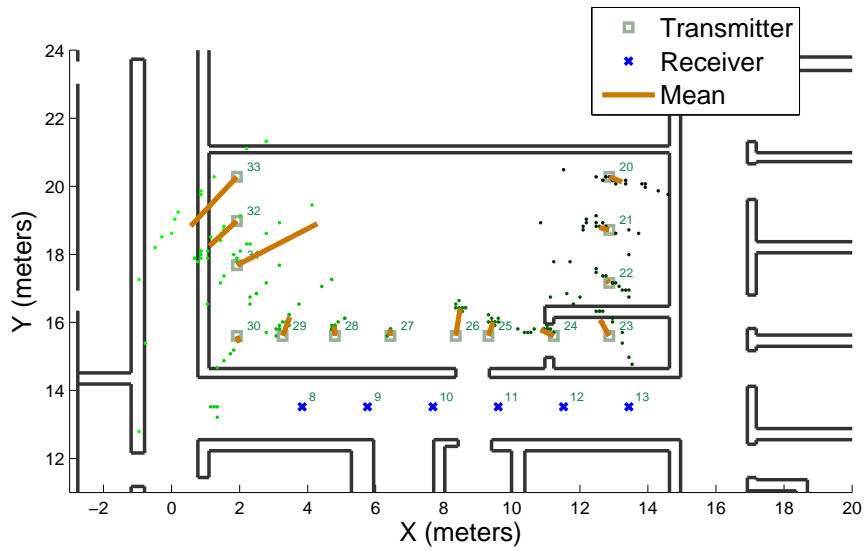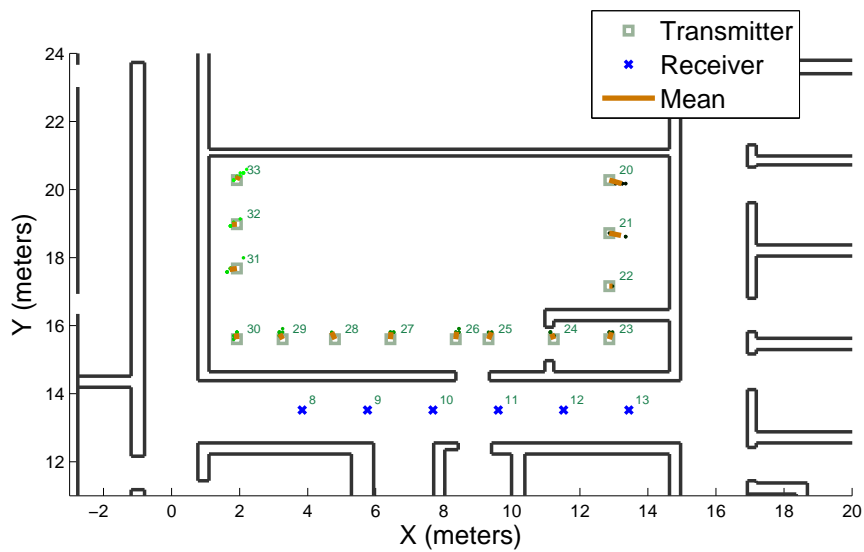
(a) SART
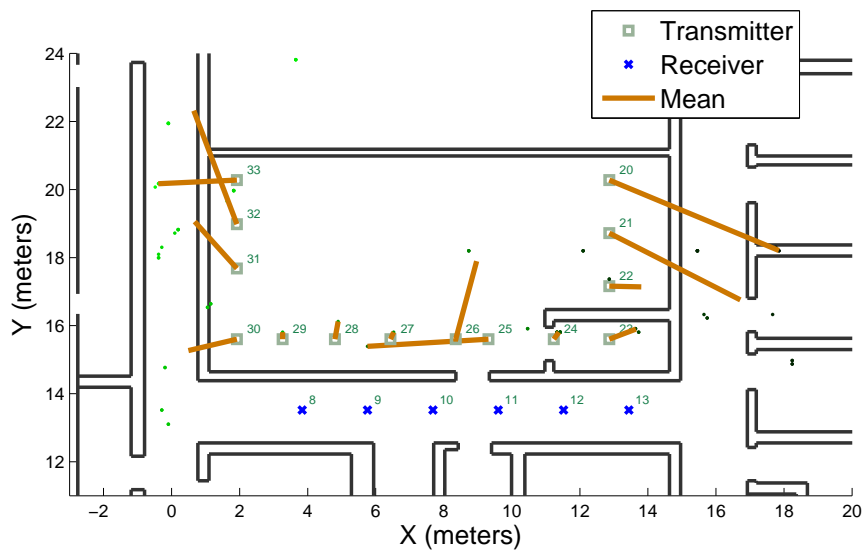
(b) TART

Figure 6.23: Shows all measurements for each transmitter location along with mean error vectors using algorithms (a) SART, and (b) TART

(a) LED

(b) CART

Figure 6.24: Shows all measurements for each transmitter location along with mean error vectors using algorithms (a) LED, and (b) CART

6.2.6   Comparison to ISART

We can compare our results using the CART algorithm to the performance of the ISART algorithm published in [26] and obtained in the AK317A computer laboratory. There are several differences between the two experiments, but we can still get a sense of their performance with the known differences. The ISART test was conducted using 12 or 16 antennas placed around the hallway similar to the 19 receiver locations seen in Figure 6.13a. For the ISART test, the INS unit was mounted onto a boot that was approximately 0.2 to 0.4 meters off the ground as the user walked a path in the computer lab. The waveform used by the ISART algorithm is the Multi-carrier wide band (MCWB) signal structure, which transmits about 100 tones from 550 to 700 MHz using about 10 dBm of power. In addition, the ISART algorithm uses 32 measurements, where a new measurement is captured each time the boot hits the ground as the user walks. For more information on the ISART algorithm or the associated AK317A testing, see [26].

	Algorithm	Antennas	Measurements	Bandwidth	Power	RMS Error
this	SART	6	1	2 GHz	-15 dBm	3.79
test	CART	6	1	2 GHz	-15 dBm	0.25
	SART	12	1	150 MHz	10 dBm	4.00
Ref. [26]	SART	16	1	150 MHz	10 dBm	2.52
	ISART	12	32	150 MHz	10 dBm	1.02
	ISART	16	32	150 MHz	10 dBm	0.61

Table 6.4: Total RMS position errors

As stated earlier in this chapter, the CART algorithm test in AK317A was conducted using a 2 GHz wide waveform using -15 dBm of power with the device placed 0.56 meters off the floor. Our bandwidth is about 13 times bigger, but we have 25 dB less transmit power. This degrades detection for the UWB system, but improves range resolution due to the larger bandwidth. We also do not have an INS system to enable integration over time to increase our synthetic aperture size.

Table 6.4 summaries the performance difference between the CART and ISART algorithms in the same test environment. First, we note that the SART algorithm with a single frame using the UWB system and 6 antennas performs similarly to the single frame 12 antenna 150 MHz setup shown by Cavanaugh [26]. The SART UWB RMS error is 3.79 meters and the 12 antenna 150 MHz single frame RMS error is 4.00 meters. By integrating 32 frames of RF data based on the motion solution generated by the INS unit, the ISART algorithm is able to improve the localization performance to 1.02 meter RMS error. This represents an aperture size of 348 antennas. Without the benefit of the INS and

derived motion solution, we are able to improve the performance using the CART algorithm alone to 0.25 meters RMS error, a factor of 4 times better than the ISART algorithm with 12 antennas and 32 RF frames based on INS motion. The CART algorithm with an aperture size of 6 antennas is seen to outperform the ISART algorithm with an aperture size of 512 antennas by a factor of greater than 2.

Chapter 7

Fire Fighter Homing Device Application

The development of a fire fighter homing device has been an area of interest for the Precision Personal Locator (PPL) project at Worcester Polytechnic Institute (WPI) for many years. The concept is that if a first responder is incapacitated inside a burning or dangerous structure, a rescue can be executed by a single homing device operator. The fire fighter homing device would be a simple wand or stick, which provides feedback to the operator on the direction of the incapacitated individual in order to facilitate the rescue.

A previous system developed to provide this homing capability by the WPI PPL project uses the Very Low Frequency (VLF) band in the near field. The concept of the device was described by [37], which resulted in some good initial results in some structures. Ultimately, the system did not perform up to desired standards due to waveguide modes in metal pipes, giving inaccurate directional results, leading to unacceptable performance. The desire is now to develop a new fire fighter homing device based on the promises of UWB and the new CART algorithm. Similar to the ISART algorithm, we wish to develop a motion solution that can be used to estimate the position of the receive antennas when a TOA preserved RF measurement is taken. In our case, we simplify the motion solution to a simple single axis gyroscope, which enables a 2 dimensional solution that is consistent with our previously presented experimental data. Using the estimated receive antenna positions and the captured RF data, we should be able to estimate the position of the transmitter.

This chapter first describes the mathematical model associated with the fire fighter homing device. Then, we present the wand prototype hardware, data collection effort in the AK315 research laboratory,

the Kalman Filter tracker that estimates transmitter position, and finally the transmitter position estimation results. Some thoughts on wand length are provided in Appendix B. As shown, the CART algorithm is certainly a capable algorithm in this indoor localization application in it's ability to determine the transmitter position using highly multipath corrupted inputs.
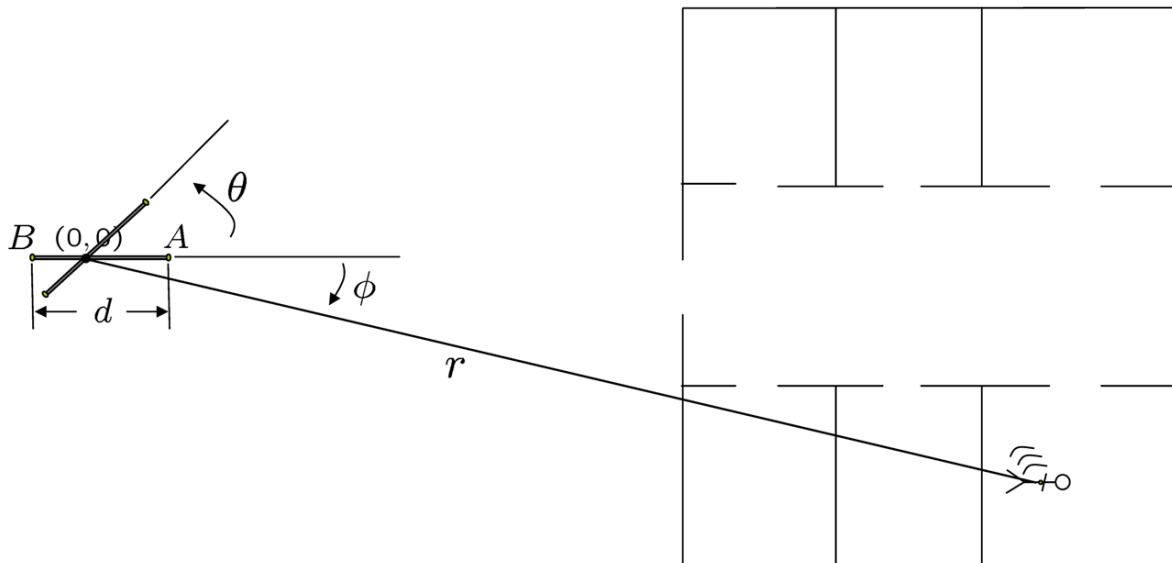
7.1   Overview

Figure 7.1: Fire fighter homing device modeled scenario

The fire fighter homing device scenario considered in this dissertation is shown in Figure 7.1. A point on the wand is labeled as the origin for this scenario. There are two antennas, an A antenna and a B antenna. The location of the transmitter is at some range, r, from the origin at some angle ϕ relative to the axis defined by a line the goes through antenna A and antenna B. The angle θ describes the angle that the wand has rotated relative to the starting orientation of the wand. The length of the wand is d. The operator would hold the wand device at the defined origin, where a single axis gyroscope measures the angular velocity in the direction of θ, which is accumulated for an estimate of θ.

Using this definition, we can examine the localization performance of an unbiased estimator of the transmitter position. If a single measurement of range was made from antenna A and antenna B, we would get the intersection of two circles as seen in Figure 7.2a. If the wand was rotated 90 degrees ($\theta = 90$ deg), and we take another measurement with antenna A, we would get three independent
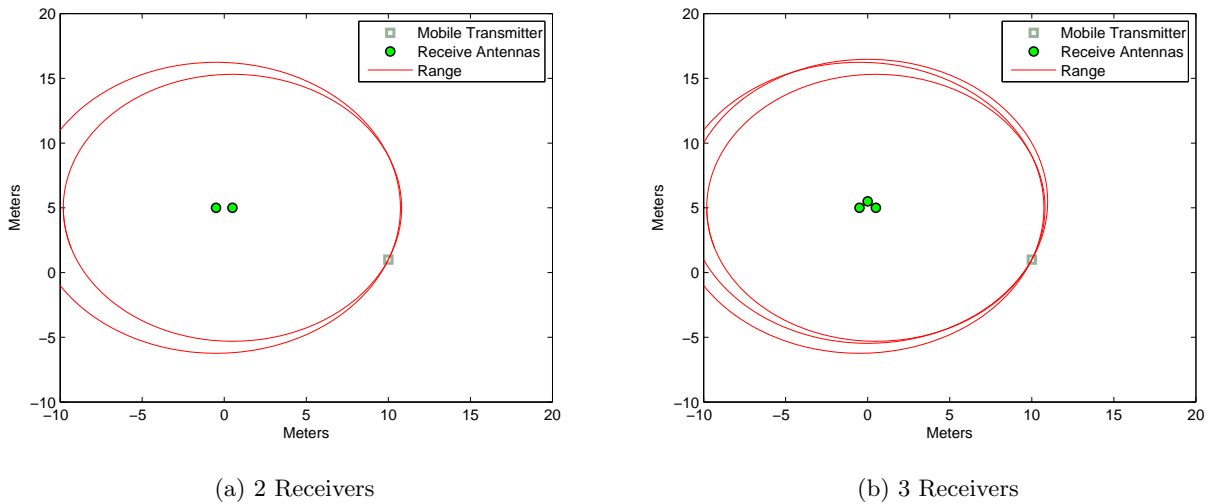
(a) 2 Receivers   (b) 3 Receivers

Figure 7.2: Intersection of circles for wand scenario using (a) 2 receivers or (b) 3 receivers

measurements of range. These three measurements would result in a unique range position as shown in Figure 7.2b. This example shows that some wand rotation is necessary in order to determine a unique transmitter position in 2 dimensions. In this case, we show a transmitter about 10 meters from the wand center position. Even in these figures, the geometry is such that a unique position as defined by the intersection of the three circles is difficult to see by examination. How well can we locate the transmitter with this difficult geometry? If we reduce the wand length, the intersection of the three circles becomes even more difficult to determine. Another question then arises: what effect does the wand length have on our ability to determine the transmitter position?

Feedback from the fire fighter community also makes it clear that a long wand is not acceptable in a practical search and rescue mission. The desire is to reduce the length of the wand as much as possible to allow rescue in confined spaces and to reduce the size and weight of equipment worn. As presented in Appendix B and with the assumption that a reasonable rotation of an operator's wrist would be about 90 degrees, we recommend a 0.5 meter wand length as the optimal length. This ensures a sufficiently small wand for the fire fighter as well as a wand that can produce a submeter accurate estimate at 20 meters regardless of the angle to the transmitter. We also observe a good rule of thumb that there is a 6 dB loss in MSE performance for every time we halve the wand length.
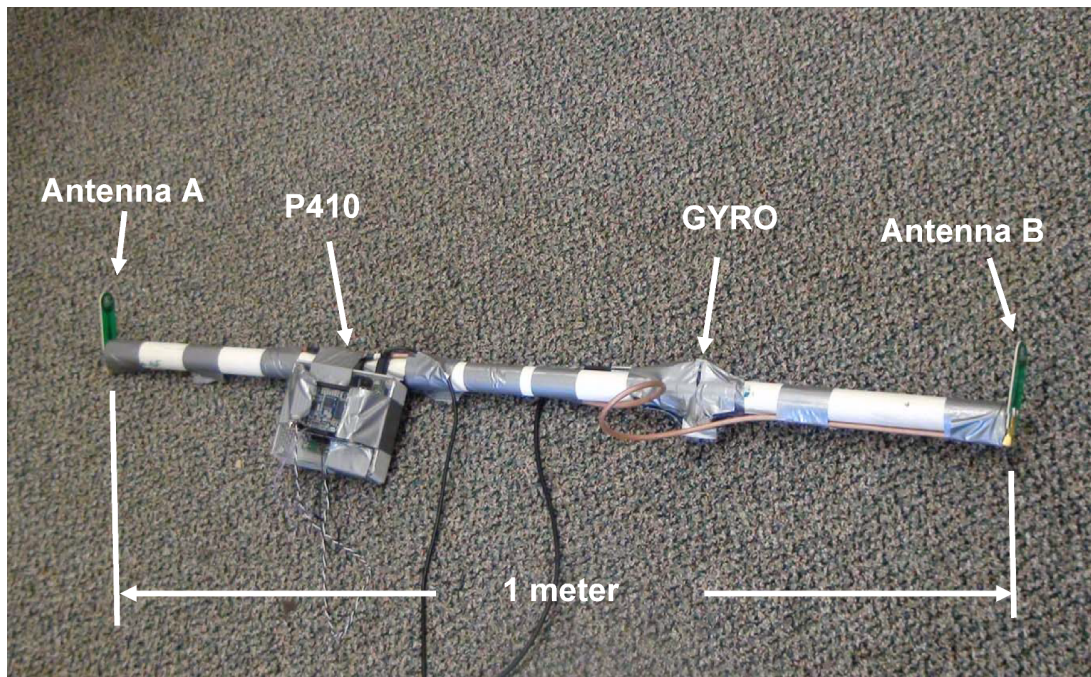
Figure 7.3: Wand to be used by rescuer

7.2 Wand Prototype Hardware

The prototype wand device is constructed using a Pulse On 410 (P410) from TimeDomain and a single Navchip gyroscope. The P410 device that is attached to the wand was previously described as the receiver in Chapter 5. The gyroscope is positioned 0.71 meters from antenna A and 0.29 meters from antenna B, making the total wand length 1 meter. Figure 7.3 shows a picture of the wand prototype, calling out the gyroscope and P410 device. For data collection, a host laptop is connected to the wand through two USB ports, one for the P410 device and one for the Navchip gyroscope. The final wand would consist of an embedded device to perform the communications and processing required for transmitter localization and operator feedback. The transmitter hardware used by the wand experimentation is the same as the transmitter hardware described in Chapter 5 and was used for experimentation and validation in Section A with fixed transmitter and receiver positions.

A custom MATLAB program is used to send range request messages to the transmitter unit, which then responds as described in Section A. The range request message is first sent from antenna A then antenna B in an alternating manner. The RCM_RANGE_INFO, RCM_FULL_SCAN_INFO, and RCM_DATA_INFO packets are stored into allocated memory on the host computer until the end of the data collection. Once data collection ends, the allocated memory is saved into a file on the hard

drive to be processed at a later time. This method of data collection allows us to collect the data as fast as possible without risk of buffer overflows.
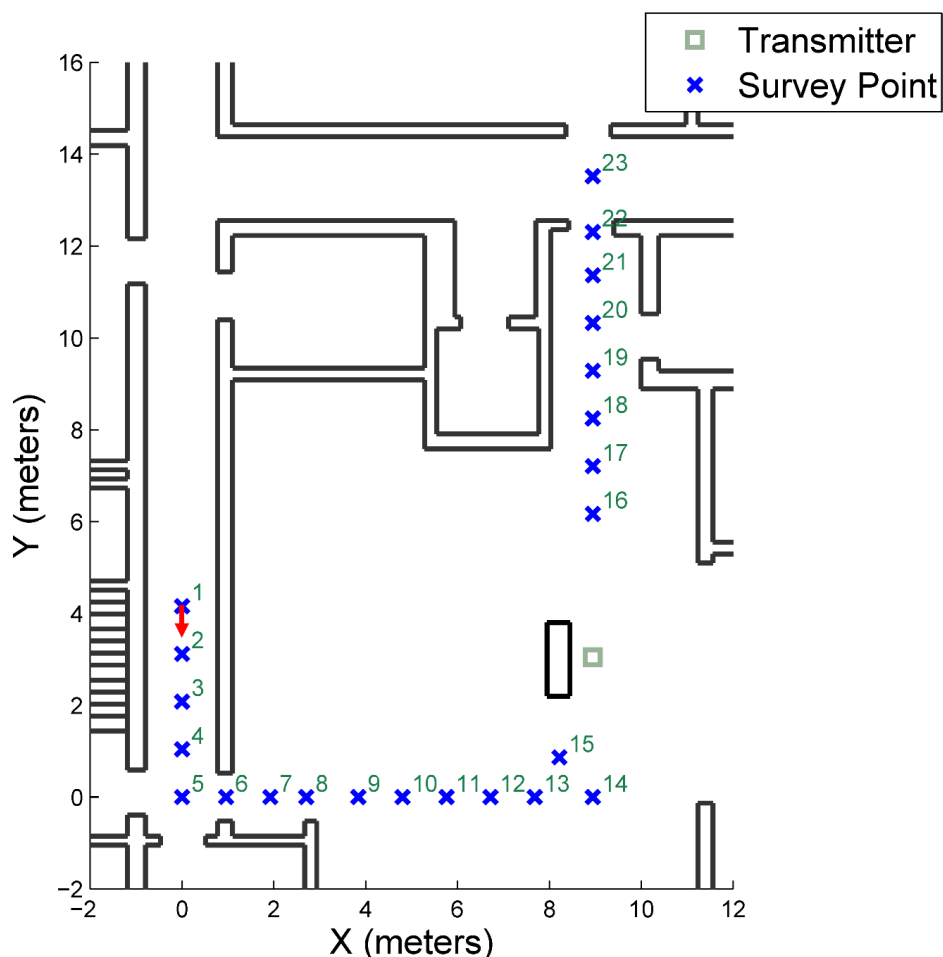
7.3 Data Collection

Figure 7.4: Floor plan of AK315 used for data collection with a red arrow indicating the start position and orientation of the wand

Data collection was carried out in the same AK315 research laboratory used in Section 6.1 during fixed transmitter and receiver position testing. Figure 7.4 shows the floorplan view along with a red arrow indicating the starting position and orientation of the prototype wand device. The transmitter was placed behind the large metal cabinet at a height of 1.77 meters. As indicated by the red arrow, the wand antenna A was pointing down the y axis at the beginning of each run. A gyroscope calibration

was performed at the start of each run for 10 seconds, which allows us to estimate a gyroscope bias that is then subtracted from the raw data.

After calibration, the wand was held by hand where the gyroscope is attached and rotated while held at each survey point from 1 to 15. The rotation went left and then right and back to the left to position antenna A towards the next survey point. At each survey point, a rotation of 90 degrees in each direction was attempted. At some survey points, the rotation was limited to about 35 degrees in one direction due to physical obstructions. After the rotation was complete at the current survey point, the wand was moved in a swift motion to the next survey point and the process was repeated until survey point 15 was reached. The wand height was about 0.95 meters above the floor for the entire run and care was taken to limit the tilt of the wand into the z dimension.

In the next section, we introduce the data processing performed on the collected data. It is noteworthy to point out that the data processing and analysis is performed in two dimensions, consistent with the previous stationary experiments in Chapter 6. These results could be extended into a three dimensional solution using an INS system similar to Cavanaugh [26], but we chose to minimize the mathematical overhead for this demonstration. The limitation this simplified implementation imposes on the real application is that we now only localize the transmitter on a 2 dimensional plane, which would practically limit our localization to the operator's floor of a multilevel building.

7.4   Data Processing

After data collection, the recorded data is post processed as shown in the processing block diagram of Figure 7.5. The P410 data is time aligned according to the alignment algorithm described in Section 5.3 and stored in allocated memory along with a timestamp. The gyroscope angle and computed mean of the 10 second calibration data are passed to an accumulator block. Mathematically, the accumulator performs

$$\theta_k \quad = \quad \sum_{i=1}^{k} (\dot{\theta}_z - \beta_z) \tag{7.1}$$

where β_z is the computed mean of the 10 second calibration, $\dot{\theta}_z$ is the raw gyroscope data, and θ_k is the current estimated gyroscope angle at time step k relative to the starting orientation. The current estimated gyroscope angle is then stored in allocated memory along with a time stamp. The sample rate of the P410 data is around 10 Hz and that of the gyroscope is around 100 Hz. A time alignment is performed on the stored data based on the RF data and gyroscope timestamps.
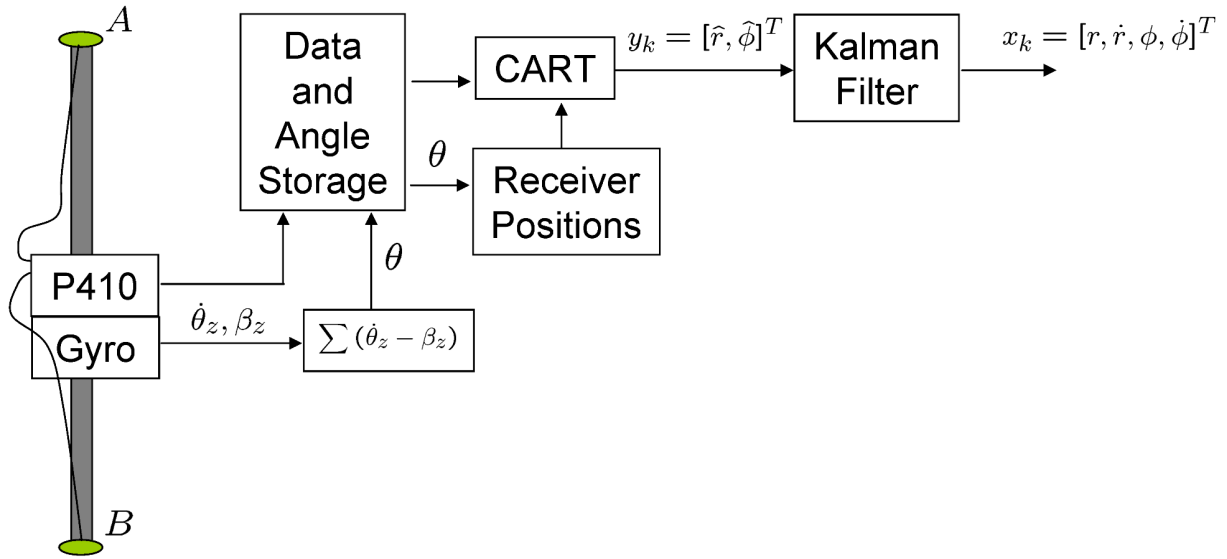
Figure 7.5: Block diagram of data processing

After data alignment, we now have a gyroscope angle and an associated RF data measurement at a 10 Hz rate. If we define the starting position of the wand antennas as

$$\begin{bmatrix} A_x \\ A_y \end{bmatrix} = \begin{bmatrix} 0.71 \\ 0.00 \end{bmatrix} \tag{7.2}$$

$$\begin{bmatrix} B_x \\ B_y \end{bmatrix} = \begin{bmatrix} -0.29 \\ 0.00 \end{bmatrix} \tag{7.3}$$

where A_x and A_y describe the starting Cartesian position of antenna A and B_x and B_y describe the starting Cartesian position of antenna B, we can compute the receive antenna positions at time step k using a rotation. This is done using

$$A_k = \begin{bmatrix} cos(\theta_k) & -sin(\theta_k) \\ sin(\theta_k) & cos(\theta_k) \end{bmatrix} \begin{bmatrix} A_x \\ A_y \end{bmatrix} \tag{7.4}$$

$$B_k = \begin{bmatrix} cos(\theta_k) & -sin(\theta_k) \\ sin(\theta_k) & cos(\theta_k) \end{bmatrix} \begin{bmatrix} B_x \\ B_y \end{bmatrix} \tag{7.5}$$

where θ_k is the stored and time aligned angle that corresponds to the current RF measurement.

An example of the gyroscope estimated angle can be seen in Figure 7.6a where the wand first moves left, then right, and then left again. We are showing 33 frames of gyroscope data, which is the number of RF frames that are fused together based on the receiver position estimates. It is also noteworthy to
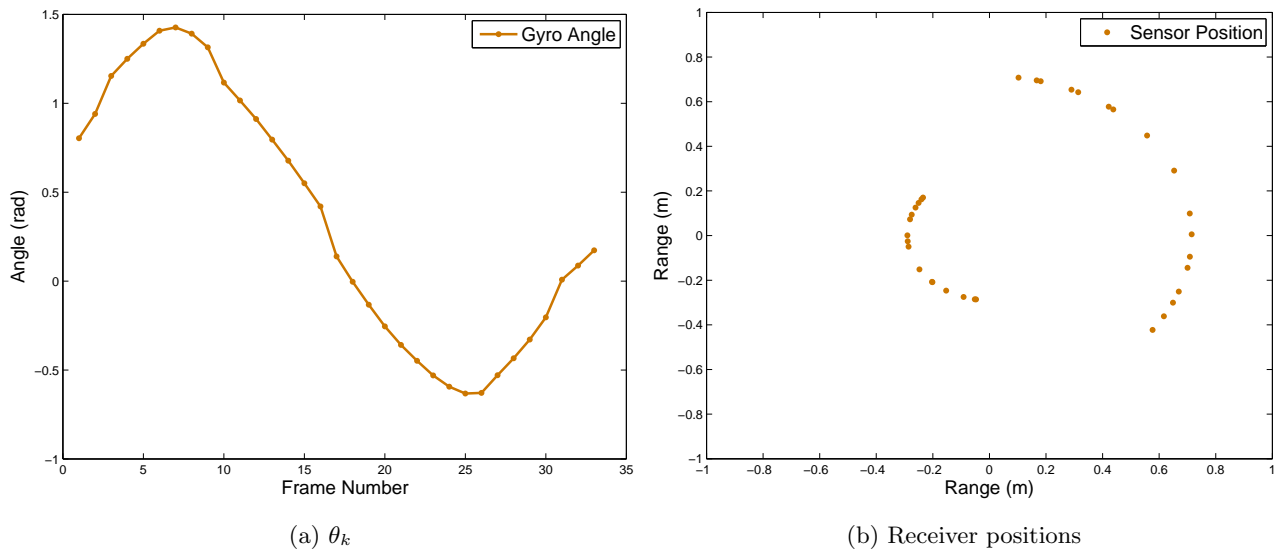
(a) θ_k

(b) Receiver positions

Figure 7.6: Shows stored (a) gyroscope derived angle data and (b) computed receiver positions relative to wand center

examine the intermittent nature of the angular data. This is primarily the result of three factors: first, if the RF frame measurement fails, the frame is dropped from the allocated storage buffer, second, the wand rate of movement was determined by the rate at which the operator manually manipulated the wand so it is not moving at a constant rate, and last, the amount of time between RF measurements is not constant. Figure 7.6b shows the corresponding calculated receiver positions based on the rotation of the wand and the antenna used for the measurement. We notice in this example that there is a good angular rotation on the order of 135 degrees. Since the receiver positions are calculated only based on the rotation for a given 33 frame window, there are gross errors in the receiver positions during the swift movement from one survey point to the next. The result of this error is seen in the final section of this chapter when we examine the results of this wand processing algorithm.

Figure 7.7a shows the magnitude of the TOA preserved raw RF scan data for each of the 33 receiver positions seen in Figure 7.6. Careful examination of the image shows that the direct path is blocked since the multipath components have a greater intensity. Some structure is also visible in the leading edge, but by and large, it is difficult to determine what is happening by looking at the raw scan data alone. If we use the estimated receiver positions and the RF data as inputs to a polar version of CART algorithm, we can produce an estimate of the range and angle to the transmitter relative to the center of the wand. The computed polar CART metric image is seen in Figure 7.7b for this example. The CART algorithm was able to produce an incredibly accurate estimate of transmitter position under

this poor geometry with highly multipath corrupted RF data and estimated receiver positions based on the gyroscope. The detected position is taken as the peak of the computed CART metric image. The estimated transmitter positions are given to a Kalman Filter, which is described in the next section.
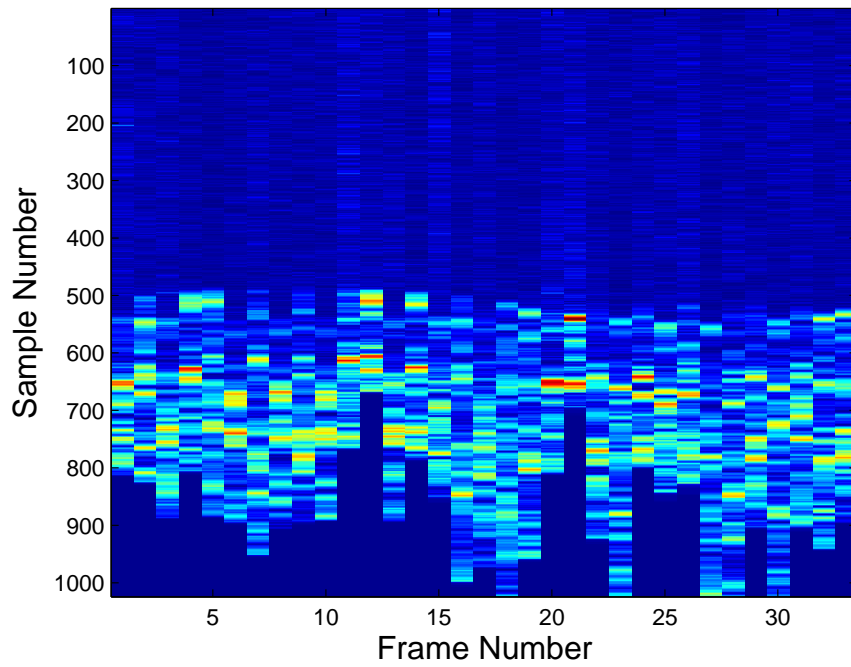
(a) Scan Data
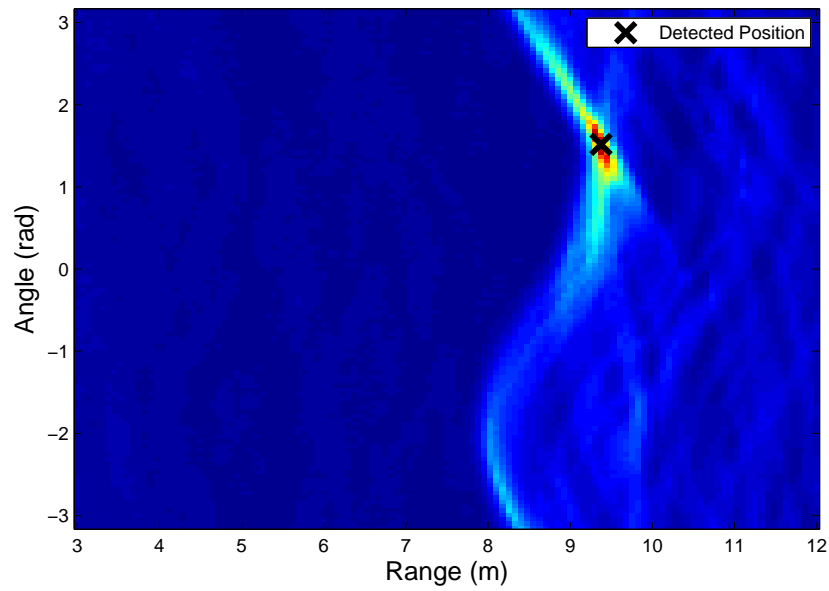
(b) Polar CART metric image

Figure 7.7: Shows stored (a) P410 RF scan data for each measurement of θ and (b) resulting polar CART metric image using computed receiver positions

7.5 Kalman Filter Tracker

The Kalman Filter tracker we use to estimate the position of the transmitter as we walk the path defined in Section 7.3 is a linear Kalman Filter with data editing. Data editing is added to restrict faulty range measurements from affecting the Kalman Filter states. Following Dan Simon's book [38], the discrete linear dynamic system at the current time step k is defined by

$$x_k = F_{k-1}x_{k-1} + w_{k-1} \tag{7.6}$$

$$y_k = H_kx_k + v_k \tag{7.7}$$

where F_{k-1} is the state transition matrix, x_k is the current state with state covariance P_k, w_{k-1} is the process noise, assumed to be white Gaussian with covariance Q_{k-1}, y_k is the measurement, H_k is the observation matrix, and v_k is the observation noise assumed to be white Gaussian with covariance R_k. For our Kalman Filter we have 4 states defined by

$$x_k = \begin{bmatrix} r \\ \dot{r} \\ \phi \\ \dot{\phi} \end{bmatrix} \tag{7.8}$$

where r is the current range from the center of the wand to the transmitter and ϕ is the angle from antenna A to the transmitter as seen in Figure 7.1. The state transition matrix is defined by

$$F_k = \begin{bmatrix} 1 & T_k & 0 & 0 \\ 0 & 1 & 0 & 0 \\ 0 & 0 & 1 & T_k \\ 0 & 0 & 0 & 1 \end{bmatrix} \tag{7.9}$$

where T_k defines the amount of time that has elapsed from the previous state to the current state. The observation of these states occurs directly in the polar domain and is written as

$$H_k = \begin{bmatrix} 1 & 0 & 0 & 0 \\ 0 & 0 & 1 & 0 \end{bmatrix} \tag{7.10}$$

where we observe the range and angle from the center of the wand directly using the polar CART algorithm. To execute the Kalman Filter, we first assign the initial conditions as

$$x_0^+ = [10\ 0\ 0\ 0]^T \tag{7.11}$$

$$P_0^+ = diag([10\ 10\ 10\ 10]) \tag{7.12}$$

where the initial state is set to a transmitter position 10 meters straight ahead with very little certainty about the position as indicated by a large variance in range and angle. We also assign the process noise as

$$Q_k = diag([1e-2\ 1e-2\ 1e-5\ 1e-5]) \tag{7.13}$$

which restricts the way the model is allowed to be influenced by the measurements when we run the Kalman Filter. The first 5 frames of the Kalman Filter use a scan grid that is defined by a 40x50 point scan grid of size ± 5 meters and ± 120 degrees. All scan grids afterwards are defined by a sequence of 9 frames that are determined by the state covariance P_k and the 10th frame that is a 40x50 point scan grid of size ± 5 meters and ± 120 degrees. This sequence ensures the current point being tracked is indeed the correct global maximum in the metric image. The 9 frames that are defined by P_k are limited to a 26x26 point scan grid centered on the current estimated transmitter position covering a range of parameter values defined by $\pm 3\sigma_{\hat{r}}$ and $\pm 3\sigma_{\hat{\phi}}$. If the state variances are smaller than 0.25 meters or 0.25 radians, the size is limited to a ± 0.25 meter and ± 0.25 radian scan grid size.

Once the first estimate is made based on the initial conditions for the first frame, we run the Kalman Filter forward using the time update

$$x_k^- = F_{k-1}x_{k-1} \tag{7.14}$$

$$P_k^- = F_{k-1}P_{k-1}F_{k-1}^T + Q_{k-1} \tag{7.15}$$

followed by a computation of the Kalman gain and the innovation bounds

$$K_k^- = P_k^- H_k^T (H_k P_k^- H_k^T + R_k)^{-1} \tag{7.16}$$

$$S_k = H_k P_k^- H_k^T + R_k \tag{7.17}$$

which enables data editing on the measurement update. We then compute the innovation as

$$r_k = y_k - H_k x_k \tag{7.18}$$

where the innovation r_k is not to be confused with the the state variable r. The innovation measures the level of surprise in the measurements of the states as compared to the predicted states based on the model. For our implementation, if the innovation is outside the $\pm 2\sigma_{\hat{x}}$ bounds as defined by the innovation bound S_k, then we discard the measurement. This is important for the large scan grid window where we introduce the possibility of a measurement that is far from the current tracked position.

The final step is to compute the measurement update based on the time update state and state covariance, Kalman gain, and innovation. Without data editing, the measurement update equations are

$$x_k^+ = x_k^- + K_k r_k \tag{7.19}$$

$$P_k^+ = (I - K_k H_k) P_k^- (I - K_k H_k)^T + K_k R_k K_k^T \tag{7.20}$$

and with data editing, we update each individual measurement using a loop through all the observations. If the measurement falls in the $\pm 2\sigma_{\hat{x}}$ bound, we use

$$K_k(l) = P_k H_k^T(l)(H_k(l) P_k H_k^T(l) + R(l))^{-1} \tag{7.21}$$

$$x_k^+(l) = x_k^+(l) + K_k(l) r_k(l) \tag{7.22}$$

$$P_k^+(l) = (I - K_k(l) H_k(l)) P_k^+(l)(I - K_k(l) H_k(l))^T + K_k(l) R_k(l) K_k(l)^T \tag{7.23}$$

where $l = 1..2$ observations for this problem, $H_k(l)$ selects the lth row that defines the observation from H_k, $R(l)$ selects the $_{l,l}$th element of the measurement covariance R_k, $x_k^+(l)$ is initialized to x_k^-, $P_k^+(l)$ is initialized to P_k^-, and $x_k^+ = x_k^+(l)$ and $P_k^+ = P_k^+(l)$ once the loop as completed. The result is a measurement update if the measurement made is close to where the model predicted the measurement should fall.

As stated before, the gyroscope data is handled separately in this implementation and is not part of the Kalman Filter other than being used to produce the receiver position estimates, about the center of rotation, when a RF position measurement is taken. We hold the wand steady for 10 seconds at the beginning of the data collection to estimate a bias for the entire run. This bias is then subtracted from the raw gyroscope data and then the result is integrated between each Kalman Filter step and added to the current prediction of the wand angle relative to the starting orientation.

7.6   Results

We can quantify the performance of our transmitter tracking algorithm using the same CDF of errors and RMS analysis used in the previous chapter. Since we rotated the wand over a survey point, we have truth data for each rotation. Comparing the truth to the estimate, we are able to determine the error. Before we show those results, we show the range and angle track results in Figure 7.8 and Figure 7.9 along with the true range and angle determine by examining the gyroscope angle rotation data. The figures also shows the survey point number for each truth position. The range track in Figure
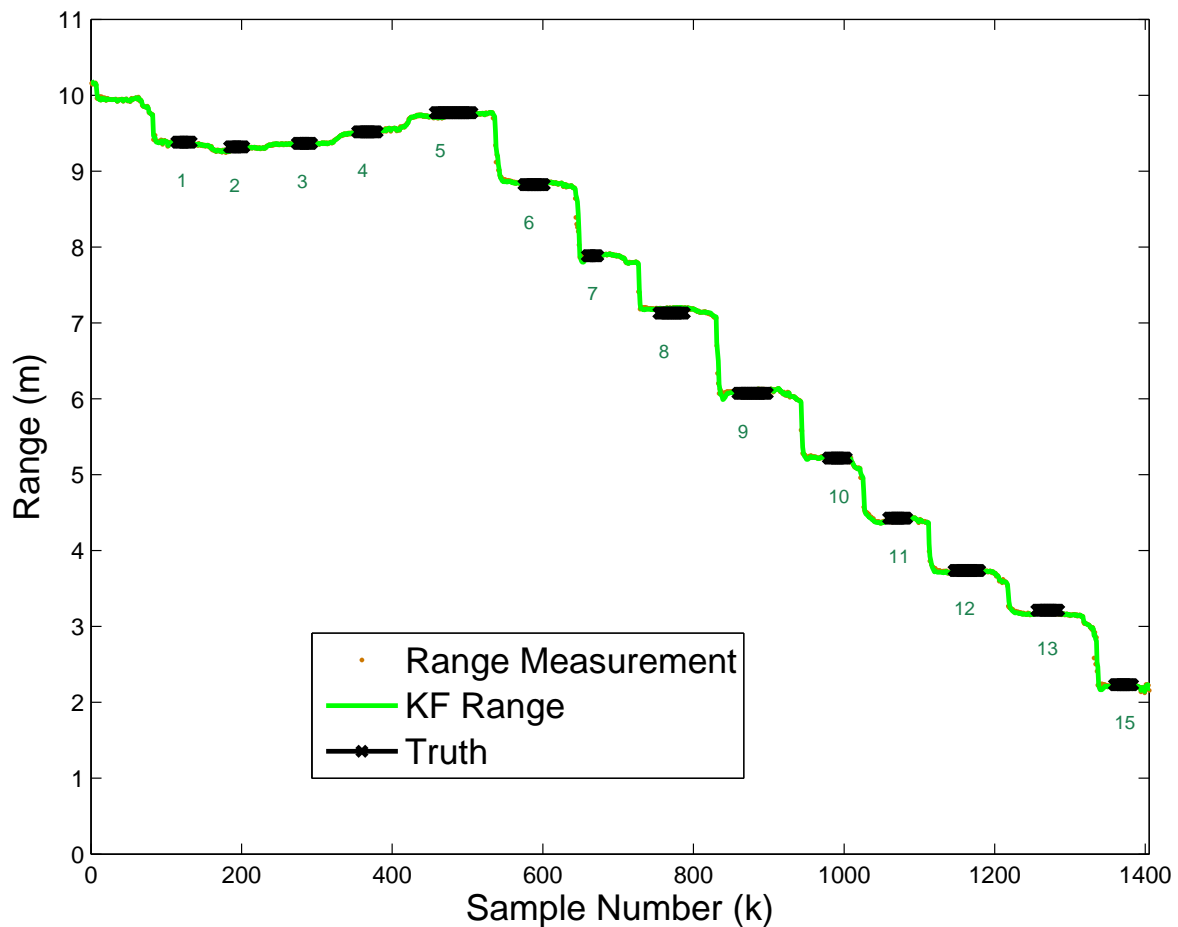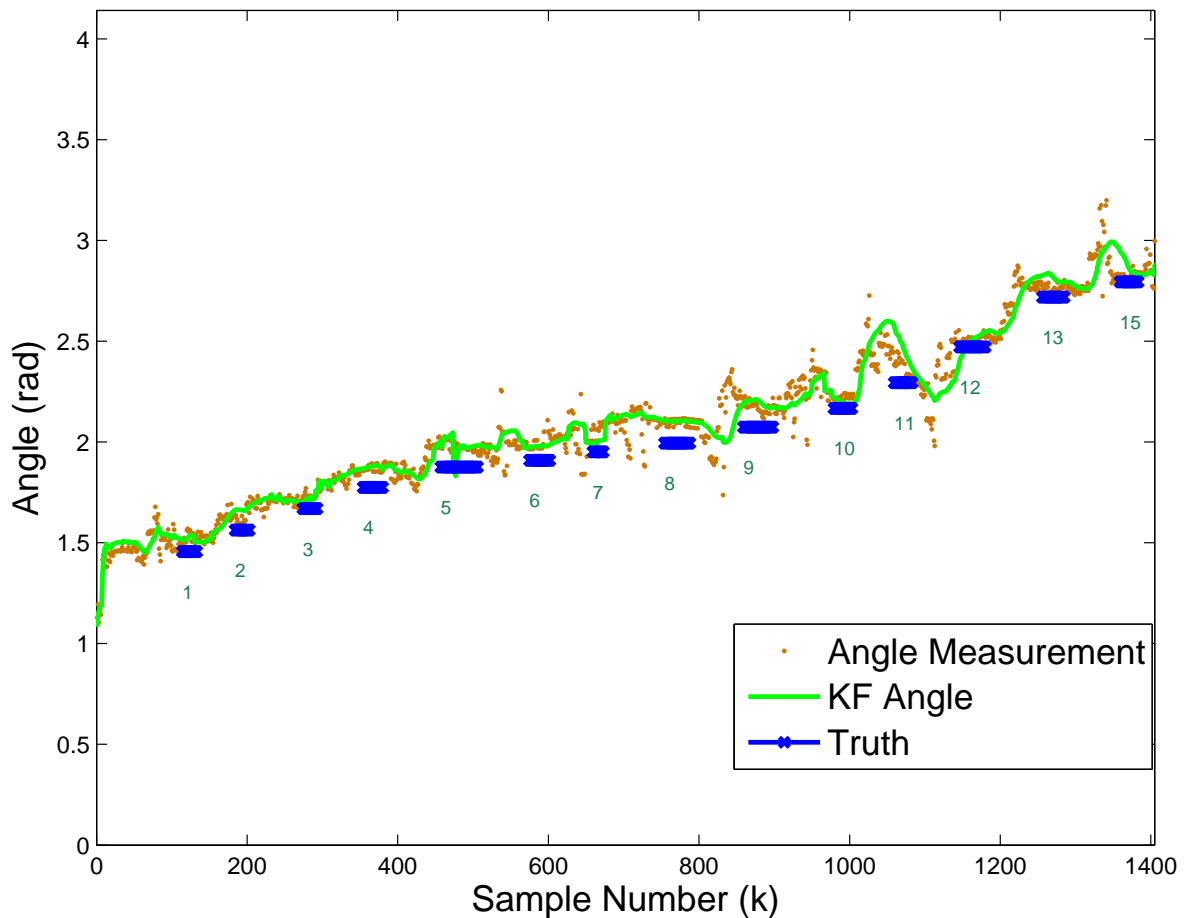
Figure 7.8: Shows range estimates, Kalman Filter range track result, and true range for the wand homing device test. The numbers are the surveyed truth position number at that time.

7.8 shows the remarkable precision of the CART algorithm. The green tracked position is shown going through each truth position marked in black with an imperceivable difference. The individual range measurements are also so incredibly closely clustered that they cannot be seen in the image. The angle track seen in Figure 7.9 does not perform as well, but is still remarkably accurate. The track appears to drift farther from the true angle in between the truth locations where the wand is moved swiftly as we do not model movement in the receiver position calculations.

We plot the CDFs of the errors at each survey point in Figure 7.10 with one side showing all the CDFs on a single plot and the other side showing the image of the CDFs, limiting the errors in both cases to 2 meters. These errors show that submeter accurate estimates are possible even with the poor geometry and heavy multipath of this application. Measurements from all 15 survey points were able

Figure 7.9: Shows angle estimates, Kalman Filter angle track result, and true angle for the wand homing device test. The numbers are the surveyed truth position number at that time.

to produce estimates with less than 0.5 meters error all of the time in this experiment.

Figure 7.11 shows the RMS error at each survey point along with a 1 meter targeted error limit indicator. Consistent with previous experimentation, we are able to produce incredibly accurate estimates of the transmitter position, even from the hallway outside the laboratory where we encounter blocked direct path conditions. The maximum RMS error is at survey point 10, which is about 0.4 meters. The minimum error is on the order of 0.05 meters at survey point 13, near to the transmitter position. The RMS errors in the hallway are on the order of 0.2 meters, similar to what we had with stationary experimentation using 3 pairs presented in Section 6.1.

If we have an estimate of the range and angle to the transmitter, we can calculate the wand center position using simple geometry. We plot the raw estimates of the wand position based on the transmitter

(a) CDFs on single plot

(b) CDFs as an image
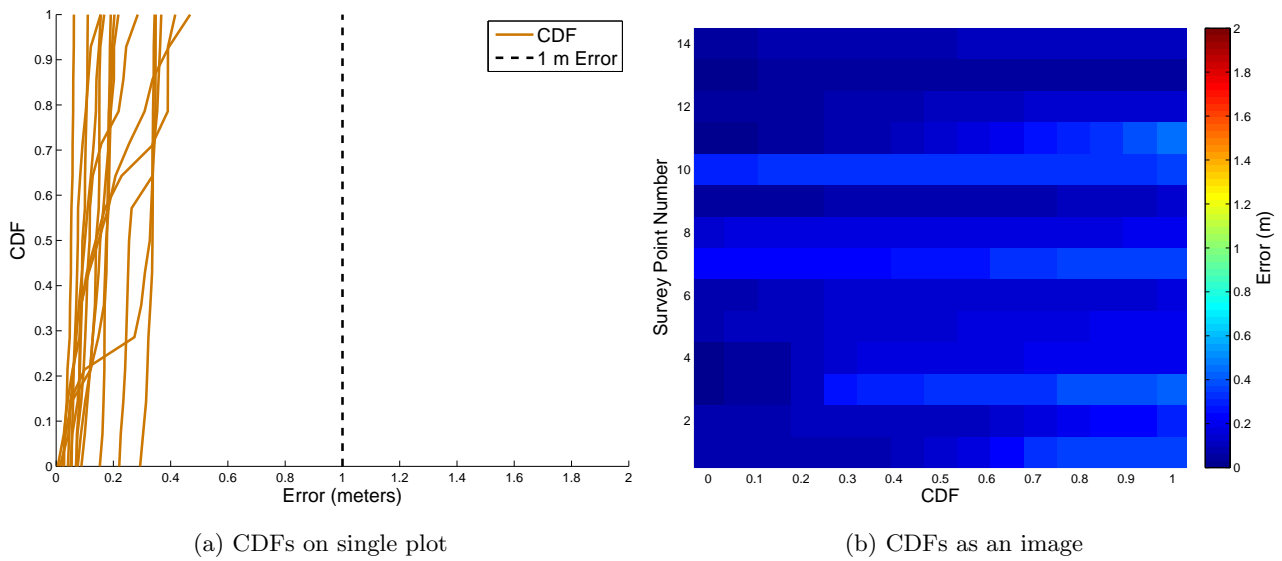
Figure 7.10: Shows the CDF of the error at each survey point from 1 to 15 (a) using single plot and (b) using an image
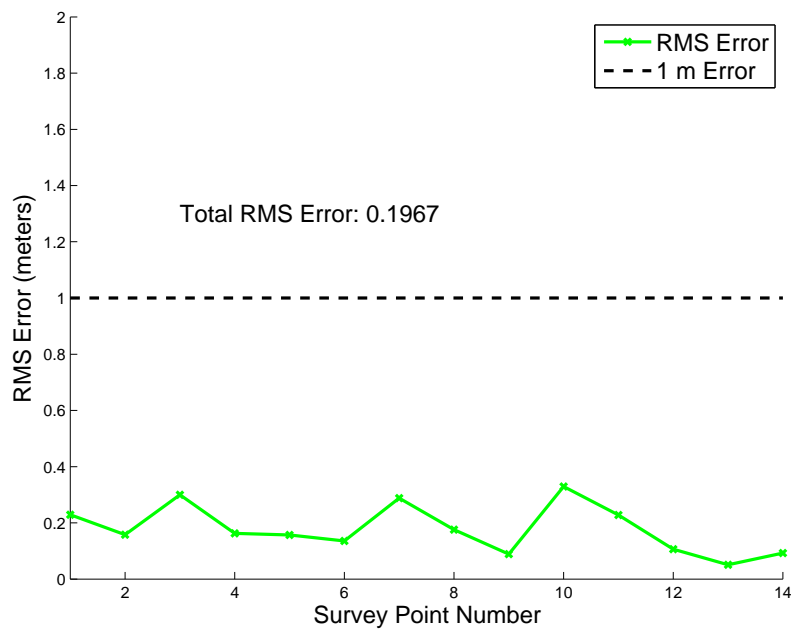

Figure 7.11: Shows the transmitter position estimate RMS errors for all survey points 1 to 15

position estimate in Figure 7.12 for all 15 survey points where the wand was rotated. In addition, we also plot the error vectors associated with the wand position estimates at each survey location. These raw errors again show a robust set of position estimates in this highly multipath indoor environment.
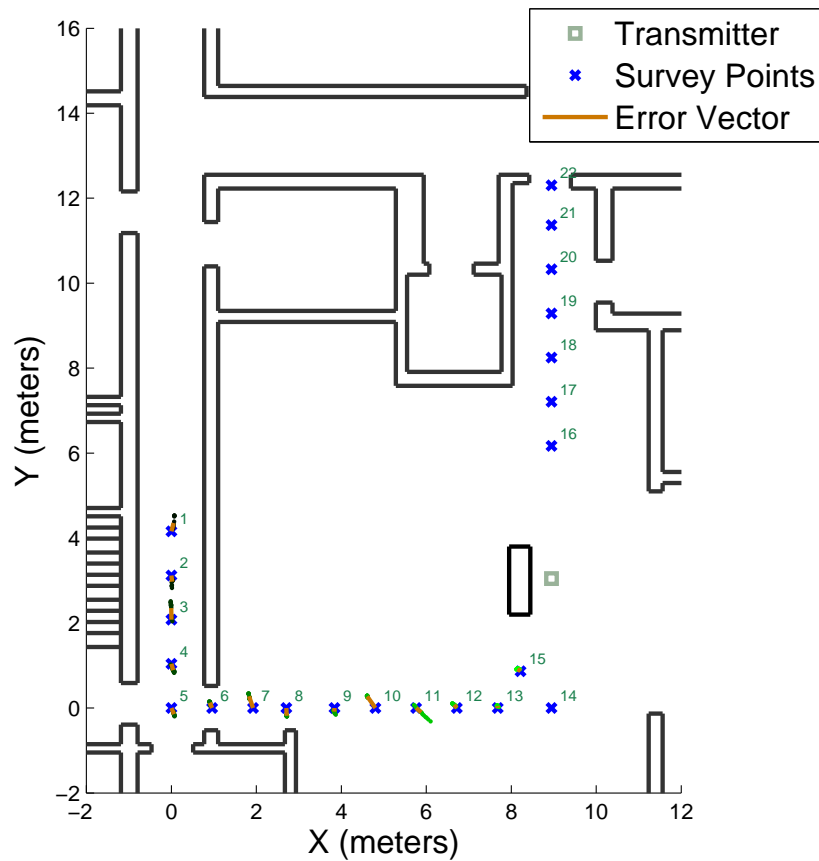
Figure 7.12: Shows the raw estimates of the wand center position along with an error vector at each survey point from 1 to 15

The fire fighter homing device application suffers from a difficult geometry, which usually would result in poorer estimates of transmitter position. By fusing multiple RF measurements as the wand is rotated, we are able to increase the performance to an acceptable level of less than 1 meter error. As long as a direct path exists with sufficient SNR in the captured RF scan data and a reasonable estimate of receiver positions exist, we can produce an accurate estimate that is largely immune to the multipath. In this chapter, we have shown by application the ability of the CART algorithm to produce robust and accurate estimates in a high multipath indoor environment.

Chapter 8

Summary and Conclusions

This dissertation introduces a new algorithm for indoor localization using an Ultra-Wideband (UWB) Impulse Radio (IR) waveform. The existing Singular value Array Reconciliation Tomography (SART) and Transactional Array Reconciliation Tomography (TART) algorithms developed at Worcester Polytechnic Institute (WPI) were designed for a multi-carrier wideband non-impulsive signal and were not designed to take advantage of UWB IR waveform features. In fact, the UWB IR waveform is detrimental to the SART and TART algorithm performance in the presence of heavy multipath when compared to the traditional two step Leading Edge Detection (LED) method that literature describes for UWB IR. The problem with the traditional two step LED method is that it presents an inconsistent set of constraints to the position solver due to range estimation errors, resulting in decreased performance. In addition, the traditional two step LED method does not take advantage of a coherent integration gain of the direct path signal that is possible when properly combining the ensemble of data from all receivers. We recognized the need for a new approach that takes advantage of the UWB IR features in heavy multipath that overcome the limitations of the traditional two step LED method.

A new approach introduced in this dissertation called Coherent Array Reconciliation Tomography (CART) is developed for the UWB IR waveform in which only consistent solutions are searched. The CART algorithm was designed based on the segmentation of the received signals into two segments: one that should contain the leading edge of the received signals embedded in noise and one that should contain noise only. The CART algorithm produces a simultaneous leading edge and position estimate based upon a search of consistent ranges to produce the simultaneous best estimate using signal fusion. The computation is performed in a greedy manner typically using a single independent data capture

from each receiver using a combination of three submetrics based upon the two segments: the similarity submetric, the SVD based submetric, and the power based submetric. Each submetric was incorporated to improve the performance and robustness of the algorithm in both a simulated environment and under experimental conditions.

Simulation using the IEEE 802.15.4a CM4 indoor multipath model suggests that the CART algorithm is nearly statistically efficient in that it closely follows the Cramer Rao Lower Bound (CRLB) and outperforms the traditional two step LED method commonly used in literature. In addition, it was demonstrated that under conditions of heavy multipath in which the existing SART and TART algorithms both fail, the CART algorithm continues to provide robust solutions. In fact, the CART algorithm continues to follow the CRLB until the Signal to Noise Ratio (SNR) degrades to about -12 dB, at which point it has comparable performance to the two step LED method, and 15 dB better performance than the SART algorithm and 20 dB better performance than the TART algorithm as measured by the Mean Squared Error (MSE). In the simulated case of 10 dB SNR, the CART algorithm produces errors with a MSE of 20 dB smaller than the two step LED.

Experimental data was collected using an off the shelf PulseOn 410 (P410) device developed by TimeDomain in order to validate the CART algorithm and compare it's performance to the SART, TART, and two step LED by experimentation in two indoor environments. The P410 devices have a RF waveform that is approximately 2 GHz wide centered at 4 GHz and transmits -15 dBm of power. Several operating modes including ranging and communications are achieved by transmitting a series of narrow pulses at a repetition rate of approximately 10.1 MHz using time and phase coded pulses. This dissertation introduced a way to synchronize the two P410 devices in order to preserve TOA information, resulting in a synchronized transmitter/receiver pair. The synchronization method introduced preserves the TOA information by estimating the sample that corresponds to the responder transmit time in the requester raw data. The estimate of the transmit time is only dependent on a single robust correlation estimate between the requester and responder raw channel data from a single two way transaction. The results show remarkable precision is possible with Root Mean Squared (RMS) errors on the order of 0.10 meters for the CART algorithm despite poor receiver placement geometry compared to more than a 3 meter error for two step LED, SART and TART algorithms. In the first test (Section 6.1), the localization performance of the CART algorithm is about 30 times better than existing methods. Specifically, the two step LED algorithm produced a position estimate with a RMS error of 3.00 meters, the SART algorithm produced a 7.35 meter error, the TART algorithm produced a 8.89 meter error, and the CART algorithm produced a 0.10 meter error. In the second

test (Section 6.2), the localization performance of the CART algorithm is about 9 times better than existing methods. In the second test, the two step LED algorithm produced a position estimate with a RMS error of 2.16 meters, the SART algorithm produced a 3.79 meter error, the TART algorithm produced a 2.81 meter error, and the CART algorithm produced a 0.24 meter error.

We also compared the performance of the CART algorithm to the performance of the Inverse Synthetic Array Reconciliation Tomography (ISART) algorithm in the same harsh multipath environment of the AK317A computer laboratory. It was shown that using just a single independent data capture at each of the 6 receivers with the CART algorithm outperforms the ISART algorithm by a factor of greater than 4 times. The ISART algorithm used 32 independent data captures at each of the 12 receivers that have been compensated for motion using an Inertial Measurement Unit (IMU) based solution, which produced a position estimate with RMS error of 1.02 meters. The CART algorithm produced a position estimate with RMS error of 0.25 meters. The 32 independent data captures at each of the 12 receivers represent an aperture size of 384 antennas for the ISART algorithm as compared to the aperture size of 6 antennas for the CART algorithm. This again shows the superiority of the CART algorithm compared to existing methods.

After successful experimentation using stationary transmitter and receiver positions, the CART algorithm was applied to the problem of the fire fighter homing device. The fire fighter homing device is an indoor localization device that contains a single transmitter affixed to a first responder and two receivers attached to a small wand. We use a single P410 device to capture the RF waveform at the two receiver locations attached to the ends of the wand device and a single axis gyroscope to measure the rotation of the wand. The gyroscope data is used to estimate the antenna positions at the same time the P410 measured the received waveform. A polar form of the CART algorithm was then used to determine the estimates of the range and angle from the gyroscope (origin) to the transmitter. It was demonstrated that submeter accuracy on the order of 0.2 meters can be achieved under an indoor test scenario, which is consistent with the previous simulations and stationary experimentation carried out earlier.

Historically, fire fighters have expressed concern about the size of the wand due to the confined spaces frequently encountered in search and rescue operations. Thus, we have also shown by Cramer Rao Lower Bound (CRLB) analysis, that for every time we half the length of the wand, we lose 6 dB of performance from the MSE of the Cartesian position estimate. Assuming a 10 dB SNR for the received signal and if we are able to rotate the wand 90 degrees in a stationary position, we can use a wand length of approximately 0.5 meters to achieve a submeter position estimate at a 20 meter range.

The wand homing device innovation also overcame several technical issues associated with the commercialization of a wand homing device. We demonstrated dynamic synchronization of data from a moving wand using gyroscopic measurements. We also demonstrate high precision location solutions with extraordinarily limited sensor geometry. In addition, we apply Kalman Filtering to tie outcomes together over full duration to achieve robust estimation in a highly dynamic multipath environment. Even though we only demonstrate an implementation that finds 2 dimensional results using a single axis gyroscope, a final commercial product could be realized using our methods to obtain a full three dimensional motion solution derived from 3 accelerometer measurements as well as 3 gyroscopic measurements. Examples of such three dimensional motion models using Kalman Filters can be found in [26], [39], [40].

In addition to a full 3 dimensional solution, another potential future improvement to the wand homing device application is the addition of other transmitters into the operational scenario. We recall that the performance of the range track seen in Figure 7.8 is superior to the angle track due to the limited sensor geometry. Even a single transmitter positioned outside of the building in addition to the one the fire fighter wears while entering a burning building can be used to improve the localization performance of both transmitters. The placement of the additional transmitter outside will also provide the wand operator additional directional awareness when they wish to exit the building. In this operational scenario, the wand operator would first use the wand to find the fire fighter's transmitter inside the burning building and then find the transmitter outside to exit the building with the recovered fire fighter.

The currently implemented wand homing device operates at approximately a 10 Hz RF data capture rate, which limits the speed at which the operator can move as well as the accuracy of the localization solution. This limitation is due to the current P410 firmware, which limits the baud rate to 115200. A new firmware is available from TimeDomain that allows selectable baud rates up to 921600, which would enable increased performance. The new datasheet, however, suggests instability may result from increased baud rates and that 230400 has been the only stable baud rate as reported by one customer.

Another limitation of UWB technology in practice is the limited power available due to Federal Communication Commission (FCC) limitations. In the 3 - 5 GHz range in which these experiments were performed, we can only transmit a maximum of -15 dBm spread over our entire 2 GHz in order to prevent interference to primary users in that band. This power places a limit on the operating range of the wand homing device on the order of tens of meters in an indoor environment. In the future, we can explore using a multi-band approach whereby a narrow band signal in the Industrial, Scientific,

and Medical (ISM) radio frequency band is synchronized to the UWB waveform in order to ensure a detection, coarse synchronization, and perhaps a coarse range and angle estimate. Once the operator gets close enough to the transmitter, UWB can be used for precision localization. It may also be worth exploring the integration of the UWB received signal over a long period of time using the coarse synchronization provided by the narrow band solution to achieve a useful position solution. The other alternative to increase the operating range is to pursue permission from FCC to operate with higher power in case of an emergency.

In addition to these future enhancements to the wand homing device, the CART algorithm could be improved by introducing excess delay into the model in order to account for the various building materials and environments. This is likely to be unnecessary due to the limited geometry of the wand application, but is worthy of consideration if additional precision is desired under difficult long distance scenarios where the RF waveform propagates through many walls.

This dissertation contributes to the field of indoor localization using an UWB IR waveform by presenting a robust and near optimal localization algorithm. The wand homing device is just one example application where we can apply precision localization using the CART algorithm. We invite the reader to explore other applications and improvements in order to positively influence our lives.

Appendix A

Embedded Device Hardware Details

As seen in Figure A.1, the transmitter hardware consists of a single battery operated P410 unit and a FPGA based soft core host embedded processor attached by USB. A single antenna port is used with the standard antenna supplied with the evaluation kit. An Arduino USB Shield kit hosts the USB interface chip and enables connection between the DE0-Nano board and the P410 through the USB 2.0 interface. Initially, the connection was implemented through the P410 3.3V serial interface, but in order to test higher serial baud rates the connection was moved to the USB interface. Unfortunately, 115200 baud is the only baud rate that works on this P410 unit through either the 3.3V serial or USB interface.
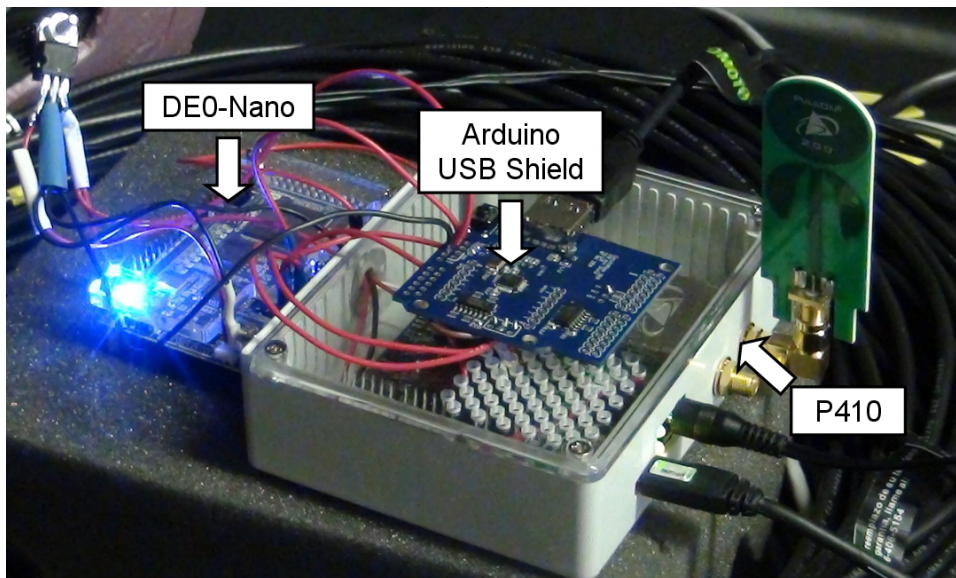
Figure A.1: Transmitter Hardware

Figure A.2 shows a simplified block diagram. A single 8.4V Lithium Ion battery is used to power the P410 unit and the Linear Technology regulators are used to produce the required 5V for the DE0-Nano FPGA evaluation kit and the Arduino USB Shield. The DE0-Nano FPGA evaluation kit and P410 boards both contain internal regulators for proper operation. The USB Shield also requires 3.3V, which is taken from the DE0-Nano board. There is a standard 4-wire SPI interface that operates at 10 MHz that acts as the interface between the DE0-Nano board and the USB Shield. The DE0-Nano board contains an Altera Cyclone IV EP4CE22F17C6N FPGA with a NIOS soft core processor that has at 100 MHz clock. The USB Shield contains a MAX3421 USB interface chip that maintains the USB bus protocol requirements, making the driver development for the NIOS processor more manageable.

Figure A.3 shows the wiring table for the USB Shield. The 4 wires of the SPI interface are connected through the DE0-Nano 40 pin header J2 to the Cyclone IV FPGA. The SPI_RST reset pin is always tied to 3.3V to disable any hard resetting since a similar reset can be achieved through the SPI interface. The 3.3V for the USB Shield board also comes from the DE0-Nano 40 pin header J2 as shown. The 5V supply and ground come from the regulator as shown in the previous block diagram in Figure A.2.

The Arduino USB Shield kit comes with a C++ driver for the Arduino board that was used as the basis for the NIOS driver. It was heavily modified to be C compatible with the NIOS Eclipse compiler. The result was that only a single USB device address is allowed on the bus at one time, but the basic USB commands from the driver work.

The boot process for the NIOS processor starts by setting the DE0-Nano evaluation kit LEDs to an alternating pattern followed by a delay of 5 seconds. This allows the P410 unit to fully initialize prior to the NIOS processor attempting to access the P410. The next step is to initialize the MAX3421 by writing 0x10 (FDUPSPI) to address 17 (PINCTL) to ensure 4-wire SPI communication is being used. By default, the MAX3421 operates in 3-wire SPI, which uses a single wire for data in and data out instead of separate wires. The register information for the MAX3421 can be found in the programming guide [41]. Then, we need to reset the MAX3421 chip to ensure we always start in a known state. This is done by writing 0x00 to address 15 (USBCTL), waiting a bit, re-enabling 4-wire SPI as before, and waiting until the MAX3421 indicates the PLL is stable by asserting bit 1 (OSCOKIRQ) of address 13 (USBIRQ). We then clear the PLL stable interrupt and the frame interrupt by writing a 0x41 (VBUSIRQ and OSCOKIRQ) to address 13 (USBIRQ). Out of extra caution, we also add a delay of 1 second to ensure the MAX3421 is ready. Now that the reset is complete, we can set the USB shield into USB HOST mode to allow the NIOS processor to control the P410 device. This is done by writing a 0x01 (HOST) to address 27 (MODE) in the MAX3421.
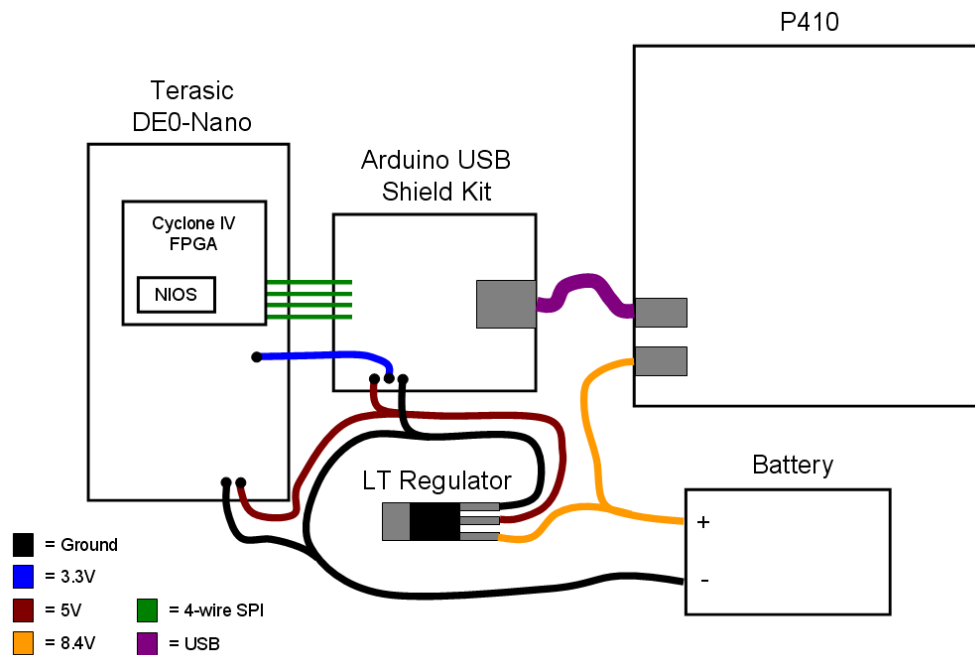
Figure A.2: Mobile P410 Block Diagram

Description	FPGA Pin	DE0-Nano Pin	USB Shield Pin
SPI_SS	M10	J2 Pin 35	SS
SPI_SCLK	L13	J2 Pin 36	SCK
SPI_MOSI	J16	J2 Pin 37	MOSI
SPI_MISO	K15	J2 Pin 38	MISO
SPI_RST			3.3V
3.3V		J2 Pin 29	3.3V

Figure A.3: Pin Locations

Once the reset is complete a USB bus reset is initiated. This is done by writing a 0x01 (BUSRST) to address 29 (HCTL) and waiting until bit 1 (BUSEVENTIRQ) of address 25 (HIRQ) asserted. Once bit 1 (BUSEVENTIRQ) of address 25 (HIRQ) is asserted, we can reset the interrupt by writing a 0x01 (BUSEVENTIRQ) to address 25 (HIRQ). We also need to enable the automatic generation of Start of Frame (SOF) packets in Full Speed USB by writing a 0x09 (SOFKAENAB and HOST) to address 27 (MODE) and waiting for bit 7 (FRAMEIRQ) of address 25 (HIRQ) to be asserted. Once the bit is asserted, we write 0x40 (FRAMEIRQ) to address 25 (HIRQ) to clear the interrupt.

After the USB bus has been reset, we are able to begin communication with the P410 USB device. The first order of business on any USB host to device communication is to get the USB device descriptor. This is done by instructing the MAX3421 to send a USB control request on address 0 endpoint 0 (all USB devices must respond to these commands) requesting 18 bytes of the P410 USB device descriptor. Since we requested data from the USB device, we must initiate 8 byte bulk-in transfers through the MAX3421. This is done by writing 0x00 address 30 (HXFER), waiting for the transfer interrupt to complete, and read the data out of the receive fifo. Only 8 bits at a time can be transferred so this process needs to be repeated until all 18 bytes are received. For more information on the USB protocol, see [42] and [43]. The device descriptor tells us information about the USB device including the vendor, device class, and number of configurations. Table A.1 shows the Device Descriptor for the P410 Unit. Typically, a USB device will only have a single configuration since Windows drivers only support one configuration. The manufacture string is set to "Time Domain", the product string is set to "P400 Radio", and the serial number string of this device is set to "102". The next step is to set the device address for communication. This is done by sending another control request to address 0 endpoint 0 requesting the address to be set to 1. Once the communication address is set, we can get the configuration descriptor by sending a control request requesting 9 configuration descriptor bytes to address 1 endpoint 0. Again, we need to read the 9 bytes repeating the bulk-in transfer request done before. The configuration descriptor tells us the configuration value, max packet size, and configuration type that we need for proper communication to the P410 device. Table A.2 shows us the configuration descriptor of the P410 device. Once we have the configuration value, we can set it by sending a set configuration control request to address 1 endpoint 0. The P410 USB device is now ready for communication.

To increase the bandwidth over the USB interface, it is desirable to increase the baud rate between the NIOS processor and the P410 device. The P410 device is configured as a Communications Device class and claims to have a baud rate control through communication device class commands. After sending control requests to address 1 endpoint 0 to set the baud to 921600 and reading back the configured baud, it appears that the commands have no effect. The P410 device always reports a baud rate of 115200 baud.

Now that the USB interface is configured, we are ready to control the P410 device. Control of the P410 is achieved through a set of messages defined in the P410 API documentation [32]. The first message sent to the P410 is the RCM_SET_SLEEPMODE_REQUEST intended to ensure the device is in the active state. The next message sent is the RCM_SET_OPMODE_REQUEST to enable RCM mode,

bLength	18
bDescriptorType	0x01
bcdUSB	0x200
bDeviceClass	0x02
bDeviceSubClass	0x00
bDeviceProtocol	0x00
bMaxPacketSize0	0x08
idVendor	0x3700
idProduct	0x300
bcdDevice	0x00
iManufacturer	0x01
iProduct	0x02
iSerialNumber	0x03
bNumConfigurations	0x01

Table A.1: P410 Device Descriptor

bLength	9
bDescriptorType	0x02
wTotalLength	0x43
bNumInterfaces	0x02
bConfigurationValue	0x01
iConfiguration	0x00
bmAttributes	0xC0
bMaxPower	0x32

Table A.2: P410 Configuration Descriptor

which puts the P410 into two way time of flight ranging mode. Once the P410 is configured in RCM mode, we can get the current configuration using RCM_GET_CONFIG_REQUEST. The configuration tells us how the ranging mode is currently configured, including the transmit gain of the transmit RF channel, which messages will be passed to the host processor if available (what type of scan info, etc..), which antenna is being used, the integration index which defines how many samples will be averaged in the scan data, and things of that nature. For our purposes, we want to ensure the transmit gain is set to the maximum (a value of 44), the flags are set to (0x13) to get RCM_FULL_SCAN_INFO packets and not get Coarse Range Estimate (CRE) packets, channel code set to 0, antenna mode set to antenna A (0), integration index of 5, and the electrical delays set to 0. Once we read the contents of the configuration, we can modify these parameters and use RCM_SET_CONFIG_REQUEST to set the P410 in the proper configuration.

Once the P410 is fully configured, the NIOS processor waits in an infinite loop waiting for packets. Packets are produced when the receiver device (requester) connected to a laptop initiates a range request to the mobile P410 device. When a range request is initiated, a RCM_FULL_SCAN_INFO packet is generated and captured by the NIOS processor. When the NIOS processor receives this message, it prepares the scan data and submits the modified scan data as the next response data packet using the RCM_SET_RESPONSE_DATA_REQUEST (0x0005) message. Due to P410 hardware limitations, the data package can only be 1024 bytes long whereas the full scan data is 1623 32-bit words long. In addition, we need to send the mobile unit's leading edge, lockspot, time stamp, and vPeak (max value) to the wand device. The embedded host performs a simple Automatic Gain Control (AGC) function to reduce the number of bits per scan data sample from 32 to 8. Each sample in the scan data is shifted right by the minimum amount required to achieve 8 bits of data resolution. This compression method is sufficient since we are guaranteed to have sufficient Signal to Noise Ratio (SNR) if a meaningful lockspot was achieved by the mobile P410 unit. This compression maintains the maximum signal power and reduces the dynamic range from the bottom.

Since the responder scan data is used only for the purpose of estimating $\hat{n}_\Delta$, the sample difference between the requester unit and the responder unit, we must verify the compression method chosen will not have a detrimental impact on the estimate. The Figure A.4a shows the full scale requester and responder scan data from a single range request measurement. After compression, each sample is forced into an 8 bit value as seen in Figure A.4b.

If we compute the cross correlation as described by equation (5.8) for both the original waveform and the compressed waveform, we see in Figure A.5 there is virtually no distinguishable difference. Many

(a) Scan data

(b) Compressed responder scan data
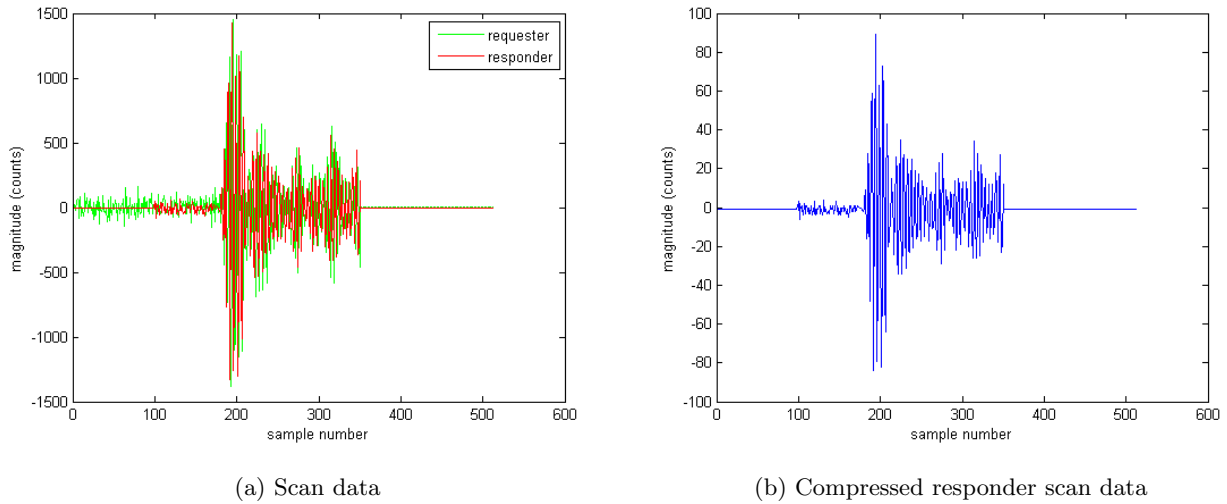
Figure A.4: Shows (a) requester and responder scan data and (b) compressed responder scan data

such cases were tested to validate this compression method and further error analysis was deemed unnecessary.
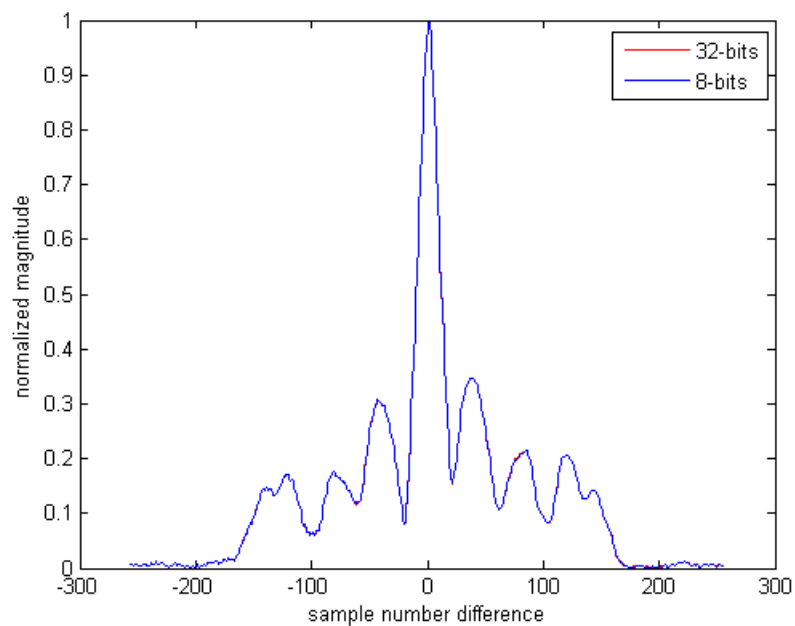
Figure A.5: Cross correlation of requester data with original responder data and compressed responder data

The full data packet sent from the responder to the requester for the purpose of alignment is as

follows: lockspot (32-bits), ledIndex (32-bits), time stamp (32-bits), antenna ID (8-bits), operational mode (8-bits), vPeak (16-bits), compressed scan data (1008 bytes) starting from sample 624 to the end sample at 1632. The ledIndex, antenna ID, operation mode, and vPeak are currently not used. The lockspot and compressed scan data are used for the data alignment of the requester scan data. Other compression methods are possible to reduce the amount of data sent over the data channel, but have not been explored at this time.

This embedded device was used as part of the transmitter unit for both the experimental collection described in Chapter 6 and the wand application discussed in Chapter 7. On the receiver side, a laptop is connected by USB to the requester unit. A custom MATLAB program is used to send range request messages to the transmitter unit, which then responds as described above. The RCM_RANGE_INFO, RCM_FULL_SCAN_INFO, and RCM_DATA_INFO packets are stored into allocated memory on the host computer until the end of the data collection. Once data collection ends, the allocated memory is saved into a file on the hard drive to be processed at a later time. This method of data collection allows us to collect the data as fast as possible without risk of buffer overflows.

(a) Worst case SNR scenario   (b) Signal to Noise Ratio difference
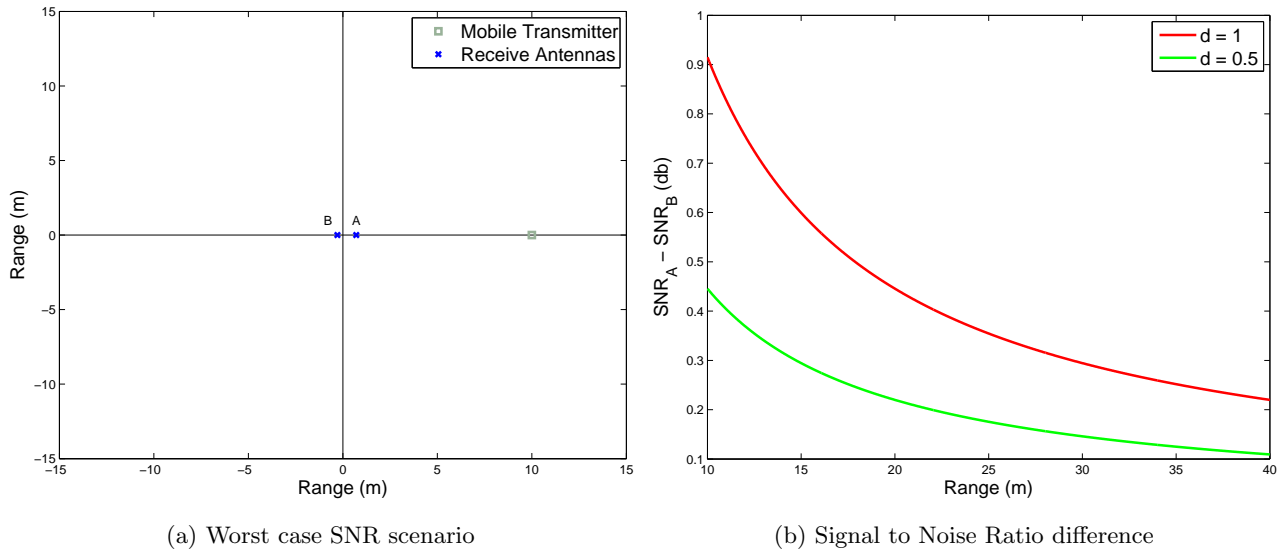
Figure B.1: Shows (a) the worst case geometry and the (b) resulting difference in SNR in Antenna A compared to Antenna B with a transmitter that ranges from 10 to 40 meters

Appendix B

Wand Length Analysis

In this Appendix, we present the results of the theoretical wand length analysis based on the CRLB that was derived in Section 4.2.

During the derivation of the CRLB of the parameters $[x_m \; y_m]^T$, we made an assumption that allowed a simplification which resulted in equation (4.18). The simplification required the SNR in all antennas to be the same. In this section we also keep the same assumption. Prior to proceeding with the wand length analysis, we quickly examine the differences in SNR that may be present in the two antennas with a 1 meter wand length and a 0.5 meter wand length. Figure B.1a shows the geometry

Variable	Value
Wand Angle (θ)	0 Degree
Wand Length (d)	1 meter
Mobile Range (r)	20 meters
Mobile Angle (ϕ)	-30 Degrees
SNR	10 dB

(a) Model Parameters
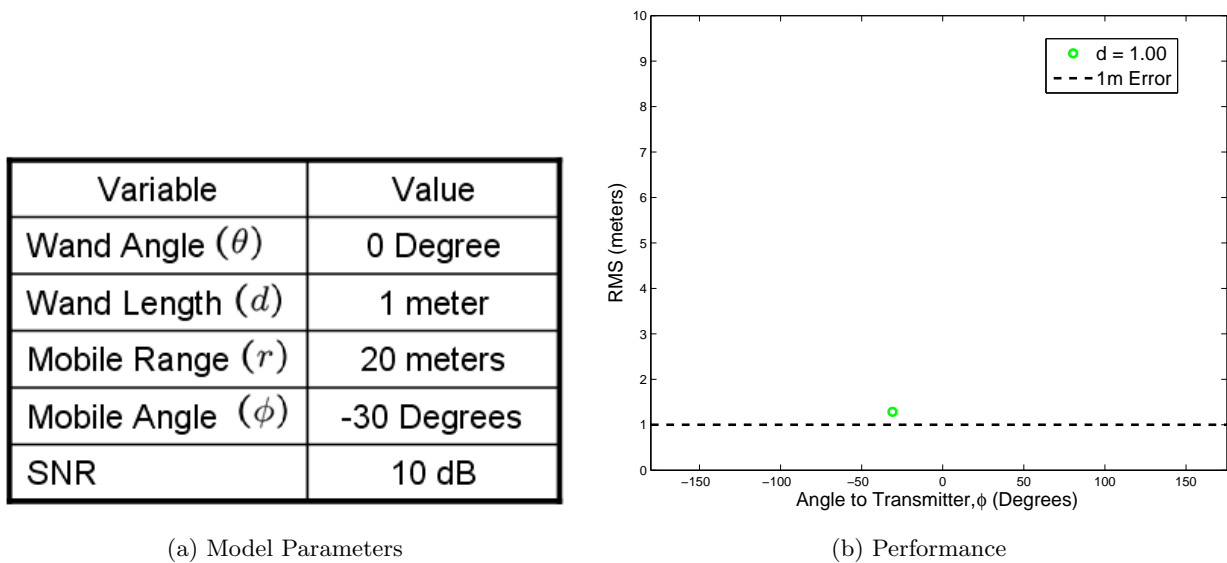
(b) Performance

Figure B.2: Fixed (a) model parameters and resulting (b) performance using CRLB calculation

that results in the worst case difference in SNR between antenna A and antenna B with a 10 meter or greater transmitter range. This is the worst case geometry since the transmitter is the closest possible to one antenna and farthest from the other while still being at least 10 meters from the center of the wand. Figure B.1b shows the resulting SNR difference. The calculation assumes the following parameters: mobile transmit power = -15 dBm, transmit gain = 2 dB, receive gain = 2 dB, frequency = 4 GHz, bandwidth = 2 GHz, noise figure = 0 dB, and range = 10 to 40 meters. In both of these examples, the difference in the SNR is less than 1 dB, with a smaller and smaller difference as the range to the transmitter increases. Our analysis assumes that the transmitter is at a range of 20 meters, which results in a SNR difference of only 0.43 dB for a 1 meter wand. Our assumption of equal SNR for this scenario is therefore considered reasonable for this wand length analysis.

If we assume that the wand angle θ is 0 degrees, the wand length d is 1 meter, the transmitter range r is 20 meters, the SNR is 10 dB, and the transmitter angle relative to antenna A ϕ is -30 degrees as shown in Figure B.2a, we can compute a single CLRB point. In order to conform with the computed CRLB parameters of $[x_m \ y_m]^T$, we convert the polar position of the transmitter to the equivalent Cartesian position. The metric used in this analysis is the RMS position error described by (4.32). The position of antenna A is (0.5, 0) and the position of antenna B is (-0.5, 0), which suggests that the exact center of the wand is the origin. As discussed in the next section, the actual wand prototype has a different distance to antenna A than to antenna B. The resulting CRLB for the simulation point

Variable	Value
Wand Angle (θ)	0 Degree
Wand Length (d)	1 meter
Mobile Range (r)	20 meters
Mobile Angle (ϕ)	variable
SNR	10 dB
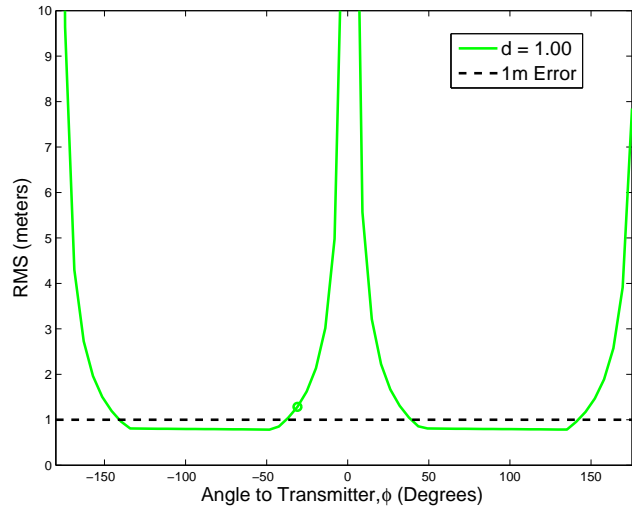
(a) Model Parameters

(b) Performance

Figure B.3: Variable mobile angle ϕ CRLB calculation showing (a) all model parameters and resulting (b) performance

is shown in Figure B.2b, which also shows the desirable 1 meter performance bound. This one point is about 0.25 meters greater than the 1 meter bound desired.

Now, we allow the mobile angle to vary from -180 to 180 degrees. As we move the true position of the transmitter, there are some geometries that result in poor performance with a stationary wand. Figure B.3a shows the model parameters under this variable condition and Figure B.3b shows the resulting CRLB calculated performance as a function of true transmitter angle ϕ relative to the axis defined by antenna A and antenna B. The intersection of two circles at the 0 degree geometry is very difficult and results in a very large RMS error, greater than the 10 meter limit shown. This is precisely the reason that a gyroscope is necessary; in order to improve the geometry and allow a unique position result in 2 dimensions.

We now allow the wand length d to vary from 0.1 to 2 meters, the edges of which are verge of being reasonable. The new parameters are shown in Figure B.4a and the resulting performance is seen in Figure B.4b. The wand length roughly raises or lowers the entire curve depending on the length. A very short wand length of 0.1 meters results in RMS position errors greater than about 8 meters. A very long wand length of 2 meters can have good geometry resulting in less than 1 meter RMS error for many angles. It still, however, suffers from the same poor geometry at 0 degrees for ϕ.

If we change θ, the wand angle, from 0 to 45 degrees, we are finally able to positively influence the

Variable	Value
Wand Angle (θ)	0 Degree
Wand Length (d)	0.1 to 2 m
Mobile Range (r)	20 meters
Mobile Angle (ϕ)	variable
SNR	10 dB
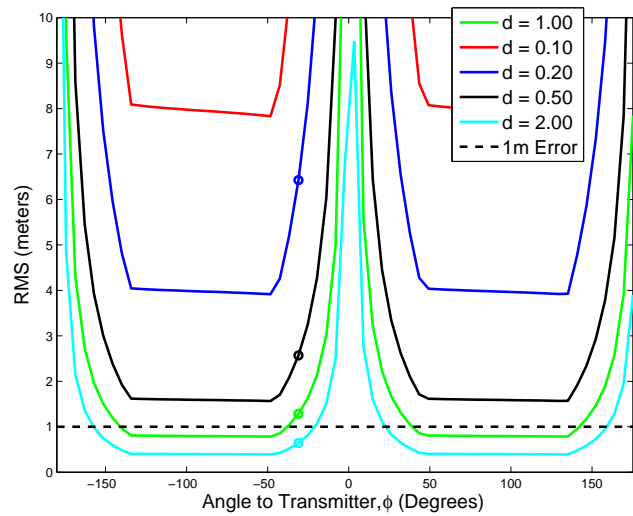
(a) Model Parameters

(b) Performance

Figure B.4: Variable mobile angle ϕ and wand length d CRLB showing (a) all model parameters and resulting (b) performance

Variable	Value
Wand Angle (θ)	45 Degrees
Wand Length (d)	0.1 to 2 m
Mobile Range (r)	20 meters
Mobile Angle (ϕ)	variable
SNR	10 dB
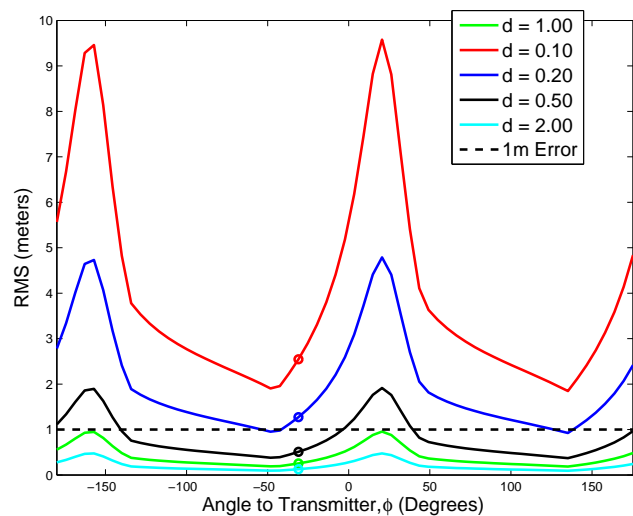
(a) Model Parameters

(b) Performance

Figure B.5: Variable mobile angle ϕ, wand length d, and fusing 45 degrees of wand rotation CRLB calculation showing (a) all model parameters and (b) resulting performance

performance at the 0 degree transmitter angle. The parameters in Figure B.5a and performance in Figure B.5b show the result after fusing measurements from antenna A and antenna B as the wand rotates from 0 to 45 degrees about the center of the wand. A measurement is made every 2 degrees in

(a) $\theta = 90$ Performance
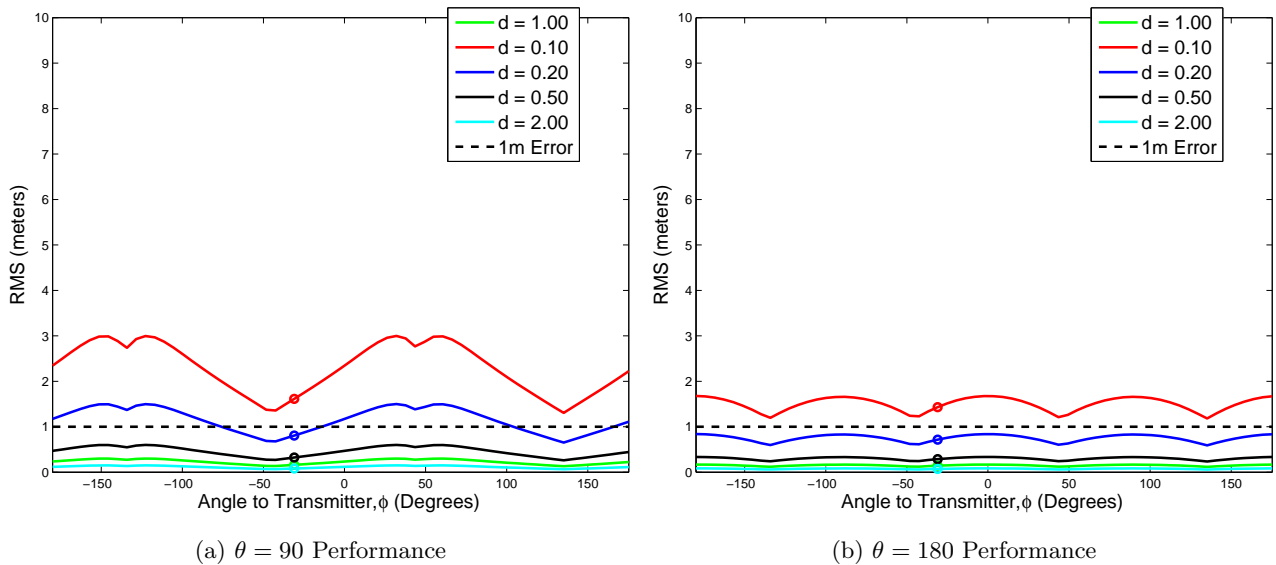
(b) $\theta = 180$ Performance

Figure B.6: Shows performance for variable mobile angle ϕ, wand length d, and fusing (a) 90 degrees of wand rotation or (b) 180 degrees of wand rotation

this simulation in both antennas. We immediately see in Figure B.5b that all angles of ϕ result in an improvement due to the additional information available. The 0.5 meter wand length shown in black results in a 1 meter or better performance for most angles of ϕ, whereas before (without wand rotation) the 0.5 meter wand length never produced an estimate less than 1 meter. The shape of the curve as a function of ϕ is also flatter, with two lower peaks of poor geometry around 35 and -155 degrees.

Additional rotation of the wand and continuing to fuse the measurements taken every 2 degrees results in improved performance. Figure B.6a shows the performance of fusing 90 degrees of wand rotation and Figure B.6b shows when we fuse 180 degrees of wand rotation. The results indicate that better than 1 meter error can be achieved for all angles of ϕ with 90 degrees of wand rotation and a 0.5 meter wand length.

A reasonable rotation of an operator's wrist would be about 90 degrees. Based on this characterization, we recommend a 0.5 meter wand length as the optimal length. This ensures a sufficiently small wand for the fire fighter as well as a wand that can produce a 1 meter accurate estimate regardless of the angle to the transmitter. We also observe a good rule of thumb that there is a 6 dB loss in MSE performance for every time we halve the wand length.

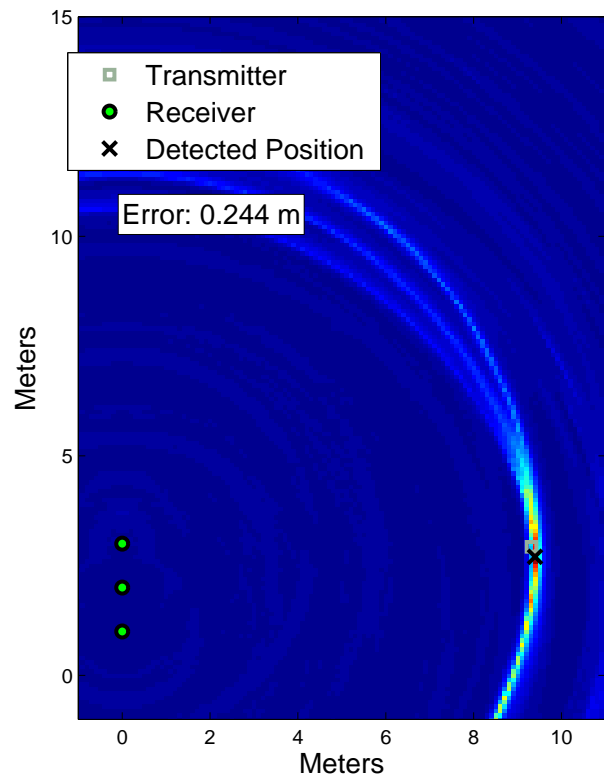**Appendix C**

Additional Location Metric Images for the AK315 Test
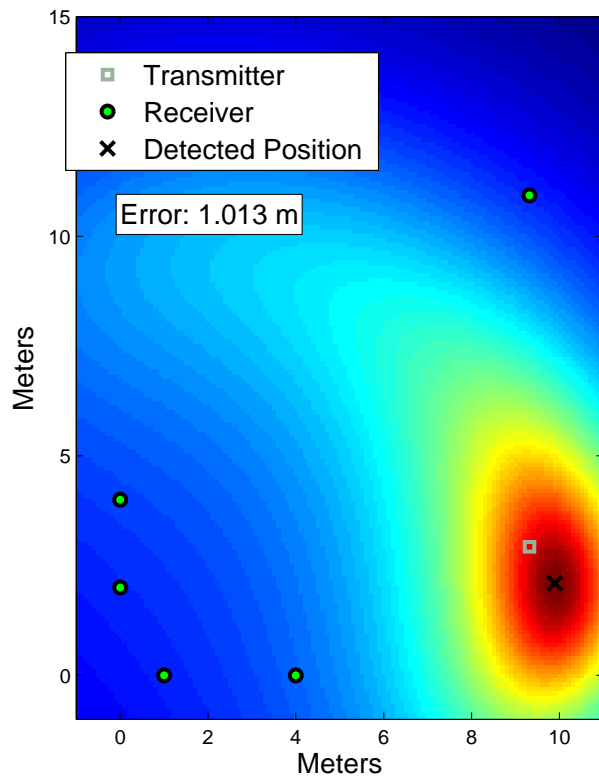
(a) LED
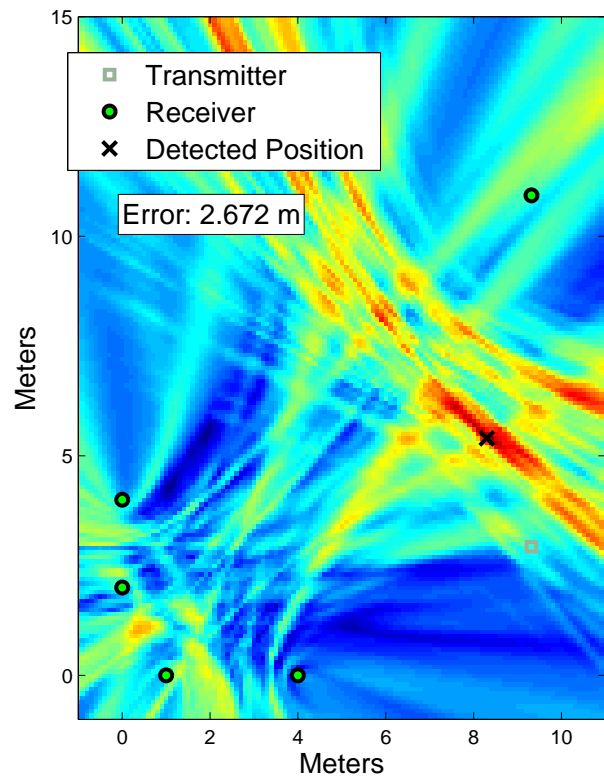
(b) SART
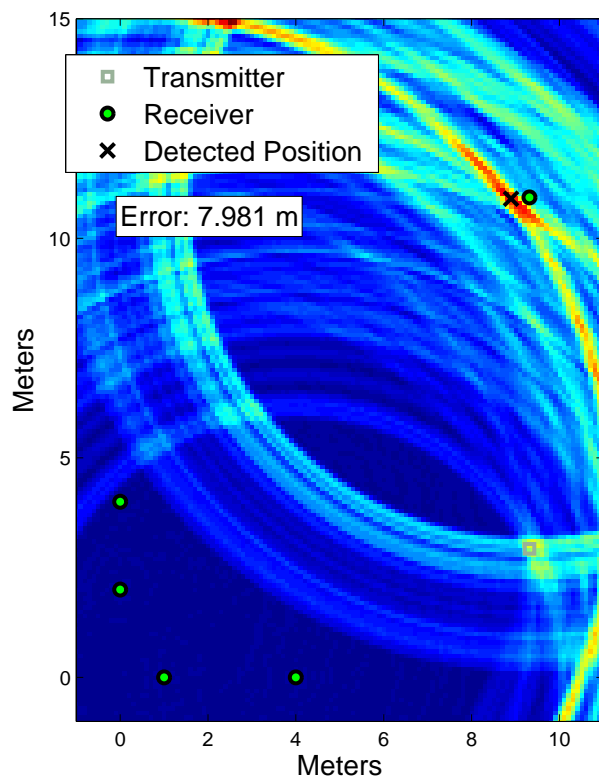
(c) TART
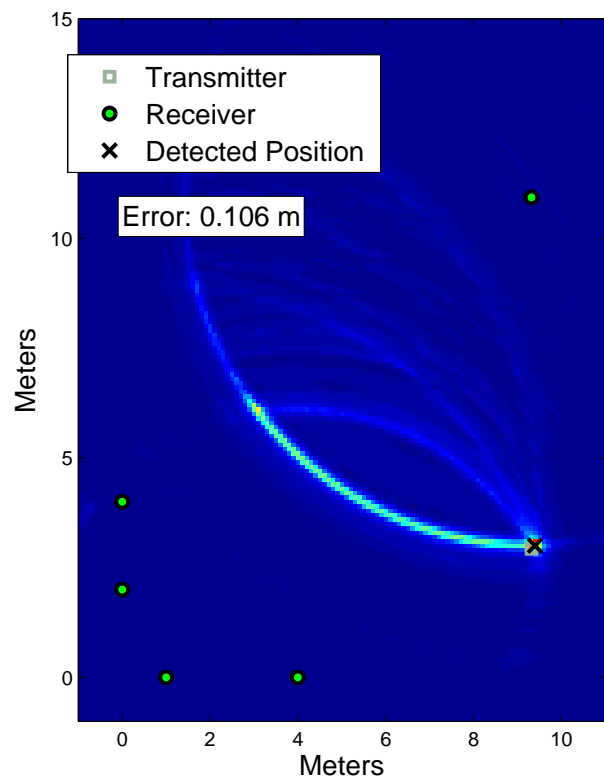
(d) CART

Figure C.1: Atwater Kent 3rd floor metric image examples using data from 5 survey points
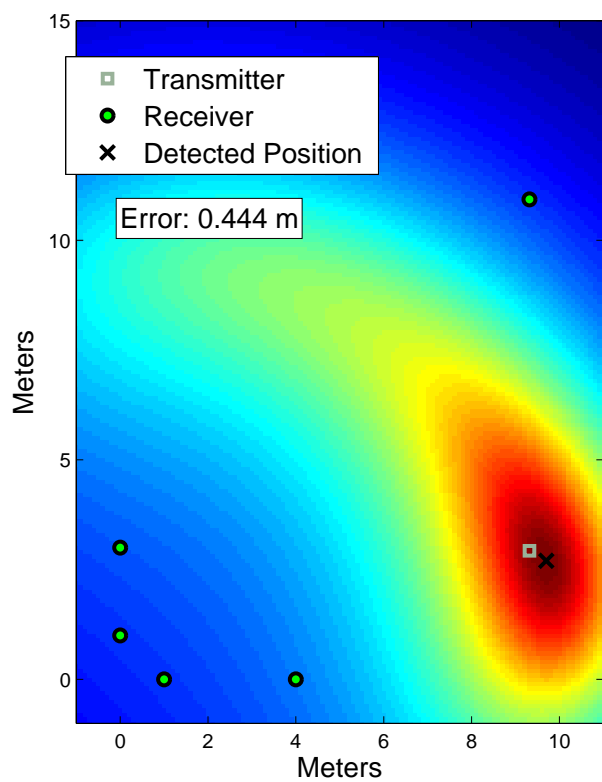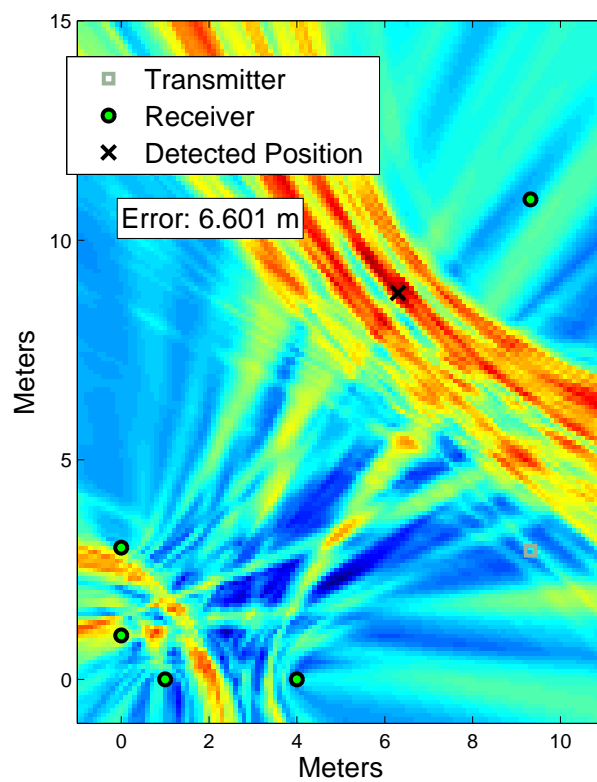
Figure C.2: Atwater Kent 3rd floor metric image examples using data from 5 survey points
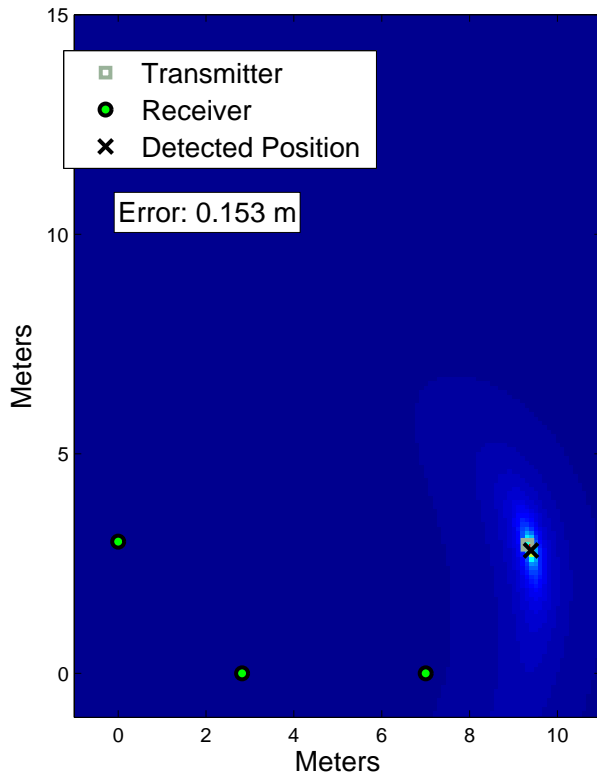
(a) LED
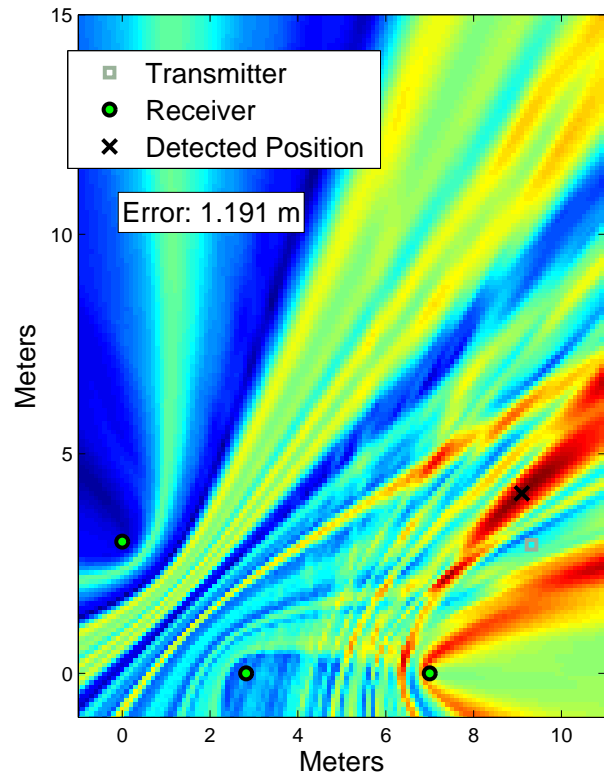
(b) SART
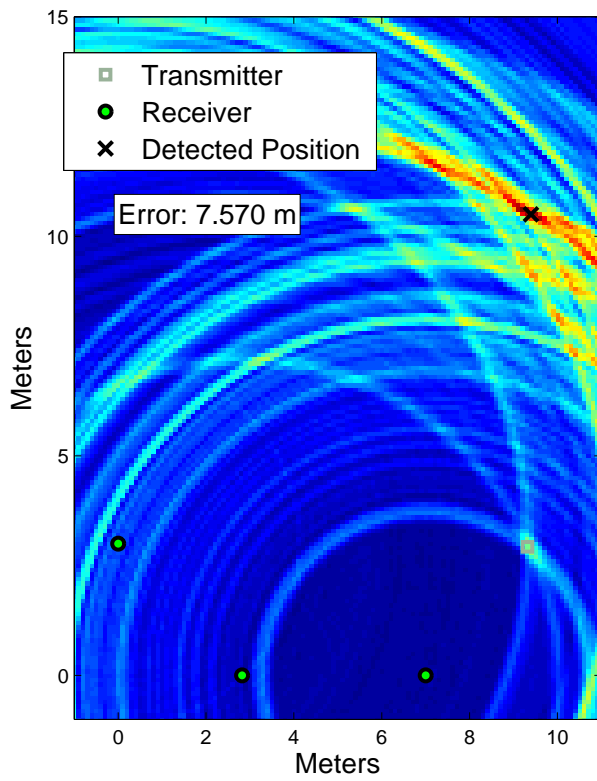
(c) TART
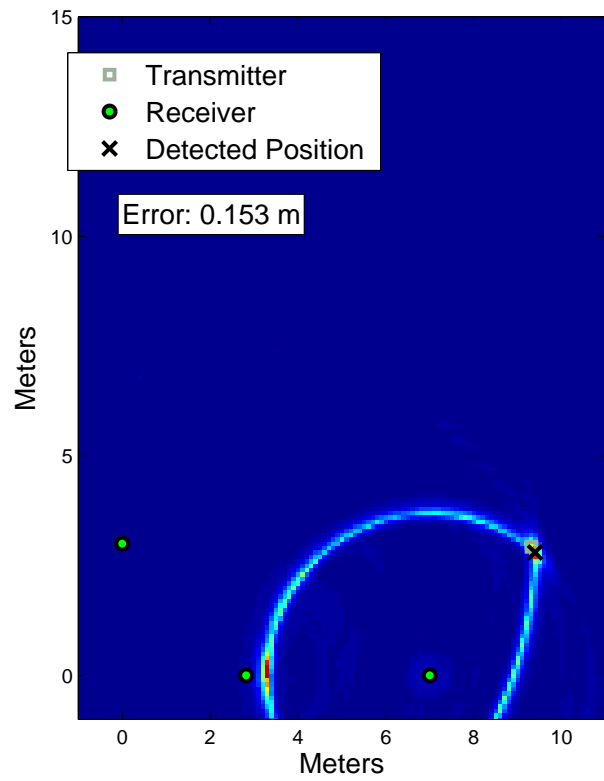
(d) CART

Figure C.3: Atwater Kent 3rd floor metric image examples using data from 3 survey points: 2, 8, 12
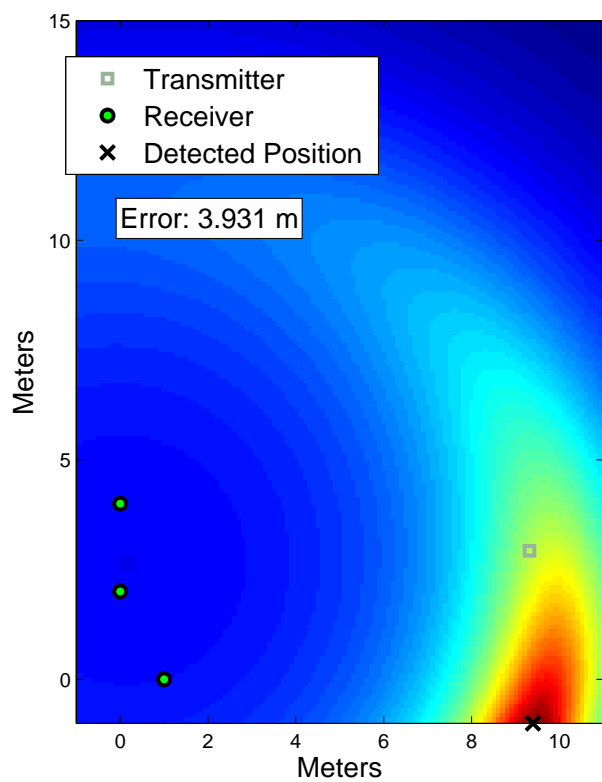
(a) LED
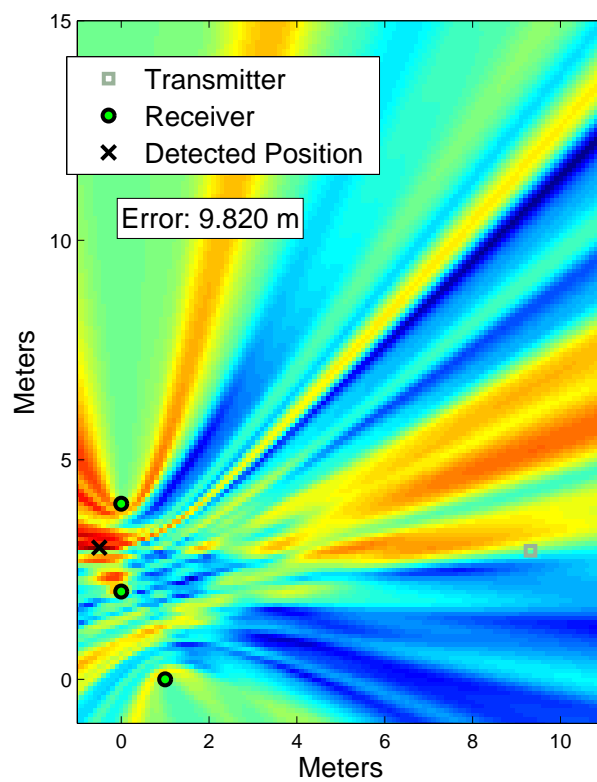
(b) SART
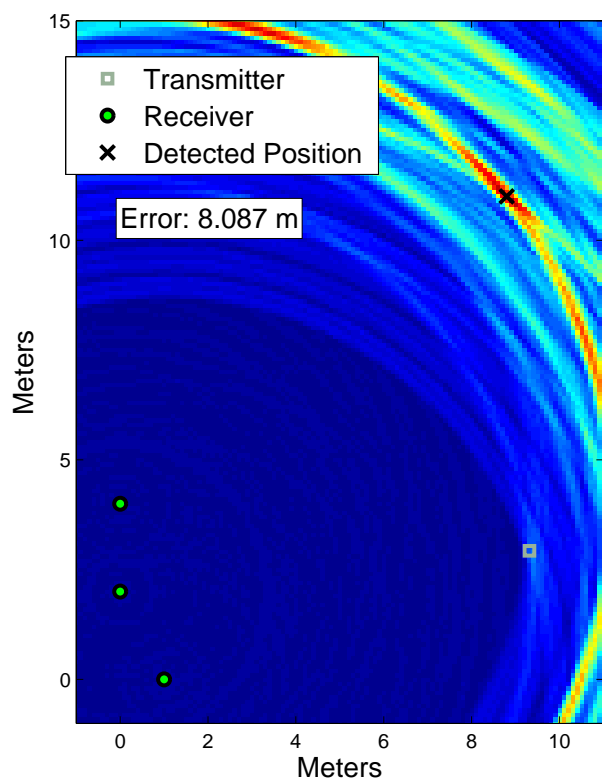
(c) TART
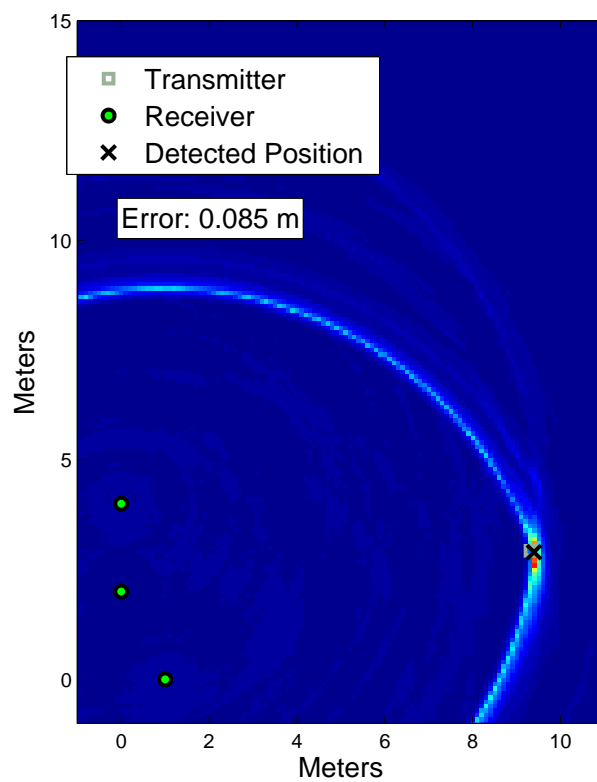
(d) CART

Figure C.4: Atwater Kent 3rd floor metric image examples using data from 3 survey points: 1, 3, 6
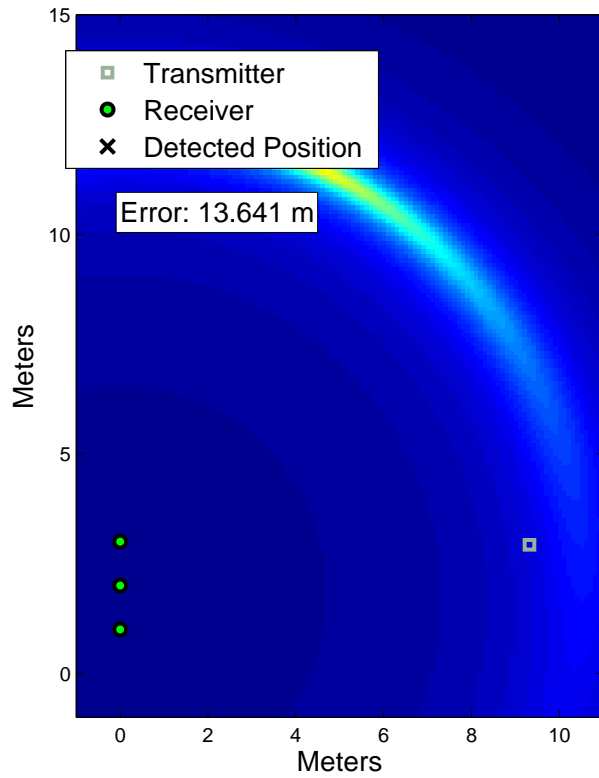
(a) LED
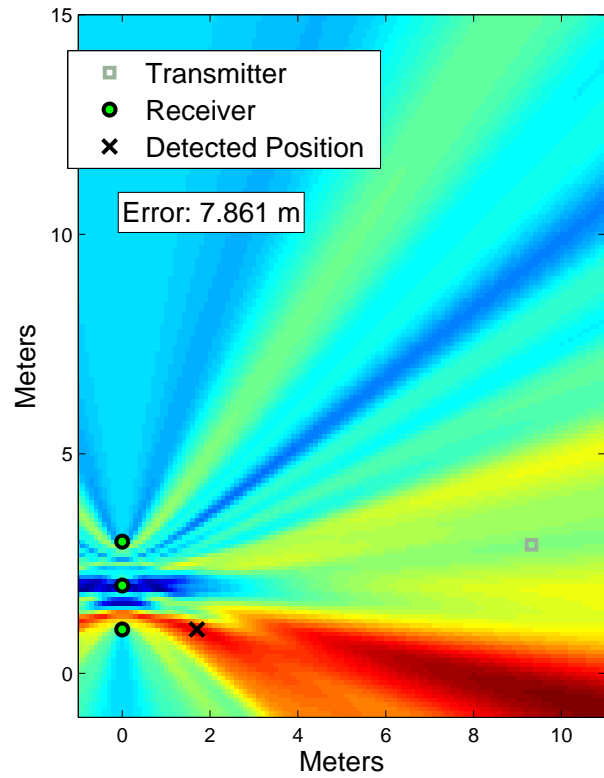
(b) SART
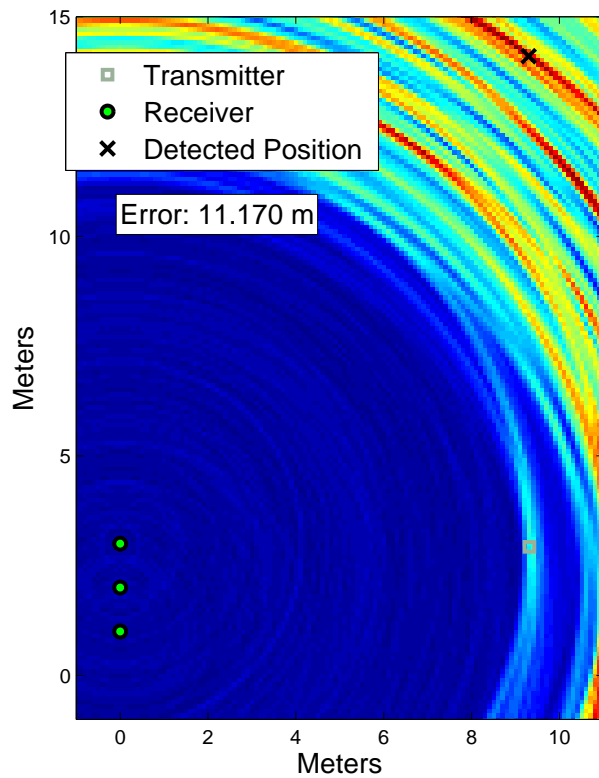
(c) TART

(d) CART

Figure C.5: Atwater Kent 3rd floor metric image examples using data from 3 survey points that produce the poor geometry: 2, 3, 4

Appendix D

Additional Location Metric Images for the AK317A Test
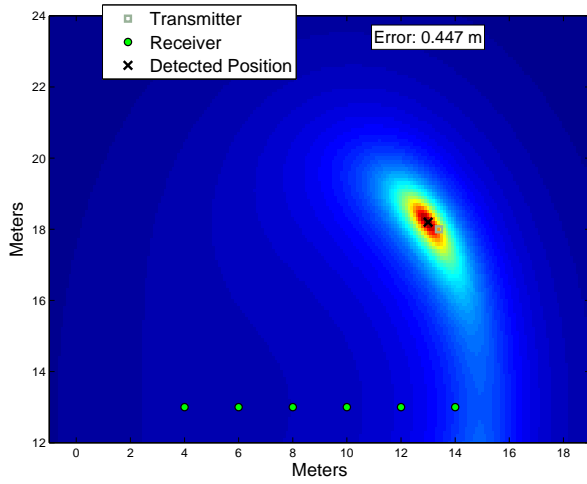
(a) LED
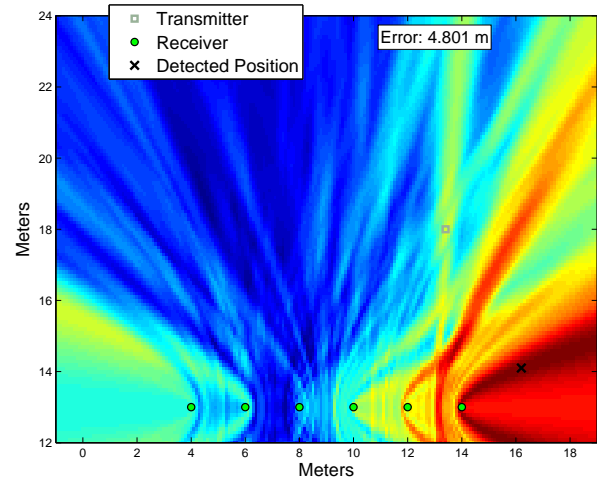
(b) SART
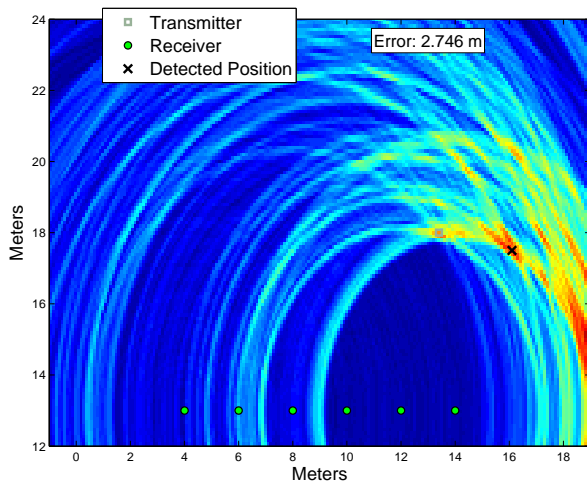
(c) TART
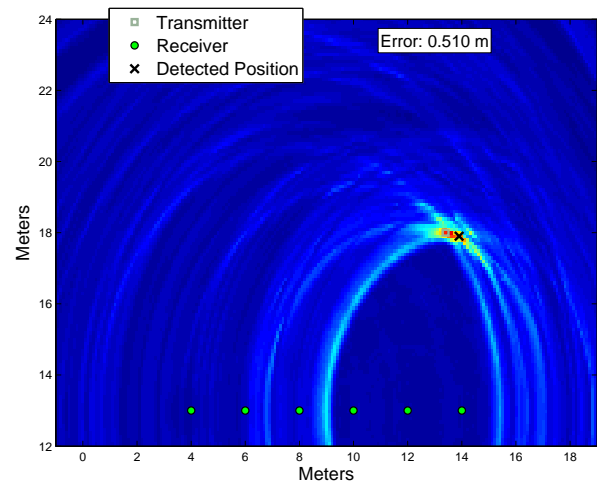
(d) CART

Figure D.1: Example metric images for a transmitter at survey point 21 using algorithms (a) LED, (b) SART, (c) TART, and (d) CART
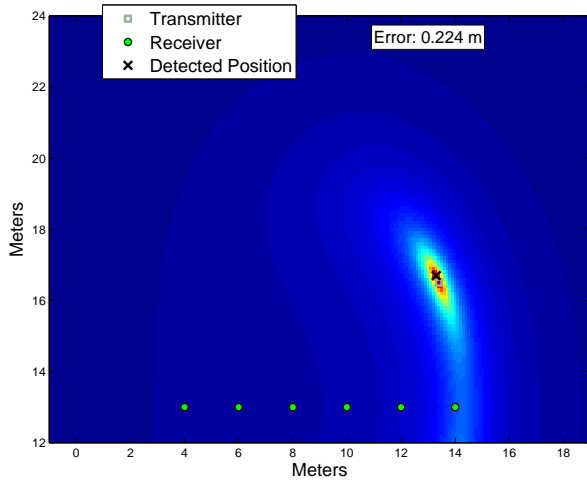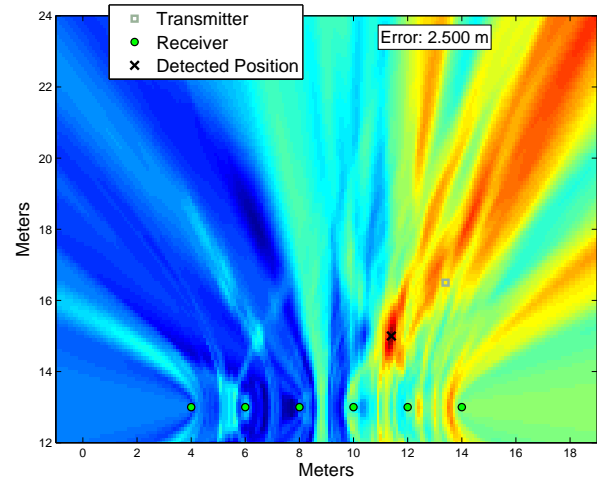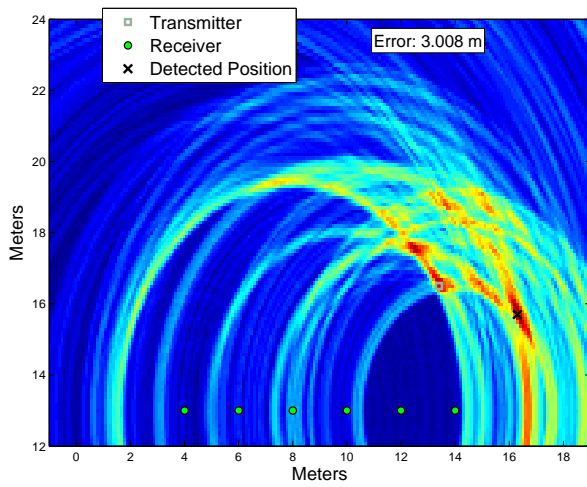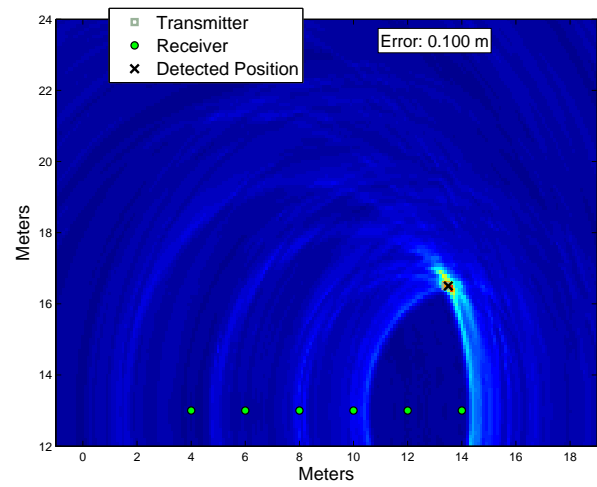
(a) LED

(b) SART

(c) TART

(d) CART

Figure D.2: Example metric images for a transmitter at survey point 22 using algorithms (a) LED, (b) SART, (c) TART, and (d) CART
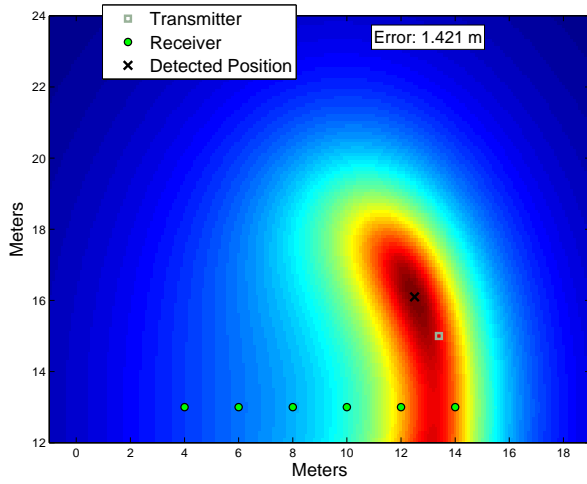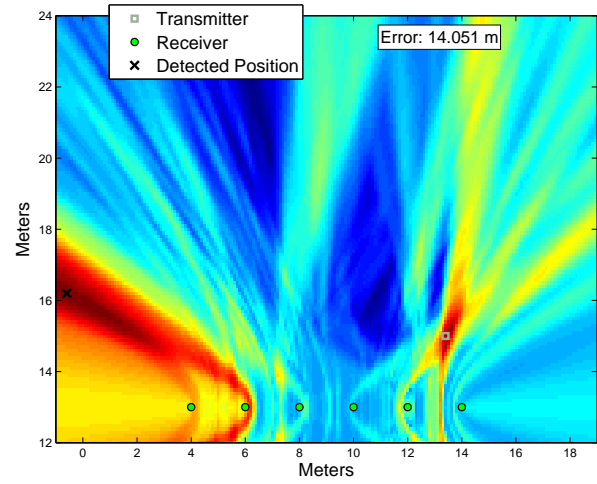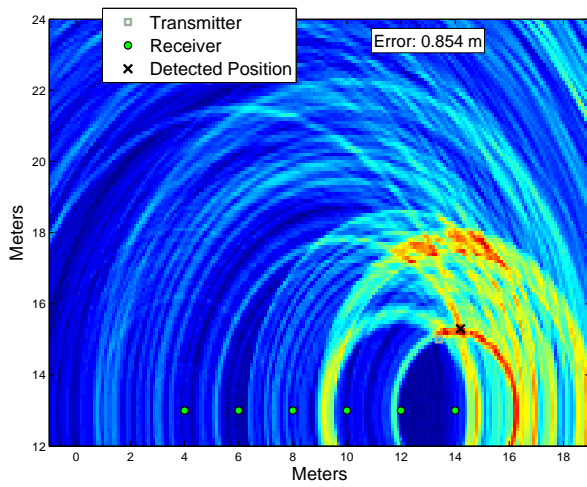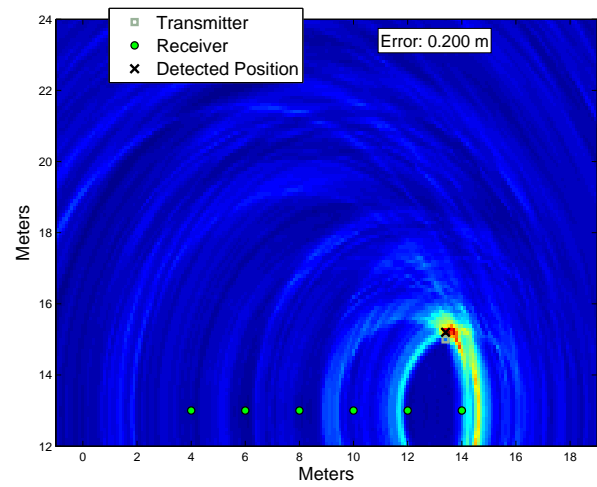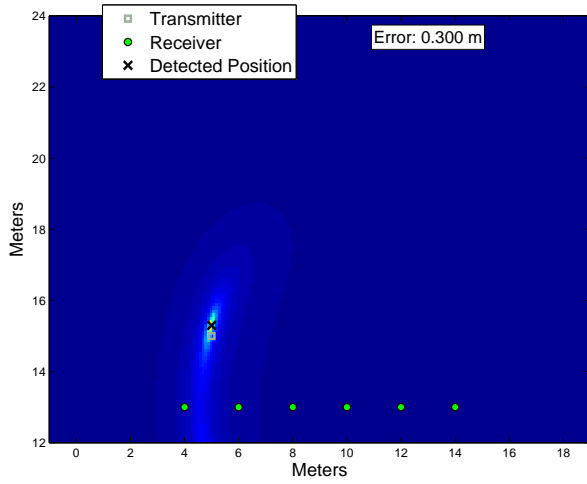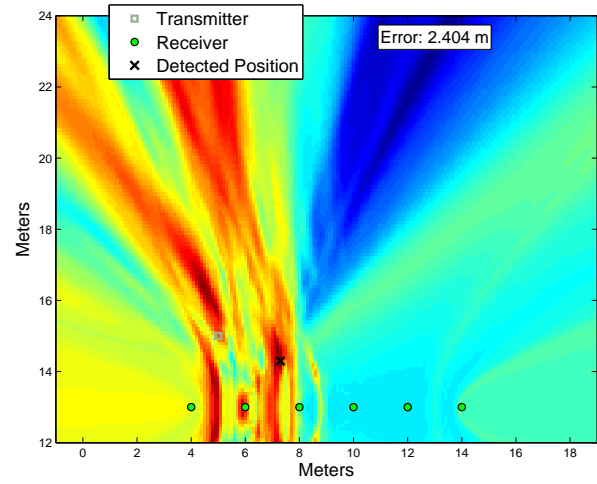
(a) LED

(b) SART

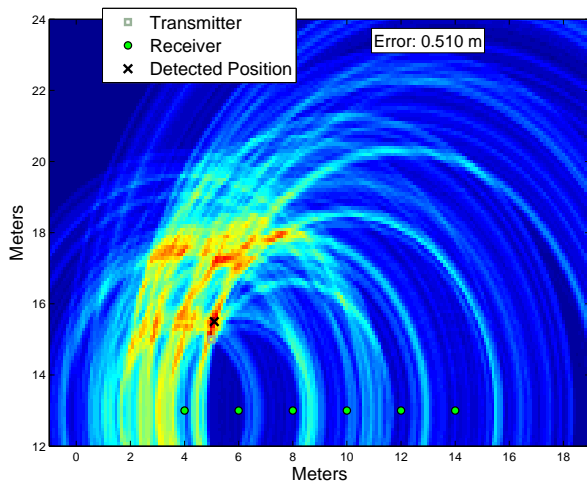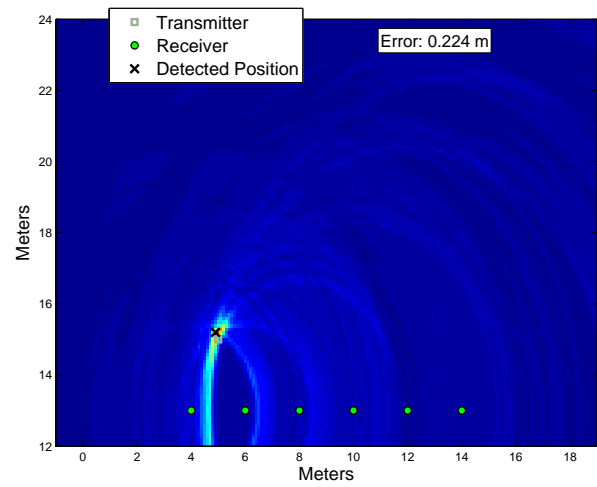(c) TART

(d) CART

Figure D.3: Example metric images for a transmitter at survey point 23 using algorithms (a) LED, (b) SART, (c) TART, and (d) CART

Figure D.4: Example metric images for a transmitter at survey point 28 using algorithms (a) LED, (b) SART, (c) TART, and (d) CART
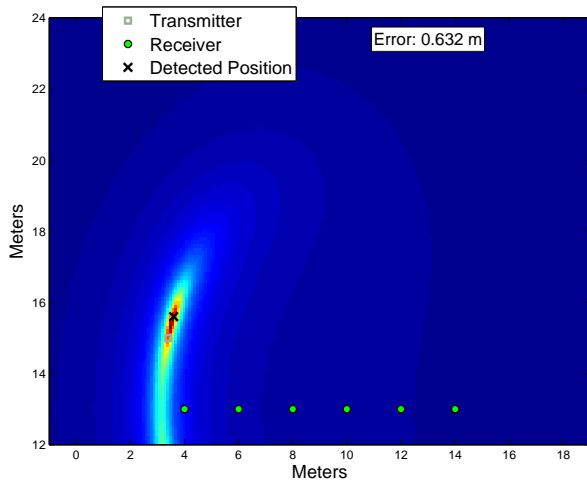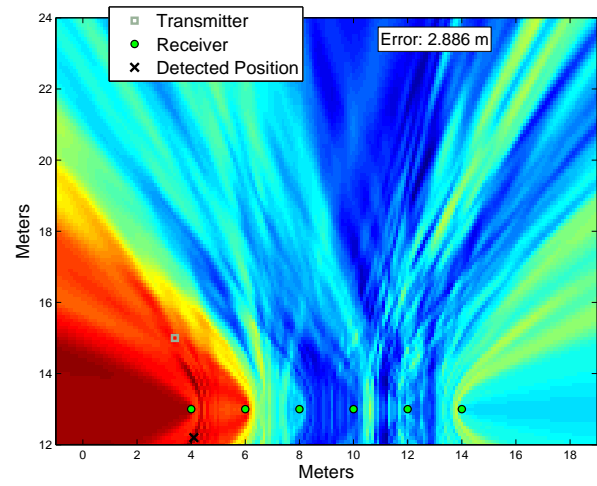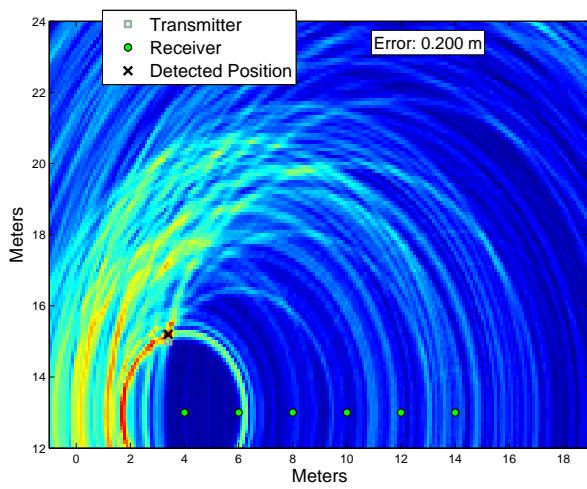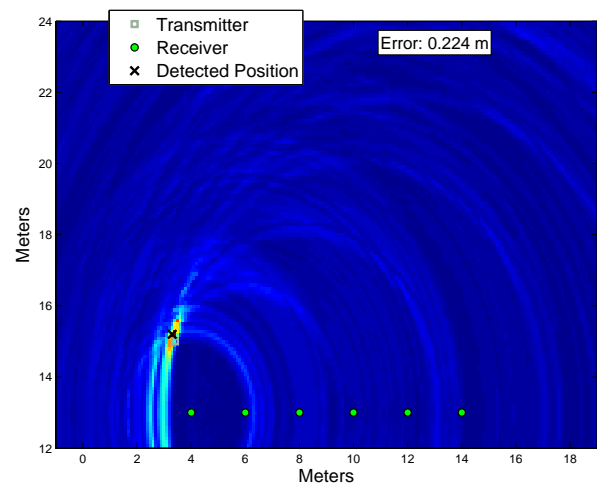
Figure D.5: Example metric images for a transmitter at survey point 29 using algorithms (a) LED, (b) SART, (c) TART, and (d) CART

Bibliography

[1] M. Z. Win and R. A. Scholtz, "On the robustness of ultra-wide bandwidth signals in dense multipath environments," *IEEE Communications Letters*, vol. 2, Feb. 1998.

[2] L. Li, A. E. Tan, K. Jhamb, and K. Rambabu, "Buried object characterization using ultra-wideband ground penetrating radar," *IEEE Transactions on Microwave Theory and Techniques*, vol. 60, Aug. 2012.

[3] S. Gezici, Z. Tian, G. Giannakis, H. Kobayashi, A. Molisch, H. V. Poor, and Z. Sahinoglu, "Localization via ultra-wideband radios," *IEEE Signal Processing Magazine*, 2005.

[4] N. Arrue, M. Losada, L. Zamora-Cadenas, A. Jiménez-Irastorza, and I. Vélez, "Design of an ir-uwb indoor localization system based on a novel rtt ranging estimator," *IEEE International Conference on Sensor Device Technologies and Applications*, 2010.

[5] M. Segura, V. Mut, and H. P. no, "Mobile robot self-localization system using ir-uwb sensor in indoor environments," *IEEE International Workshop on Robotic and Sensors Environments*, Nov. 2009.

[6] D. Dardari, A. Conti, U. Ferner, A. Giorgetti, and M. Win, "Ranging with ultrawide bandwidth signals in multipath environments," *Proceedings of the IEEE*, vol. 97, Feb. 2009.

[7] W. Ping, R. Huailin, and F. Fuhua, "A method of indoor multipath ir-uwb localization based on baysian compressed sensing," *IEEE International Conference on Signal Processing*, Oct. 2012.

[8] P. Closas, C. Fernandez-Prades, and J. A. Fernandez-Rubio, "Cramer-rao bound analysis of positioning approaches in gnss receivers," *IEEE Transactions on Signal Processing*, vol. 57, Oct. 2009.

[9] M. Navarro, P. Closas, and M. Najar, "Assessment of direct positioning for ir-uwb in ieee 802.15.4a channels," *IEEE International Conference on Ultra-Wideband*, 2013.

[10] J. Coyne, D. Cyganski, and R. J. Duckworth, "Fpga-based co-processor for singular value array reconciliation tomography," *International Symposium on Field-Programmable Custom Computing Machines*, Apr. 2008.

[11] D. Cyganski, R. J. Duckworth, J. Orr, and W. Michalson, "Precision location methods and systems," *United States Patent PTC/US2008/007446*, Dec. 2008.

[12] V. Amendolare, D. Cyganski, and R. Duckworth, "Transactional array reconciliation tomography for precision indoor location," *IEEE Transactions on Aerospace and Electronic Systems*, vol. 50, Jan 2014.

[13] S. Boonsriwai and A. Apavatjrut, "Indoor wifi localization on mobile devices," *IEEE International Conference on Electrical Engineering/Electronics, Computer, Telecommunications and Information Theory*, May 2013.

[14] J. Biswas and M. Veloso, "Wifi localization and navigation for autonomous indoor mobile robots," *IEEE International Conference on Robotics and Automation*, May 2010.

[15] O. Bialer, D. Raphaeli, and A. J. Weiss, "Maximum-likelihood direct position estimation in dense multipath," *IEEE Transactions on Vehicular Technology*, vol. 62, June 2013.

[16] O. Bialer, D. Raphaeli, and A. J. Weiss, "Efficient time of arrival estimation algorithm achieving maximum likelihood performance in dense multipath," *IEEE Transactions on Signal Processing*, vol. 60, Mar. 2012.

[17] V. Amendolare, D. Cyganski, and R. Duckworth, "Wpi precision personnel location system: Synchronization of wireless transceiver units," *Joint Services Data Exchange/Institute of Navigation Joint Navigation Conference*, June 2009.

[18] D. Kirchner, "Two way time transfer via communication satellites," *Proceedings of the IEEE*, vol. 79, Jul 1991.

[19] D. Dardari, A. C. andU. Ferner, A. Giorgetti, and M. Win, "Ranging with ultrawide bandwidth signals in multipath environments," *Proceedings of the IEEE*, vol. 97, Feb 2009.

[20] H. Kim, "Double-sided two-way ranging algorithm to reduce ranging time," *IEEE Communications letters*, vol. 13, Jul 2009.

[21] M. Kwak and J. Chong, "A new double two-way ranging algorithm for ranging system," *IEEE International Conference on Network Infrastructure and Digital Content*, Sept 2010.

[22] "Time domain," *www.timedomain.com*, 2014.

[23] D. Cyganski, R. J. Duckworth, S. Makarov, W. Michalson, and J. Orr, "Wpi precision personnel locatator system," *Institute of Navigation, National Technical Meeting*, Jan 2007.

[24] "Hadamard product," *https://en.wikipedia.org/wiki/Hadamard product (matrices)*, 2014.

[25] V. Amendolare, *Transactional Array Reconciliation Tomography for Precision Indoor Location.* PhD thesis, Worcester Polytechnic Institute, Apr 2010.

[26] A. Cavahaugh, *Inverse Synthetic Array Reconciliation Tomography.* PhD thesis, Worcester Polytechnic Institute, May 2013.

[27] A. F. Molisch, K. Balakrishnan, D. Cassioli, C. Chong, S. Emami, A. Fort, J. Karedal, J. Kunisch, H. Schantz, U. Schuster, and K. Siwiak, "Ieee 802.15.4a channel model - final report," 2004.

[28] R. Kaune, "Accuracy studies for tdoa and toa localization," *IEEE Information Fusion Conference*, July 2012.

[29] S. Kay, *Fundamentals of Statistical Signal Processing: Estimation Theory.* Prentice Hall, 1993.

[30] TimeDomain, "Part two: Uwb definition and advantages," *PulsON©Ranging and Communications*, June 2012.

[31] J. Johnson and B. Dewberry, "Ultra-wideband aiding of gps for quick deployment of anchors in a gps-denied ad-hoc sensor tracking and communication system," *ION GNSS*, Sept 2011.

[32] TimeDomain, "Ranging and communications application programming interface (api) specification," *PulsON 400 RCM*, vol. v2.1, June 2012.

[33] S. L. Marple, "Computing the discrete-time analytic signal via fft," *IEEE Transactions on Signal Processing*, vol. 47, Sept 1999.

[34] S. Stein, "Algorithms for ambiguity function processing," *IEEE Transactions on Acoustics, Speech and Signal Processing*, vol. 29, Jun 1981.

[35] "Pulseon cat: Channel analysis tool," *http://www.timedomain.com/cat.php*, 2014.

[36] "Time domain," *Using Channel Analysis Tool to Implement Multistatic Radar*, 2012.

[37] V. Varshney, "Source localization via near field signal processing," Master's thesis, Worcester Polytechnic Institute, February 2009.

[38] D. Simon, "Optimal state estimation: Kalman, h infinity, and nonlinear approaches," *John Wiley and Sons*, 2006.

[39] M. Lowe, "Inertial system modeling and kalman filter design from sensor specifications with applications to indoor localization," Master's thesis, Worcester Polytechnic Institute, May 2011.

[40] T. Tzanetos, "Embedded avionics with kalman state estimation for a novel micro-scaled unmanned aerial vehicle," Master's thesis, Massachusetts Institute of Technology, June 2013.

[41] M. Integrated, "Max3421e programming guide," DEC 2006.

[42] "Usb made simple," *www.usbmadesimple.co.uk*, 2013.

[43] "Usb 2.0 specification," *www.usb.org*, 2013.

[44] "Wikipedia minimum mean square error," *http://en.wikipedia.org/wiki/Minimum mean square error*, 2014.

[45] TimeDomain, "Data sheet," *PulsON 410*, June 2012.

[46] J. Youssef, B. Denis, C. Godin, and S. Lesecq, "New toa estimators within energy-based receivers under realistic uwb channel statistics," *IEEE Vehicular Technology Conference*, May 2010.

[47] A. Papoulis and S. Pillai, *Probability, Random Variables and Stochastic Processes, 4th ed.* McGraw Hill, 2002.